UNIVERSITÀ DEGLI STUDI DI PARMA

Ph.D. Program in Industrial Engineering
(XXX Ciclo del Dottorato di Ricerca in Ingegneria Industriale)

THE STATISTICAL CHARACTERIZATION OF GLASS STRENGTH: FROM THE MICRO- TO THE MACRO-MECHANICAL RESPONSE

A thesis submitted in partial fulfillment of the requirements for the Degree of

Doctor of Philosophy
(Dottore di Ricerca)

Advisor and Director of the graduate studies:
Chiar.mo Prof. Dr. Ing. Gianni Royer-Carfagni

Ph.D. Candidate:
Gabriele Pisano

Parma, Italy, 2014/2017

"Dr. Einstein, why is it that when the mind of man has stretched so far as to discover the structure of the atom we have been unable to devise the political means to keep the atom from destroying us?"
"That is simple, my friend. It is because politics is more difficult than physics!"

Albert Einstein

ABSTRACT

This work discusses an innovative micromechanically-motivated statistical characterization of the strength of annealed and heat-treated glass, with the aim of achieving a reliable definition of the mechanical properties of this material for structural applications also taking into account the effects of natural aging, thus avoiding either unsafe or redundant design.
The 2-parameter Weibull distribution, based upon the weakest-link-in-the-chain model, is by far the most common statistics to interpret the glass strength. However, its universal use has to be questioned, because comparison with the experimental evidence indicates that it cannot accurately interpret the left-hand-side tail of the population. This has very strong implications for structural design where the tails play the decisive role, because only very low probabilities of failure are tolerated. Starting from the observation that many experimental campaigns recorded in the technical literature seem to indicate that the measured strength of float glass cannot fall beyond a certain limit, even when the material is heavily damaged either naturally or artificially, we present arguments to support this conjecture. The lower bound can be attributed to factory production controls for marketed glass, which tends to discard the material that does not meet severe aesthetic and optical requirements. Since these are associated with the presence of surface cracks, the control should indirectly limit their depth and size, thus providing a threshold for the average strength according to well-established models in fracture mechanics. How the potential interaction between pre-existing cracks and cracks added by abrasion may affect the corresponding stress intensity factor is further discussed, demonstrating that the variation is in any case limited, and, consequently, the lower bound for the strength may be reduced, but not annihilated, by natural aging.
For a better interpretation of the aforementioned hypothesis, the connection between an assumed statistics for the crack-size population and the population of macroscopic strengths is further established. If one assumes a statistical distribution *à la* Pareto to interpret the variability of crack depths, the 2-parameter Weibull distribution is obtained for the strengths. Remarkably, the effect of an upper-truncation of the population of crack lengths, possibly consequent to factory production controls, provides a left-truncated Weibull distribution that excellently fits most of the experimental results for annealed float glass, at least when it is the air-side under tensile stress in bending. Other generalized Weibull statistics, either bounded or unbounded, have been considered for the sake of comparison. For each of them, proper expressions for data re-scaling, to take into account the effects of size, type of applied stress and subcritical crack propagation, are provided.
Certainly, aging in the form of corrosion or abrasion can produce a variation of the defectiveness scenario originally present on the glass surface. The established

correlation between the micro-defects and macroscopic strength allows to predict how the latter can be affected by variations in the defectiveness scenario. In particular, corrosion is assumed to be equivalent to the removal of a thin surface layer of glass, which reduces the depth of the micro-cracks, whereas abrasion consists in adding new defects to the pre-existing ones. This approach is used to interpret the difference in strength experimentally-measured at the tin-side with respect to the air-side, by assuming that the contact with the tin bath and the steel rollers during manufacturing is equivalent to a mild abrasion process.

This micro-macro approach is also employed to discuss the mechanical properties of heat-treated glass, where a compressive eigenstress is permanently induced by heating and successive cooling. Several experimental campaigns, recorded in the technical literature, have demonstrated that the characteristic strength of heat-treated glass can be much higher than the simple sum of the pristine material characteristic strength and the characteristic value of the prestress. A micromechanically-motivated cumulative probability function for the population of strengths of heat-treated glass is proposed, which accounts for the statistical interference between the mechanical properties of pristine glass and the eigenstress. The statistical interference is deeply affected by the applied state of stress: the benefic effect of the heat-treatment is maximum when the applied stress is uniaxial, minimum when this is uniform equibiaxial. This model justifies and confirms the results of experiments recorded in the technical literature. Moreover, an *ad hoc* experimental campaign has been conducted, from which it has been observed that the lower quantiles of the distribution are well interpreted by the statistical model, whereas the higher the quantile is, the higher is the distance between expected and observed data. This may be attributed to a further beneficial effect due to crack healing.

All the previous findings are applied to the calibration of material partial factors to be used in the semi-probabilistic (level I) method of design, in order to guarantee the target probability of failure established by structural standards. The calibration is made on paradigmatic case-studies, comparing the results with those obtainable with full-probabilistic (level III) methods of design. For annealed glass, the partial material factors calculated from the proposed statistics are much lower than those obtainable with a 2-parameter Weibull model. Moreover, heat-treated glass reveals a quite surprising strength capacity, which seems to have been hardly appreciated before.

The refined statistical models presented here, motivated on the basis of micromechanical considerations, should increase the confidence in the structural applications of glass, achieving its optimal exploitation and, thus, improving its competitiveness on the market with respect to other construction materials.

ACKNOWLEDGEMENTS

Firstly, I would like to express my sincere gratitude to my advisor Professor Gianni Royer Carfagni for his valuable guidance and for the continuous support of my graduate studies. His knowledge, experience and suggestions have been the basis for my scientific growth.

A special thank goes to Professor Jens Schneider for his kind hospitality in the nice city of Darmstadt and for the work carried out together on the characterization of heat-treated glass strength and on the calibration of partial factors for prestressed glass. He allowed me to perform an experimental campaign very important for my research program, and the insightful discussions incented me to widen my research.

Thank you also to Professor Roberto Ballarini for his precious contributions to the research of the best statistical model for the statistical characterization of float glass strength and to the calibration of partial material factors for annealed glass.

I must express infinite gratitude to my family for the endless support, whose value is inestimable.

I could never forget to thank my old friends. Despite the distance, they are always present in my life.

I cannot forget the true friends I met in Parma. They contributed to make these three years easier to live far from my girlfriend and from my family, and they are now part of my life.

Thanks to all the fantastic guys that I met at the Institute of Structural Mechanics and Design of the Technical University of Darmstadt, who helped to make the period I spent in Germany one of the most intriguing experiences of my life.

Finally, a special word goes to Viviana, simply because she puts up with me since so many years, and this is not so easy.

TABLE OF CONTENTS

CHAPTER 1

INTRODUCTION

1.1 Glass: an "innovative ancient" material

Many researchers think that the first forms of primitive glass were probably developed in the Mitannian or Hurrian region of Mesopotamia 5000 years before Christ, as an extension of the production of glazes [24]. In that era, a new material called faience was developed in Egypt, constituted by a glaze layer over a silica core. Traditionally, the Ancient Mesopotamians are considered the first producers of glass as an independent material around 3,600 years ago. However, in the last years, some researchers have questioned about this hypothesis, claiming that Mesopotamians may have created second-rate knock-offs of glass objects from Egypt. The techniques for making colorless glass were discovered in Syria and Cyprus, in the 9th century BC. Furthermore, cuneiform tablets discovered in the library of the Assyrian king *Ashurbanipal* contain instructions on how to make glass. The Romans began to use glass for architectural purposes from *circa* the year 100 AD, when clear glass, albeit with poor optical quality, were discovered in Alexandria. Cast glass windows appeared in the most important buildings of Rome and the most luxurious villas of Herculaneum and Pompeii.

The first glass factory in the United States was built in Jamestown, Virginia in 1608. The process by *George Ravenscroft*, invented in 1674, made glass easier to melt and improved its optical properties. In the middle of the XVIII century, *De Nehou*'s process of rolling molten glass poured on an iron table led to the production of very large plates. In the 1851, *Joseph Paxton* built the *Crystal Palace* to house *The Great Exhibition*, whose illustration is shown in Figure 1.1(a). This building revolutionized the public use of glass as a material for domestic and horticultural architecture.

Several processes were patented between the middle of the XIX and the middle of the XX centuries to advance the automating in glass manufacturing. The revolutionary float glass process was developed by *Sir Alastair Pilkington* and *Kenneth Bickerstaff* of the UK's Pilkington Brothers between 1954 [15] and 1959 [16]. In this process, a continuous ribbon of glass is formed using a molten tin bath on which the glass paste flows, providing uniform thickness and very flat surfaces to the sheet. The success of this process was mainly due to the balance of the volume

(a) (b)

Figure 1.1: (a) Illustration of The Great Exhibition of 1851 at the Crystal Palace. (b) Model factory at the Werkbund exhibition in Cologne (1914) by Walter Gropius and Adolf Meyer.

of glass fed onto the bath, where it was flattened by its own weight. Today, the 90% of marketed glass is still manufactured through the float process.

Since the first decades of the XX century, glass transparency, together with its mechanical properties and its durability, gave the green light to a completely novel approach for thinking and designing civil structures. Glass in architecture applications allowed to preserve the interior spaces, without inhibiting the view to the outside. Thus, the design of the interior spaces was strictly related to the outside. Already in the 1910s, some of the maximum exponents of the European architecture, such as *Mies van de Rohe* and *Walter Gropius*, tried to minimize the size of the structural components so as to make the most of glass transparency. Figure 1.1(b) shows the model factory designed by Walter Gropius and Adolf Meyer for the Werkbund exhibition in Cologne in the 1914. Through the decades, glass has increased its appeal upon designers and architects, whose challenge has been to find new forms of transparency and amazing lighting effects.

The main factor that has limited the structural role of glass is certainly its brittle nature, together with the possibility of spontaneous breakages due to the presence of inclusions. In recent years, glass has overcome its traditional role of simple infill-panels, to acquire a well-defined structural identity. This represents the last step for glass in architecture, which has given an innovative function to this "ancient" material, employed nowadays for balustrades, load-bearing beams, floors, roofs, stairs and frames. Remarkably, the demand for architectural glass, which accounts for approximately 80% of glass production, has increased by 5% per annum since 2009. The "*Nuvola*" by *Massimiliano Fuksas* shown in Figure 1.2(a), designed in the 1998 and inaugurated in Rome in the 2016, certainly represents a remarkable and recent example of transparent structure. Another famous buildings whose load-bearing components are all made of glass is the Apple Store located in Shangai, shown in Figure 1.2(b), made with glass panels of 12 m in height.

Nowadays, the challenge for designer and architects is to best exploit the optical and aesthetic properties of this material. Many companies are actively involved in this challenge and, year by year, larger and larger plates are produced (monolithic glass of geometry up to 3.51 m $\times$ 20 m will be manufactured in the 2018). At the

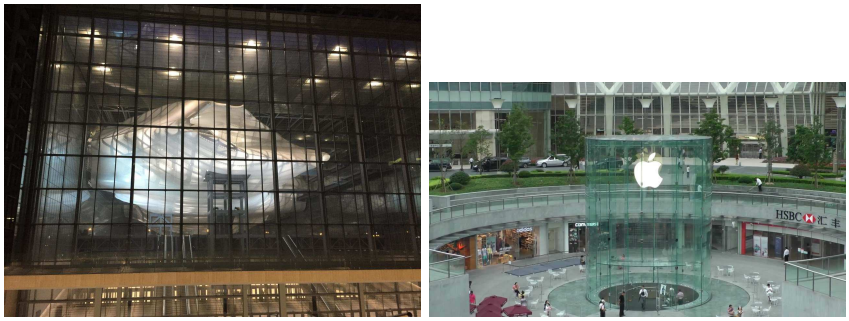

(a) (b)

Figure 1.2: (a) Fuksas' "Nuvola" in Rome, designed in the 1998 and inaugurated in 2016. (b) Apple store in Shangai.

same time, researchers are engaged in improving the understanding of the structural glass capacity, in order to meet the requirements prescribed by standards in terms of safety and serviceability for structural members. Certainly, the reliability of any structural design is definitely based upon the capability of determining the material strength with the appropriate degree of accuracy. The knowledge about the mechanical and statistical characterization of float glass strength still has "dark spots", because of which extremely cautious verification formula and safety factors are used in the structural design of elements made of glass. Hence, the correct statistical modeling of glass strength, based on micro-mechanical motivations, is certainly of paramount importance for the optimization of the use of the material in the engineering design and, consequently, for the improvement of its competitiveness on the market.

1.2 Research objectives and scopes

The main scope of the current research project is to improve the statistical modeling of glass strength, either annealed or heat-treated or abraded/corroded, so as to optimize the use of this material in structural design. To this aim, the relationship between micro-crack lengths and macroscopic material strengths distributions is analyzed, taking into account the effects of variation in the defectiveness scenario upon the distribution of glass strengths. More specifically, the principal objectives and scopes of this research are:

- To establish a reliable statistical model for interpreting glass strength variability, corroborated by micromechanically-motivated considerations. The statistical analysis is explicitly focused on the left-hand-side tail of the distribution of strengths, since only this part of the population substantially affects the structural design.
- To explain why the distributions of strengths for the air-side and the tin-side are different-in-kind.
- To present a micro-mechanical approach for studying the variations in the statistical distribution of the macroscopic strengths distribution as a con-

sequence of changes in the defectiveness scenarios, induced by abrasion or corrosion processes.

- To propose a refined statistical model for the distribution of the strengths of heat treated glass, which accounts for the statistical interference with the distribution of the heat-induced compression eigenstress. Such a statistical interference certainly depends upon the type of applied stress (equibiaxial vs. uniaxial).

- To calibrate on a statistical basis partial material factors for the structural design of float glass. How the use of different statistical distributions for interpreting annealed glass strengths variability affects the values of the resulting partial factors is investigated. Remarkably, many standards suggest values that are chosen on basis of technical experience, while only recently partial material factors have been calibrated on a statistical basis by using the 2-parameter Weibull model, but the so-obtained values are extremely high and, consequently, they are hardly accepted by industries and designers.

- To calibrate on a statistical basis the partial safety factors associated with the heat-induced surface prestresses in heat-strengthened and toughened glass.

1.3 Outline

This thesis is divided into seven chapters, including the introductive Chapter 1, and five appendixes. The chapters are organized as follows:
Chapter 2 - The main technological and mechanical aspects of glass for structural applications, in particular soda-lime float glass, are illustrated. The material mechanical properties are summarized and the float and the tempering processes are described.
Chapter 3 - A micro-mechanically motivated model is proposed for interpreting the annealed glass strength variability, which spells out the connection between crack size population and the strength statistics. The effect of an upper-truncation of the population of crack lengths upon the glass strengths distribution, induced by the factory quality controls, is investigated. Arguments are presented that support the existence of a lower bound for strength. Various generalized statistical distributions *à la* Weibull, either providing or not a lower bound, are compared in their ability at interpolating experimental data.
Chapter 4 - The statistical interference between the distribution of strengths in the pristine material and the corresponding distribution for surface compressions, induced through thermal treatment, is analyzed. A micro-mechanically motivated model is proposed to study how a deviation from the equibiaxiality in the stress state affects the failure probability. The results of a properly-designed experimental campaign performed at the Technical University of Darmstadt are recorded and the ability of the proposed model at interpolating the experimental data is discussed.
Chapter 5 - A micro-mechanical derivation of the macroscopic strengths statistics for corroded or abraded float glass is presented. How potential variations in the defectiveness scenario due to natural corrosion or abrasion phenomena may affect the statistical distribution of pristine glass strength is discussed. By considering the tin-side of float glass as a mildly abraded surface, due to the contact with the

tin bath and the steel rollers during the production process, the difference in the strengths distribution between the air-side and the tin-side is interpreted.
Chapter 6 - Partial material factors have been calibrated, in order to guarantee the target failure probability in glass structures according to the semi-probabilistic (level I) method of design. Calibration is made by comparison with results obtainable with the full-probabilistic approach (level III) on paradigmatic case studies, by interpreting float glass variability with various generalized Weibull distributions. The so-obtained partial factors are compared with those previously obtained with a 2-parameter Weibull model. The partial safety factors associated with the heat-induced surface prestress in strengthened and tempered glass are also calibrated, by comparison with fully probabilistic methods in paradigmatic examples.
Chapter 7 - Conclusions from this study are given and the principal findings are summarized. Contributions and recommendations for further research are recorded.

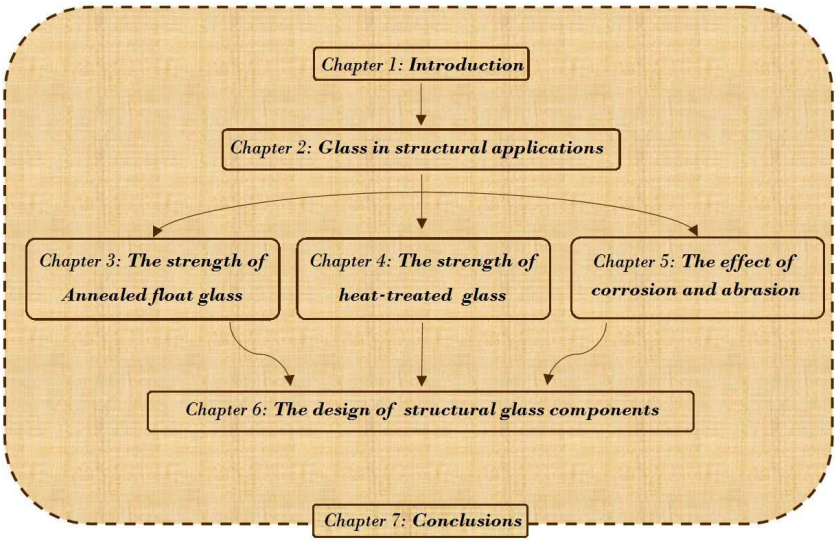

Figure 1.3: Organization of the chapters.

The material treated in the Appendixes is the following:
Appendix A - Different unbounded and bounded generalized Weibull distributions, based upon the weakest-link-in-the-chain rationale, are presented. The physical motivations underlying these distributions are discussed. The graphical methods for the estimation of the statistical parameters characterizing the various generalized distributions are illustrated. The Chi-square statistical test for evaluating the goodness of fit with the experimental data exhibited by a statistical model is shortly described.
Appendix B - A deep analysis of the stress state acting within a specimen tested under Coaxial Double Ring (CDR) configuration is presented, both in the linear and in the non-linear regime. An analytical expression for the effective area, according to the 2-parameter Weibull model, is proposed. An overview of the most used standardized testing configurations is recalled with particular reference to the

CDR test, for which a new set-up is proposed.
Appendix C - The probabilistic models for wind loads and snow loads, recorded in the Eurocode (EN 1991-1-3 and EN 1991-1-4), are recalled.
Appendix D - The main aspects of the normal and of the log-normal distributions are summarized. Methods for the parameter estimation and for investigating the deviation from normality (or log-normality) are illustrated.
Appendix E - Tables summarizing all the relevant data corresponding to the measurement and experimental campaigns described in Chapter 4 are recorded.

CHAPTER **2**

GLASS IN STRUCTURAL APPLICATIONS

2.1 The "float" process

Today, the float process is by far the most used manufacturing process, accounting for about the 90% of flat glass production worldwide, thanks to its wide applicability, the optical quality of the so-obtained glass panes, the possibility of reliably producing large panes and the low cost

The production process is divided in different stages, schematically shown in Figure 2.1. The raw materials, strictly controlled for quality, are mixed to make batch and, then, melted in a furnace at 1500°C. Several processes take place in the furnace simultaneously, e.g., melting, refining and homogenizing, which delivers smooth glass almost free from inclusions and bubbles. The molten glass is then continuously poured on a bath of molten tin, starting at 1100°C and leaving the float bath as a solid ribbon at 600°C. The tin has always been used since 1950s thanks to the large temperature range of liquid state and the high specific weight. In the original process, while floating on the tin bath, glass paste reached an equilibrium thickness of 6.8 mm, it was gradually cooled and, then, it passed on steel rollers before entering a long oven (lehr) at 600°C. Differently from the process patented in the 1950s, today's glass plates have thicknesses in the range of 2 mm to 25 mm. The higher the roller speed is, the lower is the plate thickness and *vice-versa*. During the cooling, considerable stresses can develop in the ribbon, and this is why the annealing lehr cools the glass slowly, while the temperature is strictly controlled both along and across the lamina. After annealing, automated machines inspect the products. The parts of glass ribbon with visual defects and imperfections are removed during cutting, and the waste glass is collected and fed back into the furnace. Finally, the glass is cut through diamond wheels and, then, stored. Coatings can be applied before annealing when profound changes in the optical properties of the material are required.

Since during the production process one external surface is exposed to air, whereas the other one is in contact with the tin bath and steel rollers, the two faces of glass sheets present some substantial differences. Different defectiveness scenarios are present on the two surfaces: this is why the mean value of the mechanical strength of the tin-side is usually lower than the one of the air-side. At the same time,

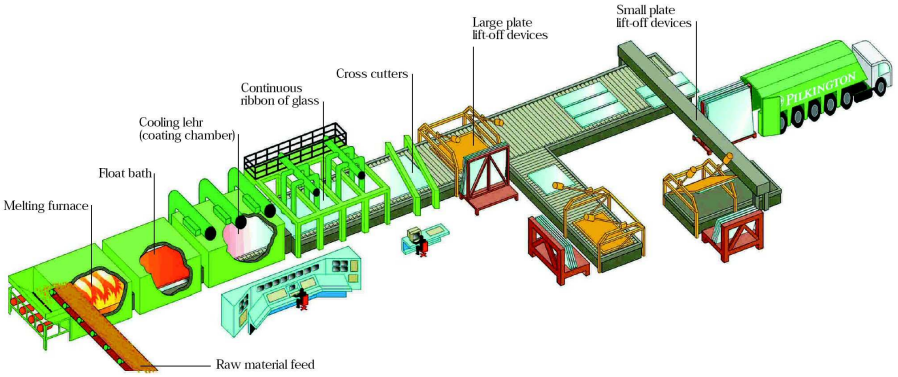

Figure 2.1: Schematic of the "float" production process. Image from https://www.pilkington.com/resources/floatplant.jpg.

the dispersion of tin-side strength distribution is lower than for air-side strength. Furthermore, some diffusion of tin atoms into the glass surface occurs, which may affect the bonding with polymeric interlayers during lamination. The tin-side can be differentiated from the air-side thanks to its bluish fluorescence when exposed to short-wave ultraviolet radiation (UV-C).

Float glass is often subjected to further processes, which can vary its shape, performance and appearance, so to meet particular requirements. This secondary processing may include edge working, curving, thermal treatments, heat soaking (to reduce the potential for nickel-induced breakages in use), laminating, surface modification processes and insulating glass unit assembly. The mass production process, together with many post-processing phases refined trough the last 50 years, have made glass cheap enough to make it very attractive for architectural applications.

2.2 Material properties

Glass behavior does not exhibit a plastic phase, such as metallic materials, and, furthermore, it is not able to develop the diffused micro-cracks which enable the anelastic mitigation of stress concentrations, as in quasi-brittle materials like concrete. Its mechanical response is almost perfectly linear elastic up to failure and isotropic. Thus, differently from the most classical structural materials, local stress concentrations cannot be disregarded.

The theoretical tensile strength of the pristine glass, i.e., without any defect, may reach 32 GPa [86]. However, the tensile strength exhibited by glass plates under bending is much lower, and generally it does not exceed 100 MPa. Since glass does not yield plastically (local stress concentrations are not reduced through stress redistribution), micro-cracks, which are unavoidably present on the external surfaces of the glass plates, govern glass fracture. Such micro-cracks are generally not visible to the naked eye and the nature of their size, shape and distribution is strongly probabilistic. Flaws open almost exclusively in mode I and, hence, fracture occurs when the combination of crack depth and tensile stress at right

angle with crack axis reaches a critical value. Because of the sensitivity to the underlying flaws, the macroscopic strength is affected not only by the maximum tensile stress acting within the plate, but also by the size of the specimen and by the acting state of stress. In fact, the higher is the specimen size, the higher is the probability of finding a crack in critical conditions. Moreover, the probability of finding the maximum principle tensile stress at right angle with the crack axis is 100% if the stress state is equibiaxial, whereas it is lower for a generic state of stress and minimum if the state of stress is uniaxial. Of course, this further source of uncertainty affects the distribution of the macroscopic strengths. Moreover, flaws can grow over time even when subjected to tensile stresses much lower than the critical value, because of a phenomenon referred to as *subcritical crack growth* or *static fatigue* [100]. It is then clear that mechanical strength of glass should be evaluated in accordance with a model of fracture mechanics and it is strongly non-deterministic. The compressive strength of glass is obviously not affected by the presence of surface flaws and, hence, it is much higher than the tensile strength.
Soda lime silica glass (SLG) is by far the most used in construction. However, the borosilicate glass (BSG), which guarantees optimal hydrolytic and acid resistance and very high resistance to temperature changes, is preferred for special applications, such as fire protection glazing and heat resistant glazing. The chemical compositions of soda lime silica and borosilicate glasses according to the European Norms EN 572-1 [40] and EN 1748-1-1 [36] are recorded in Table 2.1. It is well-known that glass micro-structure is amorphous, and, for soda lime silica glass, it is constituted by an irregular network of silicon and oxygen atoms with alkaline parts in between. The transition between liquid and solid state takes place over a certain temperature range and no crystallization takes place.

Table 2.1: Soda lime silica glass and borosilicate glass. Chemical compositions according to EN 572-1 and EN 1748-1-1.

		SLG	**BSG**
Silica Sand	SiO_2	69-74 %	70-87 %
Lime (calcium oxide)	CaO	5-14 %	-
Soda	Na_2O	10-16 %	0-8 %
Boron oxide	B_2O_3	-	7-15 %
Potassium oxide	K_2O	-	0-8 %
Magnesia	MgO	0-6 %	-
Alumina	Al_2O_3	0-3 %	0-8 %
others		0-5 %	0-8 %

The most relevant physical properties of soda lime silica and borosilicate glass are recorded in Table 2.2. Some properties of the material change consistently with the chemical composition, e.g., the melting temperature of a pure silica oxide passes from about 1700°C to 1300°C-1600°C by adding alkali, and the thermal expansion coefficient passes from $0.5\,10^{-6}\,K^{-1}$ to $9\,10^{-6}\,K^{-1}$ by adding soda.
One of the most attractive properties of glass is its excellent chemical resistance to many aggressive elements, and this is why it is one of the most durable material in structural works. The most evident optical and aesthetic property of glass is the

Table 2.2: Soda lime silica glass and borosilicate glass. Physical properties according to EN 572-1 and EN 1748-1-1.

			SLG	**BSG**
Density	ρ_g	kg/m^3	2500	2200-2500
Knoop hardness	$HK_{0.1/20}$	GPa	6	4.5-6
Young's modulus	E	MPa	70000	60000-70000
Poisson's ratio	ν	-	0.23	0.2
Coefficient of thermal expansion	α_τ	$10{-}6$ K^{-1}	9	3.1-6
Specific thermal capacity	c_p	J kg^{-1} K^{-1}	720	800
Thermal conductivity	λ	W m^{-1} K^{-1}	1	1
Average refractive index within the visible spectrum	n	-	1.52	1.5
Emissivity	ϵ	-	0.837	0.837

very high transparency within the visible range of wavelengths. For what concerns soda lime silica glass, the reflection of visual light is 8%, but the application of special coatings can improve its transparency. On the other hand, UV radiations are mostly absorbed, because of the interaction with O_2-ions in glass, and long-wave infrared radiations are absorbed by Si-O-groups. That is why the interior of a greenhouse is heated thanks to the visual light, while emitted long-wave thermal radiations cannot go out. The dynamic viscosity of glass is extremely high, as it is about 10^{20} Pas at room temperature.

2.3 The tempering process

The tempering process induces a residual stress field characterized by compressive stresses acting within the external layers of the glass plate and tensile stresses in the core part of the pane. This is a very efficient way for strengthening glass. Since volume cracks are rarely present within the thickness, the core part of a plate offers a tensile strength very close to the theoretical one. On the other hand surface cracks can only grow if exposed to opening stresses. Thus, as long as the tensile surface stress due to external actions is smaller than the residual compressive stress, the probability of fracture occurrence is null in practice (Figure 2.2).
The thermal process consists of heating the float glass plate up to approximately 100°C above the transformation temperature ($\cong$ 620 - 675°C), and then rapidly cooling through cold air jets. At the beginning of the process, the cooling gives rise to tensile stresses in the external layers, which solidify more rapidly than the internal layers, and compressive stresses in the core part. However, the tensile stress rapidly relax thanks to the viscous nature of glass in this temperature range. The glass pane solidifies and relaxation stops as soon as the temperature on the glass surface falls below T_g (approx. 525°C). Observe that an incorrect starting temperature could cause failure, since relaxation does not turn up and residual tensile stresses remains within the external surfaces of the pane. At this point, the interior core is hotter than the external surfaces and the temperature profile is approximately parabolic through the thickness. When even the interior has cooled, the characteristic residual eigenstress is such that the surfaces are under compression and the interior in tension. Residual stresses $\sigma_R(z)$ are usually assumed to follow

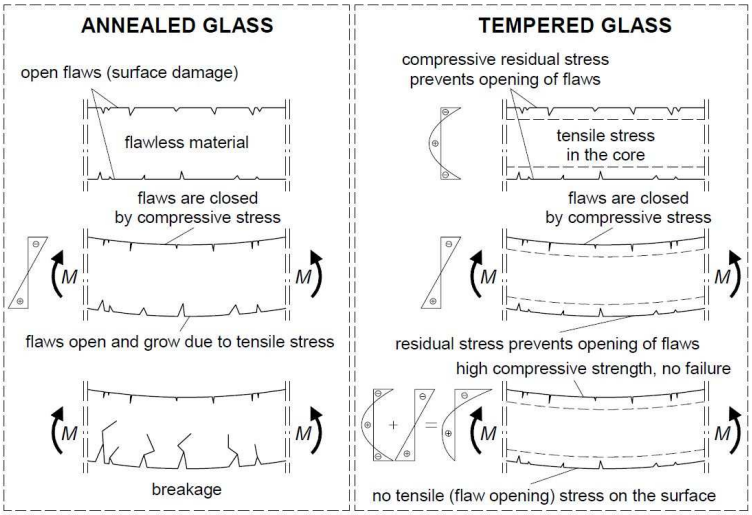

Figure 2.2: Stress profiles in annealed and heat-treated glass [49].

a parabolic curve across the thickness [23], in the form

$$\sigma_R(z) = \sigma_{pc}\left[1 - 6\frac{z}{h} + 6\left(\frac{z}{h}\right)^2\right], \tag{2.1}$$

where σ_{pc} is the residual stress acting within the external surfaces, z is the distance from the external surface of the plate and h is the plate thickness. From equation (2.1) one can notice that the plate is under compressive stresses on both the faces down to a depth of approximately 20% of the thickness, which is generally much larger than the depths of the cracks normally present on the surface[1]. Two main types of heat treated glass exist: heat strengthened and toughened. These are produced by using the same process, but with different cooling rates. The higher the cooling rate is, the higher the residual stresses are. The typical residual compressive surface stresses varies between 80 MPa and 150 MPa for toughened soda lime silica glass and between 40 MPa and 80 MPa for the heat strengthened glass. The residual stresses on the surface of tempered glass panels may vary both *locally*, generally depending upon the distance from the cooling jet, and *globally*, since near the edges and corners they are considerably different than in the middle part of the panels. To mitigate the "point by point" variation, the industrial practice is to increase the cooling rate and to let the plates oscillate during cooling [20]. Because of its low thermal expansion coefficient, borosilicate glass is difficult to temper. On the other hand, the common tempering procedure for thick plates cannot lead to the expected residual stress field: this is why glass panes of thickness higher than 12 mm cannot be heat treated using the ordinary process.

[1]However, this may not be true for very thin glasses, whose use in architectural applications has been recently explored [57].

Since the 1940s, several models have been proposed to characterize glass behavior during the tempering process. The classical "instant freezing" theory developed by *Bartenev* [11] in 1948 is based on the hypothesis that the liquid glass is suddenly changed into an elastic glass solid at the transition temperature (T_g). In the "viscoelastic" theory, *Indenbom* [50] took into account the relaxation of stresses. *Narayanaswamy* [63, 62] developed a model accounting for both the states of the structure, i.e., the structural relaxation and stress relaxation due to the viscoelastic response. Today, it is possible to numerically model the tempering process with great accuracy [83, 66]. This is certainly of importance for estimating tempering eigenstresses when the geometry is complex, such as for boreholes.

The size of the fragments that constitute the fracture pattern of broken heat-treated glass is a function of the energy originally stored in it. The highest the residual stress is, the lower is the size of size fragments. The fracture pattern of heat strengthened glass is more similar to annealed glass, with much bigger fragments than for toughened glass. When heat-strengthened material is used in laminated glass elements, this large fracture pattern results in a significant post-breakage structural capacity.

A tempering process alternative to the thermic one is the chemical tempering, but more expensive, which is based on the exchange of sodium ions in the glass surface by potassium ions. As it is evident from Figure 2.3, its residual stress profile is completely different from that of (2.1), in particular, the compressive stresses affect a thickness of approximately 0.04 mm. When the crack exceeds the compressive zone, the strengthening due to the increase in surface compression σ_{pc} is subject to saturation. Moreover, subcritical crack growth occurs without external load for surface flaws that are deeper than the compression zone, and very deep cracks could lead to catastrophic failure because of the presence of very high tensile stresses in layers of the plate that are not far from the external surfaces. Thus, the use of chemically-tempered glass in structural applications should be considered with extreme care.

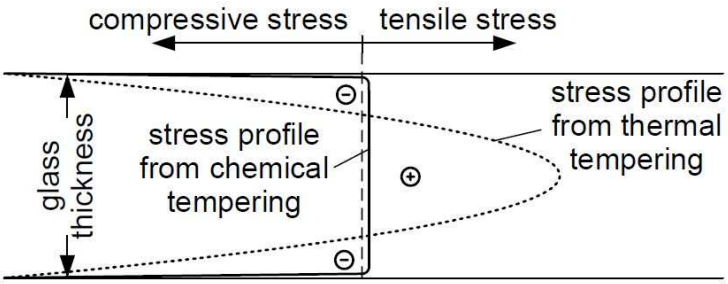

Figure 2.3: Stress profile in chemically-tempered glass [49].

Heat treated glass elements can spontaneously break because of the presence of nickel sulfide (NiS) inclusions. This presence is not common, but not negligible. NiS particles are subjected to a phase change under the influence of temperature, by increasing in volume by about the 4%. When such expansion takes place in the interior part of a panel, subject to the higher tensile stresses, micro-cracks

are formed and the collapse may occur instantaneously or after a certain period because of the subcritical crack growth. International standards and guidelines provide the heat-soak-test to mitigate the risk of spontaneous fracture due to inclusions, which consists in slowly heating up the glass and maintaining a certain temperature for several hours, so as to accelerate the phase change, and to make glass elements containing dangerous inclusions collapsed during the test.

CHAPTER 3

THE STRENGTH OF ANNEALED FLOAT GLASS

The statistical interpretation of the strength of brittle materials, and of glass in particular, has been investigated by many scientists. Most of them concluded that the 2-parameter Weibull model, described in Section A.2, was not to be rejected, although its fit with the experimental data is not good. Other researchers have emphasized the fact that material strength does not seem to fall below a certain lower limit [30, 56]. Since the strength of glass is governed by randomly distributed surface flaws that can propagate catastrophically when the applied stress reaches a critical value, a well-accepted micro-mechanically motivated model is here recalled, which spells out the connection between crack population and strength statistics [72]. It will be demonstrated that, through this model, one can reach a very accurate interpretation of the glass strength population, in particular for the lowest values.

3.1 Fracture mechanics

The theoretical strength of glass, calculated as the required force to break the covalent bonds between silicon and oxygen, has been estimated to be around 32 GPa [10], but glass plates generally break for stresses lower than 100 MPa. Such massive difference between the theoretical and practical failure stress of glass is due to the unavoidable presence of cracks on the external surfaces of marketed glass plates.

Glass mechanical behavior is almost perfectly elastic, and this is why the Linear Elastic Fracture Mechanics (LEFM) is usually considered.

Inglis [51] studied, already in the 1913, the stresses in a plate due to the presence of cracks and sharp corners. He found the exact solution for determining the stresses around an elliptic hole. Hence, such a solution applied to the extreme limits of form which an ellipse can assume, in particular, by making any of the axes very small, could be used to estimate the stresses due to the existence of a fine straight crack. He noted that holes and notched could amplify the average applied stress, justifying why a fine scratch made on the surface of brittle materials produces a local weakness that can be brought about by applied forces that produce insignificant stresses in the rest of the plate.

By starting from the work by *Inglis* [51], *Griffith* [48] in the 1920s developed an energy balance theory, according to which the total decrease in potential energy due to the formation of a crack is equal to the increase in strain energy less the increase in surface energy.
Irwin, by using the method for solving elastic crack problems developed by *Westergaard* [98], obtained the singularity term in the elastic crack tip stress field series expansion [52]. The original idea of *Irwin* was to propose a propagation criterion not expressed in terms of stress state but in terms of the "elastic crack tip stress intensity factor". Some years later, *Irwin* also defined three modes of crack tip stress fields and the elastic analysis methods to determine the corresponding Stress Intensity Factors (SIF) K_I, K_{II} and K_{III}, shown in Figure 3.1. In other words, cracks can propagate due to tensile stresses at the right angle with crack plane (opening mode - Mode I), or to shear stress parallel to the crack plane and perpendicular to the crack front (sliding mode - Mode II), or to shear stresses parallel to both the crack plane and the crack front (tearing mode - Mode III).

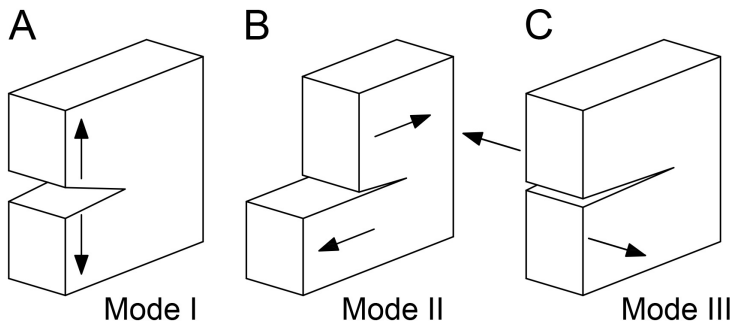

Figure 3.1: Fracture modes: opening (mode I); sliding (mode II); tearing (mode III).

Flaws in glass are generally modeled as half-penny shaped (thumbnail) surface micro-cracks, schematically represented in Figure 3.2, which propagate almost exclusively in mode I [22], since the effects of mode II and mode III are negligible [18].
Thus, unstable propagation of the critical crack occurs when the opening stress reaches a critical value. The general formulation of the stress intensity factor K_I in mode I assumes the form

$$K_I = Y\sigma_\perp\sqrt{\pi\delta}, \tag{3.1}$$

where $\sigma_\perp$ is the tensile stress at the right angle with the crack plane and Y is a factor which depends upon the shape of the crack. From equations (3.1), by recalling the Irwin fracture criterion $K_I \geq K_{Ic}$, a crack unboundedly growths if

$$Y\sigma_\perp\sqrt{\pi\delta} \geq K_{Ic}. \tag{3.2}$$

The quantity K_{Ic} is also known as the fracture toughness, as it measures the ability

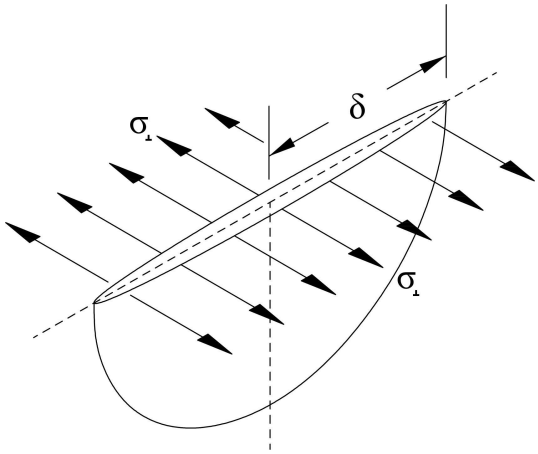

Figure 3.2: Schematic of a half-penny-shaped (thumbnail) crack.

of the material to resist fracture. Hence, it represents a characteristic material parameter ($K_{Ic} = 0.75$ MPa $\mathrm{m}^{0.5}$ is usually assumed for soda lime silica glass [99]). Thus, the stress σ_{cr}, causing failure for a crack of depth δ, and the critical crack depth δ_c, corresponding to a failure stress $\sigma_\perp$, read respectively

$$\sigma_{cr} = \frac{K_{Ic}}{Y\sqrt{\pi\delta}}, \qquad \delta_c = \left(\frac{K_{Ic}}{\sigma_\perp Y\sqrt{\pi}}\right)^2. \tag{3.3}$$

Notice that the SIF can be derived from the elastic problem of an infinite semi-space subject to a biaxial force because the size of the micro-cracks is generally much smaller than the thickness of the plate. The particular flaw that leads to collapse is generally called "critical". Note that the fracture origin does not necessarily coincide with the point of maximum stress and neither with the point in which the larger crack is present. Both the stress $\sigma_\perp$ and the crack depth δ are time-dependent, because of the phenomenon generally referred to as *subcritical crack growth* or *static fatigue* [100], recalled in Section 3.2. The stress which leads to failure when no subcritical crack growth occurs is called *inert strength*.

Table 3.1: List of shape factors Y for the most common crack geometries.

Shape Factor - Y	**Geometry**
0.64	Elliptical crack
0.67	Vickers indentation
$2.24/\pi$	Semi-circular crack
1.12	Surface crack in a semi-infinite specimen
1.20	Quarter-circle corner crack

The factor Y depends upon the stress state, the crack shape and the body ge-

ometry. However, when the crack is small so that the body can be considered to be infinite, the shape of the crack is dominant, and Y is usually referred to as the shape factor. A list of shape factors for the most common crack geometries is recorded in Table 3.1.
The SIF along the smaller axis is higher than along the larger axis [54]. Consequently, elliptical cracks, initially penny-shaped, develop into circular fracture, and hence it is assumed a shape factor $Y = 2.24/\pi \cong 0.71$. This is confirmed by the typical fracture mirror shown in Figure 3.3.

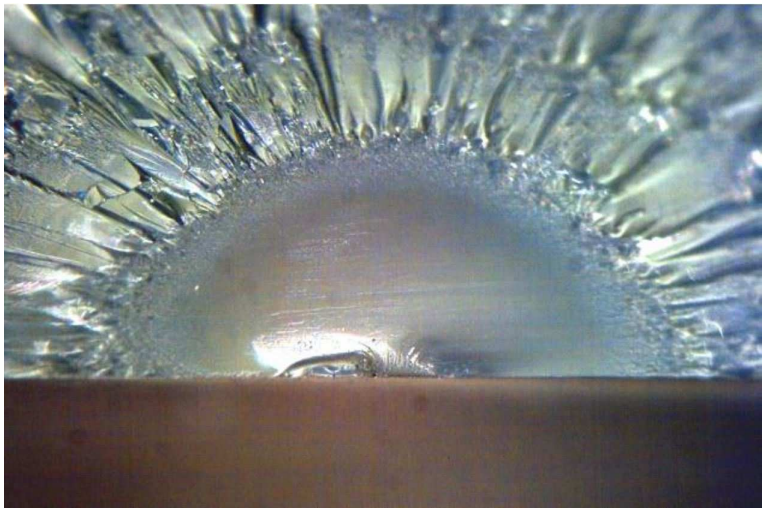

Figure 3.3: Fracture mirror of a plate broken under a four-point bending test [23].

3.2 The subcritical crack growth

Crack growth in glass is governed by the SIF K_I in mode I, and instantaneous collapse occurs when the SIF reaches its critical value K_{Ic}.
However, cracks can grow over time even for opening stresses much lower than the critical limit. Such phenomenon is usually referred to as *static fatigue* or *subcritical crack propagation* [100] and it is mainly controlled by a chemical reaction between glass and water in the environment: the activation energy for the process is stress-sensitive. The higher is the stress level, more rapidly the water is expected to react. Therefore, the fastest reaction is at the crack tip, and this is why the *subcritical crack growth* speed is universally assumed to be dependent upon the SIF. For the case of brittle materials, such a relationship is usually assumed to be a power-law equation of the type [42]

$$\frac{d\delta}{dt} = \nu_0 \left(\frac{K_I}{K_{IC}} \right)^n , \tag{3.4}$$

where δ is the crack depth, K_I is given by equation (3.1), $K_{Ic} = 0.75$ MPa m$^{0.5}$ for soda lime silica glass, ν_0 and n are the conventional sub-critical value of the crack

propagation and the crack velocity parameters, respectively, which are dependent upon the thermo-hygrometric conditions and the type of glass [101]. Chemical composition of glass has a marked effect on the rate of crack growth. For float soda-lime glass, n is comprised between 12 and 16, while ν_0 varies between 30 μm/s and 0.02 m/s. However, $\nu_0 = 0.0025$ m/s and $n = 16$ are generally assumed to be on the safe side [75]. Indeed, the relationship is more complicated and of the type represented in Figure 3.4, but equation (3.4) may be considered valid for an intermediate asymptotic phase, when $K_0 < K_I < K_{Ic}$.

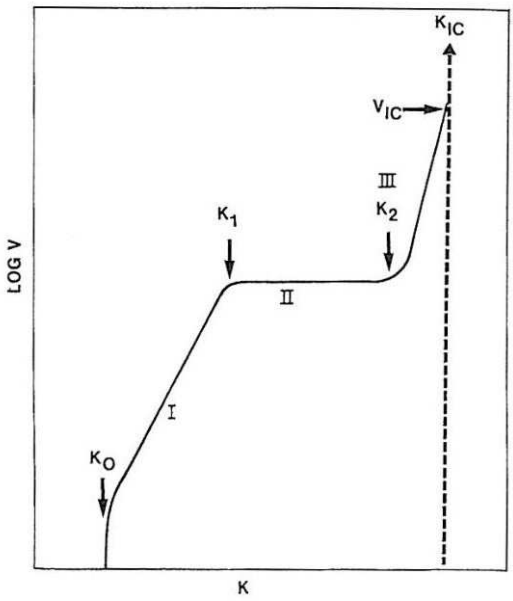

Figure 3.4: Speed of crack growth as a function of the stress intensity factor [23].

Thus, *subcritical crack growth* arises when micro-cracks are subjected to a positive crack opening stress for values of the SIF comprised between a lower bound K_{I0}, which depends upon the environmental conditions and below which no propagation occurs, and K_{IC}. Conventionally, when the stress intensity factor reaches its critical value, the crack growth rate rapidly passes from 1 mm/s to 1500 m/s. The lower limit is $K_{I0} = 0.25 \div 0.30$ MPa m$^{1/2}$ [100] for soda lime silica glass. In summary, failure does not occurs when $K_I \leq K_0$, failure is deferred over time when $K_0 < K_I < K_{Ic}$, and failure is instantaneous when $K_I \geq K_{Ic}$. The threshold K_{I0} is generally neglected to remain on the safe side. However, *Overend and Zammit* [106] proposed a computer algorithm able to normalize the effects of subcritical crack growth upon experimental failure stresses without neglecting K_{I0}.

The evaluation of the characteristic size of initial cracks by microscopic inspection is almost impossible. This is why an indirect evaluation is generally made through the crack growth model (3.4), by starting from the results of macroscopic experimental tests. When considering a load history $\sigma_\perp = \sigma(t)$ for the crack opening stress, by integrating between the time $t = 0$, when the crack length $\delta = \delta_i$, and

$t = t_f$, when $\delta = \delta_c$, one has

$$\int_{\delta_i}^{\delta_c} \delta^{-n/2} d\delta \;=\; \int_0^{t_f} \nu_0 \left(\frac{\sigma(t) Y \sqrt{\pi}}{K_{Ic}} \right)^n dt \,, \tag{3.5}$$

where t_f represents the time elapsed before failure and δ_c is the size of the critical crack at failure. This reads

$$\delta_c = \left(\frac{K_{Ic}}{Y \, f_{test} \, \sqrt{\pi}} \right)^2 , \tag{3.6}$$

where f_{test} is the tensile strength measured at the end of the test. Experimental tests are, as a rule, controlled at a constant stress rate $\dot{\sigma}_{test}$, i.e., $\sigma(t) = \dot{\sigma}_{test} t$. Let then f_{test} be the tensile strength measured at the end of the test, the initial crack size δ_i can be found integrating equation (3.5) and reads

$$\delta_i \;=\; \left[\frac{n-2}{2} \frac{\nu_0}{n+1} \left(\frac{Y\sqrt{\pi}}{K_{Ic}} \right)^n \frac{f_{test}^{n+1}}{\dot{\sigma}_{test}} + \left(\frac{Y \, f_{test} \sqrt{\pi}}{K_{Ic}} \right)^{n-2} \right]^{\frac{2}{n-2}} . \tag{3.7}$$

For realistic values of the parameters, it could be easily verified that the second term inside the square brackets is negligible with respect to the first term. Then, since δ_i is a boundary condition, $f_{test}^{n+1} / \dot{\sigma}_{test} = \Phi$ is approximately constant, whatever the stress rate during the test is.

In design practice, actions are usually schematized as loads acting constantly on the structure for a certain characteristic time, which is representative of their cumulative effect during the service-life of the structure. By assuming that the stress σ_τ at the crack tip due to the constant action provokes collapse after a time τ, integrating equation (3.5), after neglecting a term similar to the second one inside the square brackets, gives

$$\sigma_\tau^n \tau \;=\; \frac{\frac{2}{n-2} \left(\delta_i^{\frac{2-n}{2}} - \delta_c^{\frac{2-n}{2}} \right)}{\nu_0 \left(\frac{Y\sqrt{\pi}}{K_{Ic}} \right)^n} , \tag{3.8}$$

which provides the domain of the applied stress and the time of application. However, for $\tau > 0.01$ s, the size of the critical crack at the end of the test can be assumed to be much higher the the initial size. Thus, from equation (3.8), one can write

$$\sigma_\tau^n \tau \;=\; \frac{2/(n-2) \delta_i^{(2-n)/2}}{\nu_0 \left(\frac{Y\sqrt{\pi}}{K_{Ic}} \right)^n} \;=\; \frac{1}{n+1} \Phi \,. \tag{3.9}$$

Thus, the stress σ_τ can be obtained for any fixed time τ, e.g., for a time $\tau = \tau_L$

one has

$$\sigma_L = \left(\frac{1}{n+1}\right)^{1/n} \left(\frac{\tau_L}{\Phi}\right)^{-1/n}. \tag{3.10}$$

For design purpose, one introduces the coefficient k_{mod}, which allows to consider the phenomenon of *static fatigue* in a more practical way. This is defined as

$$\begin{aligned} k_{mod} &= \frac{\sigma_\tau}{f_{ref}} = \frac{1}{f_{ref}} \left(\frac{1}{n+1}\right)^{1/n} \left(\frac{\tau}{\Phi}\right)^{-1/n} \\ &= \left(\frac{1}{n+1}\right)^{1/n} (\Phi)^{\frac{1}{n(n+1)}} \left(\dot{\sigma}_{ref}\right)^{\frac{-1}{n+1}} (\tau)^{-1/n}, \end{aligned} \tag{3.11}$$

where f_{ref} is a reference value related to the bending strength of a glass plate tested at $\dot{\sigma}_{ref} = 2$ MPa/sec. For what concerns float glass, by assuming characteristic values for the various parameters, one obtains $k_{mod} = 0.585\,(\tau)^{1/16}$, where τ is measured in seconds.

3.3 The statistical population of micro-flaws

Micro-flaws, whose size, shape and distribution are totally random, are unavoidably present on the external surfaces of glass panes. Their size is generally so small that they cannot be detected with naked eyes, and their shapes can be of different types, strongly dependent upon the cause of the flaw itself. However, it is universally accepted to model such flaws as half-penny shaped (or thumbnail) micro-cracks, whose plane is orthogonal to the external surface of the glass plate. Developing the ideas of [46] and [12], assume that the surface of the pane is divided into *Representative Area Elements* (RAE), say ΔA, whose main property is that it is assumed they can host only one crack. Hence, the number of cracks present on the surface of a specimen of area A is $A/\Delta A$. If one inspects through a microscope the surface, the area can be divided in elements ΔA, and the micro-crack lengths located in each of the elements can be measured, albeit in principle. By increasing the number of elements ΔA, the statistics tends to a definite probability function, which is expected to be highly right-skewed. This is because it is reasonable to assume that the lower the crack length is, the higher will be the number of detectable micro-cracks of such size, whereas a very small number of cracks shall have a size much higher than the average value. In other words, the bulk of the distribution occurs for small micro-crack lengths, but the right-hand-side tail is very heavy. This kind of variability is certainly well-interpreted by a *power law distribution*. The most relevant analytical attribute of such statistics is that of *scale invariance*, i.e., the shape of the distribution remains unchanged, up to a multiplicative factor, if the measurements are scaled by a constant. Hence, for a material that could be considered "pristine" after the production process, the probability density function of the crack size δ in an area ΔA reads

$$p_{\Delta A,\delta}(\delta) = \Upsilon\ \delta^{-\alpha}, \tag{3.12}$$

where Υ is a normalization constant and α is a *scaling parameter*. A lower bound δ_{min} must be imposed, since the function (3.12) diverges as $\delta \to 0$, which might be interpreted as the size of cracks that are physiologically present in any glass pane produced through an industrial process. Note that the power law assumption (3.12) would be not consistent without the threshold δ_{min}. However, micro-cracks much larger than this lower bound govern the strength of glass, so that the right part of the statistical population is the only one really of importance for the case at hand. Thus, the importance of δ_{min}, which can be considered as a material parameter, is due to the fact that it affects the statistics of large cracks in the asymptotic limit $\delta \to \infty$ in the expression (3.12), because it enters in the constant Υ of (3.12).
In fact, since the probability of finding a crack of size comprised between δ and $\delta + d\delta$ reads $p_{\Delta A,\delta}(\delta)\, d\delta = \Upsilon\, \delta^{-\alpha}\, d\delta$, the constant Υ is obtained by meeting the normalization requirement that

$$\int_{\delta_{min}}^{\infty} p_{\Delta A,\delta}(\delta)\, d\delta = \int_{\delta_{min}}^{\infty} \Upsilon\, \delta^{-\alpha}\, d\delta = 1 \qquad \Rightarrow \qquad \Upsilon = \frac{\alpha - 1}{\delta_{min}^{1-\alpha}}\,. \tag{3.13}$$

Observe that the values for α must be strictly higher than unity, otherwise the integral in (3.13) would not converge. Such condition should be naturally assumed for the case of glass. Consequently, the probability density function takes the form

$$p_{\Delta A,\delta}(\delta) = \frac{\alpha - 1}{\delta_{min}} \left(\frac{\delta}{\delta_{min}}\right)^{-\alpha}. \tag{3.14}$$

From this, the probability of finding a crack of size equal or higher than δ in the representative area ΔA reads

$$P^{\geq}_{\Delta A,\delta}(\delta) = \int_{\delta}^{\infty} \frac{\alpha - 1}{\delta_{min}} \left(\frac{\delta}{\delta_{min}}\right)^{-\alpha} d\delta = \left(\frac{\delta}{\delta_{min}}\right)^{1-\alpha}. \tag{3.15}$$

The domain of equation (3.15) is $[\delta_{min}, \infty]$, whereas for $\delta < \delta_{min} \;\Rightarrow P^{\geq}_{\Delta A,\delta} = 1$.

3.4 The lower bound of glass strength

Fracture occurrence in glass is assumed to be due to the propagation of a *dominant* surface crack, under the hypothesis that the average density of the surface flaws is such that they do not affect the fracture mechanics of the simple opening defect. The Weibull statistics [94], which is based upon the weakest link-in-the-chain rationale, is by far the most widely used model for the probabilistic interpretation of the variability of the glass strength.
A production quality control, able to detect defects with high precision, would lead to an upper bound for the crack size, δ_{max} [8]. In fact, any part of the glass ribbon with a defect exceeding such allowable crack size would be removed during cutting, and the waste glass would be collected and fed back into the furnace. Actually, the value for the threshold δ_{max} is not rigorous. However, both the European Norm EN 572-2 [41] and the American standard ASTM C1036 [5] prescribe a methodology

for detecting visual faults during the factory production control. The smaller crack lengths detected through these methods are of the order of $400\,\mu m \div 500\,\mu m$: the corresponding parts of glass ribbon are discarded. By assuming that the shape of such defects is generally almost semi-circular, the depth of the crack is one half of the length measured on the surface, so that it may be assumed, on the safe side, that the maximum depth δ_{max} is approximately $250\,\mu m \div 300\,\mu m$.

The existence of a maximum value of the pre-existing flaw size in marketed glass is corroborated by several works present in the technical literature. *Yankelevsky* [103] proposed the value $\delta_{max} = 200$ μm, whereas the maximum flaw size for large annealed glass panels is $\delta_{max} = 278$ μm according to *Nurhuda et al.* [69]. Optical measurements performed by *Lindqvist* and recorded in [55] detected maximum sizes of pre-existing cracks that never exceed 120 μm, while *Wereszczak et al.* [96] found a maximum crack length $\cong 100$ μm.

The maximum allowable crack length δ_{max}, present on glass surfaces after the production process, leads to a lower bound for the crack opening stress that can cause failure. According to the LEFM, the intrinsic lower bound for glass strength reads

$$\sigma_0 = \frac{K_{Ic}}{Y\sqrt{\pi\delta_{max}}}\,, \tag{3.16}$$

with the same notation of equation (3.1). The lower bound σ_0 of (3.16) is associated with the most severe conditions, according to which the dominant crack is exactly at right angle to the direction of maximal tensile stress. Consequently, the probability of the instantaneous collapse of elements under a maximum tensile stress below such limit is null, even though failure could occur in time because of the subcritical crack growth (see Section 3.2). For example, by assuming the higher limit for crack size suggested by *Nurhuda et al.* [69] $\delta_{max} = 278$ μm, from (3.16) one would obtain $\sigma_0 = 35.58$ Mpa.

Let $P_0^{\geq}$ represents the probability that $\delta \geq \delta_{max}$ in a very large sample composed of N glass plates of unitary reference area. The number of elements will become $N(1 - P_0^{\geq})$ after the factory quality control, since all the plates that do not meet the aesthetic and optical requirements are discarded. The relation between the *truncated* distribution $P_{\Delta A,\delta}^{\geq,T}(\delta)$ and the pristine one $P_{\Delta A,\delta}^{\geq}(\delta)$ can be written in the form [94]

$$P_{\Delta A,\delta}^{\geq,T}(\delta) = \frac{\left[P_{\Delta A,\delta}^{\geq}(\delta) - P_0^{\geq}\right] N}{\left(1 - P_0^{\geq}\right) N}, \tag{3.17}$$

where $P_0^{\geq} = (\delta_{max}/\delta_{min})^{1-\alpha}$ and $P_{\Delta A,\delta}^{\geq}(\delta_{min}) = 1$. Thus, one obtains the cumulative probability function of the crack sizes for the truncated distribution, which reads

$$P_{\Delta A,\delta}^{\geq,T}(\delta) = \frac{\delta_{max}^{1-\alpha} - \delta^{1-\alpha}}{\delta_{max}^{1-\alpha} - \delta_{min}^{1-\alpha}}. \tag{3.18}$$

The same conclusion can be reached through the new normalization requirement

$$\int_{\delta_{min}}^{\delta_{max}} p^{T}_{\Delta A,\delta}\left(\delta\right) d\delta = \int_{\delta_{min}}^{\delta_{max}} \Upsilon\, \delta^{-\alpha}\, d\delta = 1 \qquad \Rightarrow \qquad \Upsilon = \frac{\alpha - 1}{\delta_{min}^{-\alpha}\,\left(\delta_{min} - \delta_{max}^{1-\alpha}\,\delta_{min}^{\alpha}\right)}\,. \tag{3.19}$$

Hence the probability density function assumes the form

$$p^{T}_{\Delta A,\delta}\left(\delta\right) = \frac{\alpha - 1}{\delta_{min} - \delta_{max}^{1-\alpha}\,\delta_{min}^{\alpha}} \left(\frac{\delta}{\delta_{min}}\right)^{-\alpha}\,, \tag{3.20}$$

and the probability of finding a crack of size equal or higher than δ in ΔA reads

$$P^{\geq,T}_{\Delta A,\delta}(\delta) = \int_{\delta}^{\delta_{max}} \frac{\alpha - 1}{\delta_{min} - \delta_{max}^{1-\alpha}\,\delta_{min}^{\alpha}} \left(\frac{\delta}{\delta_{min}}\right)^{-\alpha} d\delta = \frac{\delta_{max}^{1-\alpha} - \delta^{1-\alpha}}{\delta_{max}^{1-\alpha} - \delta_{min}^{1-\alpha}}\,. \tag{3.21}$$

Obviously, equations (3.21) and (3.18), obtained in a different way, coincide.
However, one might wonder if this lower limit persists during the whole life-time of the structural component made of glass. The pre-existing defectiveness scenario continuously changes during the service life because of various corrosive and/or abrasive phenomena. The corrosion process, which is very gradual and dissolves the external layers of glass panes, leads to the smoothing out of the glass surface, thus reducing the level of stress concentrations at the cracks, because the crack depth diminishes. On the other hand, abrasion consists of adding new cracks to the pre-existing defectiveness scenario. The damaging effects of aging have been studied by some researchers by testing specimens that had been artificially pre-damaged. The statistical analysis of the test results obtained by *Durchholtz et al.* [30], who tested float glass plates that had been pre-treated by dropping corundum (Al_2O_3) on them under the loading condition provided by the EN1288-2 [31] and EN1288-5 [34], showed that the strongest elements of the distribution shifted to lower strength values, the dispersion of the data highly reduced, whereas the minimum strength values remained of the same order as those obtained by analyzing the pristine float glass. Another very interesting experimental campaign is the one performed by *Madjoubi et al.* [56]. With the aim of detecting how sandstorms, which are very frequent in the Saharian regions, affect the structural glass strength, the Algerian researchers [56] analyzed the influence of sand particle impacts on glass strength. Three samples of 50 specimens were tested in a four-point-bending configuration after different times t of exposure to sand-blasting. The first sample was tested in the pristine state $t = 0$, whereas the second and the third ones were exposed to sandblasting for $t = 30$ and $t = 60$ minutes, respectively, before testing. Figure 3.5 summarizes the experimental outcomes in the Cartesian and the Weibull planes. All the relevant information about the Weibull model is recorded in Appendix A.
The two strength distributions, interpreting the variability of damaged glass strength associated with $t = 30$ min and $t = 60$ min of sandblasting exposure time, are not

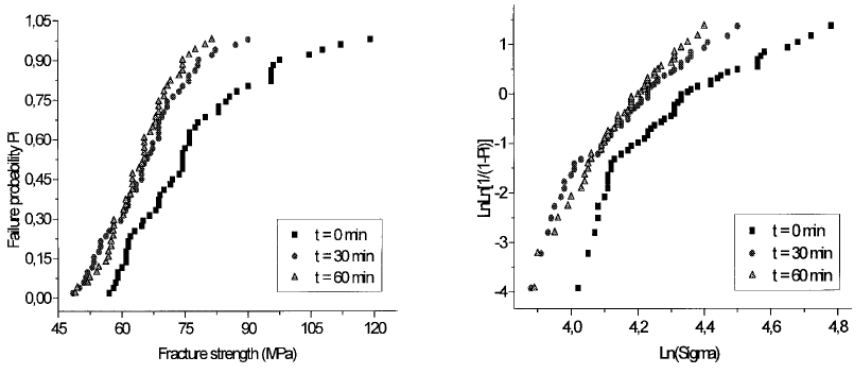

Figure 3.5: Probability plots, in the cartesian and Weibull planes, of the experimental data of [56]. Three different conditions: as-received , sand blasted for 30 minutes and for 60 minutes.

so different to one another, but some peculiarities are to be noticed. In fact, glass strength decreases when the sandblasting time increases for high probability of failure (high strengths), whereas an increasing of the sandblasting time seems to have, albeit approximately, a beneficial effect on the material strengths for low probabilities (low strengths). This finding will be analyzed more in detail in Chapter 6. Other samples were tested in order to confirm the effects of sandblasting on ultimate strength, and the sandblasting time was increased up to 2 hours. Figure 3.6 summarized the results of the whole experimental campaign in terms of average values, as well as standard deviation. By observing Figure 3.6, a sharp drop in strength after 30 min of sandblasting is evident, whereas, as the treatment time increases, a nearly constant level of strength values is observed, while the standard deviation decreases.

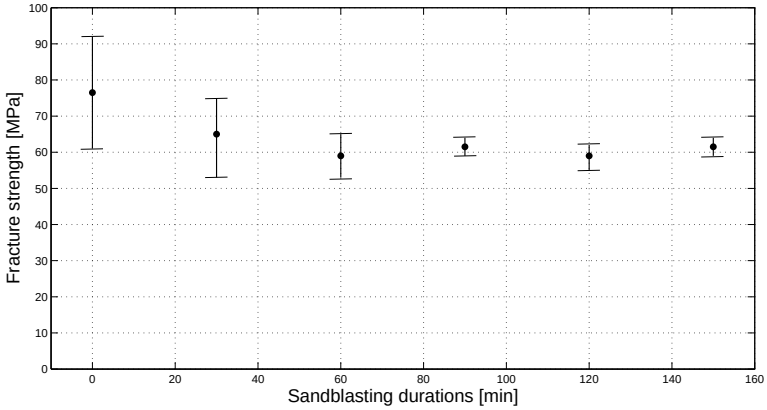

Figure 3.6: Variation of the fracture strength vs. sandblasting duration [56].

Furthermore, *Madjoubi et al.* [56] observed that the maximum length of the flaws caused by sandblasting was approximately $35 \div 40$ μm, that is much lower than the

maximum crack length δ_{max} allowed by factory production control. Such finding was confirmed by *Wang et al.* [92]. However, even though the size of the maximum allowable crack did not change because of the abrasive process, a decay of the lower limit for glass strength [56] is evident from Figures 3.5 and 3.6. In order to provide a qualitative explanation, the defects induced by impinging particles are modeled as semi-spherical cavities. It is reasonable to assume that the distribution of such cavities is uniform, and the higher is the sandblasting time, the higher is the probability that albeit one cavity intersects a pre-existing thumbnail crack. The modification of the stress intensification can be quantified by the model problem shown in Figure 3.7(a,b), with concentric cavity and thumbnail crack. *Xiao and Yan* [102] estimated the SIFs for the case shown in Figure 3.7 through the boundary element software FRANC3D. The SIF K_{Im} normalized with respect to the value $\bar{K} = \sigma\sqrt{\pi R}$ is plotted versus the ratio $a = R/r$ in Figure 3.7(c). The maximum SIF in mode I K_{Im} is attained at $\phi = 0$. Note that the SIF for a semi-circular thumbnail crack of radius R with no interacting cavity at $\phi = 0$ is equal to $1.251\bar{K}$. Observe that the maximum stress amplification is obtained when $a = a_2 = 2$. However, the SIF increment is strongly limited, of the order of 10.5%. For values of $a < 2$ and $a > 2$ the function $K_{Im}(a)$ is monotonically decreasing. It is certainly of interest to note that the semi-sphere cavity shields the crack when $a < a_1 = 1.351$, i.e. the effect upon glass strength of the presence of semi-sphere cavity is benefic when the dimensions of the long axes of the cavity and of the critical crack are comparable. On the other hand, the effect of the surface cavity can be considered negligible when $a \geq 5.5$, at which $K_{Im} = 1.010$. The stress amplification is quantitatively similar when $0 < \phi \leq \pi/2$.
The model problem of Figure 3.7 justifies the decay of the lower bound for glass strength observed in Figure 3.5 and 3.6, albeit at the qualitative level. In fact, the left-hand-side tail of the distribution corresponds to the largest critical defect, whose axis can be assumed of the order of $100 \div 150$ μm, whose stress intensity factor is amplified by cavities induced by sandblasting with radius of order of 40 μm. Furthermore, according to the model shown in Figure 3.7(c), one would obtain a maximum reduction of the strength of the order of 10 % if the dimension of induced cavities r is one half the dimension of the maximum crack size [8].
In conclusion, a maximum allowable size of existing flaws due to an adequate factory quality control gives rise to a lower bound for glass strength. Such threshold stress can be reduced but not annihilated by the effects of aging. A refined study of the effects of abrasion and corrosion upon the statistical distribution of glass strength will be the subject of Chapter 6. Obviously, glass can be easily broken if a sharp groove is produced by a diamond bit, but this type of damage is deliberately man-made, and cannot be associated with a natural degradation process.

3.5 From the population of flaws to the population of strength

Let the reference unitary surface area, say A_0, consist of N_0 elements of area ΔA. Denoting with $P^{\leq}_{\Delta A,\sigma}(\sigma_{cr})$ the probability of finding a crack of size such that its critical stress is equal or less than σ_{cr} in the element ΔA, the probability of finding a crack having critical stress between σ_{cr} and $\sigma_{cr} + d\sigma_{cr}$ reads $dP_{\Delta A,\sigma} = \frac{d}{d\sigma_{cr}} P^{\leq}_{\Delta A,\sigma}(\sigma_{cr})\, d\sigma_{cr}$. Then, denote with $\Omega(\Sigma, \sigma_{cr})$ the angle containing the normals to all the potential crack planes for which the applied stress compo-

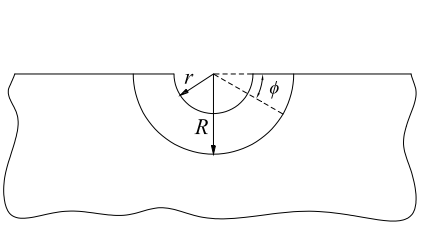

(a)

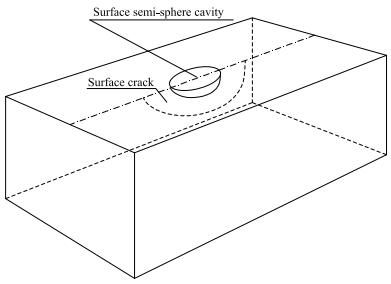

(b)

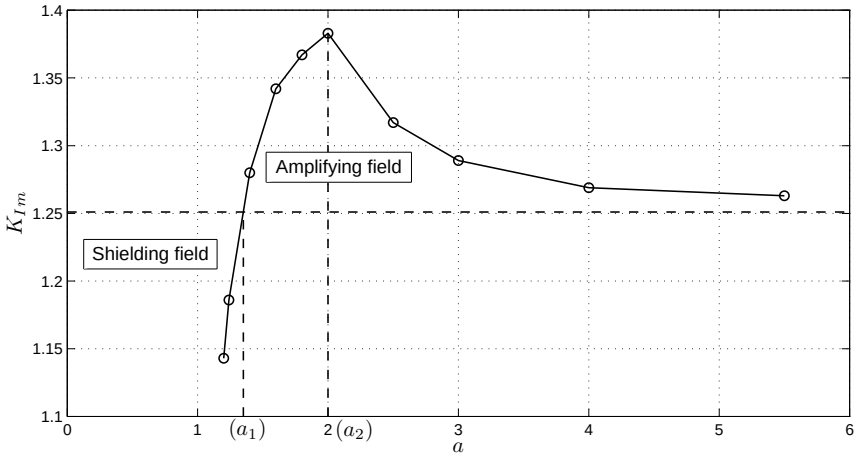

(c)

Figure 3.7: Schematic of cracks emanating from a surface semi-spherical cavity in infinite elastic body. (a) total view; (b) the symmetry plane in which the crack surface occurs; variation of normalized SIFs with the parameter $a = R/r$.

nent orthogonal to the crack plane exceeds the critical value σ_{cr}, for any generic uniform state of stress Σ. Obviously, the values reached by this angle are comprised between 0 and π. Thus, the probability of failure for a tensile surface area ΔA can be written in the form

$$dP_f(\Sigma, \Delta A) = \frac{\Omega(\Sigma, \sigma_{cr})}{\pi} \frac{dP^{\leq}_{\Delta A,\sigma}(\sigma_{cr})}{d\sigma_{cr}} \, d\sigma_{cr}, \tag{3.22}$$

which leads to the failure probability that reads

$$P_f(\Sigma, \Delta A) = \int_0^{\infty} \frac{\Omega(\Sigma, \sigma_{cr})}{\pi} \frac{dP^{\leq}_{\Delta A,\sigma}(\sigma_{cr})}{d\sigma_{cr}} \, d\sigma_{cr}. \tag{3.23}$$

Considering the unitary area A_0, composed by $N_0 = A_0/\Delta A$ elements of area ΔA, the survival probability is equal to the product of the survival probabilities of each element $P_s(\Sigma, \Delta A) = 1 - P_f(\Sigma, \Delta A)$, that is

$$P_s(\Sigma, A_0) = \left[1 - \int_0^{\infty} \frac{\Omega(\Sigma, \sigma_{cr})}{\pi} \frac{dP^{\leq}_{\Delta A,\sigma}(\sigma_{cr})}{d\sigma_{cr}} \, d\sigma_{cr}\right]^{A_0/\Delta A}. \tag{3.24}$$

Firstly, consider an equibiaxial state of stress ($\Sigma = \Sigma_{eqb}$, e.g., $\sigma_1 = \sigma_2 = \sigma_{eqb}$), which is generally assumed as the reference state for characterizing the bending strength of glass plates, since in this case the maximum tensile stress is always at right angle with crack plane. The angle $\Omega(\Sigma_{eqb}, \sigma_{cr}) = \pi$ when $\sigma_{eqb} = \sigma_{cr}$ and $\Omega(\Sigma_{eqb}, \sigma_{cr}) = 0$ when $\sigma_{eqb} < \sigma_{cr}$. Since the probability of failure is null when $\sigma_{cr} \geq \sigma_{eqb}$, the upper limit of the integration interval in equation (3.24) is σ_{eqb}, while the probability of failure is null when $\sigma_{cr} > \sigma_{eqb}$, and the survival probability of a plate of area A_0 becomes

$$P_s(\Sigma_{eqb}, A_0) = \left[1 - \int_0^{\sigma_{eqb}} \frac{dP^{\leq}_{\Delta A,\sigma}(\sigma_{cr})}{d\sigma_{cr}} \, d\sigma_{cr}\right]^{A_0/\Delta A}. \tag{3.25}$$

The strength distribution of a glass plate of generic area A will be firstly obtained by assuming a power-law distribution for micro-crack lengths. Then, how the truncation of the distribution of micro-crack lengths affects the population of strengths will be investigated.
Let the probability of finding a micro-crack of size equal or higher than δ be given by (3.15), re-written in the more convenient form

$$P^{\geq}_{\Delta A,\delta}(\delta) = \Delta A \left(\frac{\delta}{\zeta_0}\right)^{-\alpha^*}, \quad \zeta_0 = \frac{\delta_{min}}{(\Delta A)^{1/\alpha^*}} = \frac{\delta_{min}}{(A_0/N_0)^{1/\alpha^*}}, \tag{3.26}$$

where $\alpha^* = \alpha - 1$, so as to emphasize the importance of ΔA. From expression (3.1) of the SIF for cracks that grow in mode I, when the critical conditions are

reached ($K_I = K_{Ic}$), one has

$$\delta = \frac{1}{\pi}\left(\frac{K_{Ic}}{\sigma_\perp Y}\right)^2 . \tag{3.27}$$

Consequently, the probability of finding a crack having critical stress equal or lower than σ_{cr} assumes the form

$$P^{\leq}_{\Delta A,\sigma}(\sigma_{cr}) = \Delta A \left(\sigma_{cr}\frac{Y\sqrt{\pi\zeta_0}}{K_{Ic}}\right)^{2\alpha^*} , \tag{3.28}$$

and the survival probability given by equation (3.25) becomes

$$\begin{aligned} P_s(\Sigma_{eqb}, A_0) &= \left\{1 - \Delta A \int_0^{\sigma_{eqb}} \frac{d}{d\sigma_{cr}}\left[\left(\sigma_{cr}\frac{Y\sqrt{\pi\zeta_0}}{K_{Ic}}\right)^{2\alpha^*}\right]\right\}^{A_0/\Delta A} \\ \Rightarrow \qquad P_s(\Sigma_{eqb}, A_0) &= \left[1 - \Delta A \left(\frac{\sigma_{eqb}}{\eta_{0,2p}}\right)^{2\alpha^*}\right]^{A_0/\Delta A} , \end{aligned} \tag{3.29}$$

having set $\eta_{0,2p} = K_{Ic}/(Y\sqrt{\pi\zeta_0})$. Let $1/\varepsilon$ denotes $A_0/\Delta A$: hence $\varepsilon \to 0$ for very small values of ΔA. Since $\lim_{\varepsilon\to 0}\left[(1+\varepsilon\, a)^{1/\varepsilon}\right] = \exp(a)$, one can write

$$\lim_{\varepsilon\to 0} P_s(\Sigma_{eqb}, A_0) = \lim_{\varepsilon\to 0}\left[1 - \varepsilon A_0 \left(\frac{\sigma_{eqb}}{\eta_{0,2p}}\right)^{2\alpha^*}\right]^{1/\varepsilon} = \exp\left[-A_0\left(\frac{\sigma_{eqb}}{\eta_{0,2p}}\right)^{2\alpha^*}\right] . \tag{3.30}$$

Finally, for a generic surface area A, the survival and the failure probability read

$$P_s(\Sigma_{eqb}, A) = [P_s(\Sigma_{eqb}, A_0)]^{A/A_0} \quad \Rightarrow \quad P_f(\Sigma_{eqb}, A) = 1 - \exp\left[-A\left(\frac{\sigma_{eqb}}{\eta_{0,2p}}\right)^{2\alpha^*}\right] . \tag{3.31}$$

The major result of this calculation is that equation (3.31) represents the well-known 2-parameter Weibull distribution, now obtained from considerations at the microstructural level [72].

At this point, going back to equation (3.25), an upper-truncated distribution of the type (3.18) for crack lengths is assumed. By using again the expression (3.1) of the stress intensity factor in critical conditions, one has

$$\delta = \frac{1}{\pi}\left(\frac{K_{Ic}}{Y\sigma_{cr}}\right)^2 , \qquad \delta_{max} = \frac{1}{\pi}\left(\frac{K_{Ic}}{Y\sigma_0}\right)^2 , \qquad \delta_{min} = \frac{1}{\pi}\left(\frac{K_{Ic}}{Y\sigma_k}\right)^2 , \tag{3.32}$$

where σ_0 and σ_k represent the critical stresses associated with cracks of size δ_{max} and δ_{min}, respectively. Consequently, the probability of finding a crack having critical stress equal or lower than σ_{cr} becomes

$$P^{\leq,T}_{\Delta A,\sigma}(\sigma_{cr}) = \frac{\sigma_{cr}^{2\alpha^*} - \sigma_0^{2\alpha^*}}{\sigma_k^{2\alpha^*} - \sigma_0^{2\alpha^*}} = \Delta A \frac{\sigma_{cr}^{2\alpha^*} - \sigma_0^{2\alpha^*}}{(\eta_{0,lt})^{2\alpha^*}}, \tag{3.33}$$

where it has been set $\eta_{0,lt} = \left[\Delta A \left(\sigma_k^{2\alpha^*} - \sigma_0^{2\alpha^*}\right)\right]^{1/2\alpha^*}$. In this case, the probability of failure is not null when $\sigma_0 \leq \sigma_{cr} \leq \sigma_{eqb}$, i.e., the lower and the upper limits of integration interval in equation (3.24) are σ_0 and σ_{eqb}, respectively, and the survival probability for a glass pane of reference area A_0 subject to equibiaxial stress state reads

$$P_s^T(\Sigma_{eqb}, A_0) = \left[1 - \Delta A \int_{\sigma_0}^{\sigma_{eqb}} \frac{d}{d\sigma_{cr}} \left[\frac{\sigma_{cr}^{2\alpha^*} - \sigma_0^{2\alpha^*}}{\eta_{0,lt}^{2\alpha^*}}\right] d\sigma_{cr}\right]^{A_0/\Delta A}. \tag{3.34}$$

Equation (3.34) can be written in the more convenient form

$$P_s^T(\Sigma_{eqb}, A_0) = \left[1 - \Delta A \frac{\sigma_{eqb}^{2\alpha^*} - \sigma_0^{2\alpha^*}}{\eta_{0,lt}^{2\alpha^*}}\right]^{A_0/\Delta A}. \tag{3.35}$$

By assuming again $A_0/\Delta A = 1/\varepsilon$, $\varepsilon \to 0$ for large values of A_0, one obtains

$$\lim_{\varepsilon \to 0} P_s^T(\Sigma_{eqb}, A_0) = \exp\left[-A_0 \frac{\sigma_{eqb}^{2\alpha^*} - \sigma_0^{2\alpha^*}}{\eta_{0,lt}^{2\alpha^*}}\right]. \tag{3.36}$$

Finally, by following the same reasoning as above, the survival probability for a generic surface area A is given by

$$P_f^T(\Sigma_{eqb}, A) = 1 - \exp\left[-A \frac{\sigma_{eqb}^{2\alpha^*} - \sigma_0^{2\alpha^*}}{\eta_{0,lt}^{2\alpha^*}}\right]. \tag{3.37}$$

Therefore, it is found that an upper truncation of the power-law distribution of crack lengths gives rise to a *left-truncated Weibull distribution* for glass strengths [72].

From here on, the case of a uniaxial state of stress ($\Sigma = \Sigma_{unx}$, e.g., $\sigma_1 = \sigma_{unx}$ and $\sigma_2 = 0$) is analyzed. This is approximately attained when specimens are tested under three- and four-point bending. In this case, the stress component at right angle with crack axis reads

$$\sigma_\perp = \sigma_{unx} \cos^2 \psi \quad \Rightarrow \quad \sigma_{cr} = \sigma_{unx} \cos^2 \psi_{cr} \quad \Rightarrow \quad \psi_{cr} = \arccos \sqrt{\sigma_{cr}/\sigma_{unx}}, \tag{3.38}$$

where ψ is the angle between the normal to the crack plane and the maximum principal stress direction. Figure 3.8 shows the angle $\Omega(\Sigma_{unx}, \sigma_{cr})$ containing the normals to all the orientations for which $\sigma_{\perp} \geq \sigma_{cr}$, i.e., the angle within which the crack must lie for fracture occurrence. Note that $\Omega(\Sigma_{unx}, \sigma_{cr})$ is two times the angle ψ_{cr}. Thus, from (3.38), one obtains

$$\begin{aligned} &\Omega(\Sigma_{unx}, \sigma_{cr}) = 2\ \psi_{cr} = 2\ \arccos\left[\sqrt{\frac{\sigma_{cr}}{\sigma_{unx}}}\ \right], \\ &\Rightarrow \quad \frac{\Omega(\Sigma_{unx}, \sigma_{cr})}{\pi} = \frac{\arccos\left[\sqrt{\sigma_{cr}/\sigma_{unx}}\right]}{\pi/2}. \end{aligned} \tag{3.39}$$

When $\sigma_{unx} \gg \sigma_{cr}$, the angles $\psi_{cr} \to \pi/2$ and $\Omega(\Sigma_{unx}, \sigma_{cr})/\pi \to 1$, whereas for $\sigma \to \sigma_{cr}$, then $\psi_{cr} \to 0$ and $\Omega(\Sigma_{unx}, \sigma_{cr})/\pi \to 0$. Obviously, the probability of collapse is null when $\sigma_{unx} < \sigma_{cr}$.

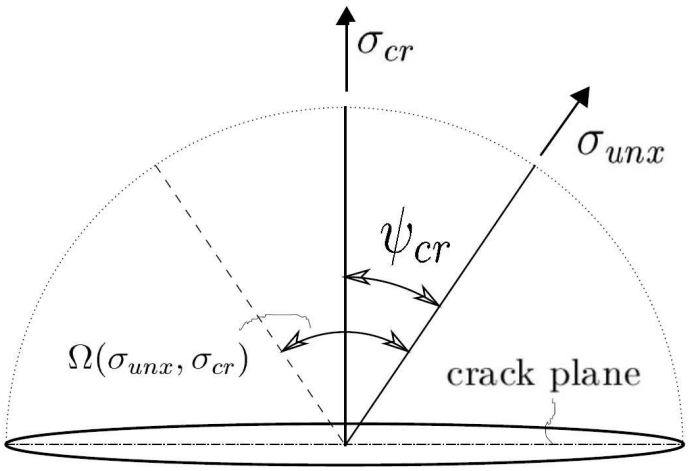

Figure 3.8: Angle within which the crack must lie for fracture occurrence.

By interpreting the micro-crack lengths variability through a power-law function of the type (3.15), the cumulative probability function $P^{\leq}_{\Delta A,\sigma}(\sigma_{cr})$ for critical stresses correlated with flaws in elements ΔA is given by equation (3.28). This leads, from equation (3.24), to the the survival probability in the form

$$\begin{aligned} P_s(\Sigma_{unx}, A_0) = \Bigg[1 - \int_0^{\sigma_{unx}} \Delta A\ \frac{\arccos\left[\sqrt{\sigma_{cr}/\sigma_{unx}}\right]}{\pi/2} \\ \frac{d}{d\sigma_{cr}}\left(\sigma_{cr}\frac{Y\sqrt{\pi\zeta_0}}{K_{Ic}}\right)^{2\alpha^*}\ d\sigma_{cr}\Bigg]^{A_0/\Delta A}. \end{aligned} \tag{3.40}$$

With some analytical manipulations, equation (3.40) assumes the form

$$P_s(\Sigma_{unx}, A_0) = \left[1 - \Delta A \left(\frac{\sigma_{unx}}{\eta_{0,2p}}\right)^{2\alpha^*} \frac{1}{2\,\alpha^*} \frac{\Gamma[\frac{1}{2} + 2\alpha^*]}{\Gamma[\frac{1}{2}]\ \Gamma[2\alpha^*]}\right]^{A_0/\Delta A}, \qquad (3.41)$$

where $\eta_{0,2p} = \frac{K_{Ic}}{Y\sqrt{\pi\zeta_0}}$ is the scale factor of the distribution and Γ is the Euler' Gamma Function. Posing again $A_0/\Delta A = 1/\varepsilon$, so that $\varepsilon \to 0$ for $A_0 \gg \Delta A$, one has

$$\lim_{\varepsilon \to 0} \left[(1 + \varepsilon\, x)^{1/\varepsilon}\right] = \exp(x)\,. \qquad (3.42)$$

Then, one can write

$$P_s(\Sigma_{unx}, A_0) = \exp\left[-A_0 \left(\frac{\sigma_{unx}}{\eta_{0,2p}}\right)^{2\alpha^*} \frac{1}{2\,\alpha^*} \frac{\Gamma[\frac{1}{2} + 2\alpha^*]}{\Gamma[\frac{1}{2}]\Gamma[2\alpha^*]}\right]. \qquad (3.43)$$

Finally, from the same arguments used above, the probability of failure for a float glass plate subjected to an uniaxial stress state on a generic area A takes the form

$$P_f(\Sigma_{unx}, A) = 1 - \exp\left[-K_{unx} A \left(\frac{\sigma_{unx}}{\eta_{0,2p}}\right)^{2\alpha^*}\right], \qquad (3.44)$$

where

$$K_{unx} = \frac{1}{2\,\alpha^*} \frac{\Gamma[\frac{1}{2} + 2\alpha^*]}{\Gamma[\frac{1}{2}]\Gamma[2\alpha^*]}\,, \qquad (3.45)$$

is the coefficient that, multiplied by A, gives the effective area $A_{eff,unx} = K_{unx} A$. The effective area synthetically takes into account the effects of the state of stress and the size of the specimen upon the statistical distribution of the strengths. It is defined as the area that is statistically equivalent, in term of strength, to an uniform equibiaxial state of stress. Figure 3.9 shows the values of the coefficient K_{unx} as a function of α^* in the representative range for float glass [72].

3.6 Statistical analysis of the experimental data

Referring to the large-scale experimental campaign of the CEN/TC129/WG8 (Technical Committee 129 - Working Group 8 of the European Committee for Standardization), various statistical distributions are compared in their ability to interpolate experimental data [70]. In particular, different generalized Weibull distributions, both bounded or unbounded, have been analyzed. Refer to Appendix A for the detailed description of the Weibull distributions considered in the current section. This experimental campaign is the widest I am aware of, aimed at analyzing the variability of structural glass strengths. Other campaigns have produced

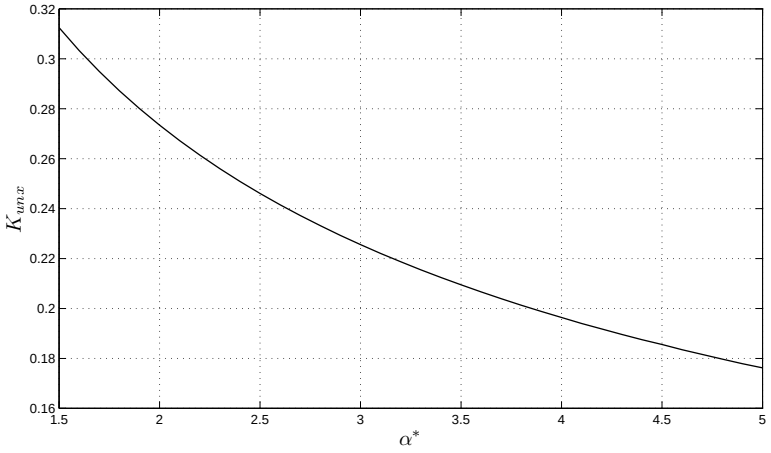

Figure 3.9: Values of K_{unx} as a function of α^*.

limited number of data points and, most of the times, the values are not available in the literature.

The campaign performed by the working group CEN/TC129/WG8 of CEN provides 741 failure stress measurements, which are recorded in [19]. It consisted of thirty samples of approximately 25, 6-mm-thick, plate specimens, which were tested under the load configuration prescribed by the EN1288-2 standard [35]. The samples were obtained from eleven different European glass manufacturing plants. Tin-side and air-side surfaces of the float glass panes were tested separately for each supplier. Since during the float production process one side of the glass paste is exposed to air (air-side), while the other one is in contact with the molten tin bath and, subsequently, with steel rollers (tin-side), different defectiveness scenarios are present on the two glass surfaces. This is why the statistical regression of the 741 values of [19] may provide misleading results if none distinction is made between the tin- and the air-side.

The EN1288-2 [31] standard prescribes a Coaxial Double Ring (CDR) test configuration, according to which large square specimens of side $l = 1000$ mm are loaded by two concentric rings of radii $R_1 = 300$ mm and $R_2 = 400$ mm and by an overpressure p^*, which is correlated with the load F^* applied by the loading device during the whole experiment according to a law recorded in the standard. A more detailed description of this standardized test is given in the Appendix B. Observe that the aim of this test would be that of inducing an almost equibiaxial stress state in the area delimited by the inner ring, far from the borders, by compensating nonlinear effects, responsible of the deviation from equi-biaxiality, through the overpressure. Each value of the failure stress recorded in [19] has been derived from the force applied by the tensometer producing the rupture of the specimen. However, the induced state of stress is not equibiaxial, because The correlation between the overpressure p^* and the load F^* provided by the standard results to be not accurate. Therefore, the failure stress values recorded in [19] have been

corrected according to the procedure shown in Appendix B, to take into account the deviation from equibiaxiality.
Figure 3.10 shows the probability plots in the 2P Weibull plane, distinguished for the tin- and air-side. It is evident from Figure 3.10 that the approximation given by the 2PW statistics is not accurate, both for the air- and the tin-side data.

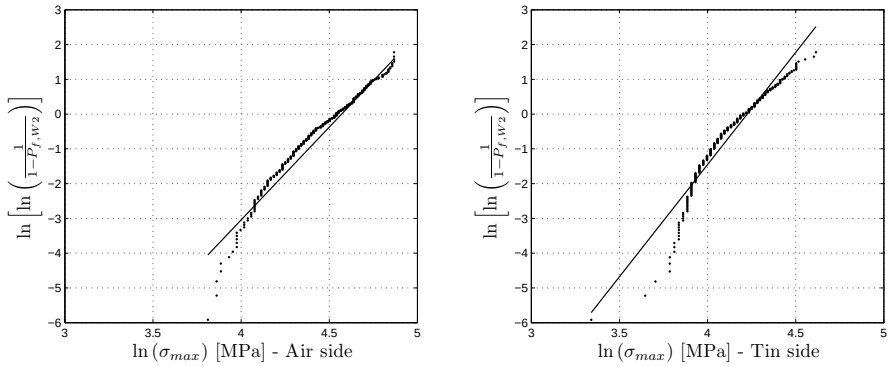

Figure 3.10: Linear interpolation in the 2P Weibull plane of the failure stress measurements by CEN/TC129/WG8. Distinction between tin- and air-side measurements.

The plot of the experimental data in the 3-parameter Weibull (3PW) plane, i.e., $\ln\ln 1/(1-P_f)$ vs. $\ln(\sigma-\sigma_0)$, is recorded in Figure 3.11, for both the tin- and air-side data.

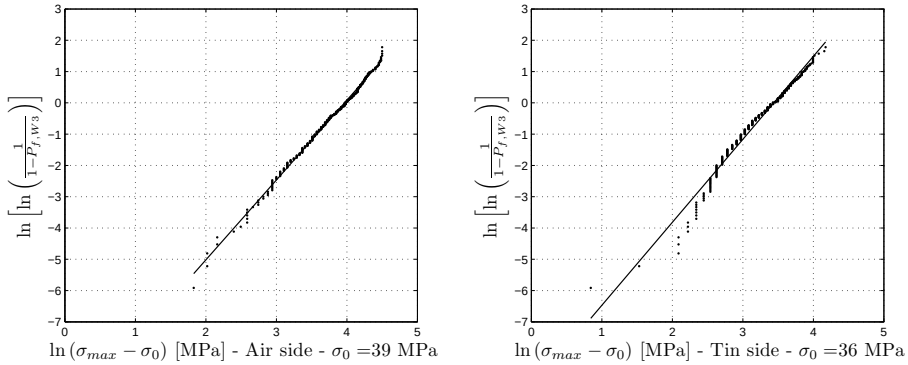

Figure 3.11: Linear interpolation in the 3P Weibull plane $\ln\ln 1/(1-P_f)$ vs. $\ln(\sigma-\sigma_0)$ of the failure stress measurements by CEN/TC129/WG8. Distinction between tin- and air-side measurements.

The *excellent* linear fit given by the 3PW model for the air side data is evident from Figure 3.11, but the approximation is not as good for the tin-side data.
The same conclusions can be reached by using a left-truncated Weibull (LTW) statistics. The Weibull plot of the experimental data for the air- and tin-side surfaces in the LTW plane $\ln[G+\ln 1/(1-P_f)]$ vs. $\ln(\sigma)$ are shown in Figure 3.12, with $G = A\sigma_0^m/\eta_{0,lt}^m$ introduced in Appendix A ($m = 2\alpha^*$, from the comparison

of equations (3.37) and (A.29)). Substantial differences in fitting the experimental data are not observed between the 3PW and LTW statistics if one compares Figures 3.11 and 3.12. Both the 3PW and the LTW distributions provide a third parameter, representing a lower bound for glass strength, but the physical meaning of such parameter is strongly different. For what concerns the 3PW model, the third parameter represents an absolute lower threshold for glass strength, that is an intrinsic property of the material. On the other hand, the third parameter provided by the LTW model arises from a selection, when all the data below a certain value are discarded. In other words, the LTW statistics comes from a left-truncation of an original 2-parameter Weibull distribution (see Section 3.5).

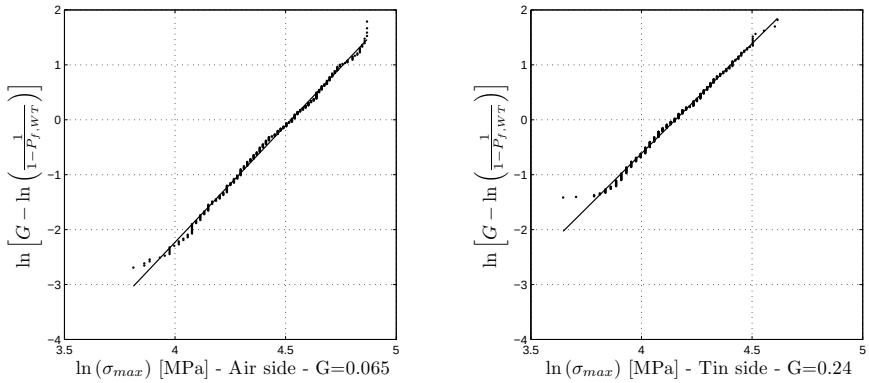

Figure 3.12: Linear interpolation in the LT Weibull plane $\ln[G + \ln 1/(1 - P_f)]$ vs. $\ln(\sigma)$ of the failure stress measurements by CEN/TC129/WG8. Distinction between tin- and air-side measurements.

However, accepting a lower bound for glass strength represents a major step change, somehow in contrast with the common engineering practice. That is why several Weibull generalized distributions which do not provide a lower bound have been investigated for the sake of comparison. The simplest idea, proposed by *Rodichev et al.* [79], consists in interpolating the experimental point with a bi-linear function in the Weibull plane (BLW). On the other hand, if one assumes that the material has undergone two independent failure mechanisms, each one governed by a specific 2PW distribution, the strengths variability should follow a bi-modal Weibull (BMW) function. The plots of the best-fit Weibull probability plots obtained by using the BLW and BMW approaches, are represented in Figure 3.13, for both tin- and air-side. As it is evident from Figure 3.13, the capability of fitting the experimental data guaranteed by the bi-linear (BLW) and the bi-modal Weibull (BMW) distributions is similar, i.e., it is good for the air-side data and fairly acceptable for tin-side data.
Consider finally the extended Weibull (EXW) distribution, which is obtained by adding a parameter to the 2PW family of ditributions through the method proposed by *Marshall & Olkin* [58]. The corresponding plots have been shown in Figure 3.14. An acceptable goodness fit is observed for the air-side data, whereas the tin-side data is again not well interpolated.
The parameters of the different generalized distributions, graphically estimated by

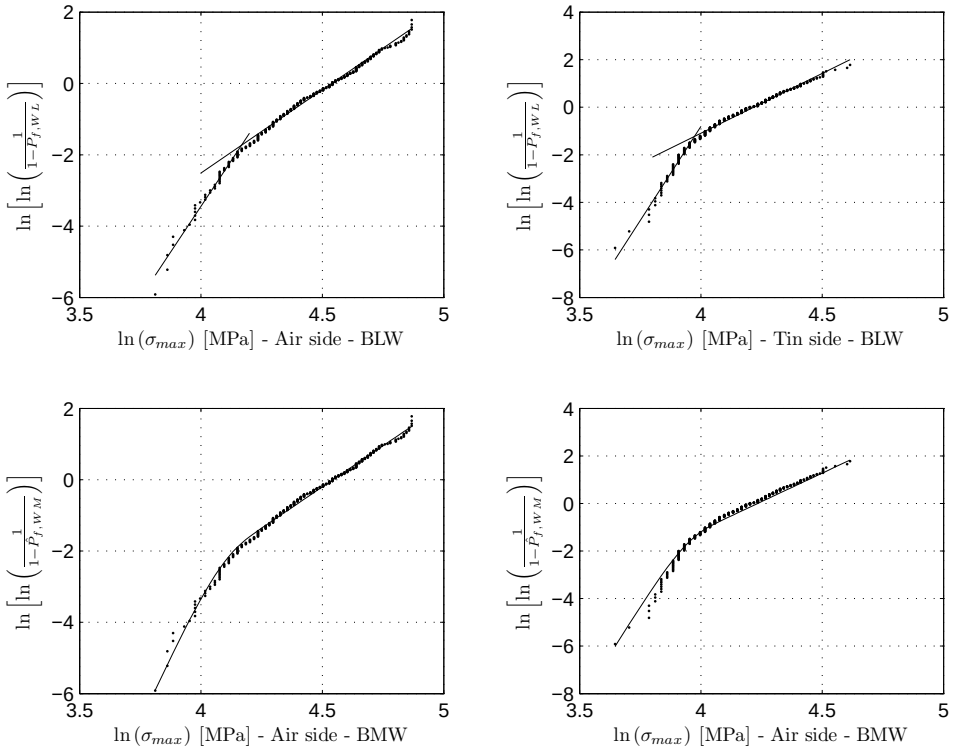

Figure 3.13: Bilinear and Bimodal Weibull probability plots of the failure stress measurements by CEN/TC129/WG8. Distinction between tin- and air-side measurements.

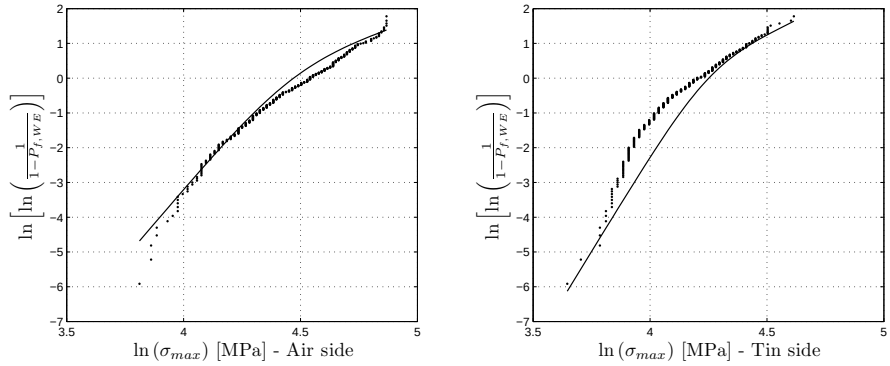

Figure 3.14: Extended Weibull probability plot of the failure stress measurements by CEN/TC129/WG8. Distinction between tin- and air-side measurements.

following the procedures recorded in the Appendix A, are summarized in Tables 3.2, 3.3 and 3.4.

Table 3.2: Weibull parameters for the 2PW, 3PW and LTW statistics, obtained by linear regression of the experimental data recorded in [19].

Statistics	m	$\eta_0/A_{eff}^{1/m}$ [MPa]	σ_0 [MPa]
Air-side			
2PW	5.37	94.17	-
3PW	2.55	52.84	39.00
LTW	4.25	58.22	41.21
Tin-side			
2PW	6.45	68.38	-
3PW	2.65	31.20	36.00
LTW	4.00	36.51	38.04

Observe from Table 3.2 that the Weibull shape parameter m for the 3PW statistics turns out to be much smaller than for the other two cases.

Table 3.3: Estimated Weibull parameters for the BLW and the BMW statistics, obtained by linear regression of the experimental data by CEN/TC129/WG8.

Statistics	m_1	m_2	$\eta_{0,1}/A_{eff}^{1/m_1}$ [Mpa]	$\eta_{0,2}/A_{eff}^{1/m_2}$ [Mpa]
Air-side				
BLW	11.15	4.85	74.07	94.18
BMW	10.25	4.62	57.50	94.03
Tin-side				
BLW	15.83	5.03	57.44	67.84
BMW	11.80	4.80	50.00	69.00

As it is possible to see from Table 3.3, not substantial differences arise between the estimated parameters for the BLW and BMW models. By comparing the data recorded in Tables 3.2 and 3.3, one can note that the shape parameter m_2 for the BLW and BMW distributions, which is associated with the right-hand-side tail of the data, is close to the value obtained for the LTW model. On the other hand, the values for m_1, associated with the left-hand-side-tail are much higher ($\cong 10$ for the air-side and $12 \div 15$ for the tin-side).
Notice that, if the EXW model is used, the shape parameter m is higher than in the case of 2PW, 3PW and LTW, but much lower than the shape parameters associated with the left-hand-side-tail of the BLW and BMW distributions.
An estimate of the goodness-of-fit of the various statistical models has been obtained with the Chi-square goodness of fit test, which is considered more objective than the simple graphical comparison in the various Weibull planes. In particular,

Table 3.4: Estimated Weibull parameters for the EXW statistics, obtained by linear regression of the experimental data recorded in [19].

Air/Tin	m	$\eta_0/A_{ef,WE}^{1/m}$ [MPa]	Θ
Air-side	7.9	139	0.0151
Tin-side	7.9	100	0.012

the p-value represents the probability that the difference between observed and expected data is due to chance alone (a more detailed description of the chi-square test is given in the Appendix A). The p-values associated with all the distributions under consideration are recorded in Table 3.5. It is useful to recall that it is customary to accept the "5% rule", i.e., the null hypothesis H_0 is accepted (rejected) if $p \geq 5\%$ ($p < 5\%$).

Table 3.5: Estimated p-values for the generalized Weibull distributions under consideration.

Statistics	**p-value**$_{air}$	**k**$_{air}$	**p-value**$_{tin}$	**k**$_{air}$
2PW	$\cong$0	19	$\cong$0	16
3PW	0.7332	20	0.0027	16
LTW	0.6676	19	0.003	15
BLW	0.2128	19	0.0235	16
BMW	0.2401	19	0.0041	17
EXW	0.0979	20	$\cong$0	15

From Table 3.5, the inability of the 2PW statistics to interpret the statistical variation of float glass strength is confirmed. Furthermore, the idea of the existence of a lower bound for the *float* glass strength is strongly supported. In fact, at least for the air side data, the bounded statistical distributions (3PW, LTW) exhibit an excellent goodness-of-fit, i.e., $p_{air,W3} = 0.7332$ and $p_{air,WT} = 0.6676$). The p-values associated with the BLW and BMW distributions are still very good ($p_{air,WL} = 0.2128$ and $p_{air,WM} = 0.2401$). As it will be shown in Chapter 5, a bi-modal Weibull distribution for strength is justified by the presence of two micro-cracks populations. However, to my knowledge, no physical justifications have been proposed for the BLW model. For pristine material strength, i.e., for the air-side strength, it is plausible to assume only one crack population. The large gap in the p-values referring to the LTW model, or the 3PW, and the BMW statistics corroborates this hypothesis. Furthermore, as it is shown in Section A.4.2, the use of a BMW distribution leads to significant analytical complication in the definition of the effective area and, consequently, in the analysis of the experimental data. Different considerations will be made in the current dissertation when aged glass is considered. Then, the EXW model provides a less accurate interpretation of the experimental data for the air-side ($p_{air,WE} = 0.0979$), even if the approximation is acceptable according to the "5% rule". Considering that the EXW model is analytically simple, it can be considered a valid alternative to the distributions

which provide a lower bound to be used in the calibration procedure of the partial material factors, as it is shown in Section 6.3. On the other hand, none of the generalized distributions under consideration is able to definitely represent the statistical population of the *tin-side* strength. This surface of glass can be considered as a "pre-damaged" surface, because of the contact with tin bath and steel rollers during the production process, and an *ad hoc* statistical characterization will be presented in Section 5.3.

In conclusion, I think that the left-truncated Weibull statistics can be considered the best model for interpreting the strength variability of pristine glass, since it guarantees an exceptional goodness of fit with the experimental data and, unlike the 3-parameter Weibull distribution, it has its direct physical justification in the production quality controls, as discussed in Sections 3.4 and 3.5.

CHAPTER 4

THE STRENGTH OF HEAT-TREATED GLASS

The ultimate strength of heat-treated glass is due to the contributions given by the residual surface compressions and the strength of the pristine float glass (before the heat-treatment). In the design practice, the characteristic strength is generally obtained by summing up the characteristic values of the pristine strengths and residual stresses. However, the final strength for heat-treated glass may be much higher than this simple sum, as it is demonstrated by the results of several experimental campaigns [105, 90, 89, 91, 67].

Two main different types of heat-treated glass exist, the heat-strengthened and the toughened. Several methods, destructive or non-destructive, have been used through the years for measuring residual stresses. Destructive methods, very seldom used nowadays, consist in imposing a local damage, which causes stress relaxation and a modification of the geometry, depending upon the residual stresses after tempering, which are measured. On the other hand, photoelasticity methods [59, 3], magneto-photoelasticity methods [59, 1, 47], acousto-elasticity methods [29, 27] and X-ray diffraction techniques [68] are all non-destructive tests. In particular, the portable scattered light polariscope (SCALP) developed by *Aben* [2] has been widely used during last years to measure residual stresses exploiting the photoelastic properties of glass.

The intensity of residual stresses varies from point to point within the same panel and from panel to panel: this is why an accurate statistical interpretation of the prestress state induced by thermal treatments is not trivial. Moreover, data that can be found in the literature from different experimental campaigns are quite fragmented and partial. A properly-designed measurement campaign has been carried out at the Technical University of Darmstadt, that allows to reach some conclusion, although partial, about the function to be used for interpreting the variability of heat-induced residual stresses.

A statistical interpretation of the complex interaction between the residual stress state and the additional state induced by the applied loads is proposed in the current chapter, using a micro-mechanically motivated analysis of the effects of prestress and applied bending [73]. The probability of failure is associated with the probability of finding a sufficiently large crack at right angle to a critical tensile stress, mutually related to the probability that the prestress is below a certain limit

at the same point. Hence, the prestress is treated as a beneficial external action.

4.1 The statistical population of surface compressions

Since during the tempering process the cooling of the panels is produced by jets, the inhomogeneity of the resulting eigenstress may be very significant [4]. Thus, so as to mitigate such inhomogeneity, the thermal treatment in the industrial practice is made while oscillating the glass panes. This, together with an increase of the cooling rate, strongly improves the homogeneity and isotropy of the induced state of stress [20]. Hence, the residual stress state can be assumed to be homogenous and equibiaxial, thus neglecting, at least as a first order approximation, the inevitable point to point variation within a single specimen [90]. This assumption is not valid for the edges, which are generally much more compressed than the core part [4]. In particular, it is customary to assume that the stress state is disturbed and deviates from the equibiaxiality up to a distance of 15 mm from the edges. Modulo this distinction, it is assumed that the major variations in the state of prestress are from plate to plate.

Veer et al. [89] tested 1100 × 360 × 10 mm glass plates, of which one third was toughened, one third was heat strengthened and one third was annealed, under four-point bending configuration. The prestresses profile through the thickness, measured with SCALP-laser measuring device, and the surface residual stresses are recorded in [89]. Arranging the data in ascending order and assigning an empirical probability of failure $P_f = i/(N+1)$ at the $i-th$ datum, where N represents the number of data, the capability of the Gaussian and log-normal function at interpolating the data is graphically investigated in Figure 4.1. Appreciable differences between the normal and log-normal distributions do not arise. However, the limited number of data does not allow to reach definite conclusions. This motivated a new properly designed measurement campaign, that was performed at the Technical University of Darmstadt.

4.1.1 Analysis of the residual stress measurements made at the Technical University of Darmstadt

A wide measurement campaign was performed at the Technical University of Darmstadt under the supervision of Prof. Dr. Ing. Jens Schneider. The eigenstress states acting within 50 toughened glass plates of size 400 mm × 400 mm were investigated. For each specimen, optical measurements of the compressive residual stresses on the air side were made with the SCALP device along two orthogonal directions at 5 points, i.e., at the center of the plate and along the two diagonals, 100 mm far from the edges, for a total of 500 measurements. The precision of the measuring device is ±5%, i.e., the analysis is marginally affected by inaccuracies in the measurements. However, to minimize such inaccuracies, each one of the residual stresses has been computed as the mean of ten SCALP measurements.

Firstly, the ratio between the two residual stresses measured at any point was calculated for verifying the hypothesis of equibiaxiality. The mean value of the ratio between the minimum and the maximum stresses acting at any point resulted to be $\sigma_{pc,II}/\sigma_{pc,I} = 0.98$, while the minimum value attained by such ratio was $\sigma_{pc,II}/\sigma_{pc,I} = 0.92$. Hence, it is certainly acceptable to assume that the stress state is equibiaxial and, consequently, the mean of the measurements taken along

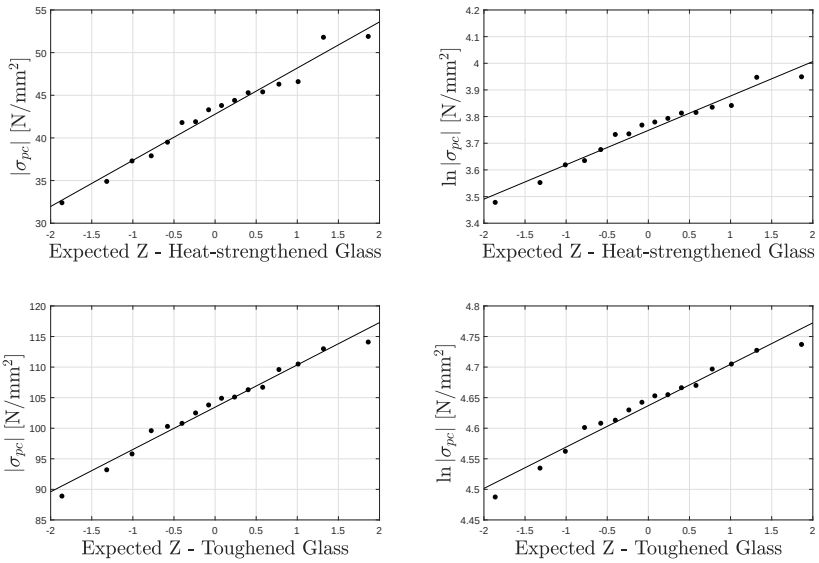

Figure 4.1: Normal σ_{pc} plot for the surface compression recorded in [89] for (a) heat-strengthened glass and (c) toughened glass. Corresponding log-normal σ_{pc} plots in (b) and (d). Here, Z represents the standardized variable.

the two orthogonal directions at any point may be considered as the equibiaxial residual stress acting at that point.

The simplest assumption is that the point to point variation of prestress can be neglected, which is equivalent to say that an almost homogeneous and equibiaxial stress state acts in the core of the specimen. Thus, in a first instance, only the plate-by-plate variation was investigated, by statistically analyzing a sample of 50 data. These data were obtained as the mean value of the 10 measurements, taken at the air side for each plate. The resulting normal and log-normal probability plots are shown in Figure 4.2.

By observing Figure 4.2, it is not possible again to detect appreciable differences between the normal and the log-normal distributions. Moreover, the Chi-square goodness of fit test, described in Section A.5, was made to evaluate the probability that the difference between observed and expected data, according to the two considered distributions, is due to chance alone, despite the size of the sample is quite small. The *p-values* obtained by grouping the data in 10 bins are 0.33 for the normal and 0.28 for the log-normal distributions. Hence, the Gaussian model can be certainly considered acceptable for statistically interpreting the variability of surface compressions. For this model, the mean value and the standard deviation are $\mu = 98.6$ MPa and $\upsilon = 2.4$ MPa, respectively. The use of the log-normal distribution does not improve the goodness of fit with the experimental data.

With the aim of investigating if it is correct to neglect the point-by-point variation, the residual stresses acting at the air side of an additional toughened specimen were

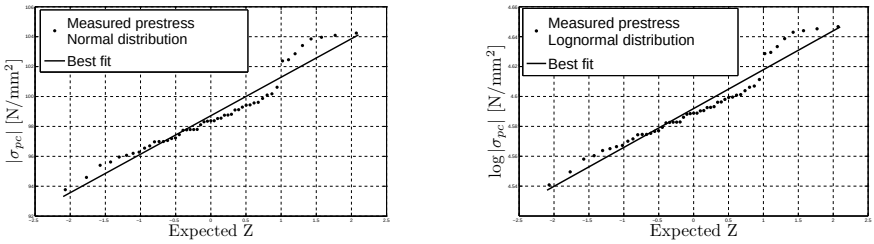

Figure 4.2: (a) Normal σ_{pc} plot of the 50 data representing the homogenous and equibiaxial residual stress acting within the toughened glass plates; (b) log-normal σ_{pc} plot of the 50 data representing the homogenous and equibiaxial residual stress acting within the toughened glass plates. Here, Z represents the standardized variable.

measured on a 40 mm regularly-spaced grid of sampling points, for a total of 81 measurements. The external sampling points were 40 mm far from the edges of the plate. How the residual stresses are distributed in the analyzed plate is shown in Figure 4.3.

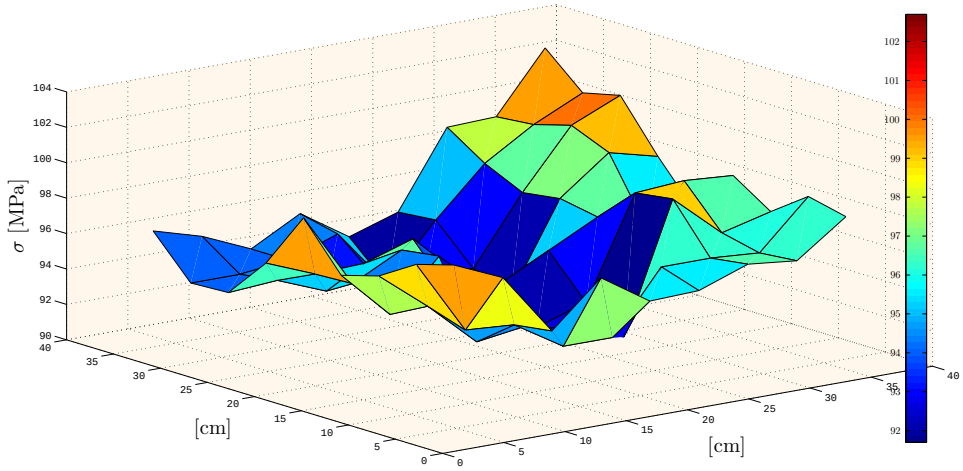

Figure 4.3: Eigenstress state at the air side of a toughened glass specimen. Residual stresses measured on 40 mm regularly-space grid. The external sampling points were 40 mm far from the borders.

Deviations in residual stresses are of the order of 10%. Thus, Figure 4.3 makes evident that the point by point variation of the prestresses may be of some importance and, hence, should be taken into account while analyzing in detail the variability of heat-treated glass strength. Most likely, the degree of uniformity of the eigenstress state depends upon the position of the plate in the oven during the

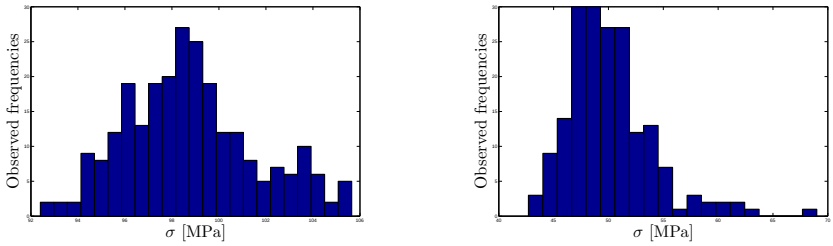

(a) (b)

Figure 4.4: (a) Observed histogram for the 250 equibiaxial residual stresses measured at the technical University of Darmstadt (23 bins); (b) observed histogram for the 184 residual stresses recorded in Prof. Schneider's Ph.D. dissertation [82] (20 bins).

cooling time in the tempering process.

Therefore, a new statistical analysis was performed on a sample of 250 data, constituted by 5 data for each specimen, representing the equibiaxial prestresses at the center and at four points along the diagonals of each plate. In this way, one approximately takes into account both the point-to-point and the plate-by-plate variations, since the data refer to different plates and different points at which measurements are made, although the number of points in the same plate is certainly limited.

It is of interest to observe from Figure 4.4(a) that a mild bi-modality has been detected in the probability density function of residual stresses. Remarkably, such bi-modality is observed even by analyzing the residual stress measurements recorded in Prof. Schneider's Ph.D. dissertation [82], shown in Figure 4.4(b), referring to an old measurement campaign and, hence, to a totally different quality of float glass and tempering process. Notice that a statistical distribution is generally bi-modal when two different sources generate the data; however, no physical explanations have been still proposed. In any case, the population of residual stress is certainly not symmetric and the right tail is heavier than the left one.

The goodness of fit with the experimental data for the normal and log-normal distributions has been investigated. The normal and log-normal probability plots referred to the new sample of 250 data are shown in Figure 4.5.

By comparing Figures 4.5 and 4.2, no qualitative differences are observed between the statistical analyses of the samples of 50 and 250 data. The *p-values* obtained from the Chi-square goodness of fit test are 0.06 for the normal and 0.046 for the log-normal distribution. Observe that the *p-values* now obtained are certainly more reliable than the ones that refer to the sample of 50 data, because of the higher number of points. Recall that it is customary to accept the 5% rule, according to which a statistical model can be considered reliable for *p-value*$\geq$ 0.05. The mean value of the distribution is almost equal to the one obtained from the sample of 50 data ($\mu = 98.77$ MPa vs. $\mu = 98.60$ MPa), whereas the standard deviation is mildly higher ($\upsilon = 2.79$ MPa vs. $\upsilon = 2.40$ MPa).

For the sake of completeness, the surface compressions were measured along two orthogonal directions for 50 annealed glass plates, but only at the center of the

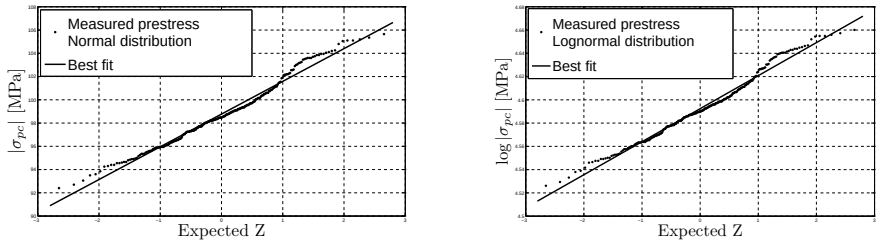

Figure 4.5: (a) Normal σ_{pc} plot of the 250 data representing the equibiaxial prestress acting in 5 points of any plate; (b) log-normal σ_{pc} plot of the 250 data representing the equibiaxial prestress acting in 5 points of any plate.

specimens. However, no further findings that may be considered of interest were obtained from the analysis of such data and, hence, they are not recorded here.
In conclusion, among the various options, interpreting the variability of the pre-stresses with a Gaussian distribution is acceptable, since the *p-value* is higher than 5%. This is certainly the simplest approach. Hence, the probability density function for the prestress state induced through thermal treatment is assumed of the form

$$f_p(|\sigma_{pc}|) = \frac{1}{\upsilon\sqrt{2\pi}} \exp\left[-\frac{(|\sigma_{pc}| - \mu)^2}{2\upsilon^2}\right], \tag{4.1}$$

where σ_{pc} represents the surface pre-compressions, μ is the mean value and υ the standard deviation.

4.2 The statistical interference between residual stresses and pristine material strength

In the design practice, heat-treated glass strength σ_{htg} is schematically calculated as the simple sum of the strength of the pristine annealed glass (before thermal processing) σ_{ann} and the surface compression from the residual stresses σ_{pc}, i.e.,

$$\sigma_{htg} = \sigma_{ann} + |\sigma_{pc}|. \tag{4.2}$$

Since experiments have provided a wealth of evidence that σ_{htg} may be much higher than this, expression (4.2) is often proposed with an additional coefficient, i.e., $\sigma_{htg} = \sigma_{ann} + \omega|\sigma_{pc}|$, with $\omega > 1$. However, by observing that the terms in equation (4.2) represent statistical descriptors of peculiar statistical distributions, like the 5% quantiles, the aforementioned difference with the experimental results may be simply due to the statistical interference between the two component distributions while evaluating the characteristic value of σ_{htg} [73].
As discussed in Chapter 3, several statistical models have been proposed through the years to interpret the strength of glass. However, here reference can be made to

the most classical two-parameter Weibull (2PW) distribution, which is certainly the simplest. In fact, for what concerns heat-treated glass, the distribution of residual stresses mostly governs the left-hand-side tail of the strengths distribution and, hence, the use of the 2PW model for interpreting pristine strengths variability certainly provides estimates on the safe side. These are not excessively conservative as in the case of annealed float glass, because the competition with the surface prestress renders less important the left-hand-side tails.
Thus, by considering a generic state of stress Σ consequent to the application of external actions, associated with principal stresses $\sigma_1(x)$ and $\sigma_2(x)$ at the point x, the failure probability of a glass panel of surface area A assumes the form

$$F_a(\Sigma) = 1 - \exp\left[\int_A \left(\frac{\sigma_{eq}(x)}{\eta_0}\right)^m dA\right], \tag{4.3}$$

where η_0 and m are the parameters of the Weibull distribution, $\sigma_{eq}(x)$ is the equivalent value of the tensile stress at x. This is dependent, in turn, upon $\sigma_1(x)$ and $\sigma_2(x)$ and upon $|\sigma_{pc}|$, which represents the prestress. Recall from Section 4.1 that the state of stress induced through thermal treatment can be reasonably considered equibiaxial. Let ψ be the angle that the direction of the maximum principle stress σ_1 forms with the normal to the dominant crack plane again, assume isotropic defectiveness, the equivalent stress $\sigma_{eq}(x)$ reads

$$\sigma_{eq}(x) = 0, \qquad when\ \sigma_1(x) < |\sigma_{pc}|\,, \quad \sigma_2(x) < |\sigma_{pc}|, \tag{4.4a}$$

$$\sigma_{eq}(x) = \frac{2}{\pi}\int_0^{\pi/2} (\sigma_1(x) - |\sigma_{pc}|)\cos^2\psi + (\sigma_2(x) - |\sigma_{pc}|)\sin^2\psi d\psi, \quad when \quad \sigma_1(x) > |\sigma_{pc}|\,, \quad \sigma_2(x) > |\sigma_{pc}|, \tag{4.4b}$$

$$\sigma_{eq}(x) = \frac{1}{\pi}\int_{-\pi/2+\beta(x)}^{\pi/2-\beta(x)} (\sigma_1(x) - |\sigma_{pc}|)\cos^2\psi + (\sigma_2(x) - |\sigma_{pc}|)\sin^2\psi d\psi, \quad when \quad \sigma_1(x) > |\sigma_{pc}|\,, \quad \sigma_2(x) < |\sigma_{pc}|. \tag{4.4c}$$

The angle β is defined as the envelope of the angles ψ such that the component of the tensile stress orthogonal to the crack plane is equal or higher than $|\sigma_{pc}|$ and reads $\beta(x) = 1/2\,\arccos\left[(\sigma_1(x) + \sigma_2(x) - |\sigma_{pc}|)/(\sigma_1(x) - \sigma_2(x))\right]$. The significance of the angle β is illustrated in the Mohr' circle representation of Fig. 4.6(b). In the case of equation (4.4a), both the principal stresses are compressive and, hence, none of the micro-cracks is subject to opening stress ($\sigma_{eq}(x) = 0$). The opposite case is represented by equation (4.4b). In this case, both the principal stresses are tensile, all the cracks are subject to opening tensile stress and $\sigma_{eq}(x)$ is defined as the spatial average of the tensile stress at x. In fact the value $[\sigma_1(x) - |\sigma_{pc}|]\cos^2\psi - [\sigma_2(x) - |\sigma_{pc}|]\sin^2\psi$ is the stress component orthogonal to the crack plane. Lastly, in the case of equation (4.4c) only part of the Mohr' circle lies in the positive half-plane, since one principal stress is tensile while the other

one is compressive. In such a case, all the cracks whose plane has an inclination with respect to the maximum principle direction comprised between $-\beta$ and β are compressed. This strongly affects the statistical distribution of strengths, because it defines the direction that corresponds to potential crack openings. The equivalent stress $\sigma_{eq}(x)$ is still the spatial average of the tensile stress at the point x, but the intensity of the stress is computed as zero along the directions where the stress is compressive (the upper and the lower limits of the integral are $\pi/2 - \beta$ and $-\pi/2 + \beta$, respectively).

For a generic experimental campaign, denote with $f_a(\sigma_{ann})$ the probability density function for the pristine *annealed* glass strength at maximum stress σ_{ann} and with $f_p(|\sigma_{pc}|)$ the probability density function of the pre-compression stress at $|\sigma_{pc}|$. Assuming that the stochastic variables σ_{ann} and σ_{pc} are mutually *independent*, referring to a generic and, for simplicity, uniform state of stress Σ consequent to the application of external loads, the probability density function $f_t(\Sigma)$ is obtained through the statistical convolution of the density functions of the operant distributions, and reads

$$f_t(\Sigma) = (f_a * f_p)(\Sigma) = \int_{-\infty}^{+\infty} f_a\left(\sigma_{eq}(|\sigma_{pc}|)\right)\ f_p(|\sigma_{pc}|)\ d|\sigma_{pc}|, \tag{4.5}$$

from which the cumulative distribution function $F_t(\Sigma)$ is obtained of the form

$$F_t(\Sigma) = \int_{-\infty}^{+\infty} F_a\left(\sigma_{eq}(|\sigma_{pc}|)\right)\ f_p(|\sigma_{pc}|)\ d|\sigma_{pc}|, \tag{4.6}$$

where $F_a(\cdot)$ denotes the cumulative function associated with $f_a(\cdot)$. Thus, by assuming a 2PW and a Gaussian statistics to represent the variability of pristine glass strengths and of residual stresses, respectively, equation (4.6) becomes

$$\begin{aligned} F_t(\Sigma) = \int_{-\infty}^{+\infty} &\left\{1 - \exp\left[-A\left(\frac{\sigma_{eq}(|\sigma_{pc}|)}{\eta_0}\right)^m\right]\right\} \\ &\left\{\frac{1}{\upsilon\sqrt{2\pi}}\exp\left[-\frac{(|\sigma_{pc}| - \mu)^2}{2\upsilon^2}\right]\right\} d|\sigma_{pc}|. \end{aligned} \tag{4.7}$$

Interestingly, observe that it is statistically very unlikely that both the strength of annealed glass and the residual stresses attain their lowest values simultaneously. This is why a statistical descriptor such as the 5% quantile obtained as the sum of two independent stochastic variables reaches higher values than the simple analytical sum of the 5% quantiles of the two operant distributions.

From here on, the dependence of the mechanical strength upon the type of applied stress is discussed, taking into account that cracks open in mode I. Such effect is certainly well-known for simple annealed glass, but it is not so well investigated for heat-treated glass. Firstly, consider the case of a plate tested in the coaxial double ring configuration, which approximately approaches the ideal condition of uniform equibiaxial stress state ($\Sigma = \Sigma_{eqb}$, e.g., $\sigma_1 = \sigma_2 = \sigma_{eqb}$). In such a case, the orientation of the dominant crack does not affect glass strength, since

the probability that maximum tensile stress is orthogonal to the crack plane is 100%. In this case, the Mohr' circle degenerates into one point (see Figure 4.6), the equivalent stress is given by equation (4.4b) and, consequently, the convolution integral (4.7) assumes the form

$$F_t(\Sigma_{eqb}) = \int_0^{\sigma_{eqb}} \left\{1 - \exp\left[-A\left(\frac{\sigma_{eqb} - |\sigma_{pc}|}{\eta_0}\right)^m\right]\right\} \left\{\frac{1}{\upsilon\sqrt{2\pi}} \exp\left[-\frac{(|\sigma_{pc}| - \mu)^2}{2\upsilon^2}\right]\right\} d|\sigma_{pc}|, \tag{4.8}$$

where A is the area under tensile stress. In this case, the sum of the surface compression and the annealed glass strength is lower than the value obtained from the compound distribution if one refers to a statistical descriptor lower than the 50% quantile, whereas the opposite is true if one refers to a statistical descriptor higher than the 50% quantile. Then, the 50% quantile of the compound distribution is equal to the sum of the 50% quantiles of the primitive functions.

On the other hand, the stress state induced through three- or four-point-bending (3PB - 4PB) tests can be approximately considered uniaxial ($\Sigma = \Sigma_{unx}$, e.g., $\sigma_1(x) = \sigma_{unx}(x)$, $\sigma_2 = 0$). This situation is somehow dual to the equibiaxial state, since the probability of finding the maximum tensile stress at the right angle with crack axis is the lowest. *Ergo*, any other type of stress state is in-between these ones. Observe that the Mohr's circle representing the surface stress state for a heat-treated glass plate under uniaxial bending, shown in Figure 4.6(a), does not lie entirely in the positive half-plane. This means that a micro-crack is compressed if its plane has an inclination comprised between $-\beta$ and β with respect to the direction of σ_1. This has a very strong implication, since a certain number of flaws cannot cause failure, whatever their size is. This outcome is unattainable for annealed float glass (Mohr's circle (b) in Figure 4.6). Observe, by passing from circle (b) to circle (a) in Figure 4.6, that the prestress state σ_{pc} causes a left-shift of the circle center (C=$\sigma_{unx}/2$ vs. C=$\sigma_{unx}/2 - |\sigma_{pc}|$) without affecting the radius ($R = \sigma_{unx}/2$). Due to this phenomenon, even the 50% quantile of the compound probability function is higher than the sum of the mean values for the prestress and the pristine glass strength.

Interestingly, heat-treated glass strength is experimentally evaluated by testing specimens under four-point-bending (4PB) configuration, leading to the state of stress illustrated by circle (a) in Figure 4.6. Thus, a certain number of cracks is not subjected to opening tensile stresses when the specimen is tested, even though such cracks could lead to failure for stress states closer to equibiaxiality. Such outcome affects the statistical distribution of heat-treated glass strength and, hence, neglecting this effect could lead to a misleading interpretation of the experimental results.

By defining the principal stresses $\sigma_1(x) = \sigma_{unx}(x) - |\sigma_{pc}|$, the equivalent stress $\sigma_{eq}(x)$ given by equation (4.4c) becomes

$$\sigma_{eq,unx} = \frac{1}{\pi} \int_{\frac{-\pi}{2}+\beta}^{\frac{\pi}{2}-\beta} (\sigma_{unx}(x) - |\sigma_{pc}|) \cos^2\psi - |\sigma_{pc}| \sin^2\psi d\psi, \tag{4.9}$$

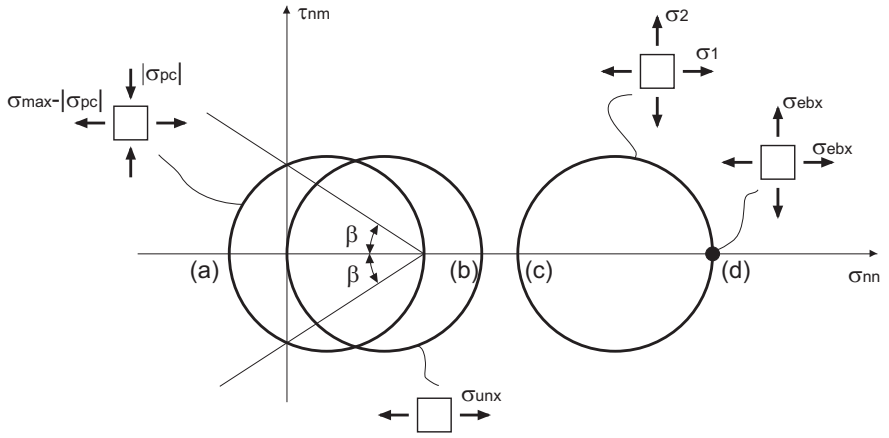

Figure 4.6: Mohr's circle representations. From left to right: (a) pure bending of a heat-treated glass plate; (b) pure bending of an annealed glass plate; (c) element under biaxial tensile stress; (d) equibiaxial stress state.

while $\beta(x) = 1/2 \arccos\left[1 - 2|\sigma_{pc}|/\sigma_{unx}(x)\right]$. Within a plate under a 4PB loading, the state of stress is homogeneous in the region A_l delimited by the inner loading points. Restricting the convolution integral to this area, equation (4.7) assumes the form

$$F_t(\Sigma_{unx}) = \int_0^{\sigma_{unx}} \left\{ 1 - \exp\left[-\left(\frac{\sigma_{unx} - |\sigma_{pc}|}{\eta_0} \right)^m \cdot \frac{A_l}{\pi} \int_{-\frac{\pi}{2}+\beta}^{\frac{\pi}{2}-\beta} \left(\cos^2\psi - \frac{|\sigma_{pc}|}{\sigma_{unx} - |\sigma_{pc}|} \sin^2\psi \right)^m d\psi \right] \right\} \cdot \left\{ \frac{1}{\upsilon\sqrt{2\pi}} \exp\left[-\frac{(|\sigma_{pc}| - \mu)^2}{2\upsilon^2} \right] \right\} d|\sigma_{pc}|. \quad (4.10)$$

If one considers even those parts of the specimens between the supporting and loading points, subject to an uniaxial tensile stress linearly varying with the distance from the supports, attaining its maximum at the loading points and being

null at the supporting points, the probability of failure becomes

$$
\begin{aligned}
F_t(\Sigma_{unx}) = & \int_0^{\sigma_{unx}} \left\{ 1 - \exp\left\{ - \left(\frac{\sigma_{unx} - |\sigma_{pc}|}{\eta_0} \right)^m \right.\right. \\
& \cdot \left[\frac{A_l}{\pi} \int_{-\frac{\pi}{2}+\beta}^{\frac{\pi}{2}-\beta} \left(\cos^2\psi - \frac{|\sigma_{pc}|}{\sigma_{unx} - |\sigma_{pc}|} \sin^2\psi \right)^m d\psi \right. \\
& + \frac{b}{\pi} \int_{d\,|\sigma_{pc}|/\sigma_{unx}}^{d} \int_{-\frac{\pi}{2}+\beta}^{\frac{\pi}{2}-\beta} \left(\frac{\frac{z}{d}\sigma_{unx} - |\sigma_{pc}|}{\sigma_{unx} - |\sigma_{pc}|} \cos^2\psi - \frac{|\sigma_{pc}|}{\sigma_{unx} - |\sigma_{pc}|} \sin^2\psi \right)^m d\psi dz \\
& \left. \left. + \frac{b}{\pi} \int_0^{d\,(1-|\sigma_{pc}|/\sigma_{unx})} \int_{-\frac{\pi}{2}+\beta}^{\frac{\pi}{2}-\beta} \left(\frac{\sigma_{unx}(1 - z/d) - |\sigma_{pc}|}{\sigma_{unx} - |\sigma_{pc}|} \cos^2\psi - \frac{|\sigma_{pc}|}{\sigma_{unx} - |\sigma_{pc}|} \sin^2\psi \right)^m \right.\right. \\
& \left. \left. d\psi dz \right] \right\} \cdot \left\{ \frac{1}{\upsilon\sqrt{2\pi}} \exp\left[- \frac{(|\sigma_{pc}| - \mu)^2}{2\upsilon^2} \right] \right\} d|\sigma_{pc}| \ ,
\end{aligned}
\tag{4.11}
$$

where b is the specimen width and d is the distance between loading and supporting points. By setting $A_l = 0$ in equation in (4.11), one obtains the function describing the probability of failure for a heat treated glass specimen under a 3PB configuration.

4.3 Statistical analysis of the experimental data

Firstly, data available in the technical literature have been analyzed for validating the theoretical model proposed in Section 4.2 [73]. However, such experimental campaigns were not properly designed to this aim, so that the consequent conclusions cannot be considered definite. This is the motivation for the ad-hoc experimental campaign performed at the Technical University of Darmstadt.

4.3.1 Analysis of data available in the technical literature

The first experimental campaign here considered is that by *Zaccaria and Overend* [104], who tested ten annealed, ten heat-treated and ten chemically-toughened glass plates under a coaxial double ring (CDR) configuration, with diameters of the loading and supporting rings respectively 51 mm and 127 mm. The aim was that of investigating the mechanical behavior of bi-treated glass. The plate dimensions were 300 × 300 × 6 mm, tested with the tin side under tension, while the residual stresses induced through the treatment were measured by SCALP-04 and SCALP-05 devices. The mean value for the surface residual stresses measured for the toughened glass plates is 117 MPa, with standard deviation 7 MPa. The mean value of the failure stresses for heat-treated glass resulting from the experimental campaign was 288 MPa. Since in [104] only the mean values of strength for pristine and heat-treated glass are recorded, Weibull statistics for pristine glass, obtained in other campaigns, have been used and combined with the statistics for prestresses derived from the measurements of [104].

Figure 4.7 shows the theoretical curves for the probability of failure obtained through equation (4.8). By following [104], the Gaussian function interpreting the residual stresses is characterized by mean value $\mu = 117$ MPa and standard

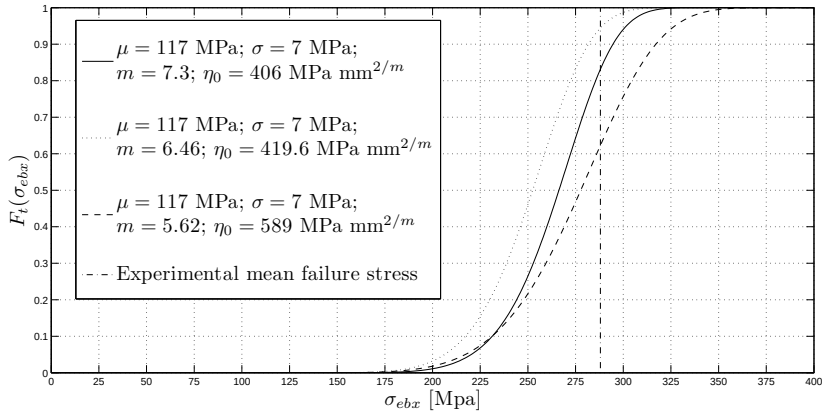

Figure 4.7: Cumulative probability function of the heat treated glass plates tested in [104] for different Weibull parameters.

deviation $\upsilon = 7$ MPa. In particular, in Figure 4.7, the continuous line refers to the Weibull parameters recorded in [25], i.e., $m = 7.3$ and $\eta_0 = 406$ Mpa mm$^{2/m}$; otherwise the dashed and the dotted curves are associated with the experimental data from the campaign by the CEN TC129/WG8 group [19], analyzed in Section 3.6. In particular, the dashed line refers to the Weibull pair estimated graphically according to the procedure recorded in Section A.2 ($m = 6.46$ and $\eta_0 = 419.6$ Mpa mm$^{2/m}$), while the dotted one to the Weibull pair estimated analytically through the Maximum Likelihood Estimation (MLE[2]) method ($m = 5.62$ and $\eta_0 = 589$ Mpa mm$^{2/m}$).
Even though only the mean strength of toughened glass plates is recorded in [104], shown by the vertical line in Figure 4.7, it seems that the dashed line obtained with the MLE pair is the most consistent with the experimental results. Since the state of stress is almost equibiaxial, the effect of the phenomenon illustrated in Figure 4.6 upon the statistical distribution of heat-treated glass strength is null. This is why the 50% quantile of the compound probability distribution (278 MPa) draws the same value as the sum of the 50% quantiles of the pristine annealed glass strength (161 MPa) and of the prestress (117 MPa) distributions. Focusing the attention on the 5% quantiles, the compound distribution draws a higher value (217 MPa) then those obtained by summing the 5% quantiles of the pristine strengths (101 MPa) and of the residual stresses distribution (105.5 MPa). The difference is not so high, of the order of 5%.
Furthermore, *Veer et al.* [89] performed a wide experimental campaign on annealed, heat strengthened and tempered glass plates tested in a 4PB configuration. For 16 heat strengthened plates and 16 toughened plates, the surface residual stresses were measured through a SCALP laser scanner. The resulting mean value and standard deviation of the Gaussian distribution for the prestresses acting within

[2]The likelihood of a set of data is the probability of obtaining that particular set of data, given the chosen probability distribution model. The value of those parameters that maximize the sample likelihood are known as the Maximum Likelihood Estimates.

the toughened glass plates were $\mu = 103.44$ MPa and $\upsilon = 6.73$, respectively. The specimens were tested at the air side. The Weibull pair for pristine strength has been directly estimated by analyzing the data reported in [89] referring to annealed glass plates. It is of importance to point out that the specimen dimensions were 300 mm × 100 mm × 10 mm, cut from a single sheet and not mechanical worked on the edges after cutting. Consequently, one can expect that the small tested specimens had been weakened because of the cutting process. The distance between loading and supporting points is $d = 75$ mm, while the area delimited by the loading points is $A_l = 9000$ mm^2, respectively, hence the cumulative probability function for annealed glass reads

$$F_a(\sigma_{ann}) = 1 - \exp\left\{ -\left(\frac{\sigma_{ann}}{\eta_0}\right)^m \left[A_l \frac{2}{\pi} \int_0^{\pi/2} (\cos^2\psi)^m \, d\psi + \right.\right.$$
$$\left.\left. \frac{2b}{\pi} \int_0^d \int_0^{\pi/2} \frac{z}{d} \cos^2\psi \; d\psi \, dz + \frac{2b}{\pi} \int_0^d \int_0^{\pi/2} \left(1 - \frac{z}{d}\right) \cos^2\psi \; d\psi \, dz \right] \right\}, \tag{4.12}$$

where σ_{ann} is the maximum stress acting within the annealed specimen at failure, while the terms between square brackets provide the effective area A_{eff}.
Since the specimens were very small with no edge finishing, the annealed glass specimens presumably failed at the border, whereas the statistical model here proposed refers to portions far from the edges. Hence, the Weibull parameters have been depurated from the influence of the edge weakening. As it is suggested by some standards [23], to pass from the "edge" to the "core" strength, the experimentally-obtained values for failure stresses have been divided by the coefficient $k_{ed} = 0.8$. Then, the values of the N data constituting the sample were putted in ascending order and an experimental value $P_i = \frac{i}{N+1}$ of the probability of failure was assigned to each i-th value. Finally, the parameters m and η_0 have been graphically estimated according to the procedure described in Section A.2.
If one considers the *complete tensile area* as per (4.11), the effective area is $A_{eff} = 3610$ mm^2, while the Weibull parameters are $m = 3,47$ and $\eta_0 = 875.41$ MPa mm$^{2/m}$, while considering only the *conventional tensile area* A_l comprised between the loading points, one would obtain quite different values of the effective area and the scale parameter with the same shape parameter m, i.e., $A_{eff} = 2630$ mm^2 and $\eta_0 = 799.1$ MPa mm$^{2/m}$. However, considering that the residual compressive stresses acting within a 15 mm wide region around the borders can be considered to be very high, this region of the specimens should not be considered in the analysis. Thus, the resulting values would be $A_{eff} = 2527$ mm^2 and $\eta_0 = 789.96$ MPa mm$^{2/m}$ for the same value of m again. In consideration of the uncertainty in the pristine glass strength characterization, all these possibilities have been compared.
For the loading case under consideration, the approximately uniaxial state of stress diminishes the failure probability, by increasing the dispersion of the cumulative density functions. Figure 4.8 illustrates a comparison between the theoretical and the experimental values for the probability of failure.
The continuous curve in Figure 4.8 is obtained from equation (4.10), which consid-

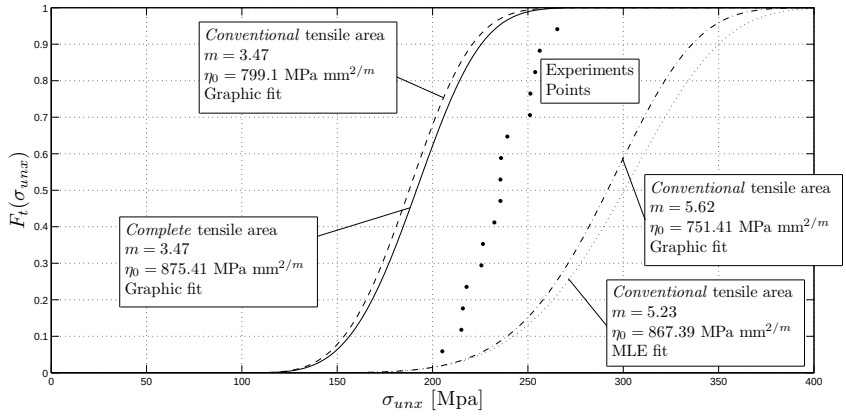

Figure 4.8: Toughened glass plates. Comparison between cumulative probability functions obtained through the convolution integral (4.10) and the experimental points recorded in [89] ($\mu = 103.44$, $\upsilon = 6.73$ and various choices of the Weibull parameters).

ers only the *conventional* area comprised between the loaded points, whereas the dashed curve is obtained if the *complete* tensile area is taken into consideration. Since the two curves are very close one another, the correction does not seem to be essential for the geometry under consideration. On the other hand, the two lines on the right-hand-side of Figure 4.8 refer to the Weibull pairs obtained by statistically analyzing the experimental data of [19] for commercial glasses, as in Section 3.6; graphically for the dash-dotted curve ($m = 5.62$ and $\eta_0 = 751.41$ MPa mm$^{2/m}$), through the MLE method for the dotted curve ($m = 5.23$ and $\eta_0 = 867.39$ MPa mm$^{2/m}$). Furthermore, the line corresponding to the Weibull parameters $m = 3.47$ and $\eta_0 = 789.96$ MPa mm$^{2/m}$, obtained by considering inactive the 15 mm wide band along the borders, is not plotted, because it is substantially superimposed to the one corresponding to $m = 3.47$ and $\eta_0 = 875.41$ MPa mm$^{2/m}$. The fact that experimental points are located in an intermediate position between the aforementioned curves is not surprising, and proves the importance of the correct estimation of the Weibull parameters. This is problematic for the case at hand because of the small-scale of the specimens, the small number of tests and the absence of edge finishing.

The results of the tests on heat-strengthened glass specimens have been analyzed in the same manner. The mean value and the standard deviation of the Gaussian distribution for residual stresses are $\mu = 42.78$ MPa and $\upsilon = 5.27$, respectively.

In Figure 4.9, the cumulative probability functions obtained through the convolution integral (4.10), with the same Weibull pairs used for (4.8) are plotted. Again, the curve referring to the case in which the 15 mm wide band along the borders is not considered is not plotted because of limited interest.

Observe that, unlike for toughened glass plates, the prestresses are mild even at the borders of the specimens and, hence, defects of the edges may affect the strength of heat-strengthened glass plates. This represents a source of uncertainty for the analysis. By looking at Figure 4.9, one can notice that also in this case,

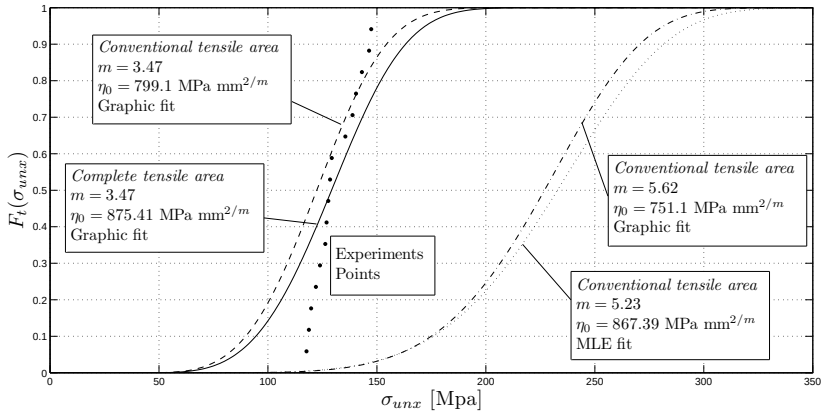

Figure 4.9: Heat-strengthened glass plates. Comparison between cumulative probability functions obtained through the convolution integral (4.10) and the experimental points recorded in [89] ($\mu = 42.78$, $\upsilon = 5.27$. Different Weibull pairs.

studying the whole tensile area rather than only the part comprised between the loading points does not cause a substantial difference. The experimental points, in particular the central ones, are consistent with the cumulative probability function obtained by using the Weibull pair characteristic of the strength exhibited by the annealed glass plates tested in [89].

All the outputs of the statistical analysis are summarized in Table 4.1. Considering the case of the *complete* tensile area, the difference between the 5% quantiles of the compound probability function (147 MPa) for tempered glass and the sum of the 5% quantiles of the component distributions (127 MPa) is of the order of the 14%, while the difference between the corresponding 50% quantiles is of the order of 8% (192 MPa vs. 178 MPa). Such differences, in percent terms, are a little higher for heat-strengthened glass ($\simeq$19% for the 5% fractiles and $\simeq$9% for the 50% fractiles). In general, the use of the the *conventional* tensile area in the calculations leads to slightly lower differences.

Furthermore, by comparing the results of the experimental campaign by *Zaccaria and Overend* [104] and by *Veer et al.* [89], notice that the differences in terms of the 5% quantiles for 4PB configuration are higher than for the CDR configuration.

4.3.2 The experimental campaign performed at the Technical University of Darmstadt

The mechanical strength of 50 annealed and 51 toughened float glass plates was evaluated by testing them under the coaxial double ring configuration proposed in Section B.3. All the samples, which were square of side 400 mm, were provided by the same supplier. The radii of the inner and of the outer rings are 75 mm and 150 mm, respectively. All the specimens were exposed to short-wave ultraviolet radiations so as to differentiate the air side from the tin side. The air side strength, which can be considered representative of the pristine material, has been investigated. The thickness of each plate was estimated as the mean value of 4

Table 4.1: *Conventional* tensile area vs *complete* tensile area. Comparison of the 5% and 50% fractiles from the compound probability functions and from the sum of the fractiles of the annealed glass strength and prestress.

CASE	**I**	**II**	**III**	**IV**
Tensile area	Conventional	Complete	Conventional	Complete
μ [MPa]	103.44	103.44	42.78	42.78
υ [MPa]	6.73	6.73	5.27	5.27
m	3.47	3.47	3.47	3.47
η_0 [MPa/mm$^{2/m}$]	799.1	875.41	799.1	875.41
$5\%_{ann}$+$5\%_{pc}$ [MPa]	127.3	127.3	68.7	68.7
$5\%_{com}$ [MPa]	144.5	147	81.2	85
$50\%_{ann}$+$50\%_{pc}$ [MPa]	177.9	177.9	117.3	117.3
$50\%_{com}$ [MPa]	188.5	192	122.5	129

measurements taken along the four sides of the plate. Before performing the tests, adhesive sheets were attached to the tin side of the specimen, so as to block the glass shards after breakage and hence to detect the points in which the plates collapsed. Only the data referred to specimens whose breakage started in the core part of the specimen (delimited by the inner ring) have been considered valid. The wide measurements campaign for the residual stresses was already mentioned in Section 4.1.1.

Firstly, the annealed glass plates were tested at a constant load rate of 270 N/sec, so to obtain a stress rate of approximately 2 MPa/sec. The maximum displacements resulting from the experimental campaign were less than half the thickness of the plate and, hence, the geometric non-linear effects have been considered negligible. Consequently, according to the static analysis recorded in Section B.1.1, the state of stress acting within the core part of the plates can be approximately considered homogenous and equibiaxial. The collapse of 38 panes started inside the circumference delimited by the inner ring, hence the results of such tests have been considered valid. From the fracture loads applied by the tensometer, FEM analyses have been made, by considering the actual thickness of any plate, so to evaluate the failure stress values $\sigma_{fail,i}$ for the i-th specimen. Strictly speaking, different fracture stresses are related to different stress histories and, hence, the *subcritical crack growth* diversely affects each specimen. For the sake of comparison, all the failure stress values were re-scaled towards the condition of constant tensile stress acting for a reference time of 60 seconds so as to normalize the *static fatigue* effects, i.e., the ramp stress history induced during the experiments was transformed to an equivalent uniform stress σ_{60} for a reference time $t_{ref} = 60$ sec through the equation

$$\int_0^{t_f} \left(\frac{\sigma_{fail} t}{t_f}\right)^n dt = \int_0^{t_{ref}} \sigma_{60}^n dt \quad \Rightarrow \quad \sigma_{60} = \sigma_{fail} \left[\frac{t_f}{t_{ref}(n+1)}\right]^{1/n}, \tag{4.13}$$

where n is the crack velocity parameter introduced in Section 3.2, here assumed to be $n = 16$. Observe that the value of n has not been experimentally evaluated.

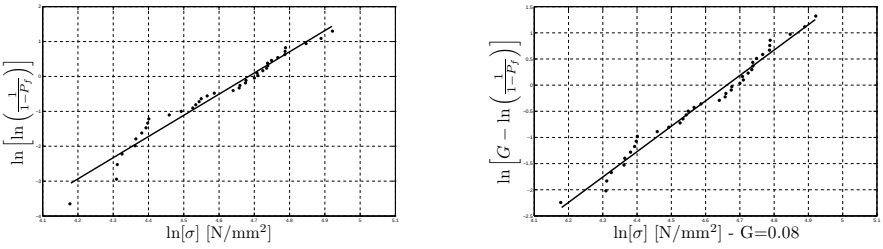

(a) (b)

Figure 4.10: (a) Weibull probability plot of the equivalent stresses σ_{60} referring to the annealed glass plates tested under CDR configuration; (b) left-truncated Weibull probability plot of the equivalent stresses σ_{60} referring to the annealed glass plates tested under CDR configuration.

However, different values of n may lead to very slightly changes in the statistical analysis. The 2-parameter and the left-truncated Weibull probability plots (see Sections A.2 and A.3.2) of the equivalent stresses σ_{60} are recorded in Figure 4.10. As it is evident from Figure 4.10, the left truncated Weibull distribution is able to interpret the variability of pristine glass strength much better than the 2-parameter Weibull distribution and, in particular, its left-hand-side-tail. However, such tail for the heat-treated glass strength population is mostly governed by the distribution of residual stresses. Hence, it is reasonable to use the 2-parameter Weibull statistics for interpreting the pristine material strength variability in equation (4.8). The Weibull parameters resulting from the graphical estimation method described in section A.2 are $m = 6.07$ and $\eta_0 = 108.14$ MPa.

For what concerns the tested full-tempered glass specimens, 35 valid results were obtained. The maximum displacements were such that membrane strains were of importance. Thus, according to the analysis recorded in Section B.1.1, the deviation from linearity makes the stress state different from the equibiaxial one. Since the statistical function (4.8) is well-founded for an almost uniform and equibiaxial stress state, whereas significant analytical complications may arise from a different-in-kind state of stress, the "effective area" defined in Section A.2, equation (A.11), has been estimated according to the 2-parameter Weibull model for each plate, and the failure stress values were re-scaled towards the reference condition of equibiaxial stress state.

The stress state within each plate has been investigated with the procedure proposed in Section B.1.1, i.e., radial and circumferential stresses can be found through equations (B.15) if the coefficient B_0 and C_1 are known, where B_0 is the value of S'_r, associated with the *membrane* stress at the center of the plate, while C_1 is proportional to the *bending* stress at the same point. Indeed, once such coefficients are known, all the other terms in the expansion (B.15) are obtained in cascade from (B.16). From simple FEM simulations, the membrane force per unit length $SF = \sigma'_{center}h$ and the bending moment per unit length $SM = \sigma''_{center}h^2/6$ at the center of the plate were evaluated for each plate by starting from the fracture load applied by the tensometer. Then, the coefficient B_0 and C_1 were obtained from expressions (B.19). However, the stress state so obtained, i.e., by considering only

the external loads, is not the one actually present within the specimen because of the eigenstress induced through thermal treatment. Thus, by assuming a homogenous and equibiaxial compressive state characterized by the mean value of the 10 measurements taken at each plate (see Section 4.1.1), the "actual" stress state was obtained. Then, assuming that the radial and the circumferential directions are the principal directions of stress, the ratio ρ between the minimum and the maximum minimal stresses and, consequently, the equivalent stress σ_{eq}, given by equation (B.21) has been found as a function of the distance from the center of the specimen. Consequently, the effective area was estimated with equation (B.22) and the data were re-scaled through the re-scaling law (A.13). Notice that the actual thicknesses were considered for each plate in the FEM simulations, since even small differences in plate thickness can lead to not negligible differences in the stress state. Finally, the surface compressions have been added to the re-scaled stresses so as to obtain the heat-treated glass strengths referring to an equibiaxial state of stress $\sigma_{ht,eqb}$. However, from a deep analysis of the data recorded in Appendix E, one can note that the deviation from the equibiaxiality is mild. Thus, potential inaccuracies of the aforementioned re-scaling procedure only slightly affect the statistical analysis. Furthermore, time to failure t_f obviously varied from specimen to specimen. Thus, the effects of the subcritical crack growth must be normalized again, but, when geometrical non-linearities arise, the experimental stress history is not any more linear. Figure 4.11 shows the experimental stress history, which was constructed through FEM analyses. By imposing again a constant load rate of 270 N/sec, the stress-time $\sigma - \tau$ relation is linear in the first part of the test, whereas it deviates from the linearity after a certain time.

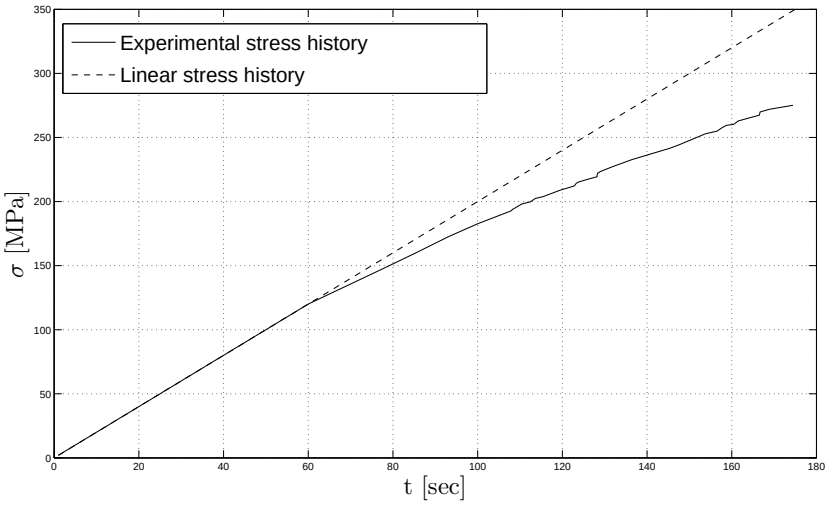

Figure 4.11: Experimental stress history for the heat-treated glass specimens under CDR loading configuration.

The equivalent uniform stress $\sigma_{ht,60}$ for a reference time $t_{ref} = 60$ sec is obtained

through the equality

$$\int_{t_{pc}}^{t_f} \left(\sigma_{ht,eqb}(t) - |\sigma_{pc}|\right)^n dt = \int_0^{t_{ref}} \left(\sigma_{ht,60} - |\sigma_{pc}|\right)^n dt, \tag{4.14}$$

where $\sigma_{ht,eqb}(t)$ is the function plotted in Figure 4.11, n is the crack velocity parameter (it is assumed $n = 16$ again), t_{pc} is the experimental time for the decompression of the external surface of the specimen and σ_{pc} is the surface compression at the beginning of the test. Notice that the underlying assumption for expressions (4.14) is that second order effects do not arise before the decompression of the external surface of the specimen. Such assumption seems to be valid since the stress history is still linear for values of stress of the same order of the measured residual stresses (90 MPa ÷ 110 MPa - see Section 4.1.1). Finally, the equivalent stresses $\sigma_{ht,60,i}$, for the i-th specimen were organized in ascending order, assigning the experimental value for the probability of failure $P_f = i/(N+1)$, where N is the total number of data.
The experimental data have been hence compared with the theoretical function (4.8). As mentioned above, the 2-parameter Weibull distribution is chosen for interpreting the pristine glass strength variability, with shape parameter $m = 6.07$ and scale parameter $\eta_0 = 108.14$ MPa. On the other hand, a Gaussian function is used for the residual stress variability, whose parameters ($\mu = 98.77$ MPa and $\upsilon = 2.79$ MPa) were obtained from a sample of 250 points, taking into account both the plate-by-plate and the point-to-point variation. The comparison between the experimental data and the theoretical function (4.8), derived from the treatment of the pristine glass strength and of the residual stresses, is shown in Figure 4.12.

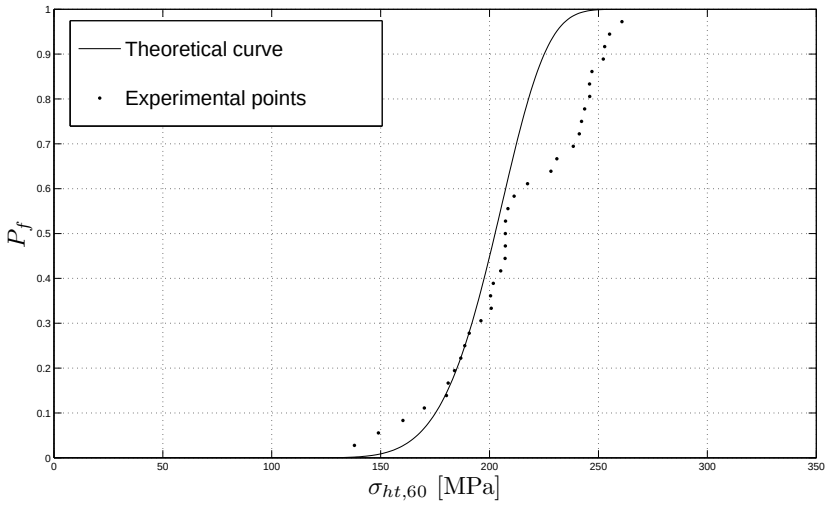

Figure 4.12: Comparison between the experimental data and the theoretical function (4.8).

Interestingly, the lower quantiles of the distribution are well interpreted by the

statistical model, whereas the higher the considered quantile is, the higher is the discrepancy between expected and observed data.
Such distance may be attributed, albeit tentatively, to the crack healing due to the thermal process. It is of interest to note that the effect of crack healing is almost null for the lower quantiles, associated with the largest cracks, whereas it is much more important for the higher quantiles, associated with the smallest cracks. Hence, the results of the experimental campaign have shown that the benefic contribution to heat-treated glass strength given by the crack healing is not negligible. The development of a refined mechanical model able to interpret the effects of the crack healing on the micro-crack lengths distribution should be the main focus of further research. The design of components made of heat-treated glass could be optimal only if one can safely take into account this benefic contribution.

CHAPTER **5**

THE EFFECT OF CORROSION AND ABRASION UPON THE STATISTICAL DISTRIBUTION OF GLASS STRENGTH

The defectiveness scenario present on the external surfaces of glass panes continuously changes during service life because of several events, that can be generally ascribed to corrosive or abrasive phenomena. A few experimental campaigns exist where specimens have been tested after aging, both natural or artificial, whose results are available in the technical literature. However, to my knowledge, no micro-mechanically motivated approaches have been proposed to analyze these data. In the current chapter, a model for interpreting how the macroscopic mechanical strength varies with microscopic changes in the flaws population is proposed. The underlying assumption is that the shape and chemistry of the flaw tip do not change over time, i.e., the changes in strength are attributed to changes in size of flaws. Since this is not strictly true, changes in length of cracks must be considered as equivalent values.

5.1 Corrosion

Corrosion phenomena continuously affect the float glass surfaces, because of reaction with gases in atmosphere. Besides visible degradation of the glass surface, corrosion leads to whitening, iridescence, loss of transparency and weight, due to the dissolution of the external layers. For what concerns the defectiveness scenario, corrosion leads to the simultaneous decreasing of micro-cracks length and the blunting of the crack tip. From a mechanical point of view, the effect of the crack blunting should be considered by properly modifying the stress intensity factor. Since the quantification of this effect is not straightforward, the underlying hypothesis in the proposed model is that corrosion leads to an *equivalent constant length reduction* for all the surface flaws constituting the defectiveness scenario.
From here on out, the suffix "1" and "2" will be referred to the glass states *before* and *after* corrosion, respectively. Thus, a generic crack of size δ_1 becomes of size $\delta_2 = \delta_1 - \varepsilon$, where ε represents the *equivalent constant length reduction*. Consequently, even the minimum size of the physiological cracks, introduced in equation

(3.13), varies, that is $\delta_{min,2} = \delta_{min,1} - \varepsilon$, supposing $\varepsilon < \delta_{min,1}$. Under the aforementioned assumptions, the probability of finding a crack of size δ in state "2" is the same as the probability of finding a crack of size $\delta + \varepsilon$ in state "1". Assume again, as in Section 3.5, that the surface of the pane is divided into *Representative Area Elements* (RAE), say ΔA, whose main property is that they can host only one crack; hence the number of cracks present on the external surface of a specimen of area A is $A/\Delta A$. Assuming that the crack size population of the state "1" follows a non-truncated power-law function, given by equation (3.15), the new cumulative probability function for the state "2" reads

$$P^{\geq,(2)}_{\Delta A,\delta}(\delta) = \left(\frac{\delta+\varepsilon}{\delta_{min,1}}\right)^{-\alpha^*} = \Delta A \left(\frac{\delta+\varepsilon}{\zeta_0}\right)^{-\alpha^*}, \tag{5.1}$$

where $\alpha^* = \alpha - 1$, with α exponent of the power-law function, and $\zeta_0 = \delta_{min} \Delta A^{-1/\alpha^*}$. From the equation of the critical SIF K_{Ic}, one can write

$$\delta = \frac{1}{\pi}\left(\frac{K_{Ic}}{Y\sigma_{cr}}\right)^2, \qquad \varepsilon = \frac{1}{\pi}\left(\frac{K_{Ic}}{Y\sigma_{\varepsilon}}\right)^2, \tag{5.2}$$

where σ_ε represents the critical stress correlated to ε. After some analytical manipulations, function (5.1) assumes the form

$$P^{\leq,(2)}_{\Delta A,\sigma}(\sigma_{cr}) = \Delta A \left(\frac{\sigma_{cr}}{\eta_{0,2p}\sqrt{1+\sigma_{cr}^2/\sigma_\varepsilon^2}}\right)^{2\alpha^*}, \tag{5.3}$$

where $\eta_{0,2p}$ has been already introduced in Chapter 3, equation (3.29). For the sake of simplicity, we refer to an equibiaxial stress state. Recalling equation (3.25), the survival probability for a corroded glass plate of area A_0 under an uniform equibiaxial stress state ($\Sigma = \Sigma_{eqb}$, e.g., $\sigma_1 = \sigma_2 = \sigma_{eqb}$) becomes

$$P_s^{(2)}(\Sigma_{eqb}, A_0) = \left[1 - \Delta A \int_0^{\sigma_{eqb}} \frac{d}{d\sigma_{cr}} \left(\frac{\sigma_{cr}}{\eta_{0,2p}\sqrt{1+\sigma_{cr}^2/\sigma_\varepsilon^2}}\right)^{2\alpha^*} d\sigma_{cr}\right]^{A_0/\Delta A}. \tag{5.4}$$

Then, take $A_0/\Delta A = 1/\varepsilon$; for small value of ΔA one has $\varepsilon \to 0$ and

$$\lim_{\varepsilon\to 0}\left[(1+\varepsilon\, x)^{1/\varepsilon}\right] = \exp(x)\,. \tag{5.5}$$

Then, one can write

$$P_s^{(2)}(\Sigma_{eqb}, A_0) = \exp\left[-A_0\left(\frac{\sigma_{eqb}}{\eta_{0,2p}\sqrt{1+\sigma_{eqb}^2/\sigma_\varepsilon^2}}\right)^{2\alpha^*}\right]. \tag{5.6}$$

Therefore, the probability of failure for a generic uniformly loaded area A takes the form

$$P_f^{(2)}(\Sigma_{eqb}, A) = 1 - \exp\left[-A\left(\frac{\sigma_{eqb}}{\eta_{0,2p}\sqrt{1+\sigma_{eqb}^2/\sigma_\varepsilon^2}}\right)^{2\alpha^*}\right]. \tag{5.7}$$

Since generally $\varepsilon \ll \delta$, hence $\sigma_\varepsilon \gg \sigma_{eqb}$ and, consequently, $\sigma_{eqb}^2/\sigma_\varepsilon^2 \ll 1$, one can expand in Taylor series $1/\sqrt{1+\sigma_{eqb}^2/\sigma_\varepsilon^2} = 1 - 1/2\left(\sigma_{eqb}^2/\sigma_\varepsilon^2\right) + o\left(\sigma_{eqb}^2/\sigma_\varepsilon^2\right)$, so that the probability of failure for the state "2" can be approximated as

$$P_f^{(2)}(\Sigma_{eqb}, A) = 1 - \exp\left\{-A\left[\frac{\sigma_{eqb}}{\eta_{0,2p}}\left[1 - \frac{1}{2}\left(\frac{\sigma_{eqb}^2}{\sigma_\varepsilon^2}\right)\right]\right]^{2\alpha^*}\right\}. \tag{5.8}$$

Assume now that the variation of the crack lengths in the pristine state "1" follows an upper-truncated power law function of the type (3.18). The probability that a crack is correlated with a critical stress equal or lower than σ_{cr} in the state "2" becomes

$$P_{\Delta A,\sigma}^{\leq,T(2)}(\sigma_{cr}) = \frac{\Delta A}{\eta_{0,lt}^{2\alpha^*}}\left[\left(\frac{\sigma_{cr}}{\sqrt{1+\sigma_{cr}^2/\sigma_\varepsilon^2}}\right)^{2\alpha^*} - \sigma_0^{2\alpha^*}\right], \tag{5.9}$$

where $\eta_{0,lt}$ has the same meaning of equation (3.34), and σ_0 is the minimal strength, associated with the maximum allowable crack length δ_{max}. By repeating the same analytical step made above, one obtains

$$P_f^{T(2)}(\Sigma_{eqb}, A) = 1 - \exp\left\{-A\left[\frac{\sigma_{eqb}^{2\alpha^*} - \sigma_0^{2\alpha^*}}{\eta_{0,lt}^{2\alpha^*}}\left[1 - \frac{1}{2}\left(\frac{\sigma_{eqb}^2}{\sigma_\varepsilon^2}\right)\right]^{2\alpha^*}\right]\right\}. \tag{5.10}$$

By assuming reference values for the power law function parameters α^* =2.5 and $\eta_{0,2p}$ =1000 MPa mm$^{1/\alpha^*}$, for the upper-truncated power law distribution α^* =2.5, $\eta_{0,2p}$ =1000 MPa mm$^{1/\alpha^*}$ and σ_0 =40 MPa, and by imposing an *equivalent constant length reduction* $\varepsilon = 10$ μm, from which σ_ε =187.62 MPa, the variation of the statistical distribution of strength by passing from the state "1" to "2" is shown in Figure 5.1. For the sake of simplicity, an uniform and equibiaxial stress state is considered again, acting on a unitary area $A_0 = 1$ m^2.

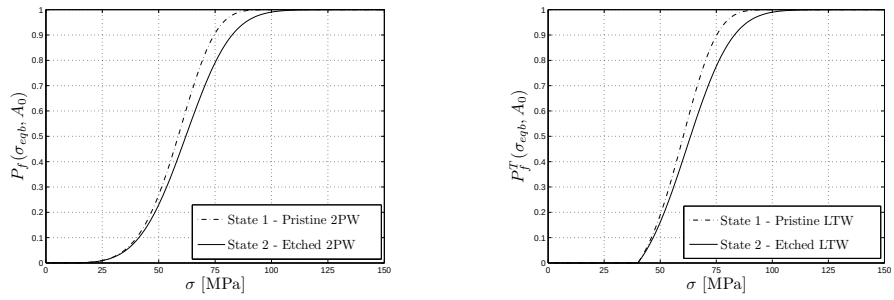

(a) (b)

Figure 5.1: (a) Effect of 10 μm-deep surface dissolution upon the 2-parameter Weibull distribution ($\varepsilon = 10\,\mu$m; α^* =2.5; $\eta_{0,2p}$ =1000 MPa mm$^{1/\alpha^*}$); (b) Effect of 10 μm surface dissolution upon the left-truncated Weibull distribution ($\varepsilon = 10\,\mu$m; α^* =2.5; $\eta_{0,2p}$ =1000 MPa mm$^{1/\alpha^*}$; σ_0 =40 MPa).

Since a 10 μm cracks reduction strongly affects the smallest cracks, whereas it is almost negligible for largest flaws, the benefic effects of corrosion upon strength distribution are much more significant for the highest quantiles, associated with small crack lengths.

Interestingly, artificial corrosion by using hydrofluoric acid (acid etching) is an efficient way for strengthening glass, since it reduces cracks size and blunt the crack tips [85, 80]. For the sake of illustration, one can refer to the statistical analysis of the experimental campaign made by *Schula* on etched glass plates, recorded in his Ph.D. thesis [84]. The specimens were firstly scratched and then subject to acid etching. Different samples, constituted by 10 data, were analyzed for different exposure to acid etching, while an adding sample of 24 data was constituted by specimens the had not been etched. Here, the cases of 1 min, 2 min and 5 min of acid etching exposure time are analyzed. Strictly speaking, the scratching of the specimens makes the distribution of the critical cracks size almost uniform, with a narrow dispersion. This is not perfectly interpreted by the LTW distribution, as it is possible to observe from the black line in Figure 5.2, referred to as the not-etched specimens.

All the data were arranged in ascending order and an experimental value of the probability of failure has been assigned as $P_f = i/(N+1)$ for the i-th datum, where N is the total number of data. The failure stress values referred to not-etched specimens were fitted through a LTW cumulative function, while the other samples through the statistical function (5.10). The theoretical curves shown in Figure 5.2 were obtained by imposing the Weibull parameters graphically obtained from the not-etched sample ($m = 43.063$, $\eta_{0,lt} = 61.73$ MPa mm$^{2/m}$ and $\sigma_0 = 48.02$ MPa), and by varying the value of σ_ϵ so as to obtain the best fit with the experimental data. The resulting values of σ_ϵ and of ϵ, obtained from $(5.2)_2$ are: $\sigma_{\epsilon,1min} = 200$ MPa, $\epsilon_{1min} = 8.88\,\mu$m, $\sigma_{\epsilon,2min} = 180$ MPa, $\epsilon_{2min} = 10.97\,\mu$m, $\sigma_{\epsilon,5min} = 145$ MPa, $\epsilon_{5min} = 16.90\,\mu$m. Even though the size of the specimens is very small and the scratching certainly disturbs the analysis, the model seems to acceptably interpret

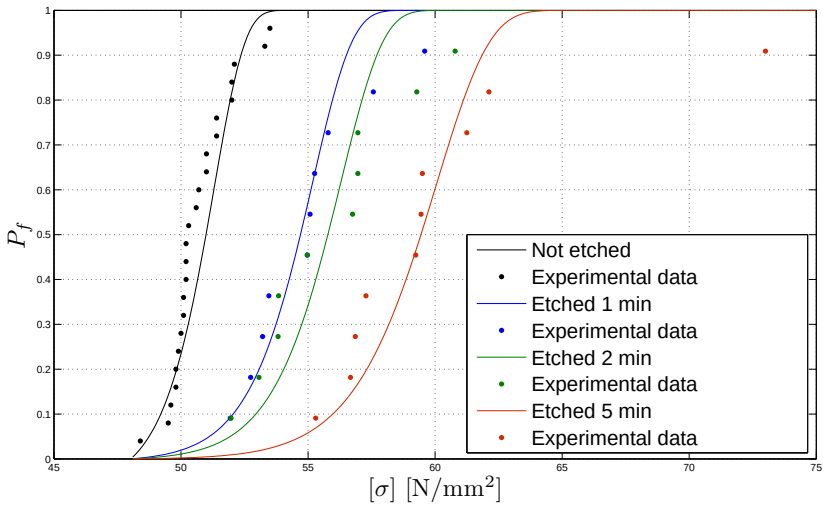

Figure 5.2: Fitting of the experimental data on scratched and etched specimen recorded in [84] through the statistical function (5.10).

the variation of the statistical distribution of strength with increasing exposure time to acid etching. In any case, it is confirmed that corrosion affects the higher quantiles of the distribution much more than the lower ones. Of course, a properly designed experimental campaign would be desirable, where test specimens are not pre-scratched before the acid etching.

5.2 Abrasion

The statistical analysis of the data referring to the strength of abraded glass panes is the subject of several contributions available in the technical literature. In particular, the results of some experimental campaigns on specimens that have been artificially scratched in order to reproduce the effect of natural abrasion are recorded in the technical literature. *Durchholz et al.* [30] tested float glass panes treated by dropping corundum (Al_2O_3) on them according to the set-up standardized by EN1288-2 [31]. From the statistical analysis of the experimental data through a 2-parameter Weibull distribution, they observed a left-shift of the distribution (lower scale parameter) accompanied by a significant rotation (much greater scale exponent), i.e., the highest strengths of the population are lowered, but the dispersion is reduced. Remarkably, the lower quantiles remained of the same order as those obtained by analyzing the pristine float glass.

Interested in studying the effects of sandstorms upon the mechanical performance of glass, Algerian scientists [56] investigated the influence of sandblasting. In particular, mechanical tests on float glass plates were made after different time of exposure to sandblasting, and the results are summarized in Figure 3.6. It is evident that, by increasing the sandblasting duration, glass strength tends to an asymptotic value. This is most likely due to the effects upon the defectiveness

scenario of a long-time exposure to the solid particle impacts.
When the hard sharp particle impacts the glass surface, high compressive and shear stresses arise; consequently, the contact area is plastically deformed and radial cracks are formed. Furthermore, lateral cracks are induced by large tensile stresses due to the plastic deformation, causing the material removal. A simplified view of such a phenomenon is shown in Figure 5.3.

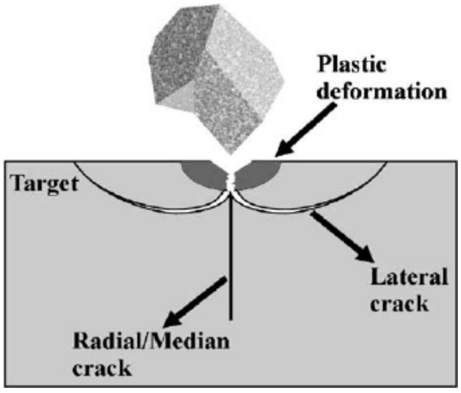

Figure 5.3: Schematic representation of cracks formation due to a single solid impact [95].

Thus, a heavy erosion process leads to the dissolution of the external layers of the specimen, which becomes thinner and, hence, to the extinction of the pre-existing micro-cracks population. Consequently, the radial crack lengths govern the mechanical strength of glass.
For the better understanding of such phenomenon, it is of interest to observe Figures 5.4(a) and 5.4(b), referring to an experimental campaign performed by *Jilbert and Field* [53], who studied the combined effect of liquid impact followed by solid impact on brittle plates, although the tested material was the zinc sulphide (ZnS) and not the glass. Firstly, the specimens were damaged through liquid impact, whose effect consists in forming an undamaged area in the central region, over which the high compressive stresses develop, surrounded by short circumferential cracks. Then, sand-blasting erosion was made for different sand impact velocities, causing elastic-plastic deformation, i.e., a plastically deformed region is formed from which radial and lateral cracks grow as it is clear from Figure 5.4(a). Figure 5.4(b) shows how the defectiveness scenario on the external surface of the specimen varies with the exposure time to sand erosion for the case of impact velocity 20 m s^{-1}, while the piece of pie chart detached from the rest shows the defectiveness scenario of a specimen subjected to sandblasting but not to liquid impact. No differences are noticeable between the specimens with harder erosion processes, with and without exposure to liquid impact. This means that the initial defectiveness scenario is completely annihilated and a new single micro-cracks population, whose dispersion in terms of length is very low, is present on the external surface of the specimen.
On the other hand, in the early erosion stages two different micro-crack populations can be distinguished. From this outcome, one question arises: what is the worst condition for a glass pane? One could superficially answer that a heavier abrasion

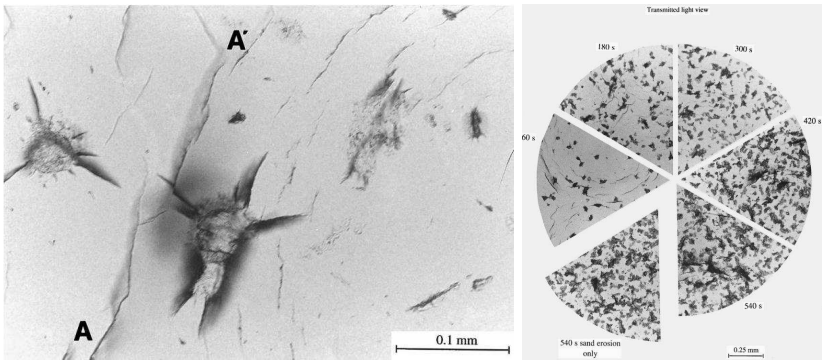

(a) (b)

Figure 5.4: (a) Selected view from a ZnS specimen impacted 100 times in a random array over 14 mm diameter by 0.8 mm jets and sand eroded at 30 ms^{-1} for 10 s at 0.15 $kgm^{-2}s^{-1}$ with C25/52 sand; (b) FLIR ZnS previously liquid impacted by 0.8 mm jets at 185 ms^{-1} (100 impact random array over 14 mm diameter circle) followed by sand erosion at 0.15 $kgm^{-2}s^{-1}$ at 10 ms^{-1} by C25/52 sand [53].

process leads to a weaker glass element, but this is not always true. Referring again to the experimental campaign performed by the Algerian scientists [56], the results of the mechanical tests for pristine material and for 30 min and 60 min of exposure time to sandblasting have been presented in Figure 3.5. An increase of the sandblasting time reduces the strength at high probabilities of failure, but the opposite is true for low probabilities, i.e., the lowest quantiles of the strength distribution do not reach their lowest values for the harder erosion processes.
Interestingly, it was observed that the maximum crack length due to exposition to sandblasting was approximately 35 μm.
Considering that the length of the largest cracks in the pristine material, just after the industrial production, can be assumed of the order of 200 - 300 μm, it can be argued that the flaws due to the extreme condition of abrasion are much smaller than the original ones. Hence, the residual cracks, whose lengths distribution is almost uniform, are smaller than the largest preexisting cracks, by causing an increase of the lower quantiles of the strengths distribution, accompanied by a decreasing of the mean value of the distribution. However, "strengthening by abrasion" for the lower quantiles may be considered limited to heavy environments or aggressive abrasion in the lab, otherwise the effects of very small cracks upon the large cracks associated to the lower quantiles is negligible. In fact, it will be shown in Section 5.3 that the contact with tin bath and steel rollers during float process slightly affects the left part of the population of strengths.
Thus, it is not sure that, during the erosion process, a condition of the external surface is reached that leads to the lowest values for all the quantiles of the strengths distribution. However, the length of the cracks induced through abrasion is strongly dependent upon several factor, among which the geometry and the composition of the particles used to erode the specimens [26]. Thus, different results in terms of strength variation could be reached by using different elements to impact with the glass plates.

The effects of a *mild* abrasion process upon the defectiveness scenario can be schematically considered as the addiction of new cracks to the pre-existing ones. We can assume the super-position of two different surface cracks populations, the *pre-existing* one and the one induced by *abrasion*. Firstly, consider that both the distributions are interpreted by power-law distributions of the same type of (3.14), i.e.,

$$p^{pre}_{\Delta A,\delta}(\delta) = \frac{\alpha_1 - 1}{\delta_{min,1}} \left(\frac{\delta}{\delta_{min,1}} \right)^{-\alpha_1}, \quad p^{abr}_{\Delta A,\delta}(\delta) = \frac{\alpha_2 - 1}{\delta_{min,2}} \left(\frac{\delta}{\delta_{min,2}} \right)^{-\alpha_2}. \quad (5.11)$$

By defining $\alpha_1^* = \alpha_1 - 1$ and $\alpha_2^* = \alpha_2 - 1$, the probabilities of finding a crack of size equal or higher than δ in the representative area element ΔA assume the form

$$P^{\geq,pre}_{\Delta A,\delta}(\delta) = \left(\frac{\delta}{\delta_{min,1}} \right)^{-\alpha_1^*}, \quad P^{\geq,abr}_{\Delta A,\delta}(\delta) = \left(\frac{\delta}{\delta_{min,2}} \right)^{-\alpha_2^*}, \quad (5.12)$$

while the probability of finding a crack lower than δ, given by the super-position of the two effects, becomes

$$P^{\leq}_{\Delta A,\delta}(\delta) = \left[1 - \left(\frac{\delta}{\delta_{min,1}} \right)^{-\alpha_1^*} \right] \left[1 - \left(\frac{\delta}{\delta_{min,2}} \right)^{-\alpha_2^*} \right], \quad (5.13)$$

which leads to the probability of finding a crack of size higher than δ of the form

$$P^{\geq}_{\Delta A,\delta}(\delta) = 1 - P^{\leq}_{\Delta A,\delta}(\delta) = \left[\left(\frac{\delta}{\delta_{min,1}} \right)^{-\alpha_1^*} + \left(\frac{\delta}{\delta_{min,2}} \right)^{-\alpha_2^*} \right] - \frac{\delta^{-(\alpha_1^* + \alpha_2^*)}}{\delta_{min,1}^{-\alpha_1^*} \, \delta_{min,2}^{-\alpha_2^*}}. \quad (5.14)$$

Strictly speaking, the numbers of pre-existing, $N_{0,1}$, and induced by abrasion, $N_{0,2}$, cracks or, equivalently, the representative surface elements ΔA_1 and ΔA_2 are different. This makes a derivation similar to that obtained through equation (3.25) in Chapter 3 not straightforward. However, we may approximately consider an average value of the representative surface element $\Delta A_m = (\Delta A_1 + \Delta A_2)/2$ so as to obtain

$$P^{\geq}_{\Delta A,\delta}(\delta) = \Delta A_m \left[\left(\frac{\delta}{\zeta_{0,1m}} \right)^{-\alpha_1^*} + \left(\frac{\delta}{\zeta_{0,2m}} \right)^{-\alpha_2^*} - \left(\frac{\delta}{\zeta_{0,3m}} \right)^{-(\alpha_1^* + \alpha_2^*)} \right], \quad (5.15)$$

where

$$\begin{aligned}\zeta_{0,1m} &= \frac{\delta_{min,1}}{(\Delta A_m)^{1/\alpha_1^*}}\,,\quad \zeta_{0,2m} = \frac{\delta_{min,2}}{(\Delta A_m)^{1/\alpha_2^*}}\,,\\ \zeta_{0,3m} &= \frac{(\delta_{min,1})^{\alpha_1^*/(\alpha_1^*+\alpha_2^*)}\;(\delta_{min,2})^{\alpha_2^*/(\alpha_1^*+\alpha_2^*)}}{(\Delta A_m)^{1/(\alpha_1^*+\alpha_2^*)}}\,.\end{aligned} \tag{5.16}$$

Assuming for simplicity a homogeneous and equibiaxial stress state $\Sigma = \Sigma_{eqb}$, e.g., $\sigma_1 = \sigma_2 = \sigma_{eqb}$, the same argument of Chapter 3, Section 3.5, can now be repeated.

Substituting expression (5.15) into the equation for the survival probability of a plate of area A_0 (3.25), the cumulative probability function, obtained by performing again the limit as *per* (5.5), reads

$$\begin{aligned}P_f(\Sigma_{eqb}, A) = 1 - \exp\Bigg\{ - A\Bigg[&\left(\frac{\sigma_{eqb}}{\eta_{0,2p,1m}}\right)^{2\alpha_1^*} + \left(\frac{\sigma_{eqb}}{\eta_{0,2p,2m}}\right)^{2\alpha_2^*}\\ &- \left(\frac{\sigma_{eqb}}{\eta_{0,2p,3m}}\right)^{2(\alpha_1^*+\alpha_2^*)}\Bigg]\Bigg\},\end{aligned} \tag{5.17}$$

where

$$\eta_{0,2p,1m} = \frac{K_{Ic}}{Y\sqrt{\pi\zeta_{0,1m}}}\,,\quad \eta_{0,2p,2m} = \frac{K_{Ic}}{Y\sqrt{\pi\zeta_{0,2m}}}\,,\quad \eta_{0,2p,3m} = \frac{K_{Ic}}{Y\sqrt{\pi\zeta_{0,3m}}}\,. \tag{5.18}$$

The resulting statistical function (5.17) represents a new generalized Weibull distribution, evidently much more complex than the classical 2-parameter one.

Assuming now an upper-truncated power law distribution for interpreting the variability of the crack lengths population in the pristine glass, the two probability functions hence read

$$p^{T,pre}_{\Delta A,\delta}(\delta) = \frac{\alpha_1 - 1}{\delta_{min,1} - \delta_{max}^{1-\alpha_1}\,\delta_{min,1}^{\alpha_1}}\left(\frac{\delta}{\delta_{min,1}}\right)^{-\alpha_1}\,,\quad p^{abr}_{\Delta_A,\delta}(\delta) = \frac{\alpha_2 - 1}{\delta_{min,2}}\left(\frac{\delta}{\delta_{min,2}}\right)^{-\alpha_2}\,. \tag{5.19}$$

From the expression for the critical SIF and from σ_0 and σ_k introduced in Section 3.5, equations (3.32), after some analytical steps, one finds that the probability of finding a crack correlated to critical stress equal or lower than σ_{cr} assumes the

form

$$
\begin{aligned}
P^{\leq}_{\Delta A,\sigma}(\sigma_{cr}) &= \Delta A_m \left(\frac{\sigma_{cr}}{\eta_{0,2p,2m}}\right)^{2\alpha_2^*} \quad when\ \sigma_{cr} \leq \sigma_0, \\
P^{\leq}_{\Delta A,\sigma}(\sigma_{cr}) &= \Delta A_m \left[\frac{\sigma_{cr}^{2\alpha_1^*} - \sigma_0^{2\alpha_1^*}}{\eta_{0,lt,1m}^{2\alpha_1^*}} + \left(\frac{\sigma_{cr}}{\eta_{0,2p,2m}}\right)^{2\alpha_2^*}\right. \\
&\quad \left. - \frac{\sigma_0^{2\alpha_1^*}\sigma_{cr}^{2\alpha_2^*} - \sigma_{cr}^{2(\alpha_1^*+\alpha_2^*)}}{\eta_{0,lt,3m}^{2(\alpha_1^*+\alpha_2^*)}}\right] \quad when\ \sigma_{cr} \geq \sigma_0,
\end{aligned}
\tag{5.20}
$$

where

$$
\begin{aligned}
\eta_{0,lt,1m} &= \left[\Delta A_m \left(\sigma_{k,1}^{2\alpha_1^*} - \sigma_0^{2\alpha_1^*}\right)\right]^{1/2\alpha_1^*}, \ \eta_{0,2p,2m} = \frac{\sigma_{k,2}}{(\Delta A_m)^{1/\alpha_1^*}}, \\
\eta_{0,lt,3m} &= \left[\Delta A_m \left(\sigma_0^{2\alpha_1^*} - \sigma_{k,1}^{2\alpha_1^*}\right)\sigma_{k,2}^{2\alpha_2^*}\right]^{\frac{1}{2(\alpha_1^*+\alpha_2^*)}}.
\end{aligned}
\tag{5.21}
$$

From the same rationale, the cumulative probability of failure is obtained. This reads

$$
\begin{aligned}
P_f(\Sigma_{eqb}, A) &= 1 - \exp\left[-A\left(\frac{\sigma}{\eta_{0,2p,2m}}\right)^{2\alpha_2^*}\right] \quad when\ \sigma \leq \sigma_0, \\
P_f(\Sigma_{eqb}, A) &= 1 - \exp\left\{-A\left[\frac{\sigma_{eqb}^{2\alpha_1^*} - \sigma_0^{2\alpha_1^*}}{\eta_{0,lt,1m}^{2\alpha_1^*}} + \frac{\sigma_{eqb}^{2\alpha_2^*}}{\eta_{0,lt,2m}^{2\alpha_2^*}}\right.\right. \\
&\quad \left.\left. - \frac{\left[\sigma_0^{2\alpha_1^*}\left(\sigma_{eqb}^{2\alpha_2^*} - \sigma_0^{2\alpha_2^*}\right)\right] + \left[\sigma_{eqb}^{2(\alpha_1^*+\alpha_2^*)} - \sigma_0^{2(\alpha_1^*+\alpha_2^*)}\right]}{(\eta_{0,lt,3m})^{2(\alpha_1^*+\alpha_2^*)}}\right]\right\} \quad when\ \sigma \geq \sigma_0.
\end{aligned}
\tag{5.22}
$$

It is evident that the resulting cumulative statistical distribution is much more complex than the left-truncated Weibull one.
Furthermore, there are cases in which abrasive phenomena precedes the post-processing acceptance phase, as it is the case for the surface of glass plates in contact with the tin bath and the steel rollers during the production process, on which I will focus in Section 5.3. In this case, both statistics should be interpreted by upper-truncated power law functions of the type

$$
\begin{aligned}
p^{T,pre}_{\Delta A,\delta}(\delta) &= \frac{\alpha_1 - 1}{\delta_{min,1} - \delta_{max}^{1-\alpha_1}\delta_{min,1}^{\alpha_1}}\left(\frac{\delta}{\delta_{min,1}}\right)^{-\alpha_1}, \\
p^{T,abr}_{\Delta A,\delta}(\delta) &= \frac{\alpha_2 - 1}{\delta_{min,2} - \delta_{max}^{1-\alpha_2}\delta_{min,2}^{\alpha_2}}\left(\frac{\delta}{\delta_{min,2}}\right)^{-\alpha_2}.
\end{aligned}
\tag{5.23}
$$

The same upper bound δ_{max} of the crack lengths for both the distributions is here

assumed, which is equivalent to impose the same truncation to both the statistical populations. By using the same arguments as above, the probability of finding a crack with length equal or larger than δ becomes

$$P^{\geq}_{\Delta A,\delta}(\delta) = \left[\frac{\delta_{max}^{-\alpha_1^*} - \delta^{-\alpha_1^*}}{\delta_{max}^{-\alpha_1^*} - \delta_{min,1}^{-\alpha_1^*}} + \frac{\delta_{max}^{-\alpha_2^*} - \delta^{-\alpha_2^*}}{\delta_{max}^{-\alpha_2^*} - \delta_{min,2}^{-\alpha_2^*}}\right] - \frac{\delta_{max}^{-\alpha_1^*} - \delta^{-\alpha_1^*}}{\delta_{max}^{-\alpha_1^*} - \delta_{min,1}^{-\alpha_1^*}} \frac{\delta_{max}^{-\alpha_2^*} - \delta^{-\alpha_2^*}}{\delta_{max}^{-\alpha_2^*} - \delta_{min,2}^{-\alpha_2^*}}, \tag{5.24}$$

which leads to a probability of failure of the form

$$P_f(\Sigma_{eqb}, A) = 1 - \exp\left\{ - A\left[\frac{\sigma^{2\alpha_1^*} - \sigma_0^{2\alpha_1^*}}{(\eta_{0,lt,1m})^{2\alpha_1^*}} + \frac{\sigma^{2\alpha_2^*} - \sigma_0^{2\alpha_2^*}}{(\eta_{0,lt,2m})^{2\alpha_2^*}} - \frac{\left(\sigma^{2(\alpha_1^*+\alpha_2^*)} - \sigma_0^{2(\alpha_1^*+\alpha_2^*)}\right) - \sigma_0^{2\alpha_1^*}\left(\sigma^{2\alpha_2^*} - \sigma_0^{2\alpha_2^*}\right) - \sigma_0^{2\alpha_2^*}\left(\sigma^{2\alpha_1^*} - \sigma_0^{2\alpha_1^*}\right)}{(\eta_{0,tt,3m})^{2(\alpha_1^*+\alpha_2^*)}}\right]\right\}, \tag{5.25}$$

where $\eta_{0,lt,1m}$ and $\eta_{0,lt,2m}$ are given by (5.21) and $\eta_{0,tt,3m}$ reads

$$\eta_{0,tt,3m} = \frac{\eta_{0,lt,1m}\,\eta_{0,lt,2m}}{\Delta A_m} = \left[\Delta A_m \left(\sigma_0^{2\alpha_1^*} - \sigma_{k,1}^{2\alpha_1^*}\right)\left(\sigma_0^{2\alpha_2^*} - \sigma_{k,2}^{2\alpha_2^*}\right)\right]^{\frac{1}{2(\alpha_1^*+\alpha_2^*)}}. \tag{5.26}$$

Remarkably, observe that all the expressions for the probability of failure recorded in the current section have been derived by assuming that the same geometric coefficient Y (expression for the critical SIF (3.1)) characterizes the two micro-cracks populations, i.e., it has been supposed that the pre-existing cracks and the cracks due to abrasion have the same shape. One may consider the case in which the probability of failure is still obtained by assuming that the flaws distributions are interpreted by the functions (5.23), i.e. both the distributions are truncated, but referring to cracks populations of different shapes. By supposing $Y_1 < Y_2 = Y_{ef}$, one obtains

$$P_f(\Sigma_{eqb}, A) = 1 - \exp\left\{ - A\left[\frac{(Y_{ef}\sigma)^{2\alpha_1^*} - (Y_1\sigma_{0,1})^{2\alpha_1^*}}{\Delta A_m[(Y_1\sigma_{k,1})^{2\alpha_1^*} - (Y_1\sigma_{0,1})^{2\alpha_1^*}]} + \frac{\sigma^{2\alpha_2^*} - \sigma_{0,2}^{2\alpha_2^*}}{(\eta_{0,lt,2m})^{2\alpha_2^*}} - \frac{(Y_{eff}\sigma)^{2\alpha_1^*} - (Y_1\sigma_{0,1})^{2\alpha_1^*}}{\Delta A_m[(Y_1\sigma_{k,1})^{2\alpha_1^*} - (Y_1\sigma_{0,1})^{2\alpha_1^*}]} \frac{\sigma^{2\alpha_2^*} - \sigma_{0,2}^{2\alpha_2^*}}{(\eta_{0,lt,2m})^{2\alpha_2^*}}\right]\right\}, \tag{5.27}$$

where $\eta_{0,lt,2m}$ is again given by (5.21). Hence, assumption of different shapes for micro-cracks populations, associated respectively with Y_1 and Y_2, would lead to

more complicated expressions.
Another potential approach for interpreting the variability of abraded glass strengths is based upon the Change of Variable Theorem (CVT) [17, 87]. In this approach, it is supposed that the defectiveness scenario observed on a surface subject to abrasion is related to a single distribution of crack lengths resulting from the distortion induced through abrasion phenomena of the pre-existing population of cracks. This concept is statistically interpreted through the CVT, which is based upon a *generating density function*, representative of the pristine material, and on a *transforming function*, modeling the effects of the event that has distorted the statistical distribution[3]. The choice of the correct forms for the *generating* and *transforming functions* for the case of abraded glass strength will be the subject of further research.

5.3 The statistical population of "tin-side" strength

It is well known that the statistical distributions interpreting the strengths variability of the air- and tin-side surfaces are different. As discussed at length in Chapter 3 while elaborating the data from the experimental campaign by TC129/WG8 of CEN [19], a left-truncated Weibull distribution of the type considered in Section A.3.2 can very well reproduce the statistics of strength when the air-side is under tensile stress, whereas the same is not true for the tin-side. Indeed, as it is shown in Section 3.6, no types of generalized Weibull distribution can acceptably fit the experimental data associated with the tin-side strength.
Here, we consider the contact with the tin bath and the steel rollers as a *mild* abrasive process, because of which two different micro-cracks population coexist in the defectiveness scenario, i.e., one referred to the air-side, as that for a pristine material, and the other one induced during the production phase as a consequence of abrasion. By assuming the same notation of equation (5.23), one has the probability density function $p^{air} = p^{T,pre}_{\Delta A,\delta}(\delta)$ for the air side, and $p^{float} = p^{T,abr}_{\Delta A,\delta}(\delta)$ for the defects induced during the float process. For the sake of simplicity, it is reasonable to assume, albeit at a first order approximation, that the crack shape is the same for both populations, i.e., $Y_1 = Y_2 = Y$. Thus, the cumulative probability of failure for the tin-side strength is given by expression (5.25).
The results of the experimental campaign by TC129/WG8 of CEN [19] are used again, in order to verify the theoretical prediction. It has been shown in Chapter 3, Section 3.6, that the air-side data are very well interpolated with a left-truncated Weibull distribution. Recall that the specimens have been tested under the coaxial double ring configuration provided by the standard EN 1288-2 [31]. In the Appendix A it is shown that the state of stress in the area delimited by the inner ring is not equibiaxial, and a method to rescale the data towards the standard conditions of equibiaxial stress state and unitary area $A_0 = 1\ m^2$ is presented. The statistical analysis of the corrected and rescaled data referred to air-side strengths is recorded in Chapter 3. For $\alpha_1^* = 2.125$, $\eta_{0,lt,1} = 1462.85$ MPa mm$^{2/m}$ and $\sigma_{0,1} = 40.2$ MPa, one obtains the excellent fitting graphically represented in the LTW plane of Figure 3.12.

[3]The most popular example of the CVT theorem is constituted by the log-normal distribution, described in Appendix D, which arises from a Gaussian generating density function whose deformation is described by an exponential function.

Thus, the statistics for the air-side is known, and now the attempt consists in fitting the tin-side data with the generalized Weibull distribution defined by expression (5.25). The function is simplified by neglecting the third term in square brackets, since $\eta_{0,tt,3m} = (\eta_{0,lt,1m}\eta_{0,lt,2m})/\Delta A_m$ is very large for the case considered here. Consequently, the distribution (5.25) turns into a *bi-modal truncated Weibull* distribution of the type

$$P_f(\Sigma, A) = 1 - \exp\left\{ - A_{eff}\left[\frac{\sigma_f^{2\alpha_1^*} - \sigma_{0,1}^{2\alpha_1^*}}{\eta_{0,lt,1m}^{2\alpha_1^*}} + \frac{\sigma_f^{2\alpha_2^*} - \sigma_{0,2}^{2\alpha_2^*}}{\eta_{0,lt,2m}^{2\alpha_2^*}}\right]\right\}, \qquad (5.28)$$

where Σ is the generic state of stress and σ_f the failure stress. Observe that the bi-modal function (5.28) is different from the one introduced in Appendix A, since it arises from two truncated populations of cracks and, hence, it provides the two lower bounds $\sigma_{0,1}$ and $\sigma_{0,2}$.

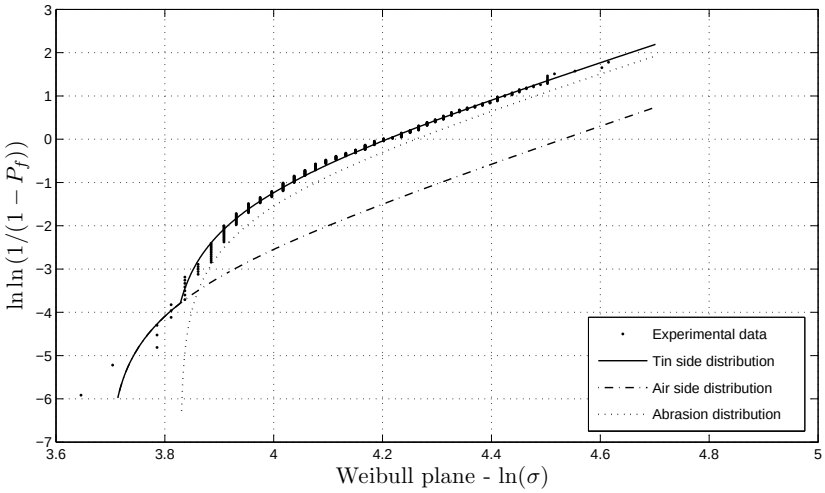

Figure 5.5: Plot in the Weibull plane of the tin-side failure stresses (experiments from [19]). Interpolation with the statistical distribution of equation (5.25) ($\alpha_1^* = 2.1$; $\eta_{0,lt,2m} = 1462.85$ MPa mm$^{2/m}$; $\sigma_0 = 40.2$ MPa; $\alpha_2^* = 2$; $\eta_{0,lt,2m} = 1276$ MPa mm$^{2/m}$; A=127170 mm^2).

The rigorous evaluation of the effective area for such a statistical distribution is analytically difficult. Hence, as a first order approximation, one may estimate the effective area A_{eff} as for the 2PW model, i.e., A_{eff} is given by equation (A.11). Remarkably, this depends upon the shape parameter m and the equivalent stress $\sigma_{eq,W2}$, which, in turn, depends upon the principal values of stress. Since geometric non-linearities arise during the coaxial double ring test according EN 1288-2 [31], the ratio between the principle stresses varies with the load level and, consequently, the effective area is not constant. However, its deviations in the range of the failure stress values can be considered small. Hence, an approximated value $A_{eff} = K\,A = 0.45\,\pi(300)^2$ mm^2 is assumed. Moreover, the function (5.25)

has been slightly generalized, by assuming that the lower bound for glass strength for the pre-existing defects ($\sigma_{0,1}$) may be different from the one due to the defects induced by abrasion ($\sigma_{0,2}$).
Finally, setting $\eta_{0,lt,1m}$, α_1^* and $\sigma_{0,1}$ equal to the corresponding values for the air-side mentioned above, the best fitting of the experimental data for the tin-side is obtained with $\alpha_2^* = 2$, $\eta_{0,lt,2m} = 1276$ MPa mm$^{2/m}$ and $\sigma_{0,2} = 46$ MPa. Interestingly, $\sigma_{0,2}$ is slightly higher than $\sigma_{0,1}$, which means that the maximum size of the cracks induced through abrasion on the tin-side is smaller than the maximum size of pre-existing cracks. Figure 5.5 shows the Weibull probability plot in the plane $\ln \ln [1/(1 - P_f)]$ vs. $\ln \sigma$ for the tin side data, which points out the optimal goodness of fit.
Remarkably, the effects of abrasion are significant for the higher quantiles of the distribution, whereas they become almost negligible for the lower quantiles. In particular, since $\sigma_{0,1} < \sigma_{0,2}$, the statistics matches the one of the air side in the interval $\sigma_{0,1} \leq \sigma \leq \sigma_{0,2}$.
The chi-square test, described in the Appendix A.5, has been used for a quantitative verification of the goodness of fit. For this analysis, one obtains *p-value* $\simeq 0.06$ (6%). Since it is customary to accept the 5% rule, it is possible to claim that the proposed statistical model, derived from micromechanical considerations, is acceptable, especially when compared with the generalized Weibull or other more classical statistical distributions.

CHAPTER **6**

THE DESIGN OF STRUCTURAL GLASS COMPONENTS

6.1 Expected performances of glass structures

Structures must guarantee a certain level of safety against failure. This is why nowadays structural design is based upon probabilistic considerations, i.e., the probability of collapse reputed acceptable is a function of the consequence of the collapse itself. In Europe, the principles and requirements for the structural safety of buildings and other civil works are established by the Eurocode EN 1990 "Basis of structural design" [37], which serves as a guide for the other nine standards EN 1991-1999. However, the approach to be followed for the design of load-bearing glass components is not prescribed. According to the EN 1990, three classes of consequences, namely CC1, CC2 and CC3, characterize the required safety level, by considering the consequences of their failure or malfunction in economic, social, and environmental terms. For example, grandstands and public buildings belong to the class CC3, residential and office buildings to CC2 and agricultural buildings and greenhouses to CC1.

However, some considerations have to be made for structural glass. First, the cost of a glass structure can only be afforded in luxury constructions, so that it would be rare, if not impossible, to find an expensive glass floor in an agricultural building. Furthermore, glass is very often employed to make isolated parts of the construction, such as facades, floors or stairs, whose failure is not accompanied by the collapse of the whole building. Hence, there is no need for assigning to all the glass elements present into a civil building the same class of the building itself, but it is necessary to make a classification on the basis of the single element. This approach has been followed by the Italian guide lines for structural glass [23]. For the sake of illustration, Table 6.1 shows the schematic proposed by the Italian CNR-DT 210 [23], including also the class CC0 referring to clearly-non-structural elements (for example, a glass pane for a small window).

The Eurocode EN 1990 [37] establishes the reference life time required for different types of civil structures, which is defined as the period during which the performances of the buildings shall not be impaired by external actions and, hence, only ordinary maintenance is required. The probabilities of collapse considered accept-

Table 6.1: Classes of consequence for glass elements indicate by CNR-DT210 [23].

Class	Definition
CC0	Specifically non-structural elements. Following failure, negligible economic, social end environmental consequences and practically null risk of loss of human life.
CC1	Following failure, low risk of loss of human life and modest or negligible economic, social and environmental consequences. Glass structural elements whose failure involves scarce consequences fall into this category.
CC2	Following failure, moderate risk of loss of human life, considerable economic, social and environmental consequences. Glass structural elements whose failure involves medium-level consequences belong to this category.
CC3	High risk of loss of human life, serious economic, social and environmental consequences: for instance, the structures of public buildings, stages and covered galleries, where the consequences of failure can be catastrophic (concert halls, crowded commercial centers, etc.). Glass structural elements whose failure involves high-level consequences fall into this category.

able are assigned on basis of the reference life time. The probabilities of failure for a reference life time of 50 years, given for two different values of the return period T_R of the applied actions, i.e., 1 year and 50 years, are recorded in Table 6.2, consistently with the EN 1990. Of course, by passing from the first to the third class of consequence, the probability of failure reputed acceptable decreases.

Table 6.2: Probability of collapse as a function of the different classes of structural elements according to EN 1990 [37].

Class	β [$T_R = 50$ **years**]	P_f [$T_R = 50$ **years**]	β [$T_R = 1$ **year**]	P_f [$T_R = 1$ **year**]
CC1	3.3	$4.83\ 10^{-4}$	4.2	$1.335\ 10^{-5}$
CC2	3.8	$7.235\ 10^{-5}$	4.7	$1.305\ 10^{-6}$
CC3	4.3	$8.54\ 10^{-6}$	5.2	$9.96\ 10^{-8}$

6.2 The probabilistic and semi-probabilistic approach

According to the semi-probabilistic method (level I), design values need to be assigned to all the basic variables. A structural component is accepted if the design resistances are higher than the design actions, i.e., $R_d > E_d$, which in practice means that the probability of failure is equal or lower than a target value. Thus, partial reduction factors for the strength and partial amplifying factors for the actions are defined, so as to guarantee the required performance level in terms of probability of failure. The values for partial factors can be obtained by performing calibration procedures based on experience and building traditions and/or based on the statistical evaluation of experimental data and field observations. The probabilistic calibration procedures for partial factors are generally obtained by comparison with more sophisticated methods divided into two main classes, the full probabilistic methods (level III) and first order reliability methods (Level II). Following the level III methods, the probability of failure is directly evaluated from the statistical distributions interpreting the action and the resistance variabilities. Assuming that actions and resistances are mutually independent variables, let $\Re$ be the domain of the resistances and f_r the statistical distribution of the values

$r \in \Re$. Moreover, denote with S the domain for actions and with f_s the statistical distribution of the values $s \in S$. Then, the probability of failure P_f can be evaluated from the convolution

$$P_f \;=\; P[\Re - S \leq 0] \;=\; \int_{-\infty}^{+\infty} \int_{-\infty}^{s \geq r} f_{\Re}(r)\, f_S(s)\, dr\, ds. \tag{6.1}$$

Considering the case that the domains of resistance and action coincide, i.e., $r = s = x$, $x \in X$. Expression (6.1) thus becomes

$$P_f \;=\; P[\Re - S \leq 0] \;=\; \int_{-\infty}^{+\infty} F_{\Re}(x)\, f_S(x)\, dx\,, \tag{6.2}$$

where $F_{\Re}(x)$ is the probability that the strength is less than x (cumulative distribution of strength). Indeed, the level III methods are the most rigorous and are considered the most accurate.

The procedure for the calibration of the partial safety factors recorded in the following (see Section 6.3) is based upon the comparison between the results of the structural design on paradigmatic case studies, obtained by using the full probabilistic approach of level III and the semi-probabilistic approach of level I. The optimal design is made by achieving the target probability of failure established in Table 6.2 through level III method. Then, the value of the material partial safety factor γ_m is obtained so to attain the same optimal design *via* level I method, with the partial coefficients for actions γ_f given by the relevant standards.

On the other hand, according to the level II methods, the estimation of the probability of collapse is simplified by some hypothesis, so that this can be more directly measured from the reliability index β. However, it is relevant to observe that an underlying assumption of these methods is that the material strength is interpreted by a Gaussian distribution, which is not the case of the glass. For the sake of completeness, the values of the reliability index β corresponding to the target values of the probability of failure for the three consequence classes are also recorded in Table 6.2, but they are not used here.

The partial safety factors provided by standards generally refer to the probability of failure associated with class CC2, whereas a further coefficient is furnished to pass from CC2 to CC1 or CC3. According to the Eurocode EN 1990 [37], the partial coefficient of the actions γ_f must be multiplied by a correction factor K_{FI}, which is $K_{FI} < 1$ when passing from CC2 to CC1, while $K_{FI} > 1$ from CC2 to CC3. Otherwise, it is here proposed to follow the approach indicated in the CNR-DT 210 [23], according to which one introduces a correction coefficient R_M of the material partial safety factor, so that $R_M < 1$ when passing from CC2 to CC1 and *vice-versa* from CC2 to CC3. Remarkably, there is no difference between decreasing the actions or increasing the resistances when the mechanical response of the structure is linear elastic, but it is important when geometric non-linearities are significant. Hence, to not underestimate the non-linear effects induced by the actions, it is more appropriate to increase the resistances through the coefficient R_M.

6.3 The calibration of partial material factors for annealed float glass

The paradigmatic case study considered here is that of a 8mm-thick square glass plate of side 3000 mm, simply supported at the edges under a uniformly distributed out-of-plane load, representative of the effects of wind on a façade panel, or of the effects of snow on a roof panel. For the case of wind actions, two different conditions are considered, one associated with characteristic wind pressures averaged over the times $t = 10$ min and the other with wing gust of $t = 3$ s. Observe that the load referred to the case $t = 10$ min is lower than the one associated to $t = 3$ s, but its effects could be more severe than in the second case, since its duration is higher and therefore the phenomenon of static fatigue is more relevant. Furthermore, the snow load will be considered applied for a time equal to one month, according to the recommendations given by the CNR-DT210 [23]. The process for the calibration of partial factors is schematically summarized in the flow chart of Fig. 6.1.
The calibration of the partial factors will be performed twice, by interpreting the glass strength variability with both the left-truncated (LTW) and the extended Weibull (EXW) functions [9]. Results will be then compared with those from the 2PW distribution obtained by *Badalassi et al.* [7].

6.3.1 Calibration procedure based upon the left-truncated Weibull (LTW) statistics

The Weibull parameters characterizing the strength distribution for the LTW model have been estimated from the results of the experimental campaign performed by the technical group TC129/WG8 of CEN [19].
Recall from Appendix A that the failure stress values recorded in [19] must be "corrected" to be representative of the actual maximum tensile stress acting within the specimens at the end of the tests. Then, the corrected data need to be re-scaled according to the effective area $K_{WT}A$, whose form is recorded in the Appendix A, equation (A.30). Recall that $K_{WT}A$ is stress-dependent if one takes into account geometric non-linearities. However, the higher the loads are, the higher are the geometric non-linearities and the lower is K_{WT} (conservative). The values of $K_{WT,air} = 0.54$ and $K_{WT,tin} = 0.55$ have been assumed that correspond to a maximum stress of 100 MPa, which is approximately equal to the maximum stress measured during the experimental campaign.
Recall that cracks in glass can grow in time when subject to opening stresses that are far below the critical limit [100] because of the phenomenon of *static fatigue* or *subcritical crack growth* (Section 3.2). Since applied actions are schematized by loads assumed to remain constant for a certain characteristic time, so to take into account the effects of static fatigue, the failure stress values have been re-scaled through the coefficient k_{mod}, given by equation (3.11). A new population is hence obtained, representing the strength variability of the specimens when the external loads are maintained constant during a characteristic time τ. These data can thus be interpolated again with a new statistical distribution, to obtain the values $\sigma_{0,\tau}$ and $\eta_{0,\tau}$ of the location and scale parameters, respectively. In this process the shape parameter m is assumed to remain uneffected. The obtained statistical distributions for the strengths thus depends upon the characteristic time τ.
It is also important to consider the effects of aging. Referring to the model schema-

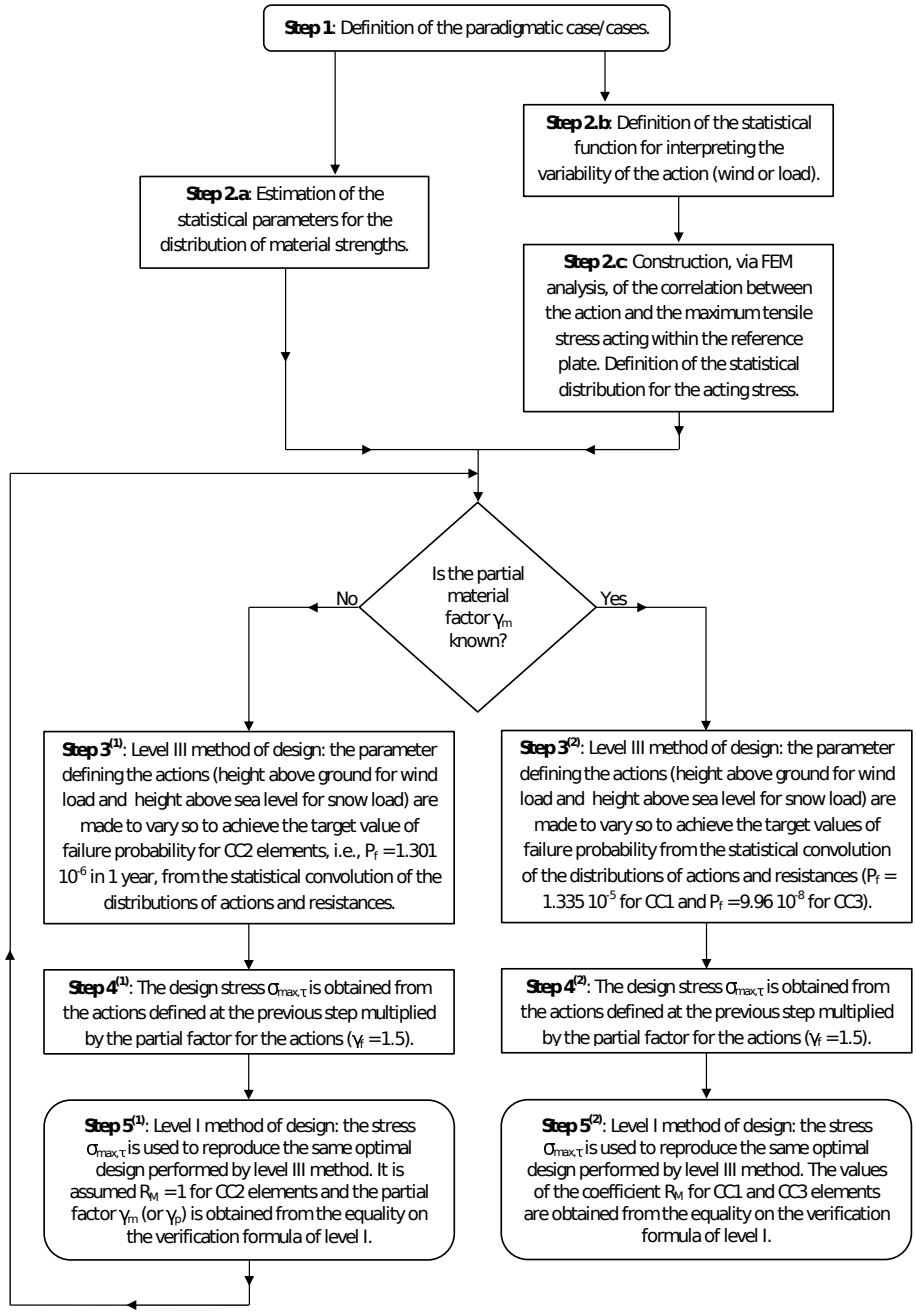

Figure 6.1: Methodology for the calibration of partial factors.

tized in Figure 3.7, i.e., a semi-sphere cavity induced through abrasion with the same center of a pre-existing thumbnail crack, two major conclusions were drawn in Section 3.4: *i*) abrasion can increase the stress intensity factor associated with a dominant crack, but *ii*) there is an upper bound for this increment. Furthermore, little defects may produce beneficial shielding (reduction in SIF) of the dominant flaw. Hence, since the location parameter σ_0 is associated with the maximum size of the micro-cracks, one can expect that the lower bound is at most reduced but not annihilated by natural abrasion phenomena. Hence, on the safe side, a further reduction of the location parameter is here operated according to the expression

$$\sigma^*_{0,\tau} = \frac{\sigma_{0,\tau}}{\omega}\,, \tag{6.3}$$

where $\omega > 1$. Observe that the precise evaluation of σ_0 is central for the calibration of partial safety factors, and even small changes in its value can lead to significant differences in the left-hand-side tail of the distribution. Of course, all the quantiles of the strengths distribution, and not only the lower bound $\sigma_{0,\tau}$, may be affected by abrasion. Hence, the parameter η_0 has been analogously reduced according to

$$\eta^*_{0,\tau} = \frac{\eta_{0,\tau}}{\omega}\,. \tag{6.4}$$

The rigorous evaluation of ω is not straightforward and would require an accurate experimental investigation, considering various possible damaging actions. Referring again to the case represented in Figure 3.7, one can expect a reduction in strength of the order of $10 \div 20\%$ due to sandblasting, which certainly represents a very severe damaging action. However, a rather conservative value $\omega = 1.5$ has been chosen here. Figure 6.2 shows the effects of the reduction of the scale parameter $\eta_{0,\tau}$ and of the location parameter $\sigma_{0,\tau}$ according to (6.3) and (6.4), which are equivalent to a leftward shift and an increase in the slope of the curve representing the cumulative probability function, i.e., a reduction of the material strength and of the data dispersion.

The parameters characterizing the statistics for glass strengths, for either the air or the tin side, graphically estimated according to the procedure recorded in the Appendix A, are recorded in Table 6.3.

Since glass plates are randomly installed into civil structures, following [7], the probability that the air-side is under maximum tensile stress is assumed equal to the probability of having the tin-side in the same condition. The cumulative probability function of material strengths is hence given by the arithmetic mean of the functions representing the strength of the two surfaces, which reads

$$F^{(air+tin)/2}_{A,\tau,WT}(\sigma) = 1 - \frac{1}{2}\sum_{sd=air}^{tin} \exp\left[-\frac{K^{sd}_{WT}\sigma^{m_{sd}} - \sigma^{*\,m_{sd}}_{0,\tau,sd}}{\eta^{*\,m_{sd}}_{0,\tau,sd}}A\right], \tag{6.5}$$

where "$sd = air$" or "$sd = air$" represent the side "sd" of glass. Let $f_{\sigma,\tau}(\sigma)$ be the density function of the maximum stress σ within the pane occurring in one year.

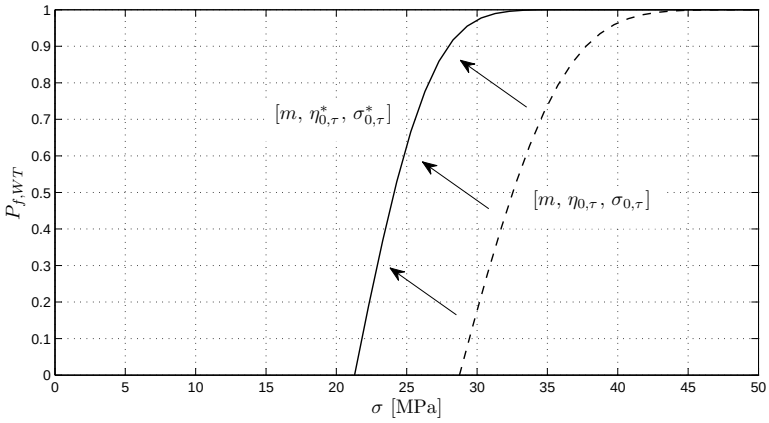

Figure 6.2: Cumulative probability distribution of the material strength modified for taking into account the effects of aging, corresponding to failure for a load applied for 10 minutes.

Table 6.3: Graphically estimated parameters characterizing the left-truncated Weibull distribution for wind (two values) and snow loads. For the test configuration of EN 1288-2 [31]: $K_{WT,air} = 0.54$; $K_{WT,tin} = 0.55$; $G_{air} = 0.065$; $G_{tin} = 0.24$; $A = 0.2826$ m^2. Various characteristic load durations.

Case study	m	$\eta_{0,\tau}$ [MPa]	$\sigma_{0,\tau}$ [MPa]	$\eta^*_{0,\tau}$ [MPa]	$\sigma^*_{0,\tau}$ [MPa]
AIR SIDE					
Wind, 10 min	4.0025	40.12	27.27	26.75	18.53
Wind, 3 s	4.0025	55.51	38.45	37.00	25.63
Snow, 1 m	4.0025	24.39	16.89	16.26	11.26
TIN SIDE					
Wind, 10 min	3.7678	26.41	25.29	19.56	18.73
Wind, 3 s	3.7678	36.53	34.98	27.06	25.91
Snow, 1 m	3.7678	16.05	15.37	11.89	11.38

Then, the convolution integral (6.2) becomes

$$P_{f,1y,WT} = \int_{-\infty}^{+\infty} F^{(air+tin)/2}_{A,\tau,WT}(\sigma) f_{\sigma,\tau}(\sigma) d\sigma \,, \tag{6.6}$$

which represents the probability of failure in one year. The parameters defining the actions are made to vary so as to achieve the target values of failure probability recorded in Table 6.2 for CC2 elements. Once the design action Q is defined, one can obtain the maximum stress acting in the glass $\sigma_{max,\tau}$ induced through action Q of characteristic duration time τ multiplied by the partial safety factor γ_f, which

is evaluated *via* FEM simulation, i.e,

$$\sigma_{max,\tau} = S(\gamma_f Q)\,. \tag{6.7}$$

At this point, the stress $\sigma_{max,\tau}$ is used to reproduce the same optimal design *via* semi-probabilistic approach of level I, whose verification formula is assumed of the form

$$\sigma_{max,\tau} - \sigma_{0,d} \leq \frac{K_{mod}\lambda_{A,\tau,WT}(f_{g,k} - \sigma^*_{0,k})}{R_M\gamma_m}, \tag{6.8}$$

where γ_m is the partial safety factor for the material, R_M provides the correlation with the various classes of consequence ($R_M = 1$ for CC2), $f_{g,k} = 45$ MPa is the usually accepted characteristic value for glass strength as established by product standards, $\sigma^*_{0,k}$ represents the reference characteristic value of the lower bound for glass strength and $\lambda_{A,\tau,WT}$ accounts for the effects of size and type of stress. The *design* value $\sigma_{0,d}$ of the location parameter is assumed in the convenient form

$$\sigma_{0,d} = \frac{K_{mod}\lambda_{A,\tau,WT}\,\sigma^*_{0,k}}{R_M\gamma_m}\,, \tag{6.9}$$

so to have a remarkable simplification in the verification formula, i.e.,

$$\sigma_{max,\tau} \leq \frac{K_{mod}\lambda_{A,\tau,WT} f_{g,k}}{R_M\gamma_m}\,. \tag{6.10}$$

The assumption (6.9) is well-founded, since it is reasonable to assume that the influence of the static fatigue, of the size and of the stress state upon the lower bound of the distribution is the same as for the other quantities. Observe that $f_{g,k} = 45$ MPa can be assumed to be representative of the 5% quantile of the equibiaxial glass strength distribution referred to the air-side. From a principle of equal failure probability between one plate subject to a generic stress state Σ acting on the area A, where σ_{max} is the maximum tensile stress, and the other one under an equibiaxial stress-state acting on the unit area ($A_0 = 1$ m^2), one obtains

$$\begin{aligned} &1 - \frac{1}{2}\sum_{sd=air}^{tin} \exp\left[-\frac{f_{g,k}^{m_{sd}} - \sigma_{0,\tau,sd}^{*\,m_{sd}}}{\eta_{0,\tau,sd}^{*\,m_{sd}}} A_0\right] \\ &= 1 - \frac{1}{2}\sum_{sd=air}^{tin} \exp\left[-\frac{K_{WT,sd}\sigma_{max}^{m_{sd}} - \sigma_{0,\tau,sd}^{*\,m_{sd}}}{\eta_{0,\tau,sd}^{*\,m_{sd}}} A\right]. \end{aligned} \tag{6.11}$$

Since the arguments of the exponential functions in the equality (6.11) can be assumed to be infinitesimal of the first order, the Taylor's expansion $e^x = 1 + x + o(x)$ can be made. Hence, after making the substitution $\sigma_{max} \to \lambda_{A,\tau,WT} f_{g,k}$, one

has

$$\sum_{sd=air}^{tin} \frac{K_{WT}^{sd}\left(\lambda_{A,\tau,WT} f_{g,k}\right)^{m_{sd}} - \sigma_{0,\tau,sd}^{*\,m_{sd}}}{\eta_{0,\tau,sd}^{*\,m_{sd}}} A = \sum_{sd=air}^{tin} \frac{f_{g,k}^{m_{sd}} - \sigma_{0,\tau,sd}^{*\,m_{sd}}}{\eta_{0,\tau,sd}^{*\,m_{sd}}} A_0 \,. \quad (6.12)$$

If one separately evaluates the fracture probability for $sd = air$ and $sd = tin$, the approximate solution reads

$$\frac{K_{WT}^{sd}\left(\lambda_{A,\tau,WT}^{sd} f_{g,k}\right)^{m_{sd}} - \sigma_{0,\tau,sd}^{*\,m_{sd}}}{\eta_{0,\tau,sd}^{*\,m_{sd}}} A = \frac{f_{g,k}^{m_{sd}} - \sigma_{0,\tau,sd}^{*\,m_{sd}}}{\eta_{0,\tau,sd}^{*\,m_{sd}}} A_0, \quad (6.13)$$

which gives

$$\lambda_{A,\tau,WT}^{sd} = \frac{1}{f_{g,k}} \left[\frac{f_{g,k}^{m_{sd}} A_0 + \sigma_{0,\tau,sd}^{*}(A - A_0)}{K_{WT}^{sd} A} \right]^{1/m_{sd}} , \; sd = air, tin \,. \quad (6.14)$$

Finally, the coefficient $\lambda_{A,\tau,WT}$ is obtained as the mean value of $\lambda_{A,\tau,WT}^{air}$ and $\lambda_{A,\tau,WT}^{tin}$, i.e.,

$$\lambda_{A,\tau,WT} \;=\; \lambda_{A,\tau,WT}^{(air+tin)/2} \;=\; \frac{1}{2}\left[\lambda_{A,\tau,WT}^{air} + \lambda_{A,\tau,WT}^{tin}\right] , \quad (6.15)$$

through which the effects of size and state of stress are taken into consideration.

6.3.2 Calibration procedure based on the extended Weibull (EXW) statistics

The parameters characterizing the extended Weibull distribution for glass strength, whose form is described in Appendix A, have been estimated from the results of the experimental campaign recalled in Section 3.6 again. From the same arguments used in Subsection 6.3.1, it has been assumed that the *effective* area is the one associated with a value of the maximum tensile stress equal to 100 MPa. Moreover, the strength data has been re-scaled so as to account for the subcritical crack growth induced by loads constantly applied for the characteristic time τ. Then, the three parameters characterizing the air and the tin side have been estimated through the graphical method proposed by *Zhang and Xie* [107], described in Section A.4.3, whose results are recorded in Table 6.4.

Assuming again to have the same probability that the tin side or the air side are under tension, the cumulative probability function for strengths becomes

$$F_{A,\tau,WE}^{(air+tin)/2}(\sigma) = 1 - \frac{1}{2} \sum_{sd=air}^{tin} \left[\frac{\Theta_{\tau,sd} \exp\left[-K_{WE}^{sd}\left(\frac{\sigma}{\eta_{0,\tau,sd}}\right)^{m_{sd}}\right]}{1 - (1 - \Theta_{\tau,sd}) \exp\left[-K_{WE}^{sd}\left(\frac{\sigma}{\eta_{0,\tau,sd}}\right)^{m_{sd}}\right]} \right] , \quad (6.16)$$

Table 6.4: Estimated parameters for the extended Weibull distribution for the wind (two values) and the snow loads. For the test configuration of EN 1288-2 [31]: $K_{WE}^{air} = 0.3$, $K_{WE}^{tin} = 0.17$. Different values of the characteristic time of load duration.

Case study	m	$\eta_{0,\tau}$ [MPa]	$\ni_\tau$
AIR SIDE			
Wind, 10 min	7.9	120	0.003
Wind, 3 s	7.9	180	0.001
Snow, 1 m	7.9	75	0.002
TIN SIDE			
Wind, 10 min	12	74	0.001
Wind, 3 s	12	100	0.002
Snow, 1 m	12	45	0.001

which leads to the probability of failure in one year of the form

$$P_{f,1y,WE} = \int_{-\infty}^{+\infty} F_{A,\tau,WE}^{(air+tin)/2}(\sigma) f_{\sigma,\tau}(\sigma) d\sigma \,. \tag{6.17}$$

The target values of collapse probability are again reached by varying the parameters defining the action and, consequently, the maximum stress induced by the resulting action Q of characteristic duration time τ multiplied by the corresponding partial safety factor γ_f. Since the EXW distribution is not bounded, the verification formula assumes the simple form

$$\sigma_{max,\tau} \leq \frac{K_{mod} \lambda_{A,\tau,WE} f_{g,k}}{R_M \gamma_m}, \tag{6.18}$$

where the terms are the same as in equation (6.8). The coefficient $\lambda_{A,\tau,WE}$ is obtained again from the assumption of equal failure probability between a plate of area A subject to a generic state of stress Σ and a plate in reference conditions (unitary area under uniformly distributed loads), i.e.,

$$\begin{aligned} &1 - \frac{1}{2} \sum_{sd=air}^{tin} \left[\frac{\Theta_{\tau,sd} \exp\left[-K_{WE}^{sd} A \left(\frac{\lambda_{A,\tau,WE} f_{g,k}}{\eta_{0,\tau,sd}} \right)^{m_{sd}} \right]}{1 - (1 - \Theta_{\tau,sd}) \exp\left[-K_{WE}^{sd} A \left(\frac{\lambda_{A,\tau,WE} f_{g,k}}{\eta_{0,\tau,sd}} \right)^{m_{sd}} \right]} \right] \\ &= 1 - \frac{1}{2} \sum_{sd=air}^{tin} \left[\frac{\Theta_{\tau,sd} \exp\left[-A_0 \left(\frac{f_{g,k}}{\eta_{0,\tau,sd}} \right)^{m_{sd}} \right]}{1 - (1 - \Theta_{\tau,sd}) \exp\left[-A_0 \left(\frac{f_{g,k}}{\eta_{0,\tau,sd}} \right)^{m_{sd}} \right]} \right], \end{aligned} \tag{6.19}$$

where $\lambda_{A,\tau,WE} f_{g,k} = \sigma_{max}$. The fracture probability of the air ($sd = air$) and tin

($sd = tin$) sides are again separately analyzed, so as to obtain an approximate solution for equation (6.19) of the form

$$\begin{aligned}&\frac{\Theta_{\tau,sd}\exp\left[-K_{WE}^{sd}A\left(\frac{\lambda_{A,\tau,WE}^{sd}f_{g,k}}{\eta_{0,\tau,sd}}\right)^{m_{sd}}\right]}{1-(1-\Theta_{\tau,sd})\exp\left[-K_{WE}^{sd}A\left(\frac{\lambda_{A,\tau,WE}^{sd}f_{g,k}}{\eta_{0,\tau,sd}}\right)^{m_{sd}}\right]}\\&=\frac{\Theta_{\tau,sd}\exp\left[-A_0\left(\frac{f_{g,k}}{\eta_{0,\tau,sd}}\right)^{m_{sd}}\right]}{1-(1-\Theta_{\tau,sd})\exp\left[-A_0\left(\frac{f_{g,k}}{\eta_{0,\tau,sd}}\right)^{m_{sd}}\right]},\end{aligned} \tag{6.20}$$

which leads to the expression

$$\exp\left[-K_{WE}^{sd}A\left(\frac{\lambda_{A,\tau,WE}^{sd}f_{g,k}}{\eta_{0,\tau,sd}}\right)^{m_{sd}}\right]=\exp\left[-A_0\left(\frac{f_{g,k}}{\eta_{0,\tau,sd}}\right)^{m_{sd}}\right]. \tag{6.21}$$

Hence, one con write

$$\lambda_{A,\tau,WE}^{air}=\left(\frac{A_0}{K_{WE}^{air}A}\right)^{1/m_{air}},\quad \lambda_{A,\tau,WE}^{tin}=\left(\frac{A_0}{K_{WE}^{tin}A}\right)^{1/m_{tin}}. \tag{6.22}$$

Again, the coefficient $\lambda_{A,\tau,WE}$ is obtained as

$$\lambda_{A,\tau,WE}=\lambda_{A,\tau,WE}^{(air+tin)/2}=\frac{1}{2}\left[\lambda_{A,\tau,WE}^{air}+\lambda_{A,\tau,WE}^{tin}\right] \tag{6.23}$$

accounting for the effects of size and state of stress.

6.3.3 Wind load

A simply supported rectangular plate, 3×3 m^2 and 8 mm thick, under the effects of a uniform wind pressure p_w is considered. The probabilistic model for the wind pressure is reported in the Annex C, which is the one mentioned in the Eurocode EN 1991 [39]. As indicated above, characteristic values for the wind pressure p_w are averaged on $t = 10$ min and on $t = 3$ s. *Via* simple FEM simulations, the correlation between the wind pressure and the maximum tensile stress acting within the plate $p_w = S_p(\sigma)$ has been found. Consequently, one can pass from equation (C.5) to the cumulative distribution function of *the maximum stress in the plate consequent to the maximum annual wind pressure*, which reads

$$F_{pr,t}(\sigma)=\exp\left[-\exp\left(\frac{1}{0.2}-\frac{2\,S_p(\sigma)}{\rho_{air}\,c_{e,t}\,c_p\,c_d\,0.2\,0.75^2\,v_{b,50}^2}\right)\right], \tag{6.24}$$

where the meaning of the various terms is given in Annex C. Observe that the distinction between the two cases, i.e., $t = 10$ min and $t = 3$ s, is made by the

exposure factor $c_{e,t}$, given by equations (C.4). Then, deriving (6.24) with respect to σ, the probability density function $f_{pr,t}$ reads

$$f_{pr,t}(\sigma) = F_{pr,t}(\sigma) \exp\left(\frac{1}{0.2} - \frac{2\,S_p(\sigma)}{\rho_{air}\,c_{e,t}\,c_p\,c_d\,0.2\,0.75^2\,v_{b,50}^2}\right) \frac{2}{\rho_{air}\,c_{e,t}\,c_p\,c_d\,0.2\,0.75^2\,v_{b,50}^2}\,\frac{d}{dx}S_p(\sigma). \tag{6.25}$$

With the aim of estimating the effective area to be used in equations (6.5) and (6.16) for the cumulative functions obtained through the LTW and the EXW models, respectively, the plate has been divided into conventional four-nodes Finite Shell Elements with reduced integration of area $\Delta A_i = 50 \times 50$ mm^2. The principal stresses σ_1 and σ_2 for each element have been computed as the mean values of the stress at the four vertexes of each Finite Element, obtained *via* numerical analyses. When the left truncated model is used to interpret the strengths variability, for both the cases $sd = air$ and $sd = tin$, the equivalent stress $\sigma_{eq,WT,sd,i}$ in the $i-$th element is computed through equation (A.32), and then the effective area $K_{WT}^{sd}\,A$ is evaluated as

$$K_{WT}^{sd}\,A = \frac{\sum_{i=1}^{N} \sigma_{eq,WT,sd,i}^{m_{sd}} \Delta A_i}{\sigma_{max}^{m_{sd}}}\ . \tag{6.26}$$

For what concerns the extended Weibull statistics, an analogous formula as (6.26) for the effective area $K_{WE}^{sd}\,A$ is obtained, as it is shown in Section A.4.3.

Recall that the assumption of negligible non-linear effects leads to noteworthy simplifications, since the effective area is not dependent upon the amount of loading in this case. Even though this assumption is generally quite accurate, the values for the effective area have been computed for a maximum stress of the same order of that used in the calibration procedure, by taking into account non linear effects, and are $K_{WT}^{air} = 0.095$, $K_{WT}^{tin} = 0.1$, $K_{WE}^{air} = 0.01$ and $K_{WE}^{tin} = 0.003$.

The optimal design for the plate under consideration is obtained from the convolution integrals (6.6) and (6.17) for the LTW and the EXW model, respectively. This is achieved by modifying the wind pressure p_w, introduced in the equations (C.3), through an artificial changing of the location where the structure is set, i.e., of the design height above ground z_d for both the cases $t = 10$ min and $t = 3$ s, so to modify exposure coefficient $c_{e,t}$ in (6.25). The chosen design heights are the ones which lead to the target probability of failure of Table 6.2 for elements in class CC2.

Then, the design stress to be used in the verification formulas of the semi-probabilistic method is obtained as $\sigma_{max,\tau} = S(\gamma_q p_{w,\tau})$ with FEM simulations, where $\gamma_f = 1.5$ is the partial coefficient for the actions. Finally, the partial material factors are obtained from the requirement of the equality in the verification formulae (6.10),

for the LTW, and (6.18), for the EXW distributions, which leads to

$$\gamma_m = \frac{K_{mod,\tau}\lambda_{A,\tau,mw}^{(air+tin)/2} f_{g,k}}{\sigma_{max,\tau,d} R_M}, \qquad with\ mw = LTW\ or\ mw = EXW, \tag{6.27}$$

where, from (3.11), $k_{mod} = 0.6652$ for $\tau = 10$ min and $k_{mod} = 0.9203$ for $\tau = 3$ s. The values of $\lambda_{A,\tau,mw}^{(air+tin)/2}$ are estimated through (6.14) when the LTW model is used; through (6.22) for the EXW distribution. Since the variation of the location parameter due to *static fatigue* only marginally affects $\lambda_{A,\tau,mw}^{(air+tin)/2}$, the same value of such coefficient for both $\tau = 10$ min and $\tau = 3$ s is assumed, which is $\lambda_{A,\tau,WT}^{(air+tin)/2} \simeq 1.034$, while $\lambda_{A,\tau,WE}^{(air+tin)/2} \simeq 1.3538$. The coefficient R_M is unitary for CC2 elements by definition. Hence, the value of γ_m is calibrated for the CC2 probability of Table 6.2, with $R_M = 1$, whereas, for the other cases of CC1 and CC3, γ_m is assumed constant in (6.27), and the values of R_M are determined which lead to the target failure probabilities, by repeating the calibration process above described.
The results of the calibration process are summarized in Table 6.5. The LTW model provides much lower values for γ_m than the EXW distribution, despite the fact that for the LTW the effects of the natural material degradation have been considered through the coefficient ω, as explained in Section 6.3.1, whereas this has not been considered in the calibration procedure according to the EXW model.

6.3.4 Snow load

The reference plate is now subject to an uniformly distributed snow load q_s. The relationship $q_s = S_q(\sigma)$ is found again *via* FEM simulation and the cumulative distribution of *the maximum stress in the plate for the snow loads in one year* is obtained from (C.9), and reads

$$F_{qs,t}(\sigma) = \exp\left[-\exp\left[\left(1 - \frac{S_q(\sigma)}{q_{sk}\mu_i C_E C_t}(1 + 2.5923V)\right)\frac{\pi}{V\sqrt{6}} - 0.57722\right]\right]. \tag{6.28}$$

Differentiating with respect to σ, the probability density function is found in the form

$$\begin{aligned} f_{qs,t}(\sigma) = F_{qs,t}(\sigma)\ \exp\Bigg[&\left(1 - \frac{S_q(\sigma)}{q_{sk}\mu_i C_E C_t}(1 + 2.5923V)\right)\frac{\pi}{V\sqrt{6}} \\ &- 0.57722\Bigg]\frac{\pi}{V\sqrt{6}}\frac{1 + 2.5923V}{q_{sk}\mu_i C_E C_t}\frac{d}{dx}S_q(\sigma), \end{aligned} \tag{6.29}$$

where all the coefficients have been introduced in Appendix C. Of course, the relationship $S_q(\sigma)$ between the uniform pressure induced by snow and the maximum tensile stress acting within the plate is the same as in the case of wind load, described in Section 6.3.3. The optimal design with the probabilistic approach is

achieved by varying the height a.s.l. so as to reach the target failure probabilities (see Table 6.2) in the convolution integrals (6.6) and (6.17), leading to the design loads $q_{s,\tau}$, given by equation (C.8). The coefficient of variation of snow loads has been assumed to be $V = 0.2$ to be on the safe side, since it has been demonstrated in [7] that this leads to the highest values for the material factors. The maximum stress $\sigma_{max,\tau} = S(\gamma_f q_{s,\tau})$, with $\gamma_f = 1.5$ is obtained through a deterministic FEM calculation, and then the partial material factors are computed from equation (6.27). From (3.11), the value of $K_{mod,\tau}$ for $\tau = 1$ month is 0.4044, while $\lambda_{A,\tau,WT}^{(air+tin)/2}$ and $\lambda_{A,\tau,WE}^{(air+tin)/2}$ attain the same values as for the case of wind load. Table 6.5 records the results. The qualitative findings are the same as the ones obtained for the wind load, i.e., the LTW gives less restrictive coefficients than the EXW approach, although the effects of natural ageing of glass are considered only for the first case.

Table 6.5: Values of the product $\gamma_m R_M$ ($R_M = 1$ for CC2), calibrated according to the left-truncated (LTW) and the extended (EXW) Weibull models.

Load case	**Wind [10 min]** $\gamma_m R_M$	**Wind [3 s]** $\gamma_m R_M$	**Snow [1 mon]** $\gamma_m R_M$
CC1 (LTW)	1.62	1.61	1.59
CC1 (EXW)	1.71	1.77	1.80
CC2 (LTW)	1.82	1.81	1.78
CC2 (EXW)	2.30	2.39	2.40
CC3 (LTW)	2.04	2.04	1.98
CC3 (EXW)	3.20	3.36	3.25

6.3.5 Comparison with previous studies

A thorough analysis of the calibration process of the material partial safety factors for glass has been proposed by *Badalassi et al.* [7]. The main difference with respect to the present derivation consists in the considered statistics, i.e., a two-parameter Weibull (2PW) distribution instead of the left-truncated or the extended ones. The effects of natural aging are not taken into account by *Badalassi et al.* [7] and the parameters m and η_0 of the 2PW statistics were derived from a particular experimental campaign performed by the Italian *Stazione Sperimentale del Vetro* [25], conducted with a different test set-up and much more limited than the one used for the current calibration, described in Section 3.6. Furthermore, the phenomenon of static fatigue on the reference time τ was not considered by re-scaling the data as in the current dissertation, but according to the expressions

$$m_\tau = \frac{n}{n+1}\, m\ , \qquad \eta_{0,\tau} = \eta_0^{\frac{n+1}{n}} \left(\frac{1}{(n+1)\,\dot\sigma\,\tau} \right)^{1/n}\ , \tag{6.30}$$

where n is the crack velocity coefficient of the power law introduced in (3.4) and $\dot\sigma$ is the experimental stress rate, which is constant at $\dot\sigma = 2$ MPa/s. The Weibull pairs used for the calibration procedure of [7] are summarized in Table 6.6.

Table 6.6: Weibull parameters used for the calibration of the material partial safety factors according to the 2-parameter Weibull distribution [7].

Load Case	**Surface**	m_τ	$\eta_{0,\tau}$ [MPa mm$^{2/m}$]
Test	Air	5.4	1096
	Tin	7.3	406
Wind, 3 s	Air	5.1	1220
	Tin	6.9	425
Wind, 10 min	Air	5.1	876
	Tin	6.9	305
Snow, 1 m	Air	5.1	541
	Tin	6.9	188

It is of importance to point out that the paradigmatic case study chosen by *Badalassi et al.* [7] for the calibration consisted of a 6 mm thick, 1×1 m^2, simply supported square plate. The product $\gamma_M\, R_M$ obtained by using the 2PW model for the different classes of consequence and load cases are recorded in Table 6.7. Observe that the values for the coefficients R_M to pass from class CC2 to CC3 are not indicated in [7]. However, for the sake of completeness, they have been calculated here by following the procedure used in [7] and reported in Table 6.7.

Table 6.7: Values of the product $\gamma_M\, R_M$ ($R_M = 1$ for CC2) calibrated according to the 2PW model.

Load case	**CC1**	**CC2**	**CC3**
Wind [10 min] - $\gamma_M\, R_M$	1.65	2.42	3.84
Wind [3 s] - $\gamma_M\, R_M$	1.78	2.51	3.90
Snow [1 mon] - $\gamma_M\, R_M$	1.60	2.41	3.86

Comparing the values recorded in Tables 6.7 and 6.5, the difference between the partial safety factors obtained through the 2PW distribution and the ones obtained through the LTW model is quite striking. This is mostly due to the assumption of null location parameter (unbounded glass strength distribution), which leads to extremely conservative estimates. By comparing the results obtained through LTW and 2PW models, for elements in class CC1 the values of Tables 6.5 and 6.7 are still comparable, whereas the gap tends to increase for CC2 and even more so for CC3. Hence, the results obtained by using the 2PW statistics are excessively conservative for the design of elements that require very low failure probabilities of failure [9]. The safety factors for CC1 and CC2 elements obtained through the EXW are very close to those calibrated according to the 2PW, while they are slightly lower for CC3. However, it is of importance to notice that the reference plate chosen by *Badalassi et al.* [7] is smaller than the one used in the present study. The use of a larger reference plate for calibrating partial factors according to the 2PW model would have led to higher safety factors.

Table 6.8: Values of R_M evaluated according to the 2-parameter (2PW), the extended (EXW) and the left-truncated (LTW) Weibull distributions.

	2PW	**EXW**	**LTW**
Wind, 10 min			
R_M (CC1)	0.68	0.74	0.89
R_M (CC3)	1.58	1.39	1.12
Wind, 3 s			
R_M (CC1)	0.71	0.74	0.89
R_M (CC3)	1.55	1.41	1.13
Snow, 1 month			
R_M (CC1)	0.67	0.75	0.89
R_M (CC3)	1.60	1.35	1.11

Table 6.8 shows for all the considered cases the obtained values of the coefficient R_M. Interestingly, the Eurocode EN 1990 [37] provides the multiplicative coefficient K_{FI} for the actions to pass from CC2 to CC1 ($K_{FI} = 0.9$) or to CC3 ($K_{FI} = 1.1$), i.e., the difference between two consecutive classes in terms of coefficient K_{FI} is of the order of 10%. Recall that such coefficient has the same effect of R_M for structure which remain in the linear elastic regime. From Table 6.8, one can note that the left truncated Weibull distribution leads to values of R_M extremely close to the ones suggested by the Eurocode, making this theoretical derivation consistent with the values used for other materials [9].

6.4 The calibration of the partial factors for prestressed glass

Three reference plates are here considered, representative of the most common applications for glass panels. Figure 6.3 schematically shows the considered cases: Figure 6.3(a) a quadrilateral 6-mm-thick plate of side 3000 mm simply supported along the whole borders; Figure 6.3(b) a rectangular 10 mm-thick plate (3000 mm $\times$ 1000 mm) simply supported along the smaller sides; Figure 6.3(c) a quadrilateral 10 mm-thick plate of side 3000 mm simply supported on four points, which are located 50 mm away from the edges.

The differences in the resulting values of the partial safety factors for the three considered examples is due to the diverse effective areas associated with the corresponding states of stress. One should notice, however, that modeling the supporting points for the case shown in Figure 6.3(c) as simple supports is not strictly accurate. Indeed, holes in the panes are needed for the application of the metallic frames supporting the plates (see Figure 6.4[4]), which cause stress concentrations dependent upon the hole size and the mechanical properties of glass, steel and of the gasket that is interposed between glass and steel [83]. How to optimize the support conditions has been studied in [65, 14]. However, since high stresses act within a quite large area in the core part of the plate, whereas stress concentrations

[4]Photo from https://www.pinterest.com/pin/540713498985573407/.

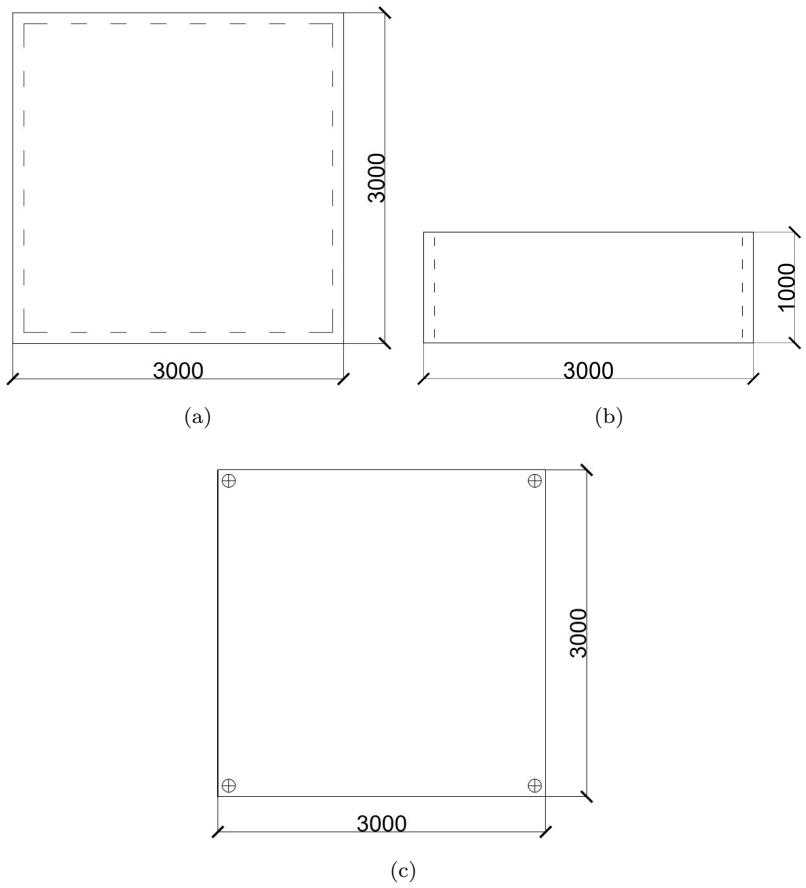

Figure 6.3: Schematic of the considered case. (a) 3000 mm × 3000 mm × 6 mm monolithic glass plate simply supported along the edges; (b) 3000 mm × 1000 mm × 10 mm plate simply supported along the smaller sides; (c) 3000 mm × 3000 mm × 10 mm monolithic glass plate simply supported on four points 50 mm away from the edges.

affect narrow areas, it is reasonable to expect that the effective area introduced in equation (A.11) is only partially affected by the stress concentrations around the holes, even though their effects is not rigorously negligible. For the sake of simplicity, such effects are not taken into consideration here, at least as a first order approximation.

6.4.1 The effects of wind

The probability density function $f_{pr,t}$ of the maximum stress within the plate consequent to the maximum annual wind pressure is given by equation (6.25), where the stresses induced by wind pressure $S_p(\sigma)$ have been evaluated *via* FEM simulations, in the geometric non-linear regime. On the other hand, the heat-treated-glass strength variability is interpreted through the function resulting from the statistical convolution of the distributions of pristine float glass strength and thermal prestresses, introduced in Section 4.2, equation (4.7). Recall from Section

Figure 6.4: Detail of the supporting points.

4.2 that, for the case of prestressed glass, the variability of the pristine glass strengths can be suitably interpreted by a 2PW distribution. In fact, in this case, the effects of left-hand-side tail are mitigated by the distribution of prestresses.

Assuming an equal probability of finding the air- or the tin-sides under tensile stresses, expression (4.7) assumes the form

$$F_t(\Sigma) = \int_0^{\sigma_{max}} \left\{ 1 - 0.5 \left[- \exp\left[\int_A \frac{(\sigma_{eq}(x, |\sigma_{pc}|))^{m_{air}}}{\eta_{0,air}^{m_{air}}} dA \right] \right.\right.$$
$$\left.\left. + \exp\left[\int_A \frac{(\sigma_{eq}(x, |\sigma_{pc}|))^{m_{tin}}}{\eta_{0,tin}^{m_{tin}}} dA \right] \right] \right\} \cdot \left\{ \frac{1}{\upsilon\sqrt{2\pi}} \exp\left[-\frac{(|\sigma_{pc}| - \mu)^2}{2\upsilon^2} \right] \right\} d|\sigma_{pc}| \,, \tag{6.31}$$

where the form of $\sigma_{eq}(x, |\sigma_{pc}|)$ is still given by equations (4.4). Observe that the probability function (6.31) is the arithmetic average of the ones referring to the two external surfaces of the specimens. On the safe side, the further contribution to heat-treated glass strength given by the crack healing during heat-treatment (see Section 4.3.2 and [83, 105]) is not taken into account. The Weibull pairs have been estimated from the results of the experimental campaign by TC129/WG8 of CEN [19], whose statistical analysis is described in Section 3.6.

Recall that the failure stress values given by CEN/TC129/WG8 [19] were re-scaled towards the reference conditions of equibiaxial strength on a unitary area ($A_0 = 1$ m^2). Furthermore, the subcritical crack growth effects of the wind action, constantly applied for a characteristic time $t = 3$ s, has been taken into consideration by re-scaling all the data through the coefficient $k_{mod} = 0.91$ given by expression (3.11), by assuming the crack velocity parameter $n = 16$ again. The estimation of the Weibull parameters, whose values are recorded in Table 6.9, has been hence performed graphically, according to the procedure described in Section A.2.

Table 6.9: Weibull parameters obtained from the rescaling of experimental data recorded in [19] ($k_{mod} = 0.91$ - $f_{ref} = 45$ MPa, $\dot{\sigma} = 2$ MPa/s, n=16, $t = 3$ s).

Surface	m	η_0 [MPa/mm$^{2/m}$]
Air-side	5.624	684.64
Tin-side	6.462	382.12

The integrals in equation (6.31) are approximated by the Reimann sums, i.e.,

$$\left\{1 - 0.5\left[\exp\left[\frac{\sum_i \sigma_{eq,i}^{m_{air}}\Delta A}{\eta_{0,air}^{m_{air}}}\right] + \exp\left[\frac{\sum_i \sigma_{eq,i}^{m_{tin}}\Delta A}{\eta_{0,tin}^{m_{tin}}}\right]\right]\right\}, \tag{6.32}$$

where 25 mm × 25 mm linear quadrilateral Finite Shell Elements were used to mesh the reference plates of Figure 6.3. The Finite Elements can be under different stressing conditions, hence the values of $\sigma_{eq,i}^{m}$ are evaluated as follows

i) $\sigma_{1,i} < |\sigma_{pc}|$, $\sigma_{2,i} < |\sigma_{pc}| \Rightarrow \sigma_{eq,i} = 0$.

ii) $\sigma_{1,i} > |\sigma_{pc}|$, $\sigma_{2,i} > |\sigma_{pc}|$
$\Rightarrow \sigma_{eq,i} = \frac{2}{\pi}\int_0^{\pi/2}(\sigma_{1,i} - |\sigma_{pc}|)\cos^2\psi + (\sigma_{2,i} - |\sigma_{pc}|)\sin^2\psi d\psi$.

iii) $\sigma_{1,i} > |\sigma_{pc}|$, $\sigma_{2,i} < |\sigma_{pc}|$
$\Rightarrow \sigma_{eq,i} = \frac{1}{\pi}\int_{-\pi/2+\beta}^{\frac{\pi}{2}-\beta}(\sigma_{1,i} - |\sigma_{pc}|)\cos^2\psi + (\sigma_{2,i} - |\sigma_{pc}|)\sin^2\psi d\psi$.

where $\sigma_{1,i}$ and $\sigma_{2,i}$ are the principal stresses acting within the i-th element, measured as the mean value of the stresses at the vertexes of each Finite Element, from the FEM simulations. The cumulative probability function for the resistance $F_r(x)$ is evaluated numerically, since the type of stress state in each of the Finite Elements can change with the wind pressure intensity and, consequently, to find a closed form expression for $F_r(x)$ is impossible. The displacements at the supporting lines or points are assumed to be negligible, even though the deformation of the supports can mildly affect the stress state acting within the plate.
By making reference to the verification formula

$$E_d \leq R_d, \qquad \sigma_{q,d}(\gamma_q) \leq \frac{\sigma_{pc,k}}{\gamma_p} + k_{mod}\frac{f_{g,k}}{\gamma_m}, \tag{6.33}$$

the equation of the partial factor for prestress reads

$$\gamma_p = \frac{\sigma_{pc,k}}{\sigma_{q,d}(\gamma_q) - k_{mod}\frac{f_{g,k}}{\gamma_m}}, \tag{6.34}$$

where $f_{g,k}$ and $\sigma_{pc,k}$ are the characteristic values of float glass strength and prestress (compression positive), respectively, $k_{mod} = 0.91$, $\gamma_q = 1.5$ and γ_m are the partial factors for actions and for the material, respectively.

By varying the height above ground z, the value of the exposure coefficient $c_e(z)$ in (C.4) is obtained that makes the convolution integral (4.7) equal to the target failure probability for CC2 class elements (see Table 6.2). The design stress $\sigma_{q,d}(\gamma_q)$, to be used in the verification formula of level I, is hence evaluated through FEM analysis from the design peak pressure $p_{w,3s,d}$, once deterministically calculated the peak pressure through equation (C.3) multiplied by the factor γ_q. Moreover, $\sigma_{pc,k}$ is taken equal to the 5% fractile of the statistical distribution of prestresses. For what concerns the residual stress distribution to be used in expression (6.31), reference is made to the results of the wide measurement campaign performed by *Schula* [84] at the Technical University of Darmstadt, that optically measured the surface compressions in the center of 255 annealed, 255 heat-strengthened and 255 toughened glass plates of size 250 mm × 250 mm and thickness 6 mm. The mean value and the standard deviation for heat strengthened glass are $\mu = 59.27$ MPa and $\upsilon = 4.58$ MPa, respectively, while the 5% fractile $\sigma_{pc,5\%} = 51.51$ MPa. The resulting Gaussian function is shown in Figure 6.5(a).

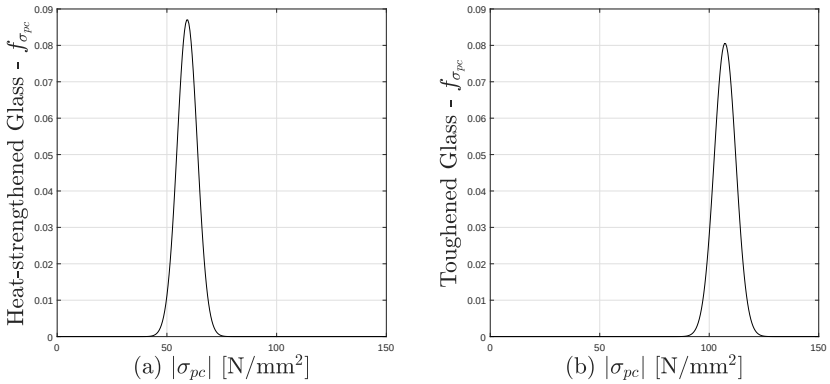

Figure 6.5: Gaussian probability density function interpreting the surface compression stress variability for (a) heat-strengthened glass and (b) toughened glass analyzed by *Schula* for 6 mm thick specimens [84].

The resulting cumulative probability functions describing the variability of the strengths in prestressed glass are plotted in Figure 6.6 for the three paradigmatic cases under consideration. Such functions are obtained by using the expression (6.31) and its approximation through (6.32).

Hence, without loosing generality, the height above ground is made to vary until the convolution integral (6.2) reaches the target failure probability ($P_{f,1y} = 1.305\,10^{-6}$) for the three considered cases, after setting $v_{b,50} = 25\,m/s$, $c_d = 1$, $c_p = 1$, $c_t = 1$, $K_r = 0.19$, $z_0 = 0.5$ m and $z_{min} = 4$ m. Then, the design wind pressure is obtained through the level I equation $(C.3)_2$. The design wind pressure is then multiplied by the partial factor for the action $\gamma_q = 1.5$ and the design stress $\sigma_{q,d}(\gamma_q)$ is obtained by inverting the correlation $S_p(\sigma)$ between σ_{max} and p_w, constructed through points *via* FEM analysis.

Finally, the values of the safety factors for prestress were evaluated through equation (6.34). The 5% fractile of the probability distribution represented in Figure

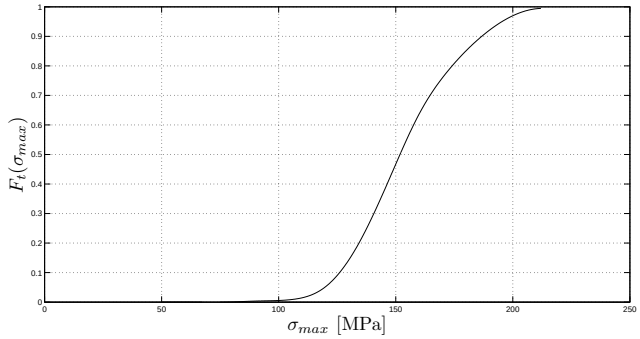

(a)

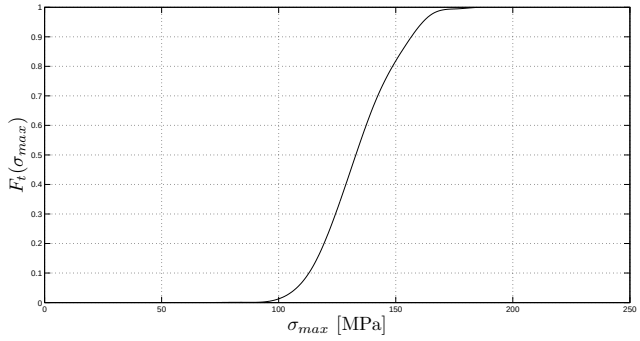

(b)

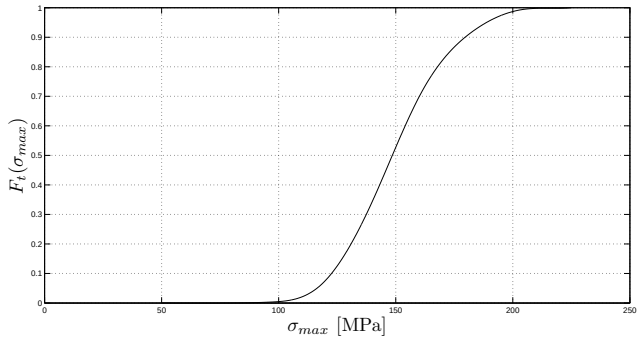

(c)

Figure 6.6: Heat-strengthened glass. Cumulative probability functions for the three different cases here considered. (a) 3000 mm × 3000 mm × 6 mm monolithic glass plate simply supported along the edges; (b) 3000 mm × 1000 mm × 10 mm monolithic glass plate simply supported along the smaller sides; (c) 3000 mm × 3000 mm × 10 mm monolithic glass plate simply supported on four points.

6.5(a) is considered as the characteristic value for surface compression ($\sigma_{pc,k} = \sigma_{pc,5\%} = 51.51$ MPa). Apart from any considerations about the best statistical model for interpreting the variability of pristine glass strength, using the partial material coefficient for glass obtained by using the LTW model leads to the highest values for γ_p. In fact, since the LTW model leads to the lower value for the partial material factor, at the same time, the higher value of the partial factor for prestress is attained. Table 6.10 records the resulting factors, which turns out to be lower than unity, and all the relevant data.

Observe that, apart from the fact that it is unlikely that both the distributions of pristine glass strengths and prestresses reach their lower values simultaneously, since the state of stress is far from the equibiaxiality, a certain number of cracks is not subject to opening tensile stress, thanks to the presence of the compressive stress state induced through the thermal treatment (see circle b of Figure 4.6). Therefore, it is not surprising that for the case at hand the risk of collapse is very small. This is the reason why one obtains $\gamma_p < 1$.

Table 6.10: Heat-strengthened glass. Values of partial factors for prestress γ_p for elements in Consequence Class 2. Different cases.

CASE	p_w [kN/m^2]	$p_w\ \gamma_q$ [kN/m^2]	$\sigma_{q,d}$ [N/mm^2]	γ_p
3000 mm x 3000 mm x 6 mm monolithic glass plate simply supported along the edges	1.804	2.706	83.37	0.85
3000 mm x 1000 mm x 10 mm monolithic glass plate simply supported along the smaller sides	0.779	1.169	80.92	0.88
3000 mm x 3000 mm x 10 mm monolithic glass plate simply supported on four points 5 cm away from the edges	0.898	1.347	83.32	0.85

For the sake of brevity, the case of snow or wind of characteristic duration $t = 10$ min are not recorded here, since values for γ_p result to be less than those just obtained. Such finding is again due to the benefic effect due to the statistical interference between pristine material strength and surface prestress.

The same arguments are used for calibrating the partial factors for prestress in the case of toughened glass. Making reference again to the experimental campaign by *Schula* [84], the mean value and the standard deviation for the surface compressions are $\mu = 107.21$ MPa and $\upsilon = 4.95$ MPa, respectively, while the 5% fractile is $\sigma_{pc,5\%} = 98.65$ MPa. Figure 6.7 shows the cumulative probability functions for the strengths of the reference plates of Figure 6.3, while Table 6.11 records the design wind pressures, design stresses and the calibrated factors.

The partial factors for prestress in the case of toughened glass reach slightly higher values than those obtained for heat-strengthened glass, as it is clear by comparing Tables 6.10 and 6.11. However, they are less than unity again. Interestingly, a single factor $\gamma_m = 1.5$ as a partial safety factor for heat-treated glass is provided by the German standard DIN 18008 [28]. Observe, in passing, that multiplying the factor $\gamma_m = 1.8$ by the values for γ_p, shown in Tables 6.10 and 6.11, one obtains values between 1.53 and 1.67, which are in good agreement with the German regulations [28].

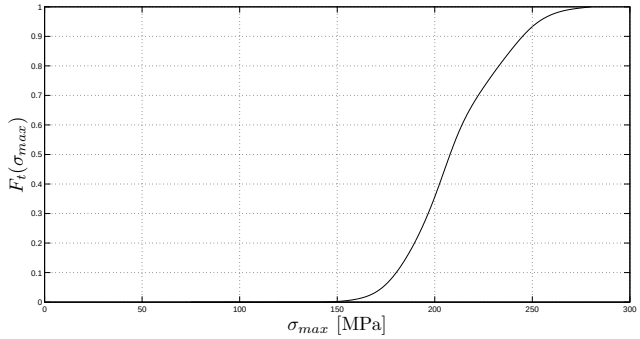

(a)

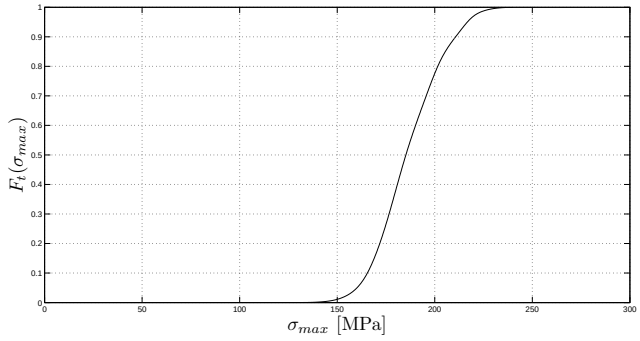

(b)

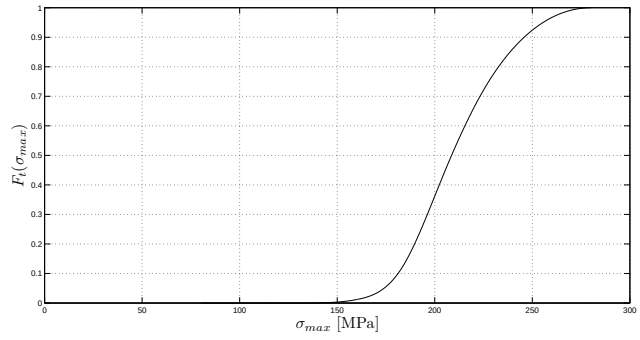

(c)

Figure 6.7: Toughened glass. Cumulative probability functions for the three considered cases. (a)3000 mm x 3000 mm x 6 mm monolithic glass plate simply supported along the edges; (b) 3000 mm x 1000 mm x 10 mm monolithic glass plate simply supported along the smaller sides; (c) 3000 mm x 3000 mm x 10 mm monolithic glass plate simply supported on four points 5 cm away from the edges.

Table 6.11: Toughened glass. Values of partial factors for prestress γ_p for elements in Consequence Class 2. Different cases.

CASE	p_w [kN/m^2]	$p_w\ \gamma_q$ [kN/m^2]	$\sigma_{q,d}$ [N/mm^2]	γ_p
3000mm x 3000mm x 6mm monolithic glass plate simply supported along the edges	3.065	4.598	136.12	0.87
3000mm x 1000mm x 10mm monolithic glass plate simply supported along the smaller sides	1.338	2.007	128.26	0.93
3000mm x 3000mm x 10mm monolithic glass plate simply supported on four points 5 cm away from the edges	1.088	1.632	129.12	0.93

6.5 Calibration of γ_p by assuming "nominal" distributions for residual stresses

The fact that the obtained factors γ_p are less than one poses serious questions about which are the values that should be considered in the structural design. Furthermore, a verification formula more refined than (6.33), taking into consideration the statistical interference between pristine glass strengths and prestresses, could optimize the use of the material. As a further analysis, the calibration procedure is here repeated by referring to "nominal" distributions for residual prestresses, in agreement with the reference values suggested by product standards. These are assumed to be representative of the 5% quantiles of the inherent statistical populations, although these could be considered excessively conservative for the today's tempering processes. Hence, a "nominal" statistics is obtained by imposing that its 5% quantile is equal to the characteristic value proposed by standards, while the standard deviation coincides with the one experimentally found in [84]. The characteristic values for prestress here assumed are 25 MPa for heat-strengthened glass and 75 MPa for toughened glass, which are suggested by several standards and guide lines, included the project of European norm prEN 16612 [77]. The resulting probability density functions, characterized by $\mu = 32.54$ MPa and $\upsilon = 4.58$ MPa for heat-strengthened glass, and $\mu = 83.15$ MPa and $\upsilon = 4.95$ MPa for toughened glass, are plotted in Figure 6.8. Observe that the mean values are lower than for the cases of Figure 6.5, while the coefficients of variation ($CV = \upsilon/\mu$) are higher. Hence, it is more likely that surface prestresses reach very low values.
For the case of wind and snow loads, the cumulative probability functions for heat-treated and toughened glass strengths have been constructed through equations (6.31) and (6.32), for the three cases of Figure 6.3.

6.5.1 Wind action

Using the same arguments used in Section 6.4.1, the design wind pressures, design stresses and the calibrated partial factors are obtained and recorded in Table 6.12. As expected, comparing Tables 6.12, 6.10 and 6.11, partial factors obtained by using "nominal" distributions for prestress are higher than for the case of Section 6.4.1, although γ_p is higher then unity (1.03) only for the case of the 3000 mm $\times$ 1000 mm $\times$ 10 mm monolithic heat-strengthened glass plate simply supported along the smaller sides. Observe that this value for γ_p becomes 1.14 if one assumes $k_{mod} = 1$ instead of $k_{mod} = 0.91$, to be on the safe side.

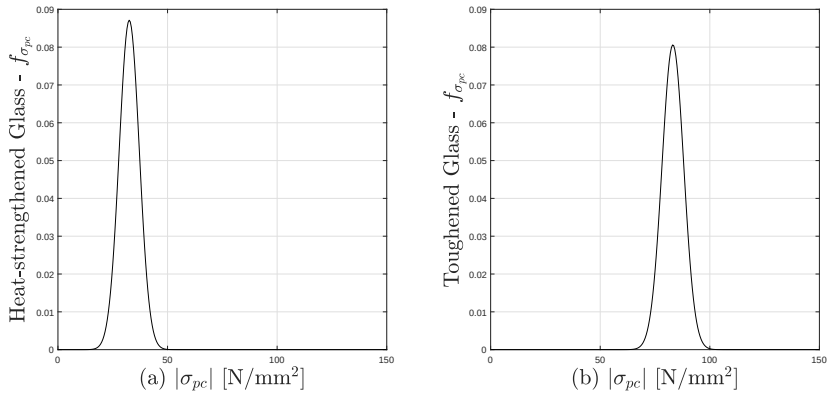

Figure 6.8: "Nominal" Gaussian probability density function for surface prestress obtained from values suggested by standards. (a) Heat-strengthened glass and (b) toughened glass.

Table 6.12: Values of partial factors for prestress γ_p for elements in Consequence Class 2 by using "nominal" distributions for surface prestresses.

CASE	p_w [kN/m^2]	$p_w\ \gamma_q$ [kN/m^2]	$\sigma_{q,d}$ [N/mm^2]	γ_p
Heat-strengthened Glass				
3000 mm × 3000 mm × 6 mm monolithic glass plate simply supported along the edges	1.151	1.727	54.78	0.77
3000 mm × 1000 mm × 10 mm monolithic glass plate simply supported along the smaller sides	0.489	0.734	46.85	**1.03**
3000 mm × 3000 mm × 10 mm monolithic glass plate simply supported on four points 5 cm away from the edges	0.459	0.689	49.46	0.93
Toughened Glass				
3000 mm × 3000 mm × 6 mm monolithic glass plate simply supported along the edges	2.503	3.755	112.87	0.83
3000 mm × 1000 mm × 10 mm monolithic glass plate simply supported along the smaller sides	0.906	1.359	106.43	0.89
3000 mm × 3000 mm × 10 mm monolithic glass plate simply supported on four points 5 cm away from the edges	1.036	1.554	103.23	0.93

6.5.2 Snow load

The Weibull pairs related to pristine glass strength to be used in the expressions (6.31) and (6.32), interpreting heat-treated glass strength variability, were estimated from the experimental campaign [19], whose results, corrected and rescaled according to the procedure described in Section B.2, have been multiplied by the coefficient $k_{mod} = 0.4$, given by equation (3.11), to account for the phenomenon of *static fatigue*. The Weibull parameters was graphically estimated, as indicated in Section A.2, obtaining for the air- and the tin-side: $m_{air} = 5.62$ and $\eta_{0,air} = 291.35$ MPa mm$^{2/m}$; $m_{tin} = 6.46$ and $\eta_{0,tin} = 162.61$ MPa mm$^{2/m}$. The correlation $q_s = S_q(\sigma_{max})$ between the uniformly distributed snow load q_s and the maximum tensile stress acting within the plate for the three cases of Figure

6.3 is again obtained *via* FEM simulation.

Of course, snow load must be considered due to a deposit on a roof. Thus, the simultaneous effect of the self-weight must be taken into consideration. The maximum stress due to self-weight acting inside the three configurations of Figure 6.3 has been evaluated *via* FEM analysis, obtaining $\sigma_{max,dl} = 6.1$ MPa for the case of Figure 4.1(a), $\sigma_{max,dl} = 10.8$ MPa for Figure 4.1(b) and $\sigma_{max,dl} = 9.4$ MPa for Figure 4.1(c).

The probability density function for the effects of the actions is given by the distribution of the maximum stress in the plate for the snow loads in one year (6.29), right-shifted of a quantity equal to the maximum stress due to self-weight $\sigma_{max,dl}$. Thus, the statistical interaction between snow load and dead load has been neglected and the maximum stress induced by self-weight is considered as a deterministic value. This assumption seems reasonable, since the variability of self-weight is certainly much lower than the one due to snow. It is assumed, without losing generality, that $C_t = 1$, $C_E = 0.9$ and $\mu = 0.5$, while $q_{sk} = 0.51[1 + (A_{sl}/481)^2]$, where A_{sl} is the altitude above sea-level. According to the EN1991-1-3 [38], the variation coefficient of the series of maximum annual snow loads V varies between 0.2 and 0.6. Firstly, it is assumed $V = 0.2$. Then, the effect of different values for the variation coefficient V upon the resulting partial factors is analyzed.

Consider the convolution integral (6.2), in the level III approach, the altitude above sea level A_{sl} is varied until the target value of the failure probability in Table 6.2 is achieved. Thus, the characteristic value of the snow load q_s is obtained through equation (C.8). From this, multiplied by the partial coefficient $\gamma_q = 1.5$, the design stress $\sigma_{s,d}$ due to snow loads is found by using a simple FEM model. On the other hand, the design value for the stress $\sigma_{dl,d}$ induced by self-weight is obtained by multiplying the maximum stress $\sigma_{max,dl}$ by the partial coefficient $\gamma_g = 1.3$. Let $f_{g,k}$ and $\sigma_{pc,k}$ be the characteristic values of the annealed glass strength and of the prestress, respectively, and denote with $n = 16$ the crack velocity parameter. The verification formula theoretically derived in [45] is used, accounting for the effects of load histories of an arbitrary number of concurrent actions with different characteristic duration. This reads

$$\sum_{j=1}^{N}\left[\frac{\left\{\left[\langle(\sum_{i=1}^{j}\sigma_i)-\sigma_{pc,k}/\gamma_p\rangle^+\right]^n-\left[\langle(\sum_{i=1}^{j-1}\sigma_i)-\sigma_{pc,k}/\gamma_p\rangle^+\right]^n\right\}}{(k_{mod,j}\ f_{g,k}/\gamma_m)^n}\right]^{1/n}\leq 1\,, \tag{6.35}$$

where $\langle\cdot\rangle^+$ is defined as $\langle x\rangle^+ = x$ when $x > 0$ and $\langle x\rangle^+ = 0$ when $x \leq 0$, while σ_i is the stress increment due to the i-th action, when the actions #1,..., #$(i-1)$ are already applied. Thus, for the case at hand, equation (6.35) can be re-written in the form

$$\frac{\langle\sigma_{dl,d}-\sigma_{pc,k}/\gamma_p\rangle^+}{k_{mod,dl}\ f_{g,k}/\gamma_m}+\left[\frac{\left(\langle\sigma_{dl,d}+\sigma_{s,d}-\sigma_{pc,k}/\gamma_p\rangle^+\right)^n-\left(\langle\sigma_{dl,d}-\sigma_{pc,k}/\gamma_p\rangle^+\right)^n}{(k_{mod,s}\ f_{g,k}/\gamma_m)^n}\right]^{1/n}\leq 1\,,$$

(6.36)

but, for the paradigmatic cases under consideration, $\langle \sigma_{dl,d} - \sigma_{pc,k}/\gamma_p \rangle^+ = 0$, and, consequently,

$$\frac{\sigma_{dl,d} + \sigma_{s,d} - \sigma_{pc,k}/\gamma_p}{k_{mod,s}\, f_{g,k}/\gamma_m} \leq 1, \tag{6.37}$$

where $\gamma_m = 1.8$. By considering a snow load applied for a nominal duration $t = 1$ month, one obtains the value of $k_{mod,s} = 0.4044$ from (3.11). Moreover, recall that $\sigma_{pc,k} = 25$ MPa for heat-strengthened glass and $\sigma_{pc,k} = 75$ MPa for toughened glass. The resulting γ_p for *heat-strengthened* glass are: $\gamma_p = 0.87$ for the case of Figure 6.3(a), $\gamma_p = 1.09$ for Figure 6.3(b) and $\gamma_p = 1.20$ for Figure 6.3(c), i.e., the point-supported square plate turns out to represent the most severe case. On the other hand, the coefficients γ_p for *toughened* glass are lower than the unity ($\gamma_p = 0.49$ for the case of Figure 6.3(a), $\gamma_p = 0.63$ for Figure 6.3(b) and γ_p=0.69 for Figure 6.3(c)).

The fact that the maximum tensile stress within a glass plate due to snow and dead loads unlikely reaches very high values partially justifies the large discrepancy between heat-strengthened and toughened glass. Infact, the high values of the residual surface compressions lead to a large number of cracks that are not subjected to opening tensile stresses. Furthermore, it is thus not surprising, by comparing Tables 6.12 and 6.13, that this effect is not so evident for plates subjected to wind load. Indeed, the mean value of the pristine glass strength in the case of wind action is much higher than in the case of snow action, since the effects of static fatigue are almost null ($k_{mod} = 0.91$ for wind gust whereas $k_{mod} = 0.4$ for snow action). Consider the circle (a) of Figure 4.6, the higher the pristine glass strength is, the lower is the angle β and, hence, the lower is the number of "inactive" cracks. This explains the different sensitivity upon such phenomenon for snow and wind loads. Table 6.13 summarizes all the relevant data resulting from the calibration procedure.

By assuming the same reference 50% quantile, i.e., $\sigma_{50\%} = 30$ MPa, the probability density functions of the maximum tensile stress in the plate of Figure 4.1(b) for snow and wind loads, given by equations (6.29) and (6.25), are plotted in Figure 6.9.

Since the coefficient of variation for the action of snow is considerably lower than for wind, it is unlikely that the maximum tensile stress due to snow loads reaches very high values with respect to gust wind and, consequently, lower values of γ_p for toughened glass plates are obtained.

The values of γ_p factors obtained by assuming variation coefficients $V = 0.4$ and $V = 0.6$ are shown in Table 6.14. An increase in the value for V leads to a higher dispersion and, at the same time, to a lower mean value of the snow load distribution. Thus, quite different values of the partial factors γ_p than in the case of $V = 0.2$ are reached, as it is clear by comparing Tables 6.13 and 6.14. It is of interest to note that the higher the value of the coefficient V, the lower is the spread of the partial factors around the unit value, i.e., the values higher than unity decrease and the values lower than unity increase.

Table 6.13: Values of partial factors for prestress γ_p for elements in Consequence Class 2 by using "nominal" distributions for residual prestresses. Snow load in different cases.

CASE	$q_s\gamma_q$ [N/m^2]	$\sigma_{s,d}$ [N/mm^2]	$\sigma_{max,dl}$ [N/mm^2]	γ_p
Heat-strengthened Glass				
3000 mm × 3000 mm × 6 mm monolithic glass plate simply supported along the edges	1616.95	30.94	7.93	0.87
3000 mm × 1000 mm × 10 mm monolithic glass plate simply supported along the smaller sides	920.83	18.85	10.8	**1.09**
3000 mm × 3000 mm × 10 mm monolithic glass plate simply supported on four points 5 cm away from the edges	906.38	18.59	12.22	**1.20**
Toughened Glass				
3000 mm × 3000 mm × 6 mm monolithic glass plate simply supported along the edges	7875.24	153.58	7.93	0.49
3000 mm × 1000 mm × 10 mm monolithic glass plate simply supported along the smaller sides	6049.22	114.42	10.8	0.63
3000 mm × 3000 mm × 10 mm monolithic glass plate simply supported on four points 5 cm away from the edges	5692.65	105.83	12.22	0.69

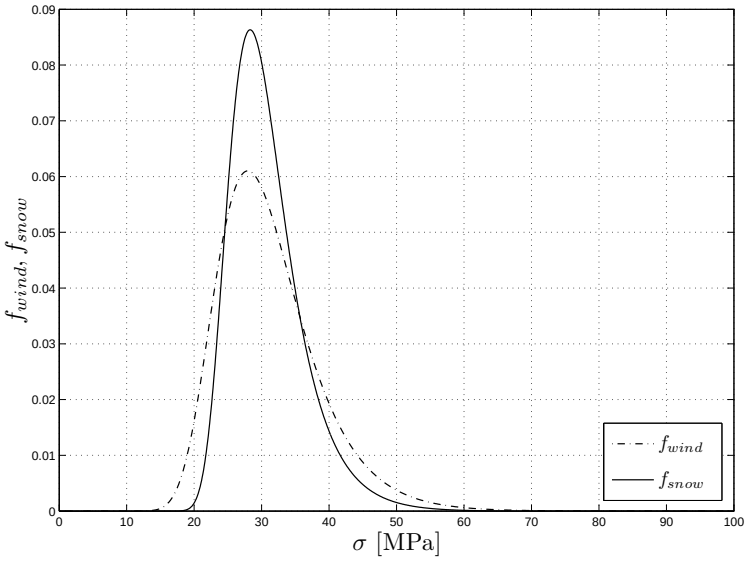

Figure 6.9: Comparison between probability density functions for maximum tensile stress in the plate of Figure 4.1(b) for snow and wind loads, normalized by the same 50% fractile $\sigma_{50\%} = 30$ MPa. Assumed coefficients: $V = 0.2$, $C_t = 1$, $C_E = 0.9$, $\mu = 0.5$ and $q_{sk} = 5.47$ kN/m^2 (snow loads) and $c_p = 1$, $c_d = 1$, $\rho_{air} = 1.25$ kg/m^3, $c_{e,t} = 1.78$ and $v_{b,50} = 25$ m/s (wind load).

Notice that dead loads were not taken into account in the calibration of the partial factors for float glass, as described in Section 6.3. In that case, consideration of the simultaneous action of snow and dead loads would lead to partial factors lower

Table 6.14: Values of partial factors for prestress γ_p for elements in Consequence Class 2 by using "nominal" distributions for residual prestresses. Snow load in different cases and different coefficients of variation (V=0.4 and V=0.6).

CASE	γ_p $(V = 0.4)$	γ_p $(V = 0.6)$
Heat-strengthened Glass		
3000 mm × 3000 mm × 6 mm monolithic glass plate simply supported along the edges	0.90	0.97
3000 mm × 1000 mm × 10 mm monolithic glass plate simply supported along the smaller sides	1.07	1.06
3000 mm × 3000 mm × 10 mm monolithic glass plate simply supported on four points 5 cm away from the edges	1.16	1.15
Toughened Glass		
3000 mm × 3000 mm × 6 mm monolithic glass plate simply supported along the edges	0.54	0.58
3000 mm × 1000 mm × 10 mm monolithic glass plate simply supported along the smaller sides	0.74	0.81
3000 mm × 3000 mm × 10 mm monolithic glass plate simply supported on four points 5 cm away from the edges	0.77	0.82

than those recorded in Table 6.5. In fact, since dead load can be considered as a quasi-deterministic action (the thickness of marketed glass has to respect strict tolerances), in the statistic competition between the various actions the self-weight indeed provides a benefic effect. This is why, on the safe side, it has been neglected. On the other hand, when high values of the resistances and, consequently, of the actions are considered, as in the case of prestressed heat-treated glass, accounting for the contribution of dead load allows to get higher values of the factors γ_p obtained from equation (6.37). However, it is certainly of importance to remark that many researchers are questioning about the reliability of the statistical model suggested by the Eurocode [38] for interpreting the variability of the snow action. This raises a lot of eyebrows about the reliability of the values recorded in Tables 6.13 and 6.14. Certainly, different models for describing snow loads variability could lead to different partial factors.

CHAPTER 7

CONCLUSIONS

7.1 Review and contributions

This study aims at improving the statistical characterization of the strength of annealed and heat-treated glass, possibly taking into account the effects of aging, in order to achieve a safe but not redundant structural design in agreement with the performance required by national and international codes. Since the accepted probabilities of failure are very low, ranging in the order of $10^{-4} \div 10^{-6}$ in one year of service life, the attention has been focused on the left-hand-side tails of the cumulative distributions P_f of the population of strengths σ, which are the parts that govern the structural design. Starting from the experimental campaign of [19], the widest ever made to my knowledge, one clearly notices that the representative points deviate from linearity in the left-hand-side tail when plotted in the Weibull plane $\ln[-\ln(1-P_f)]$ vs. $\ln(\sigma)$. This is why the expectations of strengths referring to the lower quantiles ontained from the *two-parameter-Weibull* distribution (2PW), which is by far the most used statistics for brittle materials, are much lower than what the experimental evidence would suggest.

My analysis starts from the assumption, conjectural at the beginning but demonstrated in the sequel, that glass strength cannot fall below a certain limit. Therefore, the experimental measurements have been interpolated with generalized statistics *à la* Weibull, which present a third location parameter that can be associated with the aforementioned lower bound. The ability of such statistics to interpolate the experimental data has been evaluated by using the chi-square-goodness-of-fit test, whose associated $p-$value represents the probability that the measured discrepancy between *observed* and *expected* frequencies is due to chance alone. The *three-parameter Weibull* (3PW) distribution and the *left-truncated Weibull* (LTW) distributions both provide excellent results for the air-side of the glass surface, which may be considered representative of the pristine material because not corrupted by the contact with the tin bath. Moreover, since the existence of a lower bound for strength somehow goes again the common engineering sense according to which no state of stress can be considered 100% safe, other generalized but unbounded distributions, such as the *bi-linear* (BLW), the *bi-modal* (BMW) and the *extended Weibull* (EXW) distributions, have been tested.

The statistical analysis confirms that the bounded statistics, in particular the LTW statistics, are the ones that provide the best fitting for the air-side. From a technical point of view, the observed lower bound can be attributed to the severe factory production controls in the float manufacturing process, the aim of which is to guarantee certain aesthetic and optical requirements by rejecting those panes with defects above a certain limit. Elementary considerations of linear elastic fracture mechanics indicate that the lower limit for macroscopic strength derives from the maximum size of flaws that is tolerated by the control, in agreement with the prescriptions of product standards for float glass. The LTW distribution clearly fits with this scenario, because it is derived by rejecting in a pristine population, which originally obeys to the 2PW model, those objects that fall below a certain limit. On the other hand, in the 3PW distribution, the lower bound for glass strength would be associated with an absolute material property, which is hard to justify on a micro-mechanical basis. In any case, it is important to observe that none of the considered Weibull statistics provides a remarkable goodness-of-fit for the tin-side of glass. This may indicates that the tin-side represents an example of "artificially damaged" surface, due to the contact with the tin bath and the steel rollers during the float manufacturing process.

To further investigate the effects of surface damage, a micromechanically-motivated model, where the statistical distributions of surface micro-cracks in glass is correlated with the experimentally-measured macroscopic strengths, has been considered. The defectiveness scenario at the microscopic level is interpreted by a power law distribution of crack lengths, i.e., a highly right-skewed distribution. This assumption leads to a 2PW statistics for macroscopic glass strength, which depends upon the size of the specimens and the state of stress (uniaxial vs. biaxial). Factory production controls can produce a right-hand-side truncation of the population of surface flaws, whose effect is to provide a LTW distribution for the macroscopic strength.

The effects of corrosion and abrasion due to artificial treatments or natural aging are thus interpreted by a modification of the population of micro-defects, which influences accordingly the expected macroscopic strength, eventually suggesting new forms of generalized Weibull statistics. The process of corrosion, schematized as a uniform dissolution of a thin surface layer, mostly affects the highest quantiles, associated with the smallest crack lengths. Furthermore, in "mild" abrasive phenomena new cracks are added, so that one has to consider their superposition to the defectiveness scenario already present in the pristine material. In particular, this approach is used to justify the difference in the experimentally-measured population of float-glass strengths when it is either the air- or the tin-side under tensile stress: it is the abrasion due to the contact with the tin bath and rollers that produces the damaging action. For this specific case, it is shown that the tin-side statistical population of strengths can be interpreted by a *bi-modal truncated Weibull* distribution, which provides results in very good agreement with the experimental findings. On the other hand, "heavy" abrasion processes lead to the complete dissolution of the original population of micro-cracks and the formation of a new scenario. In the case of particle impacts like in artificial or natural sandblasting, lateral cracks induced by large tensile stresses cause the material removal, while the formation of radial cracks governs the strength of the material.

The maximum length of the radial cracks depends upon various parameters but, remarkably, experiments show it remains limited in any case. This implies that the lower bound for glass strength can be reduced, but not annihilated, whatever heavy is the abrasion treatment.

All the aforementioned conclusions have been used for the calibration of partial material factors to be used in the structural design of glass with methods of level I (semiprobabilistic approach). This calibration has been obtained from the comparison of the results obtainable with methods of level III (full probabilistic) in paradigmatic case studies. Statistical models for the effects of wind and snow actions have been considered consistently with what indicated in the EN 1991-1-3 and EN 1991-1-4. The performance of the structure is defined by the maximum allowed probability of failure, established by the Eurocode EN 1990 for three classes of consequences, referred to as CC1, CC2 and CC3 in ascending order of required performance.

In order to model the strength of annealed glass, both the (bounded) LTW and the (unbounded) EXW statistics have been considered. Proper re-scaling of the glass strengths are proposed to account for static fatigue due to subcritical crack propagation and for the effects of size and type of stress. From such a re-scaling, even the assumed lower limit for glass strength is reduced, since this is associated with the opening of the largest cracks that can be found in glass, which is also affected by subcritical crack propagation. Furthermore, the lower limit and the scale parameter were reduced to account for the possible effects of natural aging, here modelled as a mild abrasion. The partial material factors so calculated have been compared to those obtained in a previous study, in which the glass strength was interpreted by a 2PW distribution. Indeed, the difference is quite striking: the partial factors from the 2PW may be as much as twice those derived from the LTW, the difference being more evident at the lowest probabilities of failure (class of consequence CC3). The EXW distribution provides values that are intermediate between the 2PW and the LTW cases.

In my opinion, on the one hand the LTW distribution is the most accurate statistics to interpret the data corresponding to the lowest probabilities, and the corresponding estimates for the partial material factors are the ones that should be considered for structural design; on the other hand, the values of partial material factors obtainable by using a 2PW model are overly-redundant. One can argue that the 2PW statistics is on the safe side, but its overly conservative nature reduces the competitiveness of glass in the construction sector, which instead asks for reliable and safe works that at the same time comply with the issues of cost-effectiveness, energy savings and reduction of pollutant emission (recall that the embodied energy per kg of glass is comparable with that of steel, and about 15 times greater than that of concrete).

It should also be mentioned that the Eurocode EN 1990 provides the coefficient K_{FI}, multiplicative of the applied actions, to pass from verifications in class of consequence CC2 to CC3 or CC1. Here, this passage of class is proposed through the coefficient R_M that multiplies not the actions, but the material strengths. This is because of the slenderness of glass structures, for which geometric non linearities may be so important to render preferable maintaining the actions unaltered. In any case, the effects of K_{FI} or R_M are completely equivalent if the structure is

linear elastic. What should be observed is that the variation associated with K_{FI}, as suggested in EN 1990, is approximately 10 %, and such a value squares very well with the results from the LTW statistics. Higher differences are obtained for the EXW, and even more so with the 2PW distributions. Although the importance of the comparison is not absolute, since the coefficients K_{FI} have been calibrated in EN 1990 on the basis of different-in-type statistics, this finding confirms the opportunity offered by the LTW statistics to comply with general principles of structural design, commonly adopted for all types of materials.

Passing to the case of heat-treated glass, where the treatment induces a permanent compressive eigenstress on the glass surfaces, it should be mentioned that the approach most commonly used in structural design consists in assuming that the macroscopic strength is the sum of the pristine material strength and of the surface prestress (in absolute value). However, such an approach should be criticized on a theoretical basis because, by treating the mechanical properties as stochastic variables, the 5% fractile of the resulting distribution of strengths is higher than the sum of the 5% fractiles of the pristine material strength and of the residual surface compression induced by the heat-treatment. In fact, pure statistical interference implies that, if low quantiles are considered, the stochastic variable obtained as the sum of two independent stochastic variables is in general more "advantageous" than its deterministic counterpart. In rough terms, it is very unlikely that at a certain point the pristine material strength and the thermally-induced prestress simultaneously reach their lowest values.

Relying upon experimental data, the heat-induced residual prestress state can be considered approximately equibiaxial, and its variation from specimen to specimen and from point to point can be acceptably described with a simple Gaussian distribution. The probability density function associated with the failure of a heat-treated glass specimen is obtained through the statistical convolution of the density functions of the operant distributions (pristine annealed glass strength and prestress). In this calculation, the population of pristine glass strength has been interpreted through the most classical 2PW distribution: this certainly facilitates the analytical derivations and, most of all, its use for this case is not excessively conservative, as for annealed float glass, because the statistical competition with the surface prestress lowers the importance of a very precise definition of the left-hand-side tails. Remarkably, the benefic effect of surface prestress strongly depends upon the type of applied stress. In fact, since glass strength is governed by the opening in mode I of surface cracks, when the stress state induced by the external loads is uniaxial, there is a number of cracks that will remain always inactive, whatever the level of the applied loads is. Only when the applied stress state is uniform equibiaxial, all the cracks are in the same potential conditions. Accordingly, comparisons with experiments has confirmed that the test set-up (three- or four-point bending vs. ring-on-ring tests) has a prominent role in the mechanical response of the heat-treated elements.

A properly-design experimental campaign has been conducted at the University of Darmstadt, in order to validate the proposed statistical approach for interpreting the variability of heat-treated glass strengths. From the optical measurements of the surface compressions induced through the thermal process, the Gaussian distribution for the description of the residual stress variability has been defined.

The results obtained from these measurements have been compared with those derived from other experimental campaigns, finding comparable conclusions. Then, 50 annealed glass plates were tested under a coaxial double ring configuration, so to obtain the statistical distribution of pristine material strengths. Finally, 51 heat-treated specimens were tested under the same loading configuration. Interestingly, the lower quantiles of the distribution are well interpreted by the statistical model, whereas the higher the considered quantile is, the higher is the discrepancy between expected and observed data. Such a distance may be attributed, albeit tentatively, to the crack healing due to the thermal process. Quite interestingly, the effect of crack healing should be almost null for the lower quantiles, associated with the largest cracks, whereas it should be much more important for the higher quantiles, associated with the smallest cracks. Proper modelling of this effect, not investigated in detail here, will be the subject of further work.
The calibration of partial material factors γ_p to be used for the surface prestress in heat-treated glass has been again obtained by comparing the results for paradigmatic case studies with both the full probabilistic methods of level III and the semiprobabilistic approach of level I, making reference again to the target values for the maximum allowable probability of failure established in the Eurocode EN 1990 for the various classes of consequences.
The resulting values of γ_p under wind action are less than unity for both heat-strengthened and toughened glass. This can be attributed to the statistical interference between pristine glass strength and surface prestress, but the measured prestress was much higher than the values usually indicated in product standards. Therefore, the calibration was repeated by using "nominal" Gaussian distributions, such that the 5% fractiles equal the values of prestress proposed by standards. Now, a difference arises between the coefficients γ_p for heat-strengthened and toughened glass under wind and snow loads. Partial factors higher than the unity have been obtained for heat-strengthened glass (γ_p=1.04 for wind actions and γ_p=1.20 for snow loads), while for toughened glass they are always lower than unity (γ_p=0.93 for wind and γ_p=0.69 for snow). Such difference is attributed to the fact that the higher the absolute value of the residual compression, the higher is the number of cracks that are inactive. This effect is not so evident for plates under wind load, because the mean value of the pristine glass strength is much higher for wind than for snow actions due to the effects of static fatigue and the different characteristic time of load duration. Indeed, the higher the pristine glass strength is, the lower is the number of cracks that, in extreme conditions, remain "inactive". It is also important to remark that there is a further beneficial effect due to crack healing, but this has not been considered here on the safe side. Moreover, the use of other statistical distributions for pristine-glass strength, such as the LTW statistics, may provide even lower values for γ_p. This analysis demonstrates that the standard practice may lead to redundant design in most cases, and that prestressed glass has many potentialities, yet to be fully explored and appreciated.

7.2 Further developments and future research

The precise statistical characterization for the strength of aged glasses is certainly of paramount importance for structural applications, but it has become a matter of debate in the scientific community only in recent years. The strength of

aged glass depends on a very large number of factors, associated with various sources of damage that have been only schematically considered in this study. Therefore, the conclusions reached here about this topic can be considered valid only at the qualitative level and, most of all, should be confirmed by appositely designed experimental campaigns. However, the approach and methods used here are of general value and definitely represent a first step towards the definition of a reliable statistical model, able to interpret how the macroscopic strength statistics may vary during the whole service life of a structural component. To this aim, it should also be recalled that another potential approach for interpreting the variability of corroded/abraded glass-strength can be based upon the Change of Variable Theorem (CVT) [17, 87], according to which it can be supposed that the defectiveness scenario observed on a damaged element is related with a single distribution of crack lengths resulting from the "distortion" of the pre-existing population of crack. This theorem is based upon a *generating density function*, representative of the pristine material, and on a *transforming function*, modeling the effects of the event causing the distortion. The search for the correct forms of the *generating* and the *transforming functions* in this alternative approach can certainly be the subject of further research.
Moreover, further experiments on heat-treated glass specimens under 3- or 4-point-bending configurations would be desirable. In such a loading condition, the stress state can be approximately considered uniaxial and, consequently, a number of cracks remains compressed whatever the level of the applied load is. In this way, one could test the capability of the proposed model at interpreting heat-treated glass strength as a function of the type of applied loading. Moreover, the development of a refined mechanical model able to take into account the effects of crack healing at the microstructural level should certainly be considered in further work. Indeed, the design of components made of heat-treated glass could be considered optimal if and only if this benefic contribution is taken into account.

APPENDIX **A**

THE WEAKEST LINK IN THE CHAIN CONCEPT: WEIBULL GENERALIZED DISTRIBUTIONS

A.1 The weakest link in the chain rationale

Weibull [94] in the 1939 developed a statistical theory that is capable of interpreting the variability of the strength exhibited by many materials. His weakest-link-in-the-chain based theory relies upon the assumptions that failure occurs from the failure of one elementary material element (one link), whose mechanical behavior is not dependent upon the response of the other "links" constituting the "chain". Assume that there are several weak places in the volume so that the theoretical strength is diminished; furthermore, assume that all these weak places are of such nature that they give rise to rupture as soon as they fall within a volume subjected to the stress σ. Thus, supposing that $N(\sigma)$ weak places are present in the unitary volume and that the stress σ acts within the small volume dV, the collapse probability is $dP_f = N(\sigma) \cdot dV$. Then, considering the case in which one has p elements dV and the rupture probability is denoted with P_f, the probability that collapse does not occur is

$$1 - P_f = (1 - dP_f)^p = (1 - N(\sigma)\, dV)^p \quad \Rightarrow \quad P_f = 1 - (1 - N(\sigma)\, dV)^p. \tag{A.1}$$

Since the total volume subjected to stress is $p \cdot dV = V$, one can write

$$P_f = 1 - \left(1 - \frac{N(\sigma)\, V}{p}\right)^p = 1 - \left(1 - \frac{N(\sigma)\, V}{p}\right)^{\frac{p}{N(\sigma)\, V} N(\sigma)\, V}. \tag{A.2}$$

For high values of p, one obtains

$$P_f = 1 - \lim_{\frac{p}{N(\sigma)\, V} = \infty} \left(1 - \frac{N(\sigma)\, V}{p}\right)^{\frac{p}{N(\sigma)\, V} N(\sigma)\, V} = 1 - e^{-N(\sigma)\, V}. \tag{A.3}$$

Denote now with $B = \int n(\sigma)\, dV = N(\sigma)\, V$, which represents the risk of rup-

ture; the function $n(\sigma)$ is a material parameter, which must be a monotonously increasing function of the variable σ. Remarkably, the material function $n(\sigma)$ for anisotropic materials is dependent upon the magnitude and direction of the stress, and can vary throughout the volume, whereas it is a function only of the stress intensity and the coordinates for isotropic materials. Of course, the general derivation of Weibull is based on volume elements, but, in the case of glass, it should be assumed that only surface cracks cause failure.

A.2 2-parameter Weibull distribution

The two-parameter Weibull distribution [94] is by far the most used statistical model for interpreting the glass strength variability [42], by reason of its simple analytical form. Firstly, assume an uniform equibiaxial state of stress, so that the maximum tensile stress is always at right angle with the dominant crack plane (opening mode - see Section 3.1). The *material function* $n(\sigma)$ is taken of the form

$$n(\sigma) = \left(\frac{\sigma}{\eta_0}\right)^m, \tag{A.4}$$

where η_0 and m are the scale and the shape parameters of the distribution, respectively. Thus, the probability of collapse for a specimen of area A [61] is given by

$$P_{f,W2} = 1 - \exp\left[-\int_A \left(\frac{\sigma}{\eta_0}\right)^m dA\right]. \tag{A.5}$$

Note that m is a measure of the data dispersion.

Then, consider a stress state different from the equibiaxial one. The component of stress $\sigma_\perp$ orthogonal to the crack plane must be found, since it is the only one that leads to failure. Let σ_1 and $\sigma_2 \leq \sigma_1$ be the principal stresses and denote with ψ the angle that the direction of σ_1 forms with the normal to the dominant crack plane, the component of stress $\sigma_\perp$ reads

$$\sigma_\perp = \left[\sigma_1 \cos^2\psi + \sigma_2 \sin^2\psi\right]. \tag{A.6}$$

Assume an isotropic and homogeneous defectiveness [44]. Such assumption is generally accepted since it is reasonable to expect that there are no preferred orientations for the crack axes and that the probability of finding a crack does not change point by point. Following [13], the *equivalent* stress for the 2PW distribution may be defined as

$$\sigma_{eq,W2} = 2/\pi \int_0^{\pi/2} \left(\sigma_1 \cos^2\psi + \sigma_2 \sin^2\psi\right)^m d\psi, \tag{A.7}$$

and the failure probability (A.5) assumes the form

$$P_{f,W2} = 1 - \exp\left[-\int_A \left(\frac{\sigma_{eq,W2}}{\eta_0}\right)^m dA\right] . \tag{A.8}$$

The failure probability can be written in a more convenient form, emphasizing the importance of the maximum tensile stress in the area A, named σ_{max}, in the form

$$P_{f,W2} = 1 - \exp\left[-K_{W2} A \left(\frac{\sigma_{max}}{\eta_0}\right)^m\right], \tag{A.9}$$

where the "*effective area*" $A_{ef,W2} = K_{W2}A$ synthetically takes into account the effect of the size and the stress state upon the population of strengths [21]. It is defined through the equality

$$1 - \exp\left[-\int_A \left(\frac{\sigma_{eq,W2}}{\eta_0}\right)^m dA\right] = 1 - \exp\left[-K_{W2} A \left(\frac{\sigma_{max}}{\eta_0}\right)^m\right], \tag{A.10}$$

so that

$$A_{ef,W2} = K_{W2}A = \frac{\int_A (\sigma_{eq,W2})^m \, dA}{(\sigma_{max})^m} . \tag{A.11}$$

In general $K_{W2} < 1$. Observe, from (A.11), that $K_{W2} = 1$ when the state of stress is equibiaxial ($\sigma_1 = \sigma_2 = \sigma_{max,eqb} \;\Rightarrow\; \sigma_{eq,W2} = \sigma_{max,eqb}$). Thus, the probability of failure reaches its maximum value for an equibiaxial state. This is why this ideal condition is universally accepted as the *reference state* for the characterization of the material strength.
The population of failure stresses obtained from a particular test configuration can be re-scaled towards the condition of uniformly distributed equibiaxial stress ($\sigma_{eqb,A_0,W2}$) acting on a unitary area A_0. By using an equal failure probability criterion, i.e., for specimens with identical defectiveness, from (A.10) one has

$$\left[-A_0 \left(\frac{\sigma_{eqb,A_0,W2}}{\eta_0}\right)^m\right] = \left[-K_{W2} A \left(\frac{\sigma_{max}}{\eta_0}\right)^m\right], \tag{A.12}$$

which leads to re-scaling law of the form

$$\sigma_{eqb,A_0,W2} = \sigma_{max} \left(\frac{K_{W2}A}{A_0}\right)^{1/m} . \tag{A.13}$$

The procedure for the estimation of the Weibull parameters through a graphically-based regression of the experimental data is now described.
The failure stress values σ_i are ranked in ascending order and an experimental failure probability P_i is assigned to each of them. The most commonly used prob-

ability estimators are

$$P_i = \frac{i}{N+1}, \qquad P_i = \frac{i-0.5}{N} \quad or \quad P_i = \frac{i-0.3}{N+0.4}, \tag{A.14}$$

where N is the total number of data. Here, the first estimator of (A.14) is selected, since it provides the most conservative results for the 2PW modulus and it is therefore the most frequently used for design purposes. From the equation for the probability of failure (A.10), one can thus write

$$\begin{aligned} P_{f,W2} &= 1 - \exp\left[-\left(\frac{\sigma_{max}}{\eta_0/A_{ef,W2}^{1/m}}\right)^m\right] \\ \Rightarrow \ln\left[\ln\left(\frac{1}{1-P_{f,W2}}\right)\right] &= m\ln(\sigma_{max}) - m\ln(\eta_0/A_{ef,W2}^{1/m}). \end{aligned} \tag{A.15}$$

As it is evident from (A.11), the quantity $A_{ef,W2}$ depends upon the state of stress in the specimen. However, a linear correspondence between $\sigma_{eq,W2}$ and σ_{max} arises when a linear elastic model is used. Thus, in this case the effective area is not dependent upon the level of load, but only upon the type of load and the boundary conditions. On the other hand, if testing procedures involving nonlinear geometric effects are used, such as the one standardized by EN 1288-2 [31], the effective area $A_{ef,W2}$ varies with the load level. When this effect can be neglected, at least as a first order approximation, the experimental data plotted in the Weibull plane, with axes $\ln\ln 1/(1-P_f)$ and $\ln\sigma$, should be aligned if the strength variability is well interpreted by the 2-parameter Weibull model. In the Weibull plane, equation (A.15) describes the line associated to the experimental data, whose slope is equal to the shape parameter m and the constant term, named T, is associated with the scale parameter η_0, which thus reads

$$\eta_0 = -A_{ef,W2}^{1/m}\exp\left(\frac{T}{m}\right), \tag{A.16}$$

and it is measured in MPa $\text{mm}^{2/m}$.

A.3 Bounded Weibull distributions. 3-parameter and left-truncated distributions

The Weibull generalized distributions which provide a lower bound for the strength population are the three-parameter (3PW) and the left-truncated (LTW) ones. The substantial difference between such distributions consists of the physical meaning of the lower limit σ_0. It is an intrinsic absolute value, characteristic of the material, for the 3PW statistics, whereas, for what concerns the LTW model, it comes from a selection, i.e., all the data below the value σ_0 are discarded. In other words, whereas in 3PW model σ_0 is an intrinsic material property, in the LTW one it is associated with a particular control that rejects the specimens that are considered "bad". However, for both cases, the value of σ_0 may be associated with the

maximum size of the pre-existing defects that can be found in the glass specimen.

A.3.1 3-parameter Weibull distribution

Considering a material with an intrinsic lower bound for strength σ_0, the *material function* proposed by Weibull [94] assumes the form

$$n(\sigma) = \left(\frac{\sigma - \sigma_0}{\eta_0} \right)^m , \tag{A.17}$$

whose domain is $[\sigma_0, \infty]$ and where, again, η_0 and m are the scale and the shape parameters of the distribution, respectively, while σ_0 is the "location parameter". Thus, the probability of failure P_f becomes

$$P_{f,W3} = 1 - \exp \left[- \int_A \left(\frac{\sigma - \sigma_0}{\eta_0} \right)^m dA \right] . \tag{A.18}$$

An equivalent stress $\sigma_{eq,W3}$ similar to (A.7) is defined for the generic stress state. Denoting with σ_1 and σ_2 the principal stresses, with $\sigma_1 \geq \sigma_2$ and with ψ the angle that the normal to the crack plane forms with the principal direction of σ_1, the crack opening stress in mode I is again given by (A.6). Assuming that glass is sensitive only to the tensile stresses that exceed σ_0, i.e., $P_f = 0$ if and only if $\sigma_1 \leq \sigma_0$ *and* $\sigma_2 \leq \sigma_0$, denoting with $|.|^+$ the positive part of the quantity in brackets, one can write

$$\sigma_{eq,W3} - \sigma_0 = \frac{2}{\pi} \int_0^{\pi/2} \left(\mid \sigma_1 - \sigma_0 \mid^+ \cos^2 \psi + \mid \sigma_2 - \sigma_0 \mid^+ \sin^2 \psi \right) d\psi . \tag{A.19}$$

Thus, the probability of failure of a specimen assumes the form

$$P_{f,W3} \; = \; 1 - \exp \left[- \int_A \left(\frac{\sigma_{eq,W3} - \sigma_0}{\eta_0} \right)^m dA \right] . \tag{A.20}$$

The effective area $A_{ef,W3} = K_{W3} A$ is introduced again, so as to obtain the simpler expression

$$P_{f,W3} \; = \; 1 - \exp \left[- A_{ef,W3} \left(\frac{\sigma_{max} - \sigma_0}{\eta_0} \right)^m \right] , \tag{A.21}$$

where

$$A_{ef,W3} \; = \; K_{W3} A \; = \; \frac{\int_A (\sigma_{eq,W3} - \sigma_0)^m dA}{(\sigma_{max} - \sigma_0)^m} . \tag{A.22}$$

Here $K_{W3} \leq 1$ and $K_{W3} = 1$ if and only if the stress state is uniformly equibiaxial and the stress intensity is higher than σ_0.
With the aim of finding a law for re-scaling the experimental data towards the

standard condition of equibiaxial stress state and unitary area, from a principle of equal failure probability, one can write

$$1 - \exp\left[-A_0\left(\frac{\sigma_{eqb,A_0,W3} - \sigma_0}{\eta_0}\right)^m\right] = 1 - \exp\left[-A_{ef,W3}\left(\frac{\sigma_{max} - \sigma_0}{\eta_0}\right)^m\right], \tag{A.23}$$

so to obtain the equation for the equivalent uniform equibiaxial stress ($\sigma_{eqb,A_0,W3}$) acting on the unitary area ($A_0 = 1$) in the form

$$\sigma_{eqb,A_0,W3} = \sigma_{max}\left(\frac{A_{ef,W3}}{A_0}\right)^{1/m} - \sigma_0\left[\left(\frac{A_{ef,W3}}{A_0}\right)^{1/m} - 1\right]. \tag{A.24}$$

Observe that the lower bound for glass strength is associated with the worst possible condition in terms of defect location and state of stress, i.e., maximum tensile stress at right angle with the deepest allowable crack, and hence does not depend upon the size of the specimen. Indeed, it attains the same value for specimens of any geometry. On the other hand, observe that the minimum strength σ_0 is associated with a defect whose size is the maximum that can be found on the glass surface. Thus, the phenomenon of static fatigue affects the value of σ_0. In other words, the value of the location parameter σ_0 obtained from the regression of experimental data has an intrinsic dependence upon the time that is necessary to provoke rupture.

For what concerns the graphical estimation of the three parameters, from equation (A.21) one can write

$$\begin{aligned} P_{f,W3} &= 1 - \exp\left[-\left(\frac{\sigma_{max} - \sigma_0}{\eta_0 / A_{ef,W3}^{1/m}}\right)^m\right] \\ \Rightarrow \ln\left[\ln\left(\frac{1}{1 - P_{f,W3}}\right)\right] &= m\ln(\sigma_{max} - \sigma_0) - \ln(\eta_0^m / A_{ef,W3})\,. \end{aligned} \tag{A.25}$$

The axes of the Weibull plane become $y = \ln\ln 1/(1 - P_f)$ and $x = \ln(\sigma - \sigma_0)$. The location parameter σ_0 is chosen by requiring that the data in the 3PW plane are as much as possible aligned. Then, from comparison with (A.25), one can obtain the shape m and the scale η_0 parameters from the interpolating line $y = m\,x + T$, with $T = -\ln(\eta_0^m / A_{ef,W3})$.

Notice that, even if second-order effects are neglected, the correspondence between $(\sigma_{eq,W3} - \sigma_0)$ and $(\sigma_{max} - \sigma_0)$ is not linear, i.e., $A_{ef,W3}$ depends upon σ_{max}. Thus, an exact estimation procedure should require an iterative procedure, where the shape parameter m is tentatively chosen, $A_{ef,W3}$ is calculated according to (A.22), then the location parameter σ_0 is obtained from the best alignment of the data, and finally η_0 from linear interpolation. The procedure must be repeated up to convergence. However, since the effective area $A_{ef,W3}$ is elevated to the $1/m$ power in (A.25) and m is in general of the order of $5 \div 7$, even if $A_{ef,W3}$ is doubled

its power increases of only $10 \div 15$ %. Therefore, in most practical cases, such a dependence can be neglected.

A.3.2 Left-truncated Weibull distribution

The lower limit σ_0 provided by the LTW distribution is the result of a truncation of the population of experimental data, whose variability is originally interpreted by a 2-parameter Weibull distribution. Following [94], $P_f(\sigma)$ is the probability of failure at stress σ and $B(\sigma) = -\log(1 - P_f)$ is the corresponding risk of failure. It is assumed that all the test specimens whose ultimate strength is less than σ_0 are discarded due to a factory quality control.
Let σ_0 correspond to the probability P_0 and N be the original number of specimens. Then, the remaining specimens after the selection will be $N(1 - P_0)$. Hence, the (truncated) probability of failure for the remaining population of specimens $P_f^T(\sigma)$ can be written in the form

$$P_f^T(\sigma) = \frac{[P_f(\sigma) - P_0]\,N}{(1 - P_0)N} = 1 - \frac{1}{1 - P_0}\exp(-B(\sigma)), \text{ for } \sigma > \sigma_0\,. \quad \text{(A.26)}$$

Considering that $P_f^T(\sigma_0) = 0 \quad \Rightarrow \quad 1 - P_0 = \exp(-B(\sigma_0))$, from (A.27) one has

$$P_f^T(\sigma) = 1 - \exp[-(B(\sigma) - B(\sigma_0))], \text{ for } \sigma > \sigma_0\,. \quad \text{(A.27)}$$

Recall that the original distribution of glass strengths is the 2PW one. Then (A.4) holds, and from (A.27) the probability of failure for an equibiaxial state of stress reads

$$P_{f,WT} = 1 - \exp\left[-\frac{\int_A (\sigma^m - \sigma_0^m)\,dA}{\eta_0^m}\right]. \quad \text{(A.28)}$$

Considering a generic stress state, the equivalent stress $\sigma_{eq,WT}$ takes a form identical to (A.7) and, consequently, the probability of failure becomes

$$P_{f,WT} = 1 - \exp\left[-\frac{\int_A (\sigma_{eq,WT}^m - \sigma_0^m)\,dA}{\eta_0^m}\right] = 1 - \exp\left[-\frac{K_{WT}\sigma_{max}^m - \sigma_0^m}{\eta_0^m}A\right], \quad \text{(A.29)}$$

where K_{WT} is the correction coefficient for the effective area of the left-truncated distribution, which has the same form as K_{W2} of equation (A.11) and reads

$$K_{WT} = \frac{\int_A \sigma_{eq,WT}^m dA}{A\,\sigma_{max}^m}. \quad \text{(A.30)}$$

From a principle of equal failure probability again, the re-scaling law towards the reference conditions of homogenous equibiaxial stress $\sigma_{eqb,A_0,WT}$ on a unitary area

A_0 is obtained from

$$1-\exp\left[-\frac{K_{WT}\sigma_{max}^m-\sigma_0^m}{\eta_0^m}A\right]=1-\exp\left[-\frac{\sigma_{eqb,A_0,WT}^m-\sigma_0^m}{\eta_0^m}A_0\right], \quad \text{(A.31)}$$

which leads to

$$\sigma_{eqb,A_0,WT}=\left(\frac{K_{WT}A\,\sigma_{max}^m}{A_0}-\sigma_0^m\frac{(A-A_0)}{A_0}\right)^{1/m}. \quad \text{(A.32)}$$

For what concerns the parameters estimation, the expression for the probability of collapse (A.29) leads to

$$\begin{aligned} P_{f,WT}&=1-\exp\left[-\frac{K_{WT}\sigma_{max}^m-\sigma_0^m}{\eta_0^m}A\right]\\ &\Rightarrow\ \ln\left[A\frac{\sigma_0^m}{\eta_0^m}+\ln\left(\frac{1}{1-P_{f,WT}}\right)\right]=m\ln(\sigma_{max})+\ln\left(\frac{A_{ef,WT}}{\eta_0^m}\right). \end{aligned} \quad \text{(A.33)}$$

where $A_{ef,WT}$ is given by (A.30). Since the equivalent stress $\sigma_{eq,WT}$ takes the same form as for the 2PW case, the same conclusions can be reached about the effective area $A_{ef,WT}$. Thus, $A_{ef,WT}$ varies with the stress intensity when second order geometric effects are of importance, but it can be considered constant, at least as a first order approximation. Then, by setting $G=A\sigma_0^m/\eta_0^m$, $T=\ln[A_{ef,WT}/\eta_0^m]$, $y=\ln\left[G+\ln 1/(1-P_{f,WT})\right]$ and $x=\ln\sigma_{max}$, equation (A.33) becomes $y=m\,x+T$. Hence, under the hypothesis that the effective area is constant ($A_{ef,WT}$ =const), the value of G must be found such that, in the LTW plane $\ln[G+\ln 1/(1-P_f)]$ vs. $\ln(\sigma)$, the best alignment of the the experimental points is obtained. From such a linear interpolation of the data, the optimal value of m and T are reached. Thus, the other parameters are obtained as

$$\eta_0=A_{ef,WT}^{1/m}\left(\exp(-T)\right)^{1/m}; \qquad \sigma_0=\eta_0\left(\frac{G}{A}\right)^{1/m}=\left(K_{WT}\exp(-T)G\right)^{1/m}. \quad \text{(A.34)}$$

The convenience of using the LTW model is also due to the significant analytical simplifications as compared with the 3PW model. Specifically, the definition of the equivalent stress (A.19) for the 3PW case makes the relationship between the effective area and the acting stress strongly non-linear. Thus, the effective area $A_{ef,W3}$ of (A.22) must be calculated for all the stress conditions. On the other hand, the definition of the equivalent stress $\sigma_{eq,WT}$ for the LTW model, which is analogous to (A.7), leads to a linear dependence upon the stress state. Consequently, if one consider a test where the load is homogeneously increased, providing negligible geometric second order effects, the correction coefficient K_{WT} of (A.30) would be independent of σ_{max}.

A.4 Unbounded generalized Weibull distributions

Since the existence of a lower bound for glass strength is somehow against the common engineering sense, other unbounded distributions have been proposed to fit the experimental results.

A.4.1 Bi-linear Weibull (BLW) distribution

The bi-linear distribution comes from the simplest idea of interpolating the experimental points with a piecewise linear function in the Weibull plane [79]. Therefore, one assumes a bi-linear function for the Weibull distribution (BLW). Defining the equivalent stress $\sigma_{eq,WL}$ through an expression identical to that of (A.7) for the 2PW distribution, one has

$$P_{f,WL} = \begin{cases} 1 - \exp\left[-\int_A \left(\frac{\sigma_{eq,WL}}{\eta_{0,1}}\right)^{m_1} dA\right] \quad , \quad \text{for } \; 0 < \sigma_{max} \leq \sigma^* \; , \\ \\ 1 - \exp\left[-\int_A \left(\frac{\sigma_{eq,WL}}{\eta_{0,2}}\right)^{m_2} dA\right] \quad , \quad \text{for } \; \sigma_{max} > \sigma^* \; , \end{cases} \tag{A.35}$$

where σ_{max} is the maximum stress acting within the plate under consideration, while $(\eta_{0,1}, m_1)$ and $(\eta_{0,2}, m_2)$ are the 2PW pairs corresponding to the left-hand-side and right-hand-side branches, respectively. However, by considering that the stress state is not in general uniformly equibiaxial, the approach is not without *ambiguity*.
It is of importance to notice that the choice of the Weibull coefficients depends upon the stress σ_*, whereas another approach would be to consider the distribution

$$\hat{P}_{f,WL} = 1 - \exp\left[-\int_A \left(\frac{\sigma_{eq,WL}}{\eta_0(\sigma_{eq,WL})}\right)^{m(\sigma_{eq,WL})} dA\right] \; , \tag{A.36}$$

where

$$[\eta_0(\sigma_{eq,WL}), m(\sigma_{eq,WL})] = \begin{cases} (\eta_{0,1}, m_1) \text{ for } \; 0 < \sigma_{eq,WL} \leq \sigma^* \; , \\ \\ (\eta_{0,2}, m_2) \text{ for } \; \sigma_{eq,WL} > \sigma^* \; . \end{cases} \tag{A.37}$$

Such a procedure leads to serious complications, since the Weibull parameters are changed for the same material.
By using the approach of (A.35), the effective area $A_{ef,WL} = K_{WL}A$ can be written in the form

$$A_{ef,WL} = K_{WL}A = \begin{cases} \frac{\int_A (\sigma_{eq,WL})^{m_1} \, dA}{(\sigma_{max})^{m_1}} \quad \text{for } \; 0 < \sigma_{max} \leq \sigma^* \; , \\ \\ \frac{\int_A (\sigma_{eq,WL})^{m_2} \, dA}{(\sigma_{max})^{m_2}} \quad \text{for } \; \sigma_{max} > \sigma^* \; . \end{cases} \tag{A.38}$$

On the other hand, under the hypothesis that (A.36) holds, a much more compli-

cated expression is reached, i.e.,

$$\hat{A}_{ef,WL} = \hat{K}_{WL} A = \begin{cases} \left(\frac{\eta_{0,1}}{\sigma_{max}}\right)^{m_1} \int_A \left(\frac{\sigma_{eq,WL}}{\eta_0(\sigma_{eq,WL})}\right)^{m(\sigma_{eq,WL})} dA, \text{ for } 0 < \sigma_{max} \leq \sigma^*, \\ \left(\frac{\eta_{0,2}}{\sigma_{max}}\right)^{m_2} \int_A \left(\frac{\sigma_{eq,WL}}{\eta_0(\sigma_{eq,WL})}\right)^{m(\sigma_{eq,WL})} dA \ , \quad \text{for } \sigma_{max} > \sigma^* \ , \end{cases} \tag{A.39}$$

where $m(\sigma_{eq,WL})$ and $\eta_0(\sigma_{eq,WL})$ are given by (A.37).

The rescaling of the experimental data towards standard conditions turns out to be not straightforward, since one of the pairs $(\eta_{0,1}, m_1)$ or $(\eta_{0,2}, m_2)$ must be selected according to the values of $\sigma_{eqb,A_0,WL}$, but such choice is quite arbitrary.

For what concerns the parameters estimation, since a model of the type (A.36) would be very hard to treat, it is convenient to use the statistical distribution given by (A.35), which can be re-written in the form

$$P_{f,WL} = \begin{cases} 1 - \exp\left[-\left(\frac{\sigma_{max}}{\eta_{0,1}}\right)^{m_1} A_{ef,WL,1}\right] \ , \quad \text{for } 0 < \sigma_{max} \leq \sigma^* \ , \\ 1 - \exp\left[-\left(\frac{\sigma_{max}}{\eta_{0,2}}\right)^{m_2} A_{ef,WL,2}\right] \ , \quad \text{for } \sigma_{max} > \sigma^* \ , \end{cases} \tag{A.40}$$

where $A_{ef,WL,1}$ and $A_{ef,WL,2}$ are the effective areas on the branches $\sigma_{max} \leq \sigma^*$ and $\sigma_{max} > \sigma^*$, respectively, according to the definition of (A.38). Neglecting again the geometric non linear effects, such values are constant for any value of σ_{max}, apart from the jump that they exhibit in the point $\sigma_{max} = \sigma^*$. The plane useful to perform the linear regression of the data is obviously the same used for the 2PW statistics, with axes $\ln\ln 1/(1 - P_f)$ and $\ln\sigma$. Once the data are split into two series delimited by the value of σ^*, the two Weibull pairs characterizing the BLW statistics are estimated by linear regression of the data contained in each of the two domains. The criterium for the choice of σ^* is the maximization of the goodness of fit with the experimental data. Obviously, the piecewise-linear distribution becomes even more complicated if more than two Weibull pairs are chosen to fit the experimental data.

A.4.2 Bi-modal Weibull (BMW) distribution

The bi-modal Weibull distribution may interpret the strength variability of materials that undergone two distinguished and independent failure mechanisms, each one governed by a specific Weibull distribution of the type (A.8), with Weibull pairs $(\eta_{0,1}, m_1)$ and $(\eta_{0,2}, m_2)$. This means that there are two types of rings in the chain, as schematically shown in Figure A.1(a). The equivalent stress $\sigma_{eq,WM}$ is

defined as *per* (A.7), hence the probability of failure reads

$$\begin{aligned}\check{P}_{f,WM} &= 1-\exp\left[-\int_A\left(\frac{\sigma_{eq,WM}}{\eta_{0,1}}\right)^{m_1}dA\right]\exp\left[-\int_A\left(\frac{\sigma_{eq,WM}}{\eta_{0,2}}\right)^{m_2}dA\right]\\ &= 1-\exp\left\{\int_A-\left[\left(\frac{\sigma_{eq,WM}}{\eta_{0,1}}\right)^{m_1}+\left(\frac{\sigma_{eq,WM}}{\eta_{0,2}}\right)^{m_2}\right]dA\right\}.\end{aligned} \tag{A.41}$$

This is the product of the probability of survival of the two constituent types of chain rings. However, observe that according to equation (A.41), the slope of the interpolating line is higher on the right-hand-side tail than on the left-hand-side tail; this is the contrary of what one generally finds from the experimental campaigns. With the aim of obtaining the desired form for the interpolating function, a cumulative probability of failure resulting from the product of the cumulative probabilities of failures for each independent failure mechanisms may be assumed. This leads to

$$\begin{aligned}\hat{P}_{f,WM} &= \left\{1-\exp\left[-\int_A\left(\frac{\sigma_{eq,WM}}{\eta_{0,1}}\right)^{m_1}dA\right]\right\}\left\{1-\exp\left[-\int_A\left(\frac{\sigma_{eq,WM}}{\eta_{0,2}}\right)^{m_2}dA\right]\right\}\\ &= 1-\exp\left[-\int_A\left(\frac{\sigma_{eq,WM}}{\eta_{0,1}}\right)^{m_1}dA\right]-\exp\left[-\int_A\left(\frac{\sigma_{eq,WM}}{\eta_{0,2}}\right)^{m_2}dA\right]\\ &\quad+\exp\left\{\int_A-\left[\left(\frac{\sigma_{eq,WM}}{\eta_{0,1}}\right)^{m_1}+\left(\frac{\sigma_{eq,WM}}{\eta_{0,2}}\right)^{m_2}\right]dA\right\}.\end{aligned} \tag{A.42}$$

A physical justification for (A.42) is schematically shown in Figure A.1(b), where one of the chains is taut while the other is loose. For the collapse occurrence, by pulling apart the lateral supports, the first chain fails before the second one becomes engaged and, in turn, breaks. Thus, for a certain stress level the probability of failure of the whole system is equivalent to the probability that both chains break, one after the other, at the assigned stress.
Consider the case of Figure A.1(a), interpreted by equation (A.41). One can define the effective area $\check{A}_{ef,WM}=\check{K}_{WM}A$ following the condition

$$\check{A}_{ef,WM}\left[\left(\frac{\sigma_{max}}{\eta_{0,1}}\right)^{m_1}+\left(\frac{\sigma_{max}}{\eta_{0,2}}\right)^{m_2}\right]=\int_A\left[\left(\frac{\sigma_{eq,WM}}{\eta_{0,1}}\right)^{m_1}+\left(\frac{\sigma_{eq,WM}}{\eta_{0,2}}\right)^{m_2}\right]dA. \tag{A.43}$$

On the other hand, if one uses equation (A.42), an analogous complicated expression is obtained for $\hat{A}_{ef,WM}=\hat{K}_{WM}A$. Finding a re-scaling law, towards the experimental condition of uniformly equibiaxial state of stress $\sigma_{eqb,A_0,WM}$ acting on the unitary area (A_0), is extremely complex again.
Referring to the parameters estimation, the best fit with the experimental data in the 2-parameter Weibull plane [$\ln\ln 1/(1-P_f)$ vs $\ln\sigma$] is obtained by varying the

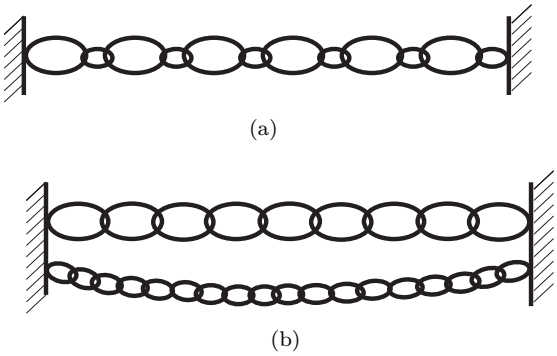

Figure A.1: (a) A "bimodal" chain, formed by two types of rings; (b) the consecutive-loss-of-strength chain concept.

four parameters of the distribution, provided that one can neglect the dependence of the effective area upon the stress level.

A.4.3 Extended Weibull (EXW) distribution

Since the presence of two Weibull exponents in the BLW and BMW models makes any re-scaling extremely complex, many authors have attempted to define more flexible distributions, but retaining only one Weibull exponent. In particular, *Marshall and Olkin* [58] proposed a method for adding a parameter to a family of distributions, whose application for the Weibull families leads to a probability of failure of the type

$$P_{f,WE} = 1 - \frac{\Theta\,\tilde{P}_s}{1-(1-\Theta)\tilde{P}_s}\ , \tag{A.44}$$

where

$$\tilde{P} = \exp\left[-\int_A \left(\frac{\sigma_{eq,WE}}{\eta_0}\right)^m dA\right]\ , \tag{A.45}$$

with the equivalent stress $\sigma_{eq,WE}$ of the same form as (A.7). The effective area $A_{ef,WE} = K_{WE}A$ is obtained by using a principle of equal failure probability, i.e.,

$$1-\frac{\Theta\exp\left[-K_{WE}A\left(\frac{\sigma_{max}}{\eta_0}\right)^m\right]}{1-(1-\Theta)\exp\left[-K_{WE}A\left(\frac{\sigma_{max}}{\eta_0}\right)^m\right]} = 1-\frac{\Theta\exp\left[\int_A\left(\frac{\sigma_{eq,WE}}{\eta_0}\right)^m dA\right]}{1-(1-\Theta)\exp\left[\int_A\left(\frac{\sigma_{eq,WE}}{\eta_0}\right)^m dA\right]}\ , \tag{A.46}$$

from which one obtains the same expressions for $A_{ef,WE} = A_{ef,W2}$ and $K_{WE} = K_{W2}$ as *per* (A.11). Analogously, the rescaling equation for the experimental data

towards the reference conditions is obtained by setting

$$1-\frac{\Theta \exp\left[-A_0\left(\frac{\sigma_{eqb,A_0,WE}}{\eta_0}\right)^m\right]}{1-(1-\Theta)\exp\left[-A_0\left(\frac{\sigma_{eqb,A_0,WE}}{\eta_0}\right)^m\right]} = 1-\frac{\Theta \exp\left[-K_{WE}A\left(\frac{\sigma_{max}}{\eta_0}\right)^m\right]}{1-(1-\Theta)\exp\left[-K_{WE}A\left(\frac{\sigma_{max}}{\eta_0}\right)^m\right]}, \tag{A.47}$$

which leads to

$$\sigma_{eqb,A_0,WE} = \sigma_{eq,A_0,W2} = \sigma_{max}\left(\frac{K_{WE}A}{A_0}\right)^m. \tag{A.48}$$

The rescaling law, hence, is exactly the same as the one of the two-parameter Weibull model of (A.13). This is probably the most important advantage of the EXW model.

Assuming $y = \ln\left[\ln 1/(1-P_f)\right]$ and $x = \ln \sigma_{max}$, from the equivalence (A.46), the probability plot is the smooth curve [107] of equation

$$y = \ln\left\{-\left\{\ln(\Theta) - \ln\left[\exp\left(\exp(x)/(\eta_0/A_{ef,WE}^{1/m})\right)^m - (1-\Theta)\right]\right\}\right\}. \tag{A.49}$$

The three parameters of the EXW statistics can be estimated through the graphical procedure proposed by *Zhang and Xie* [107]. By taking the limit of y with $x \to \infty$, equation (A.49) becomes

$$y = m\left[x - \ln\left(\eta_0/A_{ef,WE}^{1/m}\right)\right], \tag{A.50}$$

which is a straight line, say L, in the Weibull plane $\ln[\sigma]$ vs. $\ln\left[-\ln\left(1-P_f\right)\right]$ with slope m. A peculiar aspect of the extended Weibull distribution consists of the fact that the left-hand-side and right-hand-side tails present the same slope in the Weibull plane. Indeed, it is possible to demonstrate [107] that for very small value of P_f equation (A.49) becomes

$$y = m\left[x - \ln\left(\eta_0/A_{ef,WE}^{1/m}\right)\right] - \ln(\Theta), \tag{A.51}$$

which is another straight line, say L_a, parallel to the line of (A.50). Denote with X_x the intercept with the y-axis of L_a; for $y = 0$ one can write

$$\left(\eta_0/A_{ef,WE}^{1/m}\right)^m = \frac{\exp\left[m\,X_x\right]}{\Theta}. \tag{A.52}$$

Let X_0 be the intercept of the smooth curve (A.49) with the x-axis, from which,

when $y = 0$, one has

$$\exp\left[\left(\frac{e^{X_0}}{\left(\eta_0/A_{ef,WE}^{1/m}\right)}\right)^m\right] = 1 + \Theta(e-1). \tag{A.53}$$

The data from a generic experimental campaign are arranged in ascending order and an experimental probability of failure $P_f = i/(N+1)$ is assigned to each i-th datum, where N is the total number of data. Once plotted the data in the Weibull plane, the parameter m is obtained by fitting a straight line to the left-hand-side of the fitting plot. Then, the intercept X_0 and X_x are read from the fitting curves (A.49) and (A.51), respectively. Finally, the parameters η_0 and Θ are obtained by solving the simple system constituted by equations (A.52) and (A.53).

A.5 The chi-square goodness of fit test

The chi-square goodness of fit test aims at verifying that the difference between the expected values according to a certain statistical distribution and the observed data is due to chance alone [64]. To perform the test when continuous functions are under analysis, the interval between the minimum and the maximum observed values is divided into k classes $(C_1, C_2, ..., C_k)$. Let $(N_1, N_2, ..., N_k)$ be the observed frequencies for each i-th class. It is common practice to group the data into intervals of equal probabilities and in such a way that the expected count in each interval is at least 5. By denoting with $p_1, p_2, ..., p_k$ the probability that a stochastic variable (X) assumes a value inside one of the classes according to the statistical model under analysis, the expected absolute frequencies are $(Np_i, i = 1, 2, ...k)$, where N is the total number of observed data. The function X_g^2 gives a measure of the discrepancy between the observed and the expected frequencies, and it reads

$$X_g^2 = \sum_{i=1}^{k} \frac{(N_i - N\,p_i)^2}{N\,p_i}\,. \tag{A.54}$$

The form (A.54) of X_g^2 was proposed by Pearson [74] in the early 1900s. Of course, X_g^2 assumes very low values if the assumed model is correct.
The rationale of the test is that the null hypothesis[5] H_0 is verified if the observed and expected values are likely to be close one another. The test statistic, i.e., the distribution of the X_g^2 under the hypothesis that H_0 is true, approximately follows a chi-square distribution χ_g^2 of the type

$$f(X^2) = \frac{1}{2^{g/2}\Gamma(g/2)} e^{-X^2/2} (X^2)^{(g/2)-1}, \tag{A.55}$$

where g is the number of degree of freedom. Let N_{par} be the number of parameters

[5]The null hypothesis is defined as the statement being tested in a test of statistical significance. The test of significance is designed to assess the strength of the evidence against the null hypothesis [60].

characterizing the statistical distribution under analysis; then $g = k - 1 - N_{par}$. Figure A.2 shows the relationship between $f(X^2)$ and X^2 for three values of g.

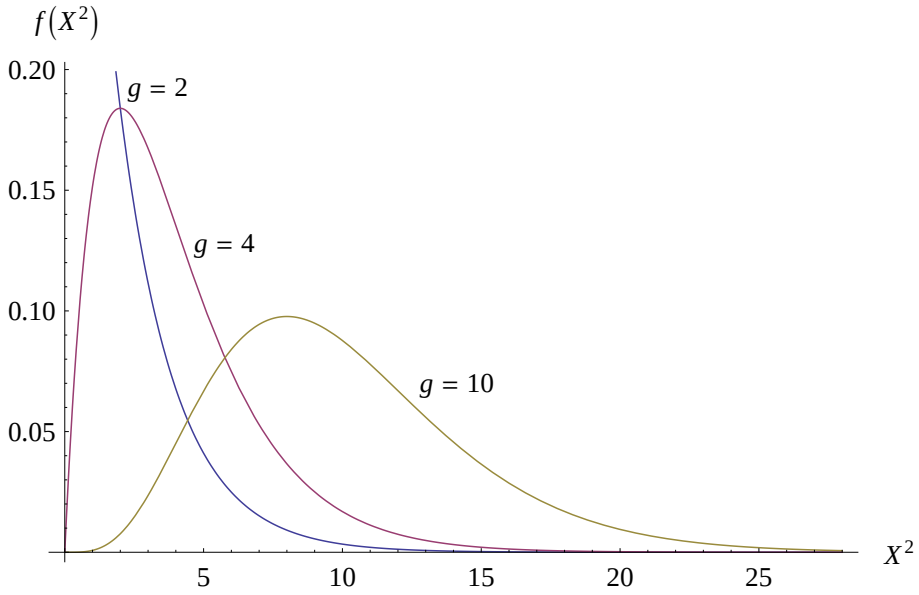

Figure A.2: The Chi-square distribution for: $g = 2, 4, 10$.

The mean value of the distribution $f(X^2)$ is equal to g, while the variance is $2g$. It is evident from Figure A.2 that the distribution is strongly right-skewed for small values of g, while it becomes almost symmetric for high values of g. A single measured value of X^2 will have a probability p of being grater than X_g^2 given by

$$\int_{X_g^2}^{\infty} f(X^2) dX^2 = p, \tag{A.56}$$

where $f(X^2)dX^2$ is the probability that a particular value of X^2 falls between X^2 and $X^2 + dX^2$. It is customary to accept the "5% rule", i.e., the H_0 hypothesis is accepted (rejected) if the difference between the expected values according to a certain statistical distribution and the observed data, named $p - value$, is such that $p \geq 5\%$ ($p < 5\%$).
Observe that this test is sensitive to the chosen number of classes k and to their distribution, but there is not an universally recognized optimal choice for the number and the width of the bins. For the chi-square tests whose results are recorded here, 20 bins of equal width have been used. However, for some of the analyzed distributions, the bins in the tails have been joined with the aim of obtaining at least five expected frequencies for each bin, so as to guarantee a good chi-square approximation. Once X_c^2 is evaluated trough equation (A.54) and the number of degrees of freedom g is fixed, the corresponding p-value can be obtained from the χ_g^2 distribution using a simple computer algorithm, tables or graphs. The comparison of the p-values obtained by using the different statistical models gives

an objective indication of their goodness of fit, since the higher the p-value, the higher is the probability that any deviation from expected results is duo to chance only.
However, different aspects must be taken into account to select the statistical model for interpreting a data population, such as the consistency of the physical interpretation of the estimated parameters, the ability of the statistics to interpret the variability of the observations, and the statistical significance of the parameters, i.e., parameters that unremarkably affect the statistical distribution have little significance.

APPENDIX **B**

TESTING METHODS FOR EVALUATING GLASS STRENGTH

B.1 The coaxial double ring (CDR) test

When the effects of geometric non-linearity are negligible, a circular plate loaded by radial couples uniformly distributed along the border achieves an uniform equibiaxial stress state. This certainly represents the most severe condition for glass, since there is 100% probability of finding the maximum tensile stress direction at right angle with the crack axis. However, it is almost impossible to reproduce in practice such loading configuration. The Coaxial Double Ring (CDR) test could be considered an approximation of the aforementioned "optimal" set-up for achieving an almost uniform equibiaxial stress state in the core part of a plate. The test set-up provides that the surface loads are applied on the plate through two concentric rings sufficiently far from the borders.

B.1.1 Analysis of the stress state

Firstly, consider a *circular* Kirchhoff-Love plate [88] of moderate constant thickness h. Let E and ν be the Young's modulus and Poisson's ratio, respectively, so that $D = Eh^3/[12(1-\nu^2)]$ is the bending stiffness of the plate. Assume the circular coordinates (r, θ) of a polar reference system, centered in the origin, and let ζ represent the vertical displacement. Since loading and constraints are axisymmetric, $\zeta = \zeta(r)$ and the shear stress in circumferential direction is null.
Denoting the shear stress in radial direction with t_r, which can be easily calculated from statics because of the symmetry, by defining

$$\varphi(r) = -\frac{d}{dr}\,\zeta(r), \tag{B.1}$$

the classical fourth-order differential field-equation in ζ can be integrated and reads [88]

$$\frac{d^2\varphi}{dr^2} + \frac{1}{r}\frac{d\varphi}{dr} - \frac{\varphi}{r^2} = -\frac{t_r}{D}\,. \tag{B.2}$$

The radial moment m_r and the circumferential moment m_θ are

$$m_r = -\frac{Eh^3}{12(1-\nu^2)}\left(\frac{d\varphi}{dr} + \nu\frac{\varphi}{r}\right),\ m_\theta = -\frac{Eh^3}{12(1-\nu^2)}\left(\frac{\varphi}{r} + \nu\frac{d\varphi}{dr}\right), \quad \text{(B.3)}$$

while the radial σ_r and circumferential σ_θ bending stresses read

$$\begin{aligned}\sigma_r &= -\frac{E}{1-\nu^2}\left(-z\frac{d^2\zeta}{dr^2} - \nu z\frac{\varphi}{r}\right) = -\frac{6}{h^2}\,m_r,\\ \sigma_\theta &= -\frac{E}{1-\nu^2}\left(-z\frac{\varphi}{r} - \nu z\frac{d^2\zeta}{dr^2}\right) = -\frac{6}{h^2}\,m_t.\end{aligned} \quad \text{(B.4)}$$

Consider the case of a circular plate of radius R_1 bent by distributed couples m_0 uniformly applied along the border as in Figure B.1(a). The shear stress in the radial direction is clearly null ($t_r = 0$) in (B.2). From the geometric and natural boundary conditions at $r = R_1$ and the symmetry condition at $r = 0$, i.e.,

$$\zeta(R_1) = 0\,,\ \ m_r(R_1) = m_0\ \ ,\varphi(0) = 0\ , \quad \text{(B.5)}$$

one obtains $\varphi(r) = \frac{1}{2}\,X_1\,r$. Since $\frac{d}{dr}\,\varphi = \varphi/r$, the corresponding solution is $m_r = m_t = m_0$ and $\sigma_r = \sigma_t = 6\,m_0/h^2$, i.e., the stress state is uniform and *rigorously equibiaxial* in the whole specimen.

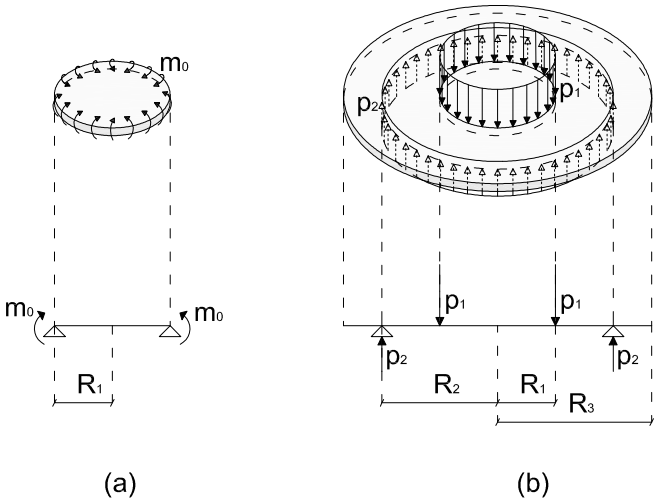

Figure B.1: a) Circular elastic plate bent by couples at the border. b) Configuration of a Coaxial Double Ring (CDR) test.

As mentioned before, it is almost impossible in practice to apply bending moments uniformly distributed at the circular border. From this, the necessity to look for an approximation of this ideal loading configuration arises. In figure B.1(b), supposing that friction is negligible, the reactions transmitted by two rings, coaxial with the center of the specimen, in contact with the two opposite sides of the plate and pushed one against the other by a tensometer, are shown. Let R_1, R_2 and R_3 be the radius of the inner ring, of the outer ring, and of the circular specimen. The reactions hence read $p_1 = F/(2\pi R_1)$ and $p_2 = F/(2\pi R_2)$, where F is the force transmitted by the tensometer. By considering the symmetry of the problem, the radial shear t_r in (B.2) is

$$\begin{aligned} t_r(r) = 0 \ \text{ for } \ 0 \le r < R_1\,, \quad t_r(r) = \frac{F}{2\pi r} \ \text{ for } \ R_1 < r < R_2, \\ t_r(r) = 0 \ \text{ for } \ R_2 < r \le R_3\,, \end{aligned} \tag{B.6}$$

while the matching conditions at the inner radius $r = R_1$ and the boundary conditions at the outer radius $r = R_2$ are

$$\begin{aligned} &\varphi(0) = 0\,, \ \ \zeta(R_1^-) = \zeta(R_1^+)\,, \ \ \varphi(R_1^-) = \varphi(R_1^+)\,, \ \ m_r(R_1^-) = m_r(R_1^+)\,, \\ &\zeta(R_2^-) = \zeta(R_2^+) = 0\,, \ \ \varphi(R_2^-) = \varphi(R_2^+)\,, \ \ m_r(R_2^-) = m_r(R_2^+)\,, \ \ m_r(R_3) = 0. \end{aligned} \tag{B.7}$$

The solution of equation (B.2) for the particular case $t_r = \frac{F}{2\,\pi\,r}$ reads

$$\begin{aligned} &\varphi(r) = -\frac{F\,r}{4\pi D}\left[\log(r) - 1/2\right] - \frac{X_1\,r}{2} - \frac{X_2}{r} \\ &\Rightarrow \ \zeta = -\frac{F\,r^2}{8\pi D}\left[\log(r) - 1\right] - \frac{X_1\,r^2}{4} - X_2 \log r + X_3\,, \end{aligned} \tag{B.8}$$

where X_1, X_2 and X_3 are determined from the boundary and matching conditions. The resulting stress state is constant and equibiaxial in the core part of the plate delimited by the inner ring $0 \le r < R_1$, whose intensity is given by the equation

$$\sigma_r = \sigma_\theta = \frac{3\,F}{4\,\pi\,h^2}\left[(1-\nu)\,\left(1 - \frac{R_1^2}{R_2^2}\right)\frac{R_2^2}{R_3^2} + 2(1+\nu)\log\frac{R_2}{R_1}\right]. \tag{B.9}$$

Observe that, considering the case $R_3 = R_2$, by expanding in Taylor series expression (B.9) in the variable R_2/R_1 around the point $R_2/R_1 = 1$, and neglecting the terms of higher order than the first, the stress state is given by

$$\sigma_r = \sigma_\theta \simeq \frac{6\,m_0^*}{h^2}\,, \ \text{ with } m_0^* = \frac{F}{2\pi R_1}(R_2 - R_1)\,, \tag{B.10}$$

which is equal to the stress acting within a circular plate of radius R_1 bent by distributed couples m_0^* at the border, where m_0^* is equal to the product of the ring-constraint reaction $\frac{F}{2\pi R_1} \simeq \frac{F}{2\pi R_2}$ and the level arm $(R_2 - R_1)$. It is of impor-

tance to remark that such approximation is acceptable only when $R_3 = R_2 \to R_1$. By contrast, the border $R_2 < r < R_3$ as well as the distance $R_2 - R_1$ can generally play a significant role. The trend of $\sigma_r = \sigma_\theta$ as a function of $m_0^* = \frac{F}{2\pi R_1}(R_2 - R_1)$ for various ratios between the radii is shown in Figure B.2. Sometimes expression (B.10) is used for estimating the stress state in the core part of a plate loaded according to the coaxial double ring configuration. Even though such approximation is certainly on the safe side (the approximation corresponds to the highest graph), it could lead to stress intensities much higher than the actual value.

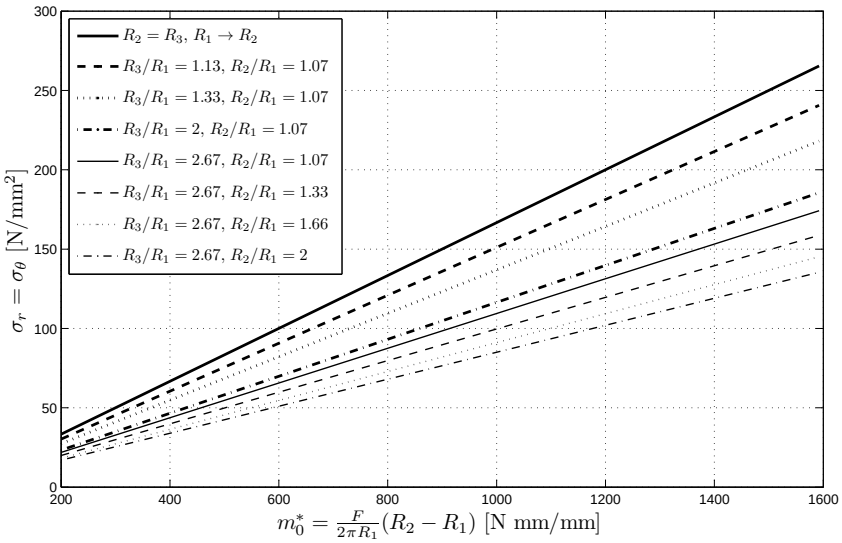

Figure B.2: Relationship between the equibiaxial stress state in the core $0 < r < R_1$ and the moment per unit length $m_0^* = \frac{F}{2\pi R_1}(R_2 - R_1)$ for different geometries.

Even though the geometry $R_3 = R_2 \to R_1$ would appear optimal, the ratios R_3/R_2 and R_2/R_1 cannot go below certain limits, otherwise dangerous stress concentrations could arise, causing localized rupture.

However, in several cases, geometric non linear effects may be of importance, i.e., surface strains of the middle plane must be taken into account when deflections are not small in comparison with plate thickness, generally larger than half the thickness. Following the Föppl-von Kármán theory [78], the curvature of a meridian is equal to $\frac{d^2}{dr^2}\zeta$ and the straight lines normal to the middle surface remain straight and normal in the deformed configuration.

Since it is very complex to find a closed form solution, an approximate solution of the non-linear problem can be obtained by using the method proposed in [93]. Denote with σ_r' and σ_θ' the radial and the circumferential components, respectively, of the membrane stress in the plate and $\varphi = \frac{d}{dr}\zeta$ again. From symmetry considerations, the field equations [88] governing the non-linear problem of a *circular* plate of moderate constant thickness h under a uniformly distributed load per unit area

p, and the bending and membrane equilibrium in radial direction read

$$D\frac{d}{dr}\left(\frac{1}{r}\frac{d}{dr}(r\varphi)\right) = p\,\frac{r}{2} + h\,\sigma'_r\,\varphi, \qquad \frac{d}{dr}(r\,\sigma'_r) - \sigma'_\theta = 0\,. \tag{B.11}$$

Let ξ be the radial displacement and z the distance from the middle surface of the plate. The radial ε'_r and circumferential ε'_θ strains of the middle surface (membrane strains), and the additional strains, ε''_r and ε''_θ, associated with bending, are

$$\varepsilon'_r = \frac{d\xi}{dr} + \frac{\varphi^2}{2}, \qquad \varepsilon'_\theta = \frac{\xi}{r}\,, \qquad \varepsilon''_r = -z\frac{d^2\zeta}{dr^2}\,, \qquad \varepsilon''_\theta = -z\frac{\varphi}{r}\,. \tag{B.12}$$

Consequently, from the constitutive equations, the membrane stresses, σ'_r and σ'_θ, and the stresses due to bending, σ''_r and σ''_θ, assume the form

$$\begin{aligned}
\sigma'_r &= \frac{E}{1-\nu^2}\left(\frac{d\xi}{dr} + \frac{\varphi^2}{2} + \nu\frac{\xi}{r}\right), \quad \sigma'_\theta = \frac{E}{1-\nu^2}\left(\frac{\xi}{r} + \nu\frac{d\xi}{dr} + \nu\frac{\varphi^2}{2}\right),\\
\sigma''_r &= \frac{E}{1-\nu^2}\left(-\,z\,\frac{d^2\zeta}{dr^2} - \nu\,z\,\frac{\varphi}{r}\right), \quad \sigma''_\theta = \frac{E}{1-\nu^2}\left(-\,z\,\frac{\varphi}{r} - \nu\,z\,\frac{d^2\zeta}{dr^2}\right).
\end{aligned} \tag{B.13}$$

The radial and circumferential moments per unit length, m_r and m_θ, are obtained by integrating the stresses in the thickness and read

$$m_r = \frac{Eh^3}{12(1-\nu^2)}\left(\frac{d\varphi}{dr} + \nu\frac{\varphi}{r}\right), \qquad m_\theta = \frac{Eh^3}{12(1-\nu^2)}\left(\frac{\varphi}{r} + \nu\frac{d\varphi}{dr}\right). \tag{B.14}$$

By expanding the displacements, the strains and the stresses in series of positive powers of the non-dimensional radial distance $u = \frac{r}{h}$, Way [93] introduced a general solution for the nonlinear problem, whose relevant expressions are

$$\begin{aligned}
&S'_r := \frac{\sigma'_r}{E} = B_0 + B_2\,u^2 + B_4\,u^4 + \dots\,, \qquad S'_\theta := \frac{\sigma'_\theta}{E} = B_0 + 3\,B_2\,u^2 + 5\,B_4\,u^4 + \dots\,,\\
&\varphi = \sqrt{8}\Big(C_1\,u + C_3\,u^3 + C_5\,u^5 + \dots\Big)\,, \qquad \frac{d\varphi}{du} = \sqrt{8}\Big(C_1\,u + 3\,C_3\,u^3 + 5\,C_5\,u^5 + \dots\Big)\,,\\
&\frac{\zeta}{h} = \sqrt{8}\left(C_1\,\frac{u^2}{2} + C_3\,\frac{u^4}{4} + C_5\,\frac{u^6}{6} + \dots\right),\\
&S''_r := \frac{\sigma''_r}{E} = \frac{m_r\,h}{2D(1-\nu^2)}\,, \qquad S''_\theta := \frac{\sigma''_\theta}{E} = \frac{m_\theta\,h}{2D(1-\nu^2)}\,,
\end{aligned} \tag{B.15}$$

where m_r and m_θ are given by equations (B.14). The correlations between the constants B_k and C_k are obtained by equilibrium considerations (B.11), leading

to

$$B_k = -\frac{\sum_{m=1,3,5\ldots}^{k-1} C_m\, C_{k-m}}{\frac{k}{2}\left(\frac{k}{2}+1\right)}\,, \quad k=2,4,6..., \qquad C_3 = \frac{3\left(1-\nu^2\right)\left(\frac{q}{2\sqrt{8}} + B_0\, C_1\right)}{2}\,,$$
$$C_k = 3(1-\nu^2)\frac{\sum_{m=0,2,4\ldots}^{k-3} B_m\, C_{k-2-m}}{\frac{k^2-1}{4}} \quad k=5,7,9....$$
(B.16)

Remarkably, B_0 is the value of S'_r, associated with the *membrane* stress at the center of the plate, while C_1 is proportional to the *bending* stress at the same point. The values of the coefficients B_0 and C_1 vary with the boundary conditions for the problem. Once such coefficients are known, all the other terms in the expansion (B.15) are obtained in cascade from (B.16).
Firstly, the case of a circular plate loaded by uniformly distributed bending couples m_0 at the border schematized in Figure B.1(a) is analyzed. An approximation of the value for C_1 can be found by assuming that the stress due to bending at the center is the same as the one predicted by linear theory, which implies a condition on the derivative of φ with respect to $u = \frac{r}{h}$ at the center $u = 0$ of the type

$$\frac{d\varphi}{du} = \frac{12\, m_0\,(1-\nu)}{E\, h^2} = \sqrt{8}\, C_1\,. \tag{B.17}$$

From this, the coefficient C_1 is easily found, while $B_2 = -\frac{C_1^2}{2}$ is obtained from $(\text{B.16})_1$. Starting from the consideration that the radial membrane stress σ'_r and consequently S'_r are null at the edge $u = R_1/h$, an approximation for the expression of B_0 can be found by neglecting terms of higher order than u^2 in $(\text{B.15})_1$, obtaining

$$B_0 + B_2\, u^2|_{r=R_1} = 0 \Rightarrow B_0 = -B_2\, \frac{R_1^2}{h^2}\,. \tag{B.18}$$

A comparison is made between the numerically determined state of stress and the one obtained with the aforementioned approximate method, consisting in assuming that the flexural stress at the center is equal to the one obtained from the linear elastic solution and in neglecting all the terms after the seconds in the expansions of (B.15). The case of a circular plate bent by radial couples, illustrated in Figure B.1(a), with $R_1 = 75$ mm, $h = 6$ mm and $m_0 = 398$ N mm/mm, is considered. The results of the comparison are shown in Figure B.3, i.e., the membrane components, σ'_r and σ'_θ, and the bending components, σ''_r and σ''_θ, are plotted as a function of the radial abscissa r. The results are good, but the accuracy decreases with increasing stress or with decreasing the plate thickness.
On the other hand, the static equivalence given by (B.10) neglects the effects of the hoop stress and, hence, it is not precise when the ratios R_3/R_2 and R_2/R_1 are far from unity (see Figure B.2). Consequently, the proposed approximate solution is certainly reliable for the case of the plate bent by couples, whereas it may give not accurate results for the geometry of the Coaxial Double Ring configuration of

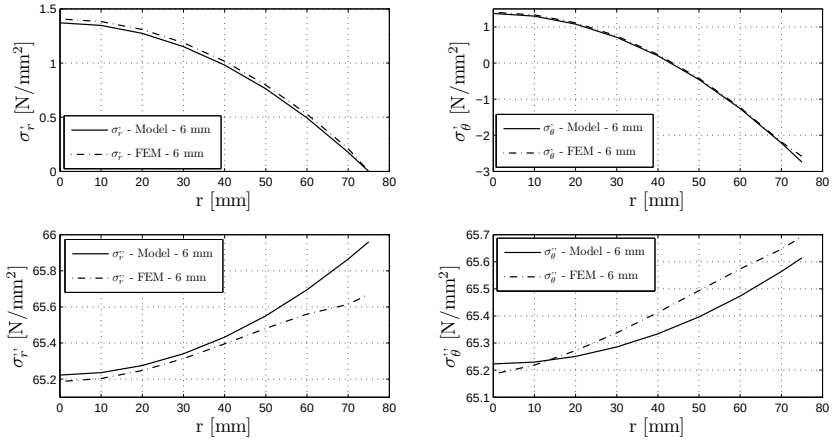

Figure B.3: Comparison between analytic solution and numerical analysis. Circular plate loaded by distributed couples. Case $m_0 = 398$ N mm/mm, $R_1 = 75$ mm, $h = 6$ mm.

Figure B.1(b). Thus, for this loading configuration, a better estimate of B_0 and C_1 could be made by using an experimental or a numerical approach. Thus, the coefficients B_0 and C_1 for the case of the Coaxial Double Ring (CDR) configuration are derived from the membrane and flexural stresses at the center of the plate obtained *via* FEM analysis. The analytic solution is hence obtained, since all the other terms in the expansion (B.15) are obtained in cascade from (B.16). The comparison for the case $R_1 = 75\,mm$, $R_2/R_1 = 2$, $R_3/R_1 = 2,67$ and $F = 5$ kN is shown in Figure B.4. The value of the force applied by the tensometer $F = 5$ kN is such that the stress state is of the same order of that in Figure B.3 for the plates bent by couples $m_0 = 398$ N mm/mm. Remarkably, $m_0 \neq \frac{F}{2\pi R_1}(R_2 - R_1)$, as *per* (B.10), since $R_2 \neq R_1$ and the effects of the geometric non-linearity are not negligible. The first two terms of the various expansions of (B.15) have been taken into account, since the accuracy of results for just two terms is very good.

Notice that B_0 is always positive for the CDR configuration and, consequently, C_1 is always negative, implying that also B_2 and C_3 are always negative. This makes the membrane radial stress be a decreasing function of r, while the bending radial stress increases with r.

Denoting with σ'_{center} and with σ''_{center} the maximum stresses at the plate center associated with the membrane and flexural response, respectively, and with $SF = \sigma'_{center} h$ and $SM = \sigma''_{center} h^2/6$ the membrane force per unit width and the bending moment per unit width at the center of the plate, respectively, one has

$$
\begin{aligned}
&B_0 = \frac{SF}{E\,h}\,, \qquad C_1 = \frac{\sqrt{8}}{8}\frac{h}{D(1+\nu)}SM\,,\\
&S'_r = B_0 + B_2\,u^2\,, \qquad S''_r = -\frac{\sqrt{8}}{2}\frac{C_1}{1-\nu} - \frac{\sqrt{8}}{2}\frac{3+\nu}{1-\nu^2}\,C_3\,u^2\,.
\end{aligned}
\tag{B.19}
$$

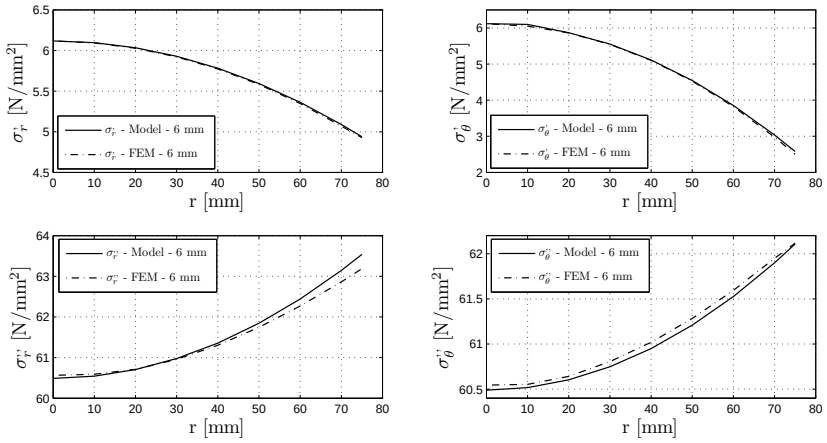

Figure B.4: Comparison between analytic solution and numerical analysis. Circular plate loaded in the CDR configuration. Case $R_1 = 75$ mm, $R_2/R_1 = 2$, $R_3/R_1 = \frac{8}{3}$, $h = 6$ mm, $F = 5$ kN.

Finally, the maximum stress is at the center (border) if

$$\frac{\sigma'_{center}}{\sigma''_{center}} < (>) \frac{1-\nu}{6(3+\nu)} \,. \tag{B.20}$$

Equation (B.20) has very important implications, since stress concentrations in the neighborhood of edges or constraints should be avoided while performing mechanical tests on glass.
The comparison between the analytic non-linear solution for a circular specimen in the CDR configuration ($R_1 = 75$ mm, $R_2/R_1 = 2$, $R_3/R_1 = \frac{8}{3}$, $l = 2R_3$, $h = 6$ mm, $F = 5$ kN) and the numerical FEM results for a square plate ($l = 2R_3$) under the same type of loading is shown in Figure B.5. The results are very similar, i.e., the proposed approximated solution can be used even for square plate of side $l = 2R_3$ loaded by the rings $r = R_1$ and $r = R_2$, which means that the effect of the four overhanging pieces in the square specimens upon the flexural response of the whole plate is marginal. This outcome is certainly of importance, since circular plates are more expensive than the square ones, due to cost of manufacturing, and hence they are rarely chosen for the experimental campaigns.

B.1.2 Analytic expressions for the effective area

As deeply discussed in Appendix A, since glass failure occurs when a micro-crack reaches its critical conditions, the weakest-link-in-the-chain concept associated with Weibull statistics [94] is commonly used to interpret the material strength variability. According to this model, a synthetical view of the influence of the size and of the state of stress upon the failure probability is given by the effective area $A_{eff} = K\,A$, given by equation (A.11) when reference is made to the 2-parameter Weibull distribution. However, introducing the parameter ρ, defined as the ratio between the minimum and the maximum principal tensile stresses, a more conve-

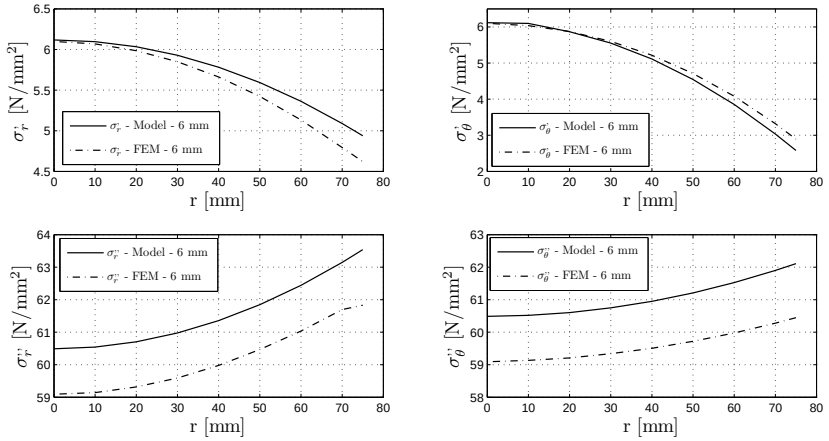

Figure B.5: Comparison between the analytic solution of a circular plate in the CDR configuration, and the numerical FEM analysis for a square plate under the same loading. Case $R_1 = 75$ mm, $R_2/R_1 = 2$, $R_3/R_1 = \frac{8}{3}$, $l = 2R_3$, $h = 6$ mm, $F = 5$ kN.

nient form for the effective area can be found. Thus, by defining the equivalent stress in the form

$$\sigma_{eq} = \sigma_1 \left[\cos^2\psi + \rho \sin^2\psi\right], \tag{B.21}$$

where ψ is again the angle that the maximum principle stress σ_1 forms with the normal at the crack axis, the effective area becomes

$$A_{eff} = K\,A = \frac{\int_A (W\sigma_1)^m dA}{(\sigma_{max})^m}\ , \tag{B.22}$$

where the correction coefficient $W = \left[\frac{2}{\pi}\int_0^{\pi/2}\left(\cos^2\psi + \rho\sin^2\psi\right)^m\right]^{1/m}$ and m is the Weibull shape parameter. The effective area allows to find the stress σ_{eqbiax,A_0} that corresponds to an equal probability of failure for another specimen, made of the same material, but of unitary area A_0 and subject to an equibiaxial state of stress, through equation (A.13).

Thus, the correction coefficient K of (B.22) depends upon the ratio $\rho = \sigma_2/\sigma_1$. By analyzing the core area $0 \le r < R_1$ for the circular plate in the CDR configuration of Figure B.1(b) and by setting $\sigma_1 = \sigma_1(r) = \sigma_r(r)$ and $\sigma_2 = \sigma_2(r) = \sigma_\theta(r)$, the expressions (B.15) are used to calculate $\sigma_r(r) = \sigma_r'(r) + \sigma_r''(r)$ and $\sigma_\theta(r) = \sigma_\theta'(r) + \sigma_\theta''(r)$. In the expansions, all the terms after the seconds are neglected, i.e., the solution depends upon the coefficients B_0, B_2, C_1 and C_3. Thus, from the

condition $\sigma_r(0) = \sigma_\theta(0) = \sigma_{center}$, one obtains

$$\rho(r) = \frac{\sigma_\theta(0) + [\sigma_\theta(r) - \sigma_\theta(0)]}{\sigma_r(0) + [\sigma_r(r) - \sigma_r(0)]} = \frac{1 + \left[\frac{\sigma_\theta(r) - \sigma_\theta(0)}{\sigma_{center}}\right]}{1 + \left[\frac{\sigma_r(r) - \sigma_r(0)}{\sigma_{center}}\right]} = \frac{1 + \left[\frac{E\left(3\,B_2 - \frac{\sqrt{8}}{2}\frac{1+3\nu}{1-\nu^2}\,C_3\right)}{\sigma_{center}}\right]\frac{r^2}{h^2}}{1 + \left[\frac{E\left(B_2 - \frac{\sqrt{8}}{2}\frac{3+\nu}{1-\nu^2}\,C_3\right)}{\sigma_{center}}\right]\frac{r^2}{h^2}}\,, \tag{B.23}$$

where $\sigma_{center} = E(B_0 - \frac{\sqrt{8}}{2}\frac{C_1}{1-\nu})$ is the stress acting at the center of the plate. Recalling that one has $\sigma_r(r) = \sigma_\theta(r)$ for $0 \le r < R_1$ in the linear elastic solution, it is clear that the terms in square brackets of (B.23) give a measure of the deviation from equibiaxiality due to second order effects. When these are much smaller than 1, expanding (B.23) in Taylor's series up to terms of the second order, one has

$$\begin{aligned}\rho(r) &= 1 + \left(2\,B_2 + \frac{\sqrt{8}\,C_3}{1+\nu}\right)\frac{E}{\sigma_{center}}\,\frac{r^2}{h^2} \\ &+ 2\left[-B_2 + \sqrt{8}\,B_2\,C_3\,\frac{1}{1+\nu} - C_3^2\,\frac{\nu^2 + 2\,\nu - 3}{(1-\nu^2)^2}\right]\frac{E^2}{\sigma_{center}^2}\,\frac{r^4}{h^4}\,.\end{aligned} \tag{B.24}$$

Analogously, the expression for W^m given by (B.22) can be expanded up to terms of the second order in the neighborhood of $\rho(r) = 1$. Then, (B.24) is inserted in the expanded W^m and, keeping only the second-order terms again, one has

$$\begin{aligned}(W(r))^m &= 1 - \frac{1-\rho(r)}{2}\,m + \frac{3}{8}\,(m-1)\,m\,[\rho(r)-1]^2 \\ &= 1 + \vartheta\,\frac{r^2}{h^2} + \kappa\,\frac{r^4}{h^4}\,\frac{m}{2} + \frac{3}{8}(m-1)m\left(\vartheta^2\,\frac{r^4}{h^4}\right),\end{aligned} \tag{B.25}$$

where

$$\vartheta = \left(2\,B_2 + \frac{\sqrt{8}\,C_3}{1+\nu}\right)\frac{E}{\sigma_{center}}\,, \quad \kappa = 4\left[-B_2^2 + \frac{\sqrt{8}\,B_2\,C_3}{1+\nu} + \frac{C_3^2\,(3 - 2\,\nu - \nu^2)}{(1+\nu^2)^2}\right]\frac{E^2}{\sigma_{center}^2}\,. \tag{B.26}$$

Moreover,

$$\big(\sigma_r(r)\big)^m = \big(\sigma_{center}\big)^m\left[1 + \frac{E}{\sigma_{center}}\left(B_2 - \frac{\sqrt{8}}{2}\,\frac{3+\nu}{1-\nu^2}C_3\right)\frac{r^2}{h^2}\right]^m\,, \tag{B.27}$$

and, expanding in Taylor's series up to the second order again, one can write

$$\big(\sigma_r(r)\big)^m = \big(\sigma_{center}\big)^m \left[1 + \varpi\, m\, \frac{r^2}{h^2} + \frac{m\,(m-1)}{2}\, \varpi^2\, \frac{r^4}{h^4}\right], \tag{B.28}$$

where

$$\varpi = \left(B_2 - \frac{\sqrt{8}}{2}\, \frac{3+\nu}{1-\nu^2}\, C_3\right) \frac{E}{\sigma_{center}}\ . \tag{B.29}$$

Thus, an analytic expression for the correction coefficient K of (B.22) valid for the central portion $0 \le r < R_1$ is obtained, which reads

$$\begin{aligned} K\, \sigma_{max}^m = \sigma_{center}^m \Bigg[1 + \frac{\vartheta\, m}{4}\frac{R_1^2}{h^2} + \frac{\kappa\, m}{6}\frac{R_1^4}{h^4} + \frac{(m-1)\, m\, \vartheta^2}{8}\frac{R_1^4}{h^4} + \frac{\varpi\, m}{2}\frac{R_1^2}{h^2} \\ + \frac{\vartheta\, \varpi\, m^2}{6}\frac{R_1^4}{h^4} + \frac{m\,(m-1)\,\varpi^2}{6}\frac{R_1^4}{h^4}\Bigg]. \end{aligned} \tag{B.30}$$

Recalling that the maximum stress σ_{max} acts along the radial direction at the center σ_{center} or at the edge σ_{edge}, these read

$$\begin{aligned} \sigma_{center} &= E\left(B_0 - \frac{\sqrt{8}}{2}\frac{C_1}{1-\nu}\right), \\ \sigma_{edge} &= E\left(B_0 + B_2\,\frac{R_1^2}{h^2} - \frac{\sqrt{8}}{2}\frac{C_1}{1-\nu} - C_3\,\frac{\sqrt{8}}{2}\frac{1+3\nu}{1-\nu^2}\frac{R_1^2}{h^2}\right). \end{aligned} \tag{B.31}$$

The proposed method for the evaluation of the correction factor K has been validated through numerical nonlinear analyses. The coefficients B_0, C_1 are obtained from equations (B.17) and (B.18), respectively, and then B_2 and C_3 from (B.16). Hence, the coefficient K has been analytically calculated through expression (B.30). The analytic estimate of K as a function of σ_{center} for a circular plate of radius $R_1 = 75$ mm and thickness $h = 6$ mm or $h = 10$ mm, bent by radial couples uniformly distributed along the border shown in Figure B.1(a) is recorded in Figure B.6, assuming either $m = 5.4$ or $m = 7.3$. Even tough the estimation of the coefficients B_0 and C_1 is here made from the linear elastic solution, as suggested in Section B.1.1, the analytical expression gives accurate results, as it is evident from the comparison with the results of the FEM simulation. Obviously, the higher are the loads and the lower is the thickness, the worst the approximation is, since the effects of geometric non-linearity become of relevance.
On the other hand, Figure B.7 is the counterpart of Figure B.6 for the case of a CDR configuration with $R_1 = 75$ mm, $R_2/R_1 = 2$, $R_3/R_1 = \frac{8}{3}$. The coefficients B_0 and C_1 are now calculated using a FEM simulation as described in Section B.1.1. The agreement with the numerical experiments is optimal, regardless of the plate thickness and the stress level.

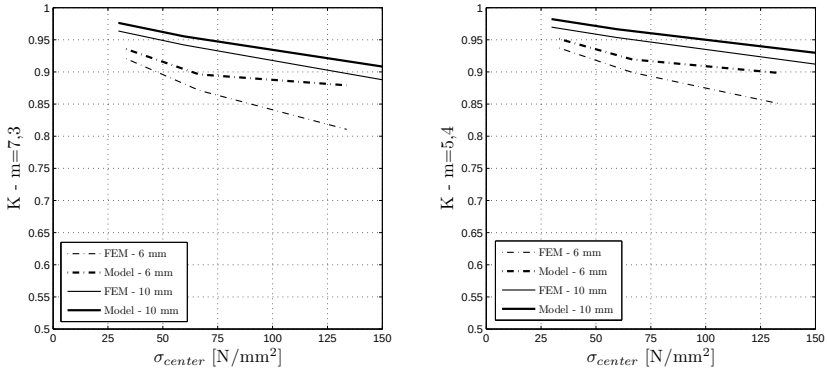

Figure B.6: Correlation between the correction coefficient K and σ_{center} for a circular plate of radius 75 mm under distributed radial couples. Comparisons of results from FEM and from the proposed analytic model. Cases $h = 6$ mm, $h = 10$ mm, $m = 5.4$ and $m = 7.3$.

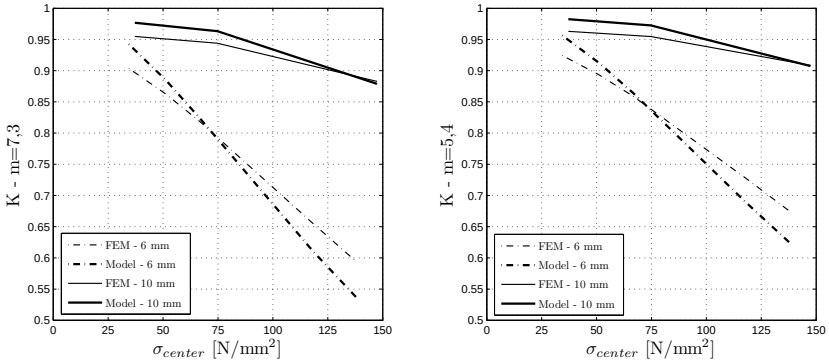

Figure B.7: Correlation between the correction coefficient K and σ_{center} for a plate in the CDR configuration ($R_1 = 75$ mm, $R_2/R_1 = 2$, $R_3/R_1 = \frac{8}{3}$). Comparisons of results from FEM and from the proposed analytic model. Cases $h = 6$ mm, $h = 10$ mm, $m = 5.4$ and $m = 7.3$.

Finally, an estimate of the coefficient K for a square plate of side $l = 2R_3$ under CDR loading has been made by using again the analytic expression (B.30). In this case, the coefficients B_0 and C_1 result from the stress at the center of the plate σ_{center} calculated from a numerical simulation, referred to the case of square plate. As it is evident from Figure B.8, and even more so from the comparison with Figure B.7, results of the analytic and numerical evaluation of the coefficient K are in excellent agreement, confirming again that the contribution to bending of the overhanging parts comprised between the external ring and the perimeter of the specimen is negligible.

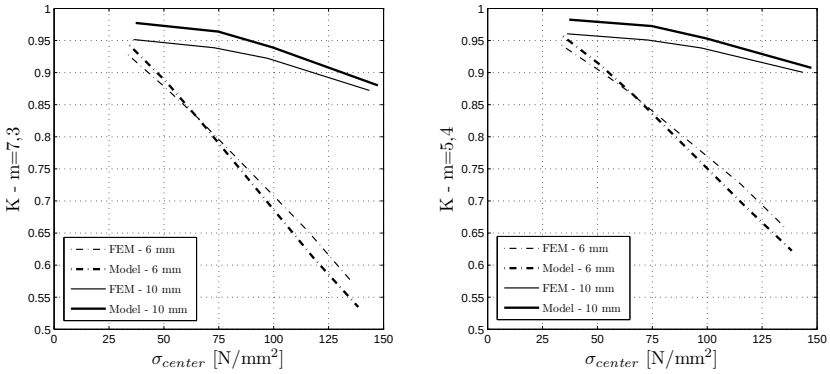

Figure B.8: Values of K as a function of σ_{center}. Comparison between results either from the analytic model for a circular specimen under the CDR configuration ($R_1 = 75\,mm$, $R_2/R_1 = 2$, $R_3/R_1 = \frac{8}{3}$), or from a FEM analysis for a square specimen (side $l = 2R_3$). Cases $h = 6$ mm, $h = 10$ mm, $m = 5.4$ and $m = 7.3$.

Three different geometries have been analyzed in order to verify the ability of the analytic solutions to interpret the mechanical response of plates under the CDR configuration:

Case I: $R_1 = 75$ mm, $R_2 = 150$ mm, $R_3 = 200$ mm,

Case II: $R_1 = 75$ mm, $R_2 = 125$ mm, $R_3 = 200$ mm,

Case III: $R_1 = 75$ mm, $R_2 = 125$ mm, $R_3 = 175$ mm.

For the three geometries under consideration, the analytic and the numerical evaluations are compared in Figure B.9, which shows the value of K as a function of σ_{center} for $h = 6$ mm and $m = 7.3$.
Recalling that the maximum stress can be either at the center of the specimen or at the inner ring $r = R_1$, according to the condition (B.20) and, hence, depending upon the ratio $\sigma'_{center}/\sigma''_{center}$, the value of such ratio as a function of σ_{center} for the case of a circular plate of radius $R_1 = 75$ mm and thickness $h = 6$ mm, bent by radial couples at the border of Figure B.1(a), is shown in Figure B.10. Assuming $\nu = 0.24$ and comparing the resulting graph with the limit $\frac{1-\nu}{6(3+\nu)}$, it is possible to notice that the maximum stress acts at the center of the specimen for stress values below the expected average strength of annealed float glass, considered of the

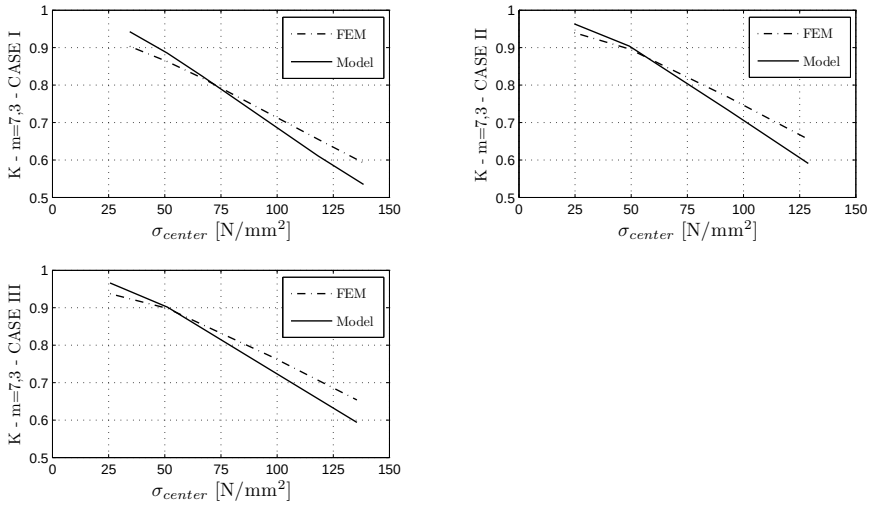

Figure B.9: Value of K as a function of σ_{center}. Comparison between three different geometries. FEM evaluation and analytic estimates from the model. Case $h = 6$ mm and $m = 7.3$.

order of $60 \div 70$ MPa. Obviously, the same conclusion holds for thicker specimens, whereas it may not be true for very thin plates.

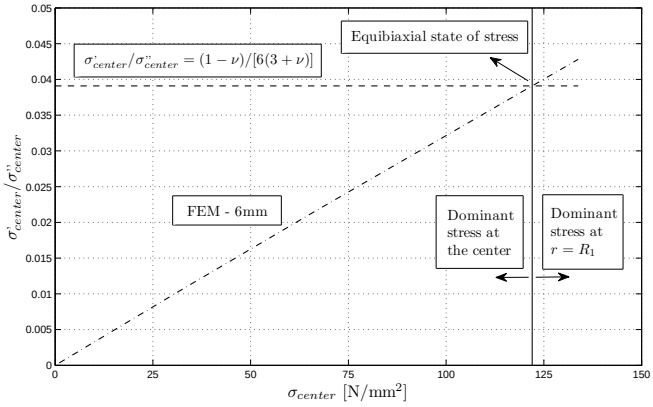

Figure B.10: Value of the ratio $\frac{\sigma'_{center}}{\sigma''_{center}}$ as function of σ_{center} for a circular plate of radius $R_1 = 75$ mm and thickness $h = 6$ mm, bent by radial couples at the border. Comparison with the limit $\frac{1-\nu}{6(3+\nu)}$ for $\nu = 0.24$.

The results of the same analysis for the case of CDR configuration of Figure B.1(a) are shown in Figure B.11 for the three aforementioned geometries. Two different thicknesses, i.e., $h = 6$ mm and $h = 10$ mm, are considered. For $h = 6$ mm, the stress below the ring R_1 overcomes the stress at the center already for values of

the order of $25 - 30$ MPa, whereas the transition stress is of the order of $70 - 80$ MPa for $h = 10$ mm.

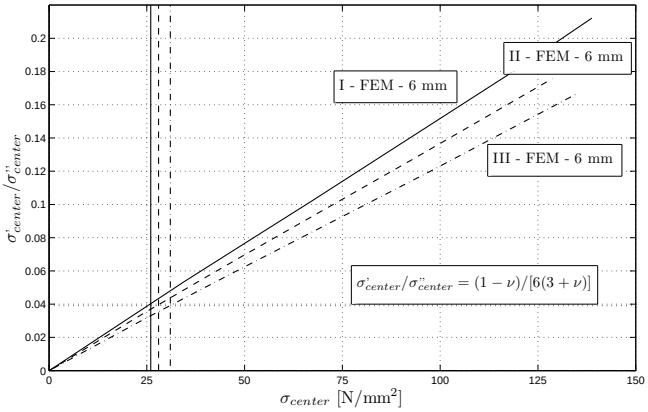

Figure B.11: Value of the ratio $\frac{\sigma'_{center}}{\sigma''_{center}}$ as function of σ_{center} for a circular plate in the CDR configurations. Case $h = 6$ mm, $\nu = 0.24$ and three different geometries. Comparison with the limit $\frac{1-\nu}{6(3+\nu)}$ for $\nu = 0.24$.

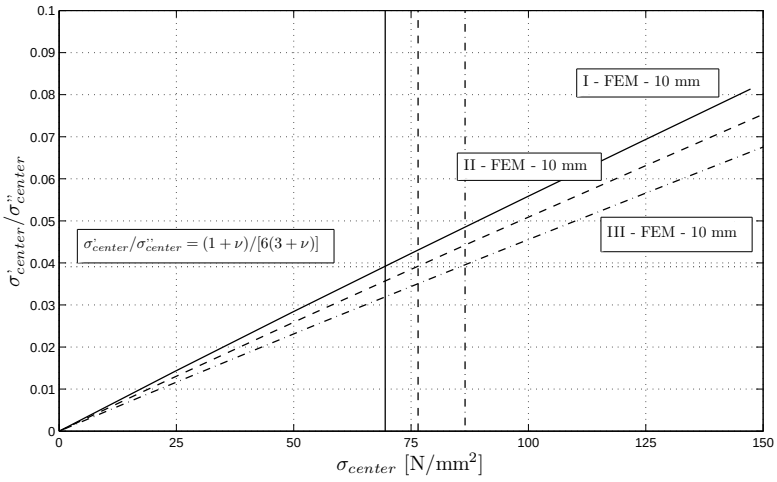

Figure B.12: Value of the ratio $\frac{\sigma'_{center}}{\sigma''_{center}}$ as function of σ_{center} for a circular plate in the CDR configurations. Case $h = 10$ mm, $\nu = 0.24$ and three different geometries. Comparison with the limit $\frac{1-\nu}{6(3+\nu)}$ for $\nu = 0.24$.

Table B.1 records a more precise comparison between the numerical (FEM) and analytic (MOD) models for the estimate of the location of the maximum stress, in the three geometries at hand and for $\nu = 0.24$. According to the analytic

model, the maximum stress σ_{max} should be at the center C when the quantity $\frac{\sigma'_{center}}{\sigma''_{center}} \frac{6(3+\nu)}{1-\nu}$ is less than the unity, otherwise at the ring R_1. The proposed model is in agreement with the numerical simulations, except that in just two cases, which however correspond to borderline cases, for which a practical distinction is arduous to make and the state of stress is almost equibiaxial.

Table B.1: Comparison between numerical (FEM) and analytic (MOD) estimates for the location of the dominant stress (at center C or at ring R_1).

Case	h [mm]	F $[N]$	$\sigma_{max,FEM}$ $[N/mm^2]$	$\sigma_{max,FEM}$ location C/R_1	$\frac{\sigma'_{center}}{\sigma''_{center}} \frac{6(3+\nu)}{1-\nu}$ FEM	$\sigma_{max,MOD}$ $[N/mm^2]$	$\sigma_{max,MOD}$ location C/R_1
I	6	2500	34.45	R_1	1.37	34.48	R_1
I	6	3750	51.62	R_1	2.00	51.69	R_1
I	6	5000	68.33	R_1	2.60	68.47	R_1
I	6	10000	128.22	R_1	4.60	129.59	R_1
I	6	12500	154.56	R_1	5.43	156.72	R_1
II	6	2500	24.7	C	0.90	24.7	C
II	6	5000	49.49	R_1	1.75	49.68	R_1
II	6	10000	96.48	R_1	3.25	97.88	R_1
II	6	15000	138.74	R_1	4.50	142.24	R_1
III	6	2500	25.66	C	0.83	25.66	C
III	6	5000	51.48	R_1	1.64	51.67	R_1
III	6	10000	100.91	R_1	3.07	102.43	R_1
III	6	15000	145.76	R_1	4.28	149.64	R_1
I	10	5000	24.66	C	0.36	24.66	C
I	10	10000	49.68	C	0.72	49.68	C
I	10	15000	74.73	C	1.08	74.76	R_1
I	10	20000	99.76	R_1	1.42	99.92	R_1
I	10	25000	124.6	R_1	1.76	124.93	R_1
I	10	30000	149	R_1	2.08	149.65	R_1
II	10	5000	17.55	C	0.24	17.55	C
II	10	15000	52.23	C	0.70	52.23	C
II	10	25000	89.04	R_1	1.16	89.13	R_1
II	10	35000	124.8	R_1	1.63	126.75	R_1
II	10	45000	160.1	R_1	2.03	160.85	R_1
III	10	5000	18.24	C	0.22	18.24	C
III	10	15000	55.3	C	0.65	55.3	C
III	10	25000	92.53	C	1.08	92.58	R_1
III	10	35000	129.7	R_1	1.49	130.1	R_1
III	10	45000	166.6	R_1	1.89	167.44	R_1

B.2 An overview of the most used standardized testing configurations

Four different types of tests are proposed by the standard EN 1288 [35] in Europe, for characterizing the bending strength of glass plates. The parts EN1288-2 [31] and EN 1288-5 [34] standardize two different Coaxial Double Ring (CDR) configurations, with and without overpressure, respectively. As indicated in the previous section, the linear elastic solution of a coaxial double ring configuration provides an uniform equibiaxial state of stress in the core part of the plate delimited by

the inner ring, but geometric non-linearities, which are the higher the thinner the specimen is with respect to its area, may lead to a deviation from this ideal condition. EN 1288-5 [34] indicates a very small diameter for the inner ring, of the order of a few millimiters, so to obtain just negligible second-order effects. However, the tested area may be considered too small to be representative of practical case, i.e., the resulting failure stress values could be too much higher and not reliable for structural applications. This is because the smaller the loaded area is, the lower is the probability of finding a crack in critical conditions.

On the other hand, the standard EN 1288-2 [31] indicates to test large square plates of area $A = 1\ m^2$. It prescribes an overpressure to act simultaneously with the loading ring, so to compensate for the effects of the geometric non-linearity and, hence, to generate an almost equibiaxial state of stress in the area delimited by the inner ring. This is certainly the most sophisticated type of test, and has been for long time considered the best for characterizing glass strength, even though just a few laboratories are able to perform it, because special equipment is needed.

The classical four point bending (4PB) tests are standardized for glass by the parts EN 1288-3 [32] and EN 1288-4 [33]. However, in this configuration the plate edges, where the defectiveness is different from the core because of the additional defects induced by the cutting process, is subject to the maximum tensile stresses. The characterization of the edge strength for glass needs a proper analysis, which however is not considered here. In any case, if one looks for the mechanical characterization of structural elements made of glass that are not stressed at the edges, the additional source of uncertainty due to the cutting process should be avoided. This means that the 4PB configuration is not suitable for pursuing this goal.

With the aim of limiting the deflection, so as to achieve an equibiaxial stress state far from the borders, the standard ASTM C1499-09 [6], originally conceived for advanced ceramics, prescribes a Coaxial Double Ring test configuration with variable geometry, according to the plate thickness. The higher is the plate thickness, the larger are the rings and the specimen.

Let me focus on the tests proposed by the European Norm EN 1288-2 [31] and the American standard ASTM C1499 [6]. According to the EN 1288-2 [31] standard, the correlation shown in Figure B.13 between the overpressure p^* and the load F^* applied by the tensometer must be met during the whole test. However, since the control system of the overpressure is available in just a few research institutes, this test is rarely used.

The specimens to be tested consist of large square plates of side $l = 1000$ mm, supported on a ring of radius $R_2 = 400$ mm and loaded through another ring coaxial to the supporting one of radius $R_1 = 300$ mm. Despite of complexity and the difficulty for performing the proposed test, numerical analyses have shown that, by following the curve of Figure B.13, the stress state sensibly deviates from the equibiaxiality condition. The plot of the correction coefficient K for the effective area, given by equation (B.22), as a function of the stress acting at the center of the plate σ_{center} is recorded in Figure B.14. Recall that the underlying assumption of equation (B.22) for the effective area is that strength variability follows a 2-parameter Weibull distribution. The dots indicate the values of K corresponding to the configuration *with overpressure*, following the graph of Figure B.13 by EN 1288-2, whereas the lines represent the case *without overpressure*, calculated *via*

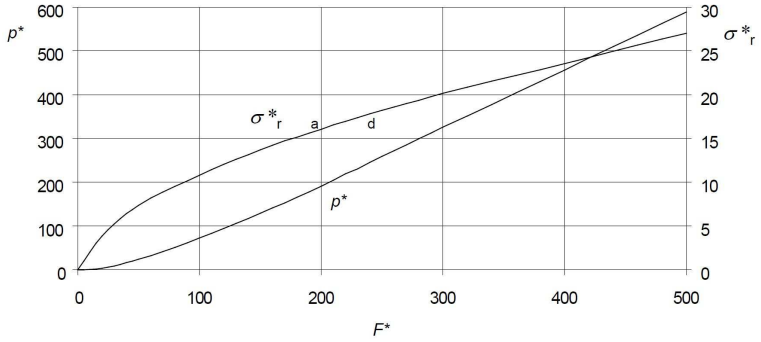

Figure B.13: Relationship between the induced radial tensile stress σ_r^*, the nominal gas pressure p^* and the piston force F^*, in a non-dimensional representation as recorded in EN 1288-2 standard.

FEM analysis. The thickness ($h = 6, 8, 10, 12$ mm) and the Weibull exponent ($m = 5.4$ and $m = 7.3$) are used as parameters of comparison. As it is evident from Figure B.14, the value of the coefficient K increases with the overpressure, but it remains quite far from the unity, corresponding to the ideal condition of uniform equibiaxial stress state. The thinner the plate is, the higher is the distance from equibiaxiality. This means that non linear effects are noteworthy for so large specimens, and the overpressure is not able to totally compensate them, i.e., the stress state is different from the desired one [71].

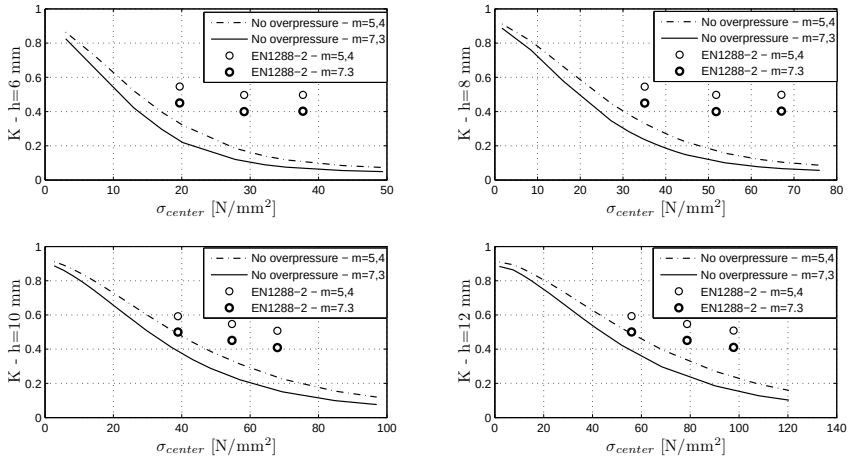

Figure B.14: Values of the correction coefficient K for the effective area as function of σ_{center}, deduced from a FEM analysis, for the same geometry of EN 1288-2 [31] but with no overpressure. Comparison with the values obtained with the overpressure prescribed by EN1288-2. Different values of thickness and Weibull exponent.

In conclusion, the proposed procedure may be considered unnecessarily complicated, especially because its results could be misleading if one assumes that they

correspond to the case $K = 1$.
A method for the correct interpretation of the experimental data is here proposed. The relationship proposed in [31] between the maximum tensile stress σ_r^* and the piston force F^* applied by the tensometer, shown in Figure B.13, is not accurate. The graph juxtaposed in Figure B.15 has been obtained *via* FEM analysis, correlating F^* with the real maximum radial tensile stress σ_{max}, when the history of the applied overpressure coincides with that prescribed by Figure B.13. Thus, one can correct the failure stress values obtained following the indications of the standard EN 1288-2 [31] by deriving the value of F^* associated with the failure stress σ_r^* and, from this, obtain the actual value σ_{max}.

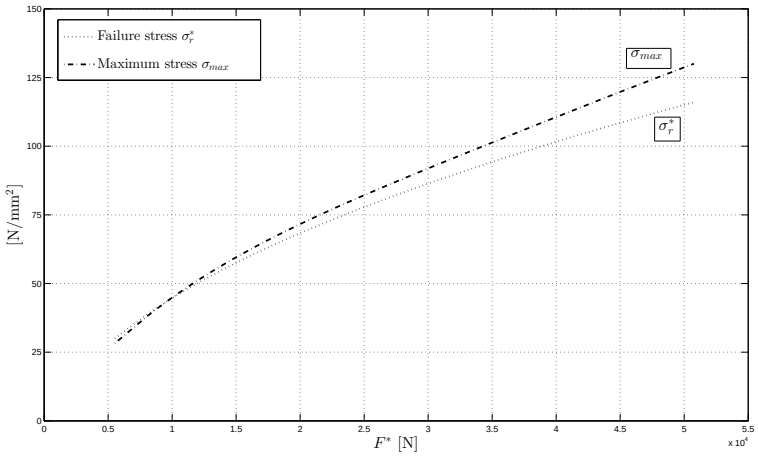

Figure B.15: Correlation between the piston force F^* and i) the radial stress σ_r^* at the specimen center indicated by [31] and ii) the maximum stress σ_{max} calculated with FEM analyses.

Conventional four-nodes shell elements with reduced integration have been used to model the loaded specimen. In particular, the surface bounded by the inner ring has been divided into 30 10-mm-thick annulus areas and 6600 shell elements have been distributed symmetrically with respect to the plate center. For several values of the force F^* applied by the tensometer, non-linear simulations have been performed, so to obtain the coefficient $W_{2,i}$, calculated from (A.27), for each i-th finite element of area ΔA_i. By approximating the integral of (B.22) with the Riemann sum, the *effective area* correction coefficient has been calculated through the expression

$$K = . \frac{\sum_{i=1}^{N} \left(W_{2,i}\sigma_{1,i}\right)^m \Delta A_i}{A\left(\sigma_{max}\right)^m}, \tag{B.32}$$

where N is the total number of finite elements. The so-obtained values for K as a function of the maximum tensile stress σ_{max} are shown in Figure B.16.
Hence, it is confirmed that the state of stress is not equibiaxial because, if this was the case, one should have found $K \simeq 1$. However, the failure stress values can

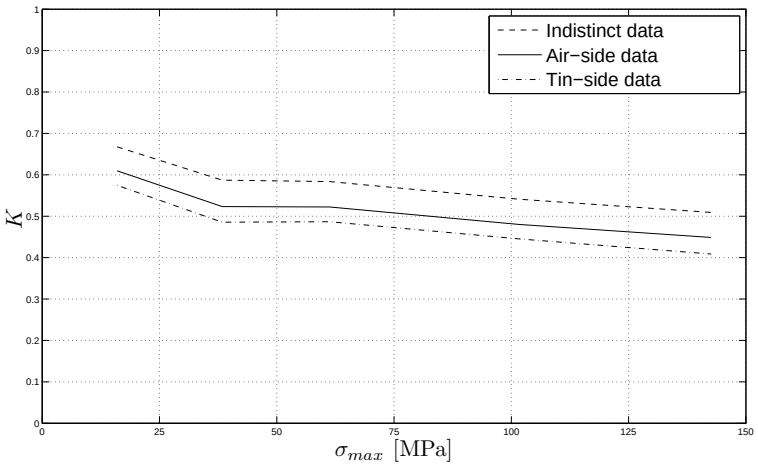

Figure B.16: Relationship between the maximum stress σ_{max} and the *effective area* correction coefficient K for the CDR configuration with overpressure [31].

be rescaled towards the condition of equibiaxial stress state through the rescaling law (A.13) [71].

Concerning the test according to the standard ASTM C1499 [6], no overpressure is required, but the geometry is variable in order to limit deflections and thus mitigate the geometric nonlinear effects [81]. The aim is again to obtain an almost uniform equibiaxial stress state in the part of the specimen delimited by the inner ring. The side of the square specimen and the radii of the support rings varies with the plate thickness. Furthermore, ASTM C1499 [6] proposes an equivalence between the response of the square specimen and the response of an effective circular plate, whose external radius R_3 has been calibrated *via* FEM analysis from a criterion of equal maximum stress. The ratio between the diameters of the supporting and loading rings must be inside the interval $[0.2, 0.5]$. In particular, for materials with a low elastic modulus, a low value of this ratio ($\simeq 0,2$) should be chosen and *vice-versa*. The cross-section of the rings is specifically indicated from the standard so to mitigate the contact stresses, and a limit for the maximum thickness of the tested plate is imposed, since the contact stress could lead to undesirable failure for very thick specimens [76]. Furthermore, limits are proposed even for the overhang. In particular, if this is too large, the state of stress can considerably vary from equibiaxiality [76], whereas if it is too small, a premature spall may lead from the contact with the ring. Moreover, a function for the effective size of the specimen is proposed in an appendix of the standard, which is based upon the theoretical analysis of a thick-plate, by considering shear effects between the load and the support rings and the effects of friction at the contacts [43]. Remarkably, the standard ASTM C1499-09 introduces the notion of "effective volume", besides that of "effective area", since the "volume-flaw hypothesis" is made in the theoretical derivations, i.e. fracture occurrence can take place in any point of the specimen and not only on the tensile surface. Both the effective area

and the effective volume are evaluated by assuming an uniform equibiaxial stress state inside the inner ring and without neglecting the part of specimen delimited by the outer radius, in which the stress state is linearly decreasing. Thus, the ASTM standard proposes a well refined analysis for the CDR test, but varying the test configuration according to the plate thickness could be considered not practical and requires a further investigations about possible size effects. Moreover, for thin plates the suggested diameter of the loading rings are very small, by causing similar problems to the ones already mentioned for the EN 1288-5 [34] set-up.

B.3 A proposal for a new CDR test

In the recent Italian code for the structural use of glass [23], a Coaxial Double Ring test configuration has been proposed without overpressure, according to the configuration shown in Figure B.17. The test specimen is a square plate of side length $l = 400$ mm, loaded by rings $R_1 = 75$ mm and $R_2 = 150$ mm. According to the study recorded in [97], the area delimited by the inner ring, wider than 100 mm^2, is large enough to incorporate enough cracks of significant size. A square shape of the specimen is proposed because it is easier to cut and, consequently, cheaper than the circular one. Moreover, it has been shown in Section B.1.1 that there is not a substantial difference in terms of stress, since the effect of the four overhanging pieces on the bending response of the plate is almost negligible. The chosen geometry represents a compromise between reducing second order effects and achieving a representative tested area, avoiding stress concentrations at the rings.

Recall that the only geometries associated with an *almost* equibiaxial stress state inside the central ring, would correspond to a very small-scale specimen, so to limit the effects of geometric non-linearities. Furthermore, the condition $l/2 \simeq R_2 \simeq R_1$ should be met, so as to render the loading configuration similar to the one referring to circular plates under couples uniformly distributed along the border of Figure B.1(a). However, such configuration cannot be achieved without producing undesired stress concentrations. Therefore, the idea is to accept a state of stress that does not have to be equibiaxial, and to re-arrange the measured data taking into account the correction coefficient K for the effective area, which can be analytically evaluated when the deviation from the equibiaxiality is mild [71]. In fact, if such deviation is large, the hypothesis underlying equation (B.24) is no more valid. The test results are hence rescaled towards the ideal reference configuration of equibiaxial stress state acting on a unitary area [44].

The determination of the bending strength of glass plates consists of a few simple steps. The force applied by the tensometer at the collapse F of the specimen is the only required datum to be measured. Then, the membrane and bending stresses at the specimen center, respectively σ'_{center} and σ''_{center}, must be calculated through a simple FEM simulation and, from these values, the coefficient B_0 and C_1 are given by equations (B.15). Figure B.18 summarizes the values reached by B_0 and C_1 for a wide range of loads for the most common commercial thicknesses. It allows to directly evaluate B_0 and C_1 as a function of the force F for the various thicknesses, without the need of a FEM model.

Then, using the coefficients indicated in (B.16), (B.26), (B.29), the value of $K(\sigma_{max})^m$ is calculated as *per* (B.30). Notice that B_0 and C_1 are independent of the Weibull

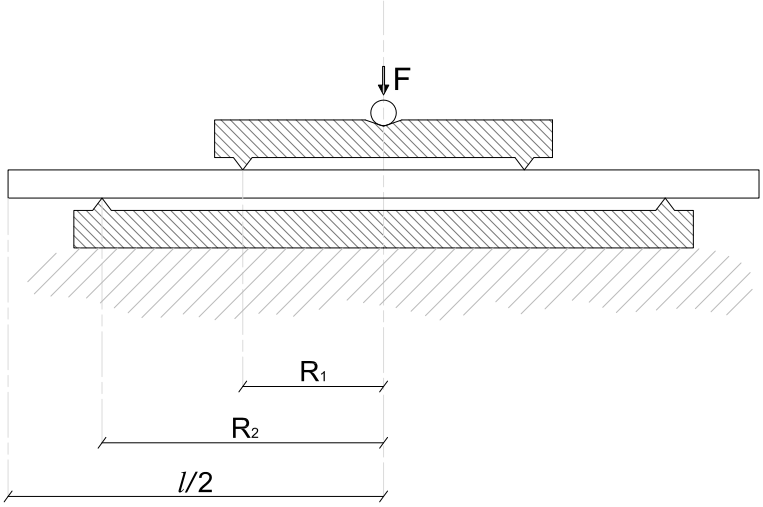

Figure B.17: Proposed CDR test configuration with no overpressure ($l = 400$ mm, $R_1 = 75$ mm and $R_2 = 150$ mm).

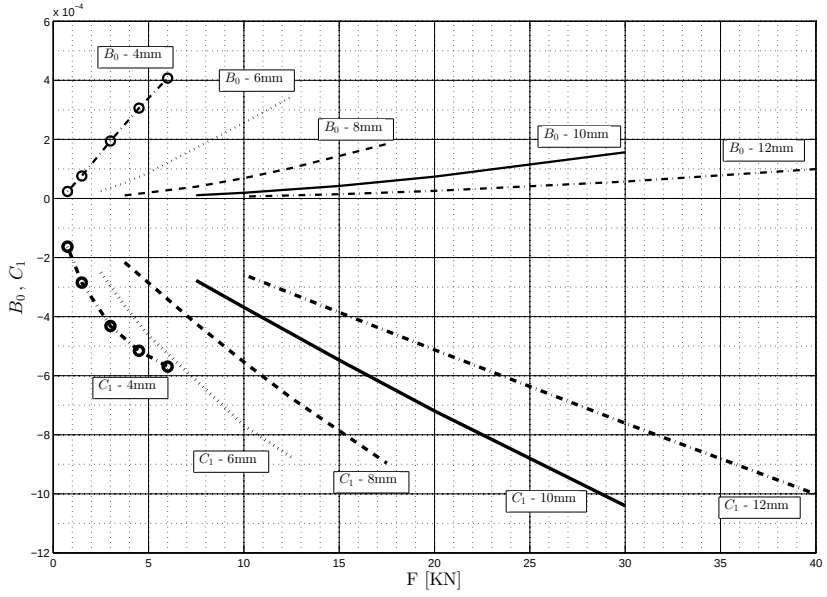

Figure B.18: Proposed CDR configuration. Values of B_0 and C_1 as a function of the piston force F, for different values of the plate thickness.

modulus m, whereas this appears in the analytic expression for $K(\sigma_{max})^m$. The rough data from the tests should be interpolated to derive the best-fit Weibull coefficient m. Once m has been determined, the values of $K(\sigma_{max})^m$ can be calculated.
Observe that, in this way, only the central area delimited by the inner radius is considered, although the stress state in the area between the two rings is such that the probability of collapse is small but not null. Thus, only the failure stress values referred to specimens which collapse in their core parts are considered valid. Finally, the valid test data must be re-scaled towards the reference conditions, according to a rescaling law given by expressions (B.31), which reads

$$\sigma_{eqb,UA} = \left(K(\sigma_{max})^m \frac{A}{A_0} \right)^{1/m} . \tag{B.33}$$

The re-scaled data can be used as the data associated with the reference configuration, in order to define the characteristic value of glass strength. The proposed testing configuration was used to characterize the strength of 50 annealed and 50 toughened glass plates of thickness 8 mm. A detailed description of the experimental campaign and of its results is recorded in Section 4.3.1.
Observe that the underlying hypothesis of equation (B.33) is that the 2-parameter Weibull model is accurate for the statistical interpretation of glass strength variability. If this is not the case, one may use the re-scaling laws introduced in Appendix A for the various generalized Weibull models, even tough such laws lead to expression much more complicated than equation (B.33).

APPENDIX **C**

PROBABILISTIC MODELS FOR WIND LOADS AND SNOW LOADS

In the design practice, pressure induced through wind action is assumed to be uniformly distributed. Various probabilistic models can be found in the technical literature for wind pressure. Reference is made here to that recorded in the Eurocode EN1991-1-4 [39], according to which the reference wind velocity corresponding to a return period T_R is

$$v_b(T_R) \,=\, \alpha_R v_{b,50}\,, \quad \alpha_R \,=\, 0.75\sqrt{1-0.2\;\ln\left[-\ln\left(1-\frac{1}{T_R}\right)\right]}\,, \qquad \text{(C.1)}$$

where $v_{b,50}$ is the characteristic wind velocity at 10 m above ground averaged over 10 minutes, determined for field exposure category II and for a return period of 50 years. The probability that the maximum averaged wind velocity over 10 minutes v_b is not exceeded in one year (cumulative probability function) is obtained from expression (C.1) and reads

$$F(v_b) \,=\, \exp\left[-\exp\left(\frac{1}{0.2}-\frac{v_b^2}{0.2\;0.75^2\;v_{b,50}^2}\right)\right]\,. \qquad \text{(C.2)}$$

The *peak* pressures, corresponding to the averages over time $t = 10$ min and $t = 3$ sec, are introduced by the EN1991-1-4 [39] in the form

$$p_{w,10min} \,=\, \frac{1}{2}\,\rho_{air}\,v_b^2\,c_{e1}(z)\,c_p\,c_d, \qquad p_{w,3s} \,=\, \frac{1}{2}\,\rho_{air}\,v_b^2\,c_e(z)\,c_p\,c_d\,, \qquad \text{(C.3)}$$

where $\rho_{air} \,=\, 1.25$ Kg/m^3 is the air density, z represents the height above ground, c_d is the dynamic factor, c_p is the pressure coefficient. The terms $c_{e1}(z)$ and $c_e(z)$ denote the exposure factors, through which the distinction between the peak pressures corresponding to the averaged time $t = 10$ min or $t = 3$ s is marked, and

read

$$c_{e1}(z) = \left[\ln\left(\frac{z}{z_0}\right)\right]^2 k_r^2\, c_t^2 \quad \text{with } z = z_{min} \text{ for } z \le z_{min},$$
$$c_e(z) = k_r^2\, c_t(z)\, \ln\left(\frac{z}{z_0}\right)\left[\ln\left(\frac{z}{z_0}\right) c_t(z) + 7\right] \quad \text{with } z = z_{min} \text{ for } z \le z_{min}, \tag{C.4}$$

where k_r is a coefficient that depends upon the field exposure category and $c_t(z)$ is the orographic coefficient, while z_0 and z_{min} represent reference heights. Finally, the cumulative distribution function for the peak pressure $F(p_{w,t})$ can be written in the form

$$F(p_{w,t}) = \exp\left[-\exp\left(\frac{1}{0.2} - \frac{2\,p_{w,t}}{\rho_{air}\, c_{e,t}\, c_p\, c_d\, 0.2\, 0.75^2\, v_{b,50}^2}\right)\right], \tag{C.5}$$

with $c_{e,t} = c_e$ when t=3 s and $c_{e,t} = c_{e1}$ when t=10 min.
For what concerns snow actions, one can refer to the case of the snow deposit on a roof, which can be considered un-drifted for uniform flat surfaces. For a return period of n years, the standard EN 1991-1-3 [38] provides the expression for the snow load (q_{sn}), which reads

$$q_{sn} = q_{sk}\left[\frac{1 - V\sqrt{6}/\pi[\ln(-\ln(P_n)) + 0.57722]}{1 + 2.5923\,V}\right], \tag{C.6}$$

where P_n is the annual probability of exceedance, q_{sk} represents the characteristic snow load value on the ground for a 50 year return period and V is the variation coefficient of the series of maximum annual snow loads, which varies from 0.2 to 0.6 according to the Eurocode. The value for q_{sk} are recorded in the EN 1991-1-3 [38] as a function of the climate zone and the altitude above sea level. The annual probability of non-exceedance, i.e., the cumulative distribution function of the *ground snow loads* for a reference period of 1 years, is obtained form equation (C.6) and reads

$$F_{qsn}(x) = \exp\left\{-\exp\left[\left(1 - \frac{x}{q_{sk}}(1 + 2.5923\,V)\right)\frac{\pi}{V\sqrt{6}} - 0.57722\right]\right\}. \tag{C.7}$$

The expression for the snow load on the roof provided by the regulations reads

$$q_s = \mu_i q_{sk} C_E C_t\,, \tag{C.8}$$

where C_E is the exposure coefficient, C_t the thermal coefficient and μ_i is the roof shape coefficient. Finally, from equations (C.8) and (C.7), the cumulative

distribution function of *undrifted snow loads on roofs* is obtained of the form

$$F_{qs}(x) = \exp\left[-\exp\left[\left(1 - \frac{x}{q_{sk}\mu_i C_E C_t}(1 + 2.5923\,V)\right)\frac{\pi}{V\sqrt{6}} - 0.57722\right]\right]. \tag{C.9}$$

The values of the various coefficients are not recorded here, but they can be found in the EN 1991-1-3 [38].

APPENDIX **D**

THE NORMAL AND THE LOG-NORMAL DISTRIBUTIONS

The Normal statistical distribution is present in a considerable number of applications and, hence, it is perhaps the most popular. A Log-Normal distribution is a continuous probability distribution of a variable whose logarithm is normally distributed. The density function of a Normal (or Gauss) stochastic variable is characterized by the mean value μ and the variance υ^2; it is defined on the whole real axis and reads

$$f(x) = \frac{1}{\sqrt{2\pi\upsilon^2}} \exp\left[-\frac{1}{2}\frac{(x-\mu)^2}{\upsilon^2}\right], \quad -\infty < x < +\infty, \tag{D.1}$$

where μ can assume any value, while υ^2 is non-negative. The Normal density function has the well-known bell shape, it is symmetrical with respect to the mean value ($x = \mu$) and it has two flex points equidistant from $x = \mu$ in correspondence of the abscissas $x = \mu \pm \upsilon$. Variations in the mean value μ cause translations of the density function, while the higher the value of the standard deviation υ^2 is, the higher is the dispersion of data. The ratio between the standard deviation υ and the mean value μ is referred to as *coefficient of variation* (CV), which is a non-dimensional measure of the dispersion of the distribution.

According to the Method of Moments, the absolute moments of the distribution coincide with the respective sample moments. Since the statistic moments are particular mean values of a stochastic variable, it is assumed that the estimator of μ is the sample mean and the estimator of υ^2 is the second order relative sample moment $\left(\upsilon^2 = 1/N \sum_{i=1}^{N} (x_1 - \mu)^2\right)$ where N is the sample dimension and i is the i-th datum. These estimators are considered the most efficient to derive the two parameters of the Normal Distribution. Indeed, they are the same that one can find by using the Maximum Likelihood Estimation (MLE) method. The likelihood of a set of data is the probability of obtaining that particular set of data, given the chosen probability distribution model. The value of those parameters that maximize the sample likelihood are known as the Maximum Likelihood Estimates.

A random variable x is standardized by subtracting the mean of the distribution from the value being standardized, and then dividing this difference by the standard deviation of the distribution, i.e.,

$$Z = \frac{x - \mu}{\upsilon}. \tag{D.2}$$

Once standardized, a normally distributed random variable has $\mu = 0$ and $\upsilon = 1$. The *normal probability plot* is a graphical technique for assessing whether or not experimental data are normally distributed, representing the most simple way to identify departures from normality. According to this technique, experimental data are organized in ascending order and an experimental probability of failure is assigned to each i-th datum through an estimator. In the current dissertation, the first estimator introduced in (A.14) is used, i.e., $P_i = i/(N + 1)$, where N is the sample size. Then, from the experimental probability of failure, the expected values of the standardized variable Z are obtained. Finally, data arranged in ascending order are plotted against the expected values for the standardized variable Z ($\mu = 0$, $\upsilon^2 = 1$) in such a way that the points should approximately form a straight line.

APPENDIX **E**

RESULTS OF THE MEASUREMENT AND EXPERIMENTAL CAMPAIGNS PERFORMED AT THE TECHNICAL UNIVERSITY OF DARMSTADT

Table E.1: Annealed glass (ANN) specimens. Measured thicknesses (measurements taken along the four sides of the plates and mean value h_m). Residual stresses measured along two orthogonal directions at the center of the plates and mean values $\sigma_{pc,m}$.

Specimen	Measurements					Measurements		
	h_1 [mm]	h_2 [mm]	h_3 [mm]	h_4 [mm]	$\mathbf{h_m}$ **[mm]**	$\sigma_{pc,I}$ [MPa]	$\sigma_{pc,II}$ [MPa]	$\sigma_{\mathbf{pc,m}}$ **[MPa]**
ANN-1a	7.884	7.913	7.890	7.861	**7.887**	4.4	4.6	**4.50**
ANN-2a	7.858	7.858	7.861	7.823	**7.850**	5.1	3.9	**4.50**
ANN-3a	7.801	7.799	7.818	7.808	**7.806**	4.6	4.0	**4.30**
ANN-4a	7.810	7.852	7.823	7.803	**7.822**	5.1	4.7	**4.90**
ANN-5a	7.877	7.977	7.971	7.983	**7.952**	5	3.9	**4.45**
ANN-6a	7.981	7.865	7.967	7.975	**7.847**	5	4.6	**4.80**
ANN-7a	7.873	7.902	7.878	7.853	**7.876**	4.0	4.0	**4.0**
ANN-8a	7.934	7.902	7.925	7.967	**7.932**	4.3	4.2	**4.25**
ANN-9a	7.891	7.858	7.876	7.905	**7.882**	4.7	4.1	**4.40**
ANN-10a	7.886	7.926	7.904	7.876	**7.898**	4.6	4.4	**4.50**
ANN-11a	7.906	7.895	7.860	7.876	**7.884**	4.9	4.7	**4.80**
ANN-12a	7.867	7.829	7.866	7.869	**7.858**	4.6	4.5	**4.55**
ANN-13a	7.814	7.809	7.808	7.825	**7.814**	4.8	4.6	**4.70**
ANN-14a	7.935	7.907	7.926	7.970	**7.934**	5.4	5.4	**5.40**
ANN-15a	7.855	7.873	7.903	7.879	**7.877**	5.1	4.3	**4.70**
ANN-16a	7.855	7.823	7.805	7.817	**7.825**	4.9	4.2	**4.55**
ANN-17a	7.803	7.804	7.821	7.808	**7.809**	4.9	4.3	**4.60**
ANN-18a	7.826	7.849	7.863	7.862	**7.850**	4.7	4.5	**4.60**

ANN-19a	7.870	7.976	7.971	7.977	**7.948**	4.9	4.7	**4.80**
ANN-20a	7.861	7.877	7.912	7.894	**7.886**	4.7	4.3	**4.50**
ANN-21a	7.870	7.866	7.833	7.866	**7.859**	5.3	4.0	**4.65**
ANN-22a	7.892	7.856	7.879	7.904	**7.883**	5.0	4.2	**4.60**
ANN-23a	7.908	7.877	7.857	7.874	**7.879**	5.3	4.6	**4.95**
ANN-24a	7.888	7.857	7.882	7.906	**7.883**	5.1	4.1	**4.60**
ANN-25a	7.957	7.976	7.978	7.877	**7.947**	5.0	4.5	**4.75**
ANN-26a	7.985	7.882	7.970	7.978	**7.954**	5.1	4.3	**4.70**
ANN-27a	7.950	7.908	7.932	7.969	**7.940**	5.2	4.8	**5.00**
ANN-28a	7.830	7.866	7.870	7.869	**7.859**	4.4	4.2	**4.30**
ANN-29a	7.970	7.976	7.881	7.976	**7.951**	4.9	3.9	**4.40**
ANN-30a	7.867	7.830	7.868	7.871	**7.859**	4.9	4.0	**4.45**
ANN-31a	7.975	7.984	7.878	7.973	**7.952**	5.1	4.2	**4.65**
ANN-32a	7.964	7.975	7.892	7.873	**7.926**	5.1	4.1	**4.60**
ANN-33a	7.813	7.805	7.805	7.824	**7.812**	4.7	3.9	**4.30**
ANN-34a	7.864	7.869	7.827	7.855	**7.854**	4.7	4.4	**4.55**
ANN-35a	7.899	7.868	7.883	7.919	**7.892**	4.7	4.2	**4.45**
ANN-36a	7.932	7.910	7.932	7.970	**7.936**	5.1	4.2	**4.65**
ANN-37a	7.907	7.925	7.972	7.943	**7.937**	5.4	4.5	**4.95**
ANN-38a	7.911	7.923	7.971	7.944	**7.937**	5.0	4.2	**4.60**
ANN-39a	7.868	7.868	7.864	7.825	**7.856**	4.9	4.0	**4.45**
ANN-40a	7.901	7.868	7.876	7.919	**7.891**	5.3	4.8	**5.05**
ANN-41a	7.972	7.984	7.881	7.966	**7.951**	5.0	4.5	**4.75**
ANN-42a	7.972	7.944	7.905	7.922	**7.936**	5.0	4.3	**4.65**
ANN-43a	7.873	7.904	7.888	7.857	**7.880**	4.8	4.0	**4.40**
ANN-44a	7.826	7.804	7.814	7.853	**7.824**	4.5	4.4	**4.45**
ANN-45a	7.864	7.870	7.868	7.830	**7.858**	4.7	4.2	**4.45**
ANN-46a	7.868	7.950	7.972	7.979	**7.942**	5.1	4.1	**4.60**
ANN-47a	7.933	7.971	7.943	7.906	**7.938**	4.8	4.4	**4.60**
ANN-48a	7.854	7.871	7.905	7.884	**7.878**	4.7	4.5	**4.60**
ANN-49a	7.805	7.814	7.847	7.822	**7.822**	5.0	4.2	**4.60**
ANN-50a	7.804	7.804	7.824	7.813	**7.811**	4.6	4.4	**4.50**

Table E.2: Annealed glass (ANN) specimens. Test results: maximum displacement ζ_{max}; fracture load F; time to failure t_f; maximum stress at failure σ_{fail}; equivalent uniform stress that leads to failure in 60 s σ_{60}.

Specimen	Test outputs			Fracture Location	Results	
	ζ_{max} [mm]	F [N]	t_f [s]	Valid/Not Valid	σ_{fail} [MPa]	$\sigma_{\mathbf{60}}$ **[MPa]**
ANN-1a	2.48	15278.02	58.94	Valid	117.30	**98.15**
ANN-2a	2.29	13812.68	53.77	Valid	107.40	**89.35**
ANN-3a	2.79	16961.56	64.17	Valid	131.70	**111.07**

ANN-4a	1.94	9817.42	37.59	Not valid		
ANN-5a	2.54	15280.20	59.44	Not valid		
ANN-6a	2.95	18030.52	67.97	Not valid		
ANN-7a	3.09	19049.74	72.92	Not valid		
ANN-8a	2.71	16591.21	63.91	Valid	125.50	**105.55**
ANN-9a	1.86	10545.63	40.27	Not valid		
ANN-10a	3.01	19909.49	74.97	Not valid		
ANN-11a	3.27	20613.94	77.53	Not valid		
ANN-12a	2.95	18621.11	70.09	Valid	142.00	**120.11**
ANN-13a	2.14	12424.35	48.56	Valid	97.83	**81.26**
ANN-14a	2.63	16586.37	62.57	Valid	125.40	**105.32**
ANN-15a	2.73	16696.77	63.02	Valid	127.80	**107.21**
ANN-16a	2.34	14544.03	55.07	Valid	113.50	**93.12**
ANN-17a	3.14	19143.59	74.18	Not valid		
ANN-18a	2.75	17634.00	67.30	Valid	135.30	**113.83**
ANN-19a	2.55	15417.64	58.26	Not valid		
ANN-20a	2.03	11828.99	46.25	Valid	91.67	**75.55**
ANN-21a	3.08	17861.89	68.96	Valid	136.60	**114.21**
ANN-22a	3.22	21456.68	80.62	Valid	160.80	**137.21**
ANN-23a	2.40	14633.13	55.33	Valid	112.80	**94.01**
ANN-24a	3.25	20762.01	78.00	Valid	156.00	**132.84**
ANN-25a	2.21	12685.32	48.18	Valid	96.71	**78.39**
ANN-26a	1.83	10447.62	39.91	Valid	79.82	**65.18**
ANN-27a	2.10	12614.92	49.15	Not valid		
ANN-28a	2.46	14831.46	56.22	Valid	115.30	**96.19**
ANN-29a	2.85	17994.73	68.21	Valid	134.80	**114.16**
ANN-30a	2.29	12670.31	48.26	Valid	98.64	**79.91**
ANN-31a	2.80	17377.64	65.88	Valid	130.50	**110.79**
ANN-32a	1.87	9478.15	36.35	Not valid		
ANN-33a	2.38	12063.83	47.94	Valid	95.13	**80.87**
ANN-34a	2.62	15964.62	63.16	Valid	123.20	**103.53**
ANN-35a	2.31	14417.61	55.26	Valid	110.80	**92.34**
ANN-36a	2.82	17496.13	66.01	Valid	131.80	**109.96**
ANN-37a	2.80	16899.30	63.78	Valid	127.50	**107.38**
ANN-38a	2.35	14679.96	56.34	Valid	111.60	**94.57**
ANN-39a	2.19	11561.23	45.89	Valid	90.29	**74.38**
ANN-40a	3.15	19876.93	76.51	Valid	149.70	**127.32**
ANN-41a	2.13	12462.91	47.39	Valid	94.97	**78.58**
ANN-42a	2.83	18517.59	70.31	Valid	138.90	**119.88**
ANN-43a	2.13	11681.23	44.50	Valid	90.67	**74.55**
ANN-44a	2.91	18456.02	69.48	Valid	141.90	**117.51**
ANN-45a	2.29	12598.40	49.98	Valid	98.12	**81.51**
ANN-46a	2.33	13630.74	54.07	Valid	103.80	**86.39**
ANN-47a	2.81	18004.21	67.85	Valid	135.30	**115.43**
ANN-48a	2.75	17511.33	66.50	Valid	133.60	**112.64**
ANN-49a	2.96	18426.45	70.27	Valid	141.70	**119.96**
ANN-50a	1.36	7001.82	28.27	Not valid		

Table E.3: Heat-treated glass (HTG) specimens. Measured thicknesses (measurements taken along the four sides of the plates and mean values h_m).

Specimen	Measurements				
	h_1 [mm]	h_2 [mm]	h_3 [mm]	h_4 [mm]	$\mathbf{h_m}$ **[mm]**
HTG-1b[6]	7.939	7.931	7.940	7.960	**7.942**
HTG-2b	7.965	7.943	7.929	7.936	**7.943**
HTG-3b	7.979	7.967	7.980	7.925	**7.962**
HTG-4b	7.977	7.918	7.980	7.961	**7.959**
HTG-5b	7.923	7.969	7.963	7.980	**7.958**
HTG-6b	7.962	7.973	7.922	7.978	**7.958**
HTG-7b	7.983	7.964	7.981	7.922	**7.962**
HTG-8a	7.839	7.822	7.831	7.876	**7.842**
HTG-9a	7.843	7.814	7.827	7.866	**7.837**
HTG-10a	7.898	7.938	7.911	7.883	**7.907**
HTG-11a	7.899	7.942	7.906	7.888	**7.908**
HTG-12a	7.900	7.940	7.911	7.886	**7.909**
HTG-13a	7.823	7.840	7.823	7.820	**7.826**
HTG-14a	7.883	7.895	7.939	7.914	**7.907**
HTG-15a	7.942	7.986	7.955	7.922	**7.951**
HTG-16a	7.880	7.881	7.844	7.882	**7.871**
HTG-17a	7.842	7.815	7.818	7.823	**7.824**
HTG-18a	7.840	7.827	7.816	7.817	**7.825**
HTG-19a	7.878	7.843	7.877	7.884	**7.870**
HTG-20a	7.873	7.883	7.879	7.842	**7.869**
HTG-21a	7.844	7.821	7.831	7.867	**7.840**
HTG-22a	7.864	7.848	7.825	7.836	**7.843**
HTG-23a	7.861	7.848	7.819	7.830	**7.839**
HTG-24a	7.818	7.843	7.825	7.823	**7.827**
HTG-25a	7.904	7.944	7.928	7.898	**7.918**
HTG-26a	7.897	7.942	7.916	7.885	**7.910**
HTG-27a	7.937	7.988	7.950	7.924	**7.949**
HTG-28a	7.821	7.820	7.841	7.828	**7.827**
HTG-29a	7.845	7.823	7.833	7.866	**7.841**
HTG-30a	7.923	7.943	7.986	7.948	**7.950**
HTG-31a	7.821	7.844	7.828	7.816	**7.827**
HTG-32a	7.823	7.840	7.828	7.821	**7.828**
HTG-33a	7.920	7.941	7.988	7.952	**7.950**
HTG-34a	7.890	7.920	7.902	7.871	**7.895**
HTG-35a	7.889	7.922	7.906	7.869	**7.896**
HTG-36a	7.873	7.833	7.872	7.875	**7.863**

[6]Sample delivered on a different date

HTG-37a	7.885	7.917	7.889	7.866	**7.889**
HTG-38a	7.819	7.828	7.867	7.843	**7.839**
HTG-39a	7.872	7.887	7.919	7.899	**7.894**
HTG-40a	7.839	7.876	7.886	7.878	**7.869**
HTG-41a	7.894	7.942	7.915	7.885	**7.909**
HTG-42a	7.890	7.937	7.914	7.882	**7.905**
HTG-43a	7.990	7.998	7.897	7.982	**7.966**
HTG-44a	7.827	7.863	7.841	7.818	**7.837**
HTG-45a	7.996	7.889	7.979	7.987	**7.962**
HTG-46a	7.923	7.935	7.986	7.955	**7.949**
HTG-47a	7.840	7.822	7.819	7.817	**7.824**
HTG-48a	7.870	7.891	7.922	7.901	**7.896**
HTG-49a	7.846	7.817	7.828	7.864	**7.838**
HTG-50a	7.820	7.817	7.816	7.831	**7.821**
HTG-51a	7.905	7.874	7.890	7.927	**7.899**

Table E.4: Heat-treated glass (HTG) specimens. Residual stresses measured along two orthogonal directions at the center of the plates and at four points on the two diagonals, 100 mm far from the edges.

Specimen	Measurements									
	$\sigma^c_{pc,I}$ [MPa]	$\sigma^c_{pc,II}$ [MPa]	$\sigma^1_{pc,I}$ [MPa]	$\sigma^1_{pc,II}$ [MPa]	$\sigma^2_{pc,I}$ [MPa]	$\sigma^2_{pc,II}$ [MPa]	$\sigma^3_{pc,I}$ [MPa]	$\sigma^3_{pc,II}$ [MPa]	$\sigma^4_{pc,I}$ [MPa]	$\sigma^4_{pc,II}$ [MPa]
HTG-1b	98.6	94.2	102.4	96.7	100.2	96.5	96.4	95.8	99.6	97.0
HTG-2b	95.1	93.7	93.7	93.5	97.4	97.1	97.4	97.1	96.2	95.0
HTG-3b	93.3	92.1	97.2	93.7	96.5	93.2	96.1	92.7	95.6	95.5
HTG-4b	98.9	94.7	99.3	97.7	97.6	96.7	95.9	94.0	98.6	96.5
HTG-5b	95.5	94.1	97.4	95.1	96.2	95.6	96.6	95.3	98.1	96.8
HTG-6b	98.8	93.2	101.4	97.5	97.2	95.0	96.3	92.9	97.8	95.4
HTG-7b	94.0	90.8	93.6	92.5	94.5	92.5	96.0	93.3	97.8	92.7
HTG-8a	100.4	97.6	102.2	102.2	102.6	101.1	104.1	104.0	105.7	104.7
HTG-9a	100.3	96.1	101.0	99.7	97.0	96.4	95.6	95.4	102	100.0
HTG-10a	100.8	97.4	101.1	99.0	99.3	97.1	100.0	97.8	101.2	100.5
HTG-11a	100.4	96.0	103.2	100.6	102.1	100.2	101.0	100.5	102.8	99.4
HTG-12a	102.3	98.9	100.1	99.4	100.9	100.3	102.5	99.0	99.7	98.7
HTG-13a	104.5	103.0	105.8	104.9	103.6	102.4	102.9	102.9	105.2	104.4
HTG-14a	98.4	96.8	101.3	96.7	100.1	96.8	101.5	101.4	101.8	101.3
HTG-15a	102.0	97.7	100.3	100.0	102.8	101.4	99.9	98.3	100.9	97.7
HTG-16a	105.4	102.3	103.4	103.0	104.4	102.6	104.9	102.3	105.3	104.9
HTG-17a	98.9	98.0	97.4	97.0	98.3	96.3	101.6	98.7	99.8	99.3
HTG-18a	99.5	99.2	98.3	96.4	98.8	97.9	100.0	99.9	101.0	100.2
HTG-19a	98.4	94.5	101.1	100.7	99.3	94.0	94.7	94.4	100.5	100.3
HTG-20a	98.6	91.4	95.3	94.0	95.3	93.2	97.1	95.1	98.2	95.8

HTG-21a	97.6	90.1	97.9	96.8	98.9	97.3	96.8	96.2	98.7	96.7
HTG-22a	100.6	95.6	99.3	97.6	98.1	98.0	100.2	98.5	100.1	99.5
HTG-23a	98.7	93.1	98.6	98.3	101.6	97.6	102.8	100.2	98.7	98.5
HTG-24a	100.4	92.6	99.9	98.2	97.8	97.6	100.0	97.9	99.0	97.7
HTG-25a	105.0	102.1	104.1	103.8	103.1	102.0	104.4	101.9	104.8	102.9
HTG-26a	99.7	96.3	101.6	101.0	98.1	96.4	96.8	95.1	99.9	98.2
HTG-27a	100.5	94.7	99.5	98.2	104.4	99.9	102.3	99.8	99.8	99.6
HTG-28a	98.9	95.6	103.5	98.8	101.9	99.1	100.8	98.5	103.5	95.1
HTG-29a	100.9	95.9	97.3	96.8	99.4	97.6	100.6	98.8	98.5	98.0
HTG-30a	104.6	101.5	105.6	104.5	103.6	102.9	105.7	101.2	105.7	105.6
HTG-31a	100.3	97.0	100.5	98.2	99.5	96.7	97.8	97.1	99.2	99.2
HTG-32a	99.6	95.8	99.2	98.7	101.7	98.6	99.3	99.2	102.0	98.8
HTG-33a	99.2	95.4	95.2	95.1	99.7	97.8	98.0	98.0	96.8	94.7
HTG-34a	99.4	95.3	100.9	99.2	99.0	98.5	100.9	98.1	99.9	99.8
HTG-35a	99.5	97.0	99.3	98.9	97.7	95.4	96.1	95.6	99.3	98.9
HTG-36a	99.6	95.1	95.9	95.4	95.8	94.0	98.1	97.7	95.8	95.4
HTG-37a	105.5	101.9	105.7	104.5	104.5	103.9	104.9	103.6	104.1	103.8
HTG-38a	99.7	95.8	99.8	99.3	96.8	93.0	94.9	93.7	99.7	97.9
HTG-39a	97.7	94.2	96.7	94.9	96.3	96.1	95.6	95.1	98.2	97.2
HTG-40a	103.2	101.4	102.5	102.0	105.0	102.2	103.1	102.0	104.5	102.7
HTG-41a	98.1	95.8	99.2	97.9	99.8	97.7	95.9	94.8	96.5	96.2
HTG-42a	99.6	97.0	100.7	100.3	100.1	97.1	100.4	99.0	101.5	98.7
HTG-43a	104.0	100.3	104.9	103.3	103.5	101.7	100.9	100.8	102.3	102.1
HTG-44a	100.0	95.6	98.4	98.2	99.1	98.0	96.4	96.2	98.6	97.4
HTG-45a	98.0	94.9	100.7	97.8	99.4	98.2	98.6	97.7	96.4	96.3
HTG-46a	97.1	92.0	97.3	96.0	99.5	97.9	98.3	98.1	98.4	97.7
HTG-47a	98.1	93.8	95.9	95.9	101.2	97.7	98.3	98.2	98.0	97.4
HTG-48a	98.9	92.9	101.2	99.2	101.2	99.4	99.6	97.4	99.3	98.5
HTG-49a	98.0	92.7	100.5	97.9	102.8	98.3	99.4	99.3	98.4	96.5

HTG-50a	99.9	93.2	99.1	95.0	97.0	95.1	98.6	97.2	98.2	96.4

Table E.5: Heat-treated glass (HTG) specimens. Ratio between the minimum and the maximum residual stresses measured along two orthogonal directions at the center of the plate and at four points on the two diagonals, 100 mm far from the edges. Mean values of the measurements taken along two orthogonal directions at any point. Mean values of the 10 measurements taken at the air side $\sigma_{pc,m}$ for each plate.

Specimen	$\frac{\sigma^c_{pc,II}}{\sigma^c_{pc,I}}$	$\frac{\sigma^1_{pc,II}}{\sigma^1_{pc,I}}$	$\frac{\sigma^2_{pc,II}}{\sigma^2_{pc,I}}$	$\frac{\sigma^3_{pc,II}}{\sigma^3_{pc,I}}$	$\frac{\sigma^4_{pc,II}}{\sigma^4_{pc,I}}$	Mean Values					
						$\sigma^c_{pc,m}$ [MPa]	$\sigma^1_{pc,m}$ [MPa]	$\sigma^2_{pc,m}$ [MPa]	$\sigma^3_{pc,m}$ [MPa]	$\sigma^4_{pc,m}$ [MPa]	$\sigma_{pc,m}$ **[MPa]**
HTG-1b	0.95	0.94	0.96	0.99	0.97	96.40	99.55	98.35	96.10	98.30	**97.74**
HTG-2b	0.98	0.99	0.99	0.99	0.98	94.40	93.60	97.25	97.25	95.60	**95.62**
HTG-3b	0.98	0.96	0.96	0.96	0.99	92.70	95.45	94.85	94.40	95.55	**94.59**
HTG-4b	0.95	0.98	0.99	0.98	0.97	96.80	98.50	97.15	94.95	97.55	**96.99**
HTG-5b	0.98	0.97	0.99	0.98	0.98	94.80	96.25	95.90	95.95	97.45	**96.07**
HTG-6b	0.94	0.96	0.97	0.96	0.97	96.00	99.45	96.10	94.60	96.60	**96.55**
HTG-7b	0.96	0.98	0.97	0.97	0.94	92.40	93.05	93.50	94.65	95.25	**93.77**
HTG-8a	0.97	1.00	0.98	0.99	0.99	99.00	102.20	101.85	104.05	105.20	**102.46**
HTG-9a	0.95	0.98	0.99	0.99	0.98	98.20	100.35	96.70	95.50	101.00	**98.35**
HTG-10a	0.96	0.97	0.97	0.97	0.99	99.10	100.05	98.20	98.90	100.85	**99.42**
HTG-11a	0.95	0.97	0.98	0.99	0.96	98.20	101.90	101.15	100.75	101.10	**100.62**
HTG-12a	0.96	0.99	0.99	0.96	0.98	100.60	99.75	100.60	100.75	99.20	**100.18**

HTG-13a	0.98	0.99	0.98	1.00	0.99	103.75	105.35	103.00	102.90	104.80	**103.96**
HTG-14a	0.98	0.95	0.96	0.99	0.99	97.60	99.00	98.45	101.45	101.55	**99.61**
HTG-15a	0.95	0.99	0.98	0.98	0.96	99.85	100.15	102.10	99.10	99.30	**100.10**
HTG-16a	0.97	0.99	0.98	0.97	0.99	103.85	103.20	103.50	103.60	105.10	**103.85**
HTG-17a	0.99	0.99	0.97	0.97	0.99	98.45	97.20	97.30	100.15	99.55	**98.53**
HTG-18a	0.99	0.98	0.99	0.99	0.99	99.35	97.35	98.35	99.95	100.60	**99.12**
HTG-19a	0.96	0.99	0.94	0.99	0.99	96.45	100.90	96.65	94.55	100.40	**97.79**
HTG-20a	0.92	0.98	0.97	0.97	0.97	95.00	94.65	94.25	96.10	97.00	**95.40**
HTG-21a	0.92	0.98	0.98	0.99	0.97	93.85	97.35	98.10	96.50	97.70	**96.70**
HTG-22a	0.95	0.98	0.99	0.98	0.99	98.10	98.45	98.05	99.35	99.80	**98.75**
HTG-23a	0.94	0.99	0.96	0.97	0.99	95.90	98.45	99.60	101.50	98.60	**98.81**
HTG-24a	0.92	0.98	0.99	0.97	0.98	96.50	99.05	97.70	98.95	98.35	**98.11**
HTG-25a	0.97	0.99	0.98	0.97	0.98	103.55	103.95	102.55	103.15	103.85	**103.41**
HTG-26a	0.96	0.99	0.98	0.98	0.98	98.00	101.3 0	97.25	95.95	99.05	**98.31**
HTG-27a	0.94	0.98	0.95	0.97	0.99	97.60	98.85	102.15	101.05	99.70	**99.87**
HTG-28a	0.96	0.95	0.97	0.97	0.91	97.25	101.15	100.50	99.65	99.30	**99.57**
HTG-29a	0.95	0.99	0.98	0.98	0.99	98.40	97.05	98.50	99.70	98.25	**98.38**
HTG-30a	0.97	0.98	0.99	0.95	0.99	103.05	105.05	103.25	103.45	105.65	**104.09**
HTG-31a	0.96	0.97	0.97	0.99	1.00	98.65	99.35	98.10	97.45	99.20	**98.55**
HTG-32a	0.96	0.99	0.96	0.99	0.96	97.70	98.95	100.15	99.25	100.40	**99.29**
HTG-33a	0.96	0.99	0.98	1.00	0.97	97.30	95.15	98.75	98.00	95.75	**96.99**
HTG-34a	0.95	0.98	0.99	0.97	0.99	97.35	100.05	98.75	99.50	99.85	**99.10**
HTG-35a	0.97	0.99	0.97	0.99	0.99	98.25	99.10	96.55	95.85	99.10	**97.77**
HTG-36a	0.95	0.99	0.98	0.99	0.99	97.35	95.65	94.90	97.90	95.60	**96.28**
HTG-37a	0.96	0.98	0.99	0.98	0.99	103.70	105.10	104.20	104.25	103.95	**104.24**
HTG-38a	0.96	0.99	0.96	0.98	0.98	97.75	99.55	94.90	94.30	98.80	**97.06**
HTG-39a	0.96	0.98	0.99	0.99	0.98	95.95	95.80	96.20	95.35	97.70	**96.20**
HTG-40a	0.98	0.99	0.97	0.98	0.98	102.30	102.25	103.60	102.55	103.60	**102.86**
HTG-41a	0.97	0.98	0.97	0.98	0.99	96.95	98.55	98.75	95.35	96.35	**97.19**

HTG-42a	0.97	0.99	0.97	0.98	0.97	98.30	100.50	98.60	99.70	100.10	**99.44**
HTG-43a	0.96	0.98	0.98	0.99	0.99	102.15	104.10	102.60	100.85	102.20	**102.38**
HTG-44a	0.95	0.99	0.98	0.99	0.98	97.80	98.30	98.55	96.30	98.00	**97.79**
HTG-45a	0.96	0.97	0.98	0.99	0.99	96.45	99.25	98.80	98.15	96.35	**97.80**
HTG-46a	0.94	0.98	0.98	0.99	0.99	94.55	96.65	98.70	98.20	98.05	**97.23**
HTG-47a	0.95	1.00	0.96	0.99	0.99	95.95	95.90	99.45	98.25	97.70	**97.45**
HTG-48a	0.93	0.98	0.98	0.97	0.99	95.90	100.20	100.30	98.50	98.90	**98.76**
HTG-49a	0.94	0.97	0.95	0.99	0.98	95.35	99.20	100.55	99.35	97.45	**98.38**
HTG-50a	0.93	0.95	0.98	0.98	0.98	96.55	97.05	96.05	97.90	97.30	**96.97**

Table E.6: Heat-treated glass (HTG) specimens. Test results: maximum displacement ζ_{max}; fracture load F; time to failure t_f; maximum stress at failure σ_{fail}; equivalent equibiaxial strength σ_{eqb}; equivalent uniform stress that leads to failure in 60 s σ_{60}.

Specimen	Test outputs			Fracture Location	Results		
	ζ_{max} [mm]	F [N]	t_f [s]	Valid/Not Valid	σ_{fail} [MPa]	σ_{eqb} [MPa]	σ_{60} [MPa]
HTG-1b	3.44	23002.14	86.34	Valid	167.10	159.59	**148.96**
HTG-2b	4.07	29126.79	109.04	Valid	205.80	192.72	**180.21**
HTG-3b	4.77	34735.19	131.55	Valid	239.20	219.44	**207.34**
HTG-4b	3.93	27213.86	102.85	Not valid			
HTG-5b	4.90	38408.56	143.29	Not valid			
HTG-6b	3.82	26489.79	99.17	Not valid			
HTG-7b	4.40	33295.85	124.39	Valid	230.80	214.37	**200.44**
HTG-8a	4.41	30677.93	119.51	Valid	215.30	202.35	**188.60**

HTG-9a	4.18	29227.15	111.45	Valid	206.50	193.85	**181.00**
HTG-10a	4.01	28634.53	107.13	Not valid			
HTG-11a	4.18	30350.31	113.56	Valid	213.30	199.73	**186.81**
HTG-12a	5.63	43614.85	170.70	Valid	288.00	260.69	**246.99**
HTG-13a	4.87	33168.93	130.21	Valid	230.10	212.23	**200.78**
HTG-14a	4.94	36830.80	141.41	Valid	251.00	232.71	**217.45**
HTG-15a	4.29	32149.70	120.18	Not valid			
HTG-16a	5.60	44313.12	165.21	Not valid			
HTG-17a	4.13	27246.26	106.75	Not valid			
HTG-18a	4.81	34176.08	133.65	Valid	235.90	217.90	**205.10**
HTG-19a	4.19	29823.70	111.60	Valid	210.10	198.15	**183.91**
HTG-20a	5.68	44961.48	172.58	Valid	295.10	267.36	**252.21**
HTG-21a	5.36	39890.49	152.71	Valid	268.00	244.52	**230.90**
HTG-22a	4.61	33471.26	125.00	Valid	231.80	215.41	**201.73**
HTG-23a	4.47	31178.71	121.19	Valid	218.30	203.86	**190.68**
HTG-24a	5.17	39632.83	148.45	Not valid			
HTG-25a	5.70	45004.16	171.32	Valid	295.40	269.86	**252.87**
HTG-26a	4.79	35556.82	132.76	Not valid			
HTG-27a	4.54	34620.24	129.23	Valid	238.50	222.39	**207.26**
HTG-28a	4.43	32269.10	120.62	Valid	224.70	208.93	**196.05**
HTG-29a	5.51	43376.58	161.68	Valid	286.80	262.91	**245.89**
HTG-30a	5.38	43309.42	161.41	Valid	286.40	259.49	**245.98**
HTG-31a	4.05	25142.23	98.70	Valid	181.00	172.64	**160.25**
HTG-32a	3.91	27032.20	102.78	Valid	192.90	182.81	**170.04**
HTG-33a	4.50	33668.54	125.91	Not valid			
HTG-34a	5.12	39232.06	147.76	Valid	264.30	241.45	**228.18**
HTG-35a	5.42	42509.72	158.60	Valid	282.10	257.13	**242.23**
HTG-36a	4.22	30613.51	114.47	Not valid			
HTG-37a	4.68	34788.30	132.18	Valid	239.50	223.18	**208.43**

HTG-38a	5.49	42857.57	160.59	Valid	284.00	260.17	**243.64**
HTG-39a	5.76	47102.26	175.50	Valid	306.30	275.07	**260.80**
HTG-40a	5.44	41532.44	162.45	Valid	276.90	252.88	**238.43**
HTG-41a	4.75	35530.16	132.67	Valid	243.80	226.89	**211.27**
HTG-42a	5.65	45613.75	172.07	Valid	299.50	272.00	**255.08**
HTG-43a	5.54	46514.94	173.41	Not valid			
HTG-44a	3.46	22417.68	85.96	Not valid			
HTG-45a	5.34	42263.55	164.67	Valid	280.80	254.90	**241.19**
HTG-46a	4.81	37150.70	141.55	Not valid			
HTG-47a	4.75	34660.25	134.41	Valid	238.80	222.53	**207.23**
HTG-48a	4.55	34616.56	129.26	Valid	238.50	220.72	**207.14**
HTG-49a	5.30	42049.00	156.81	Not valid			
HTG-50a	4.52	32382.07	123.86	Not valid			
HTG-51a	3.22	20972.53	80.77	Valid	153.70	147.69	**137.94**

REFERENCES

[1] H. K. Aben. Magnetophotoelasticity − photoelasticity in a magnetic field. *Exper Mech*, 10:97–105, 1970.

[2] H. K. Aben, J. Anton, A. Errapart, S. Hödemann, J. Kikas, H. Klaassen, and M. Lamp. On complete non−destructive residual stress measurement in architectural glass panels and automotive glazing. In *Proceedings of Glass Processing Days: 9th Int. Conf. on Architectural and Automotive Glass*, pages 1–3, 2009.

[3] H. K. Aben and C. Guillemet. *Photoelasticity of Glass*. Springer, Berlin (DE), 1993.

[4] J. Anton, A. Errepart, M. Paemurru, D. Lochegnies, S. Hodemann, and H. K. Aben. On the inhomogeneity of residual stresses in tempered glass panels. *Estonian J Eng*, 18:3–11, 2012.

[5] ASTM C1036. *Standard specification for flat glass*. The American Society for Testing and Materials, 2016.

[6] ASTM C1499. *Standard Test Method for Monotonic Equibiaxial Flexural Strength of Advanced Ceramics at Ambient Temperature*. The American Society for Testing and Materials, 2009.

[7] M. Badalassi, L. Biolzi, G. Royer-Carfagni, and W. Salvatore. Safety factors for the structural design of glass. *Constr Build Mater*, 55:114 – 127, 2014.

[8] R. Ballarini, G. Pisano, and G. Royer Carfagni. The lower bound for glass strength and its interpretation with generalized Weibull statistics for structural applications. *ASCE J Eng Mech*, 142(12):04016100/1–20, 2016.

[9] R. Ballarini, G. Pisano, and G. Royer Carfagni. New calibration of partial material factors for the structural design of float glass. Comparison of bounded and unbounded statistics for glass strength. *Constr Build Mater*, 121:69–80, 2016.

[10] N. Bansal and R. Doremus. *Handbook of glass properties*. Academic Press, Orlando (USA-FL), 1986.

[11] G. M. Bartenev. *Zh Tekh Fiz*, 18:383–388, 1948. [In Russian].

[12] S. Batdorf and J. Crose. A statistical theory for the fracture of brittle structures subjected to nonuniform polyaxial stresses. *J Appl Mech*, 2:459–464, 1974.

[13] W. Beason and J. Morgan. Glass failure prediction model. *ASCE J Struct Eng*, 110(2):197–212, 1984.

[14] F. Bernard and L. Daudeville. Point fixings in annealed and tempered glass structures: modeling and optimization of bolted connections. *Eng Struct*, 31(4):946–955, 2009.

[15] K. Bickerstaff and A. Pilkington. Improvements in or relating to the manufacture of flat glass, 1954. GB Patent 769692.

[16] K. Bickerstaff and A. Pilkington. Manufacture of flat glass, 1959. US Patent 2911759.

[17] P. Billingsley. *Probability and Measure*. Wiley, New York (USA-NY), 1995.

[18] A. Brückner-Foit, F. Fett, K. Schirmer, and D. Munz. Discrimination of multiaxiality criteria using brittle fracture loci. *J Eur Ceram Soc*, 16:1201–1207, 1996.

[19] CEN/TC129/WG8. An overview of prEN-13474 and the work of CEN/TC129/Wg8 from which it was developed. Internal document, February 2006.

[20] Y. Chen, D. Lochegnies, R. Defontaine, J. Anton, H. K. Aben, and R. Langlais. Measuring the 2D residual surface stress mapping in tempered glass under the cooling jets: the influence of process parameters on the stress homogeneity and isotropy. *Strain*, 49:60–67, 2013.

[21] S. Choi, L. Powers, and N. Nemeth. Slow crack growth behavior and life/reliability analysis of 96wt alumina at ambient temperature with various specimen/loading configurations. Technical Memorandum 210206, NASA, 2000.

[22] M. Ciccotti. Stress-corrosion mechanisms in silicate glasses. *J Phys D*, 42(21):214006, 2009.

[23] CNR-DT/210. *Guide for the Design, Construction and Control of Buildings with Structural Glass Elements*. Italian National Research Council (CNR), 2013.

[24] K. Cummings. *A history of glassforming*. A & C Black, London (UK), 2002.

[25] R. Dall'Igna, A. D'Este, and M. Silvestri. Comments on test methods for the determination of structural glass strenght. In *Proceedings XXV ATIV Conference*, pages 5–13, 2010.

[26] K. Datsiou and M. Overend. Artificial ageing of glass with sand abrasion.

Constr Build Mater, 142:536–551, 2017.

[27] D. Devos, M. Duquennoy, E. Roméro, F. Jenot, D. Lochegnies, M. Ouaftouh, and M. Ourak. Ultrasonic evaluation of residual stresses in flat glass tempering by an original double interferometric detection. *Ultrasonics*, 44:923–927, 2006.

[28] DIN 18008:2010-12. *Glass in Building - Design and construction rules.* German Institute for Standardisation (Deutsches Institut für Normung), 2010.

[29] M. Duquennoy, M. Ouaftouh, M. Ourak, and F. Jenot. Theoretical determination of rayleigh wave acoustoelastic coefficients: comparison with experimental values. *Ultrasonics*, 39:575–583, 2002.

[30] M. Durchholz, B. Goer, and G. Helmich. Method of reproducibly predamaging float glass as a basis to determine the bending strength. *Glastech Ber Glass Sci Technol*, 68:251–2, 1995.

[31] EN 1288-2. CEN/TC129. *Glass in building - Determination of bending strength of glass - Part 2: Coaxial double ring test on flat specimens with large test surface areas.* European Standard, 2001.

[32] EN 1288-3. CEN/TC129. *Glass in building - Determination of the bending strength of glass - Part 3: Test with specimen supported at two points (four point bending).* European Standard, 2001.

[33] EN 1288-4. CEN/TC129. *Glass in building - Determination of bending strength of glass - Part 4: Testing of channel shaped glass.* European Standard, 2001.

[34] EN 1288-5. CEN/TC129. *Glass in building - Determination of the bending strength of glass - Part 5: Coaxial double ring test on flat specimens with small test surface areas.* European Standard, 2001.

[35] EN 1288. CEN/TC129. *Glass in building - Determination of the bending strength of glass.* European Standard, 2001.

[36] EN1748-1-1. CEN. *Glass in building. Special basic products - Borosilicate glasses - Part 1-1: Definitions and general physical and mechanical properties.* European Standard, 2004.

[37] EN1990. CEN-TC250. *Eurocode 0 - Basis of structural design.* European Standard, 2005.

[38] EN1991-1-3. CEN-TC250. *Eurocode I - actions on structures - Part 1-3: General actions - snow loads.* European Standard, 2003.

[39] EN1991-1-4. CEN-TC250. *Eurocode I - actions on structures - Part 1-4: General actions - wind actions.* European Standard, 2005.

[40] EN572-1. CEN. *Glass in building. Basic soda lime silicate glass products. Definitions and general physical and mechanical properties.* European Standard, 2012.

[41] EN572-2. CEN. *Glass in building. Basic soda lime silicate glass products.*

Part 2: Float glass. European Standard, 2012.

[42] A. G. Evans. A general approach for the statistical analysis of multiaxial fracture. *J Am Ceram Soc*, 61:302–308, 1978.

[43] H. Fessler and D. Fricker. A theoretical analysis of the ring-on-ring loading disk test. *J Am Ceram Soc*, 67(9):582–588, 1984.

[44] A. Franco and G. Royer Carfagni. Critical issues in the design-by-testing of glass structures. *Eng Struct*, 99:108–119, 2015.

[45] A. Franco and G. Royer Carfagni. Verification formulae for structural glass under combined variable loads. *Eng Struct*, 83:233–242, 2015.

[46] A. Freudenthal. *Fracture, an Advanced Treatise*, chapter Statistical approach to brittle fracture, pages 591–619. Academic Press, New York (USA-NY), 1968.

[47] S. Gibson, G. W. Jewell, and R. A. Tomlinson. Full−field pulsed magnetophotoelasticity − experimental implementation. *J Str Anal Eng Des*, 41:171–182, 2006.

[48] A. Griffith. Full−field pulsed magnetophotoelasticity − experimental implementation. *Philos Trans R Soc London Ser A*, 221:163–198, 1920.

[49] M. Haldimann. *Fracture strength of structural glass elements - analytical and numerical modelling, testing and design*. PhD thesis, École Polytechnique Fédérale de Lausanne, 2006.

[50] V. Indenbom and L. Vidro. *Fiz Tverd Tela [English transl.: Sov Phys Solid State]*, 6:767–772, 1964.

[51] C. Inglis. Stresses in a plate due to the presence of cracks and sharp corners. In *Proceedings of the Institution of Naval Architects*, volume 55, pages 219–241, 1913.

[52] G. Irwin. Analysis of stresses and strains near the end of a crack traversing a plate. *J Appl Mech*, 24:361–364, 1957.

[53] G. Jilbert and J. Field. Synergistic effects of rain and sand erosion. *Wear*, 243:6–17, 2000.

[54] B. Lawn and T. Wilshaw. *Fracture of brittle solids*. Cambridge University Press, Cambridge (UK), 1975.

[55] M. Lindqvist and J. Lebet. Strength of glass determined by the relation of the critical flaw to the fracture mirror. *Eng Fract Mech*, 119:43–52, 2014.

[56] M. Madjoubi, C. Bousbaa, M. Hamidouche, and N. Bouaouadja. Weibull statistical analysis of the mechanical strength of a glass eroded by sand blasting. *J Eur Ceram Soc*, 19:2957–2962, 1999.

[57] I. Maniaitis, G. Nehring, and G. Siebert. Studies on determining the bending strength of thin glasses. In *Proceedings of the Institution of Civil Engineering: Structures and Buildings*, volume 169, pages 393–402, 2016.

[58] A. Marshall and I. Olkin. A new method for adding a parameter to a

family of distributions with application to the exponential and Weibull families. *Biometrika*, 84(3):641–652, 1997.

[59] H. M. McKenzie and R. J. Hand. *Basic Optical Stress Measurement in Glass*. Society of Glass Technology, Sheffield (UK), 1999.

[60] D. Moore, G. McCabe, and B. Craig. *Introduction to the practice of statistics*. W.H. Freeman and Co., New York (USA-NY), 2015.

[61] D. Munz and T. Fett. *Ceramics: Mechanical Properties, Failure Behaviour, Materials Selection*. Springer, Heidelberg (DE), 1999.

[62] O. S. Narayanaswamy. A model of structural relaxation in glass. *J Am Ceram Soc*, 54:491–498, 1971.

[63] O. S. Narayanaswamy and R. Gordon. Calculation of residual stresses in glass. *J Am Ceram Soc*, 52:554–558, 1969.

[64] W. Navidi. *Statistics for Engineers and Scientists*. McGraw-Hill, New-York (USA-NY), 2011.

[65] D. Neumer and G. Siebert. Influence of edge design and location of load introduction on the loadbearing capacity of glass. In *IABSE Symposium Report, IABSE Conference Nara 2015: Elegance in Structures*, pages 1–5, 2015.

[66] J. Nielsen, J. Olesen, P. Poulsen, and H. Stang. Finite element implementation of a glass tempering model in three dimensions. *Comput Struct*, 88(17-18):963–972, 2010.

[67] H. S. Norville, D. L. Sheridan, and S. L. Lawrence. Strength of new heat treated window glass lites and laminated glass units. *ASCE J Struct Eng*, 119(3):891–901, 1993.

[68] I. C. Noyan, T. C. Huang, and B. R. York. Residual stress/strain analysis in thin films by x-ray diffraction. *Crit Rev Solid State Mater Sci*, 20:125–177, 1995.

[69] I. Nurhuda, N. Lam, E. Gad, and I. Calderone. Estimation of strengths in large annealed glass panels. *Int J Solids Struct*, 47(18):2591 – 2599, 2010.

[70] G. Pisano and G. Royer Carfagni. The statistical interpretation of the strength of float glass for structural applications. *Constr Build Mater*, 98:741–756, 2015.

[71] G. Pisano and G. Royer Carfagni. Towards a new standardized configuration for the coaxial double test for float glass. *Eng Struct*, 119:149–163, 2016.

[72] G. Pisano and G. Royer Carfagni. A micromechanical derivation of the macroscopic strength statistics for pristine or corroded/abraded float glass. *J Eur Ceram Soc*, 37(13):4197–4206, 2017.

[73] G. Pisano and G. Royer Carfagni. Statistical interference of material strength and surface prestress in heat-treated glass. *J Am Ceram Soc*, 100(3):954–967, 2017.

[74] R. L. Plackett. Karl pearson and the chi-squared test. *Int Stat Rev*, 51(1):59–72, 1983.

[75] M. I. Porter and G. T. Houlsby. Development of crack size and limit state design methods for edge-abraded glass members. *Struct Eng*, 79(8):29–35, 2001.

[76] L. Powers, J. Salem, and A. Weaver. Stresses in ceramic plate subjected to loading between concentric rings. ASTM STP 1409, pages 30–45. ASTM International, 2002.

[77] prEN 16612:2013. CEN/TC 250. *Glass in building - Determination of the load resistance of glass panes by calculation and testing.* European Standard, 2013.

[78] J. N. Reddy. *Theory and Analysis of Elastic Plates and Shells.* CRC Press, Boca Raton (USA-FL), 2006.

[79] Y. Rodichev, Y. Yevplov, H. Soroka, F. Veer, N. Tregubov, and V. Polivyany. Surface defects and statistical characteristics of glass strength. In *Challenging Glass 3 - Conference on Architectural and Structural Applications of Glass*, pages 535–552, 2012.

[80] C. Saha and A. Cooper. Effect of etched depth on glass strength. *J Am Ceram Soc*, 67(8):C158–C160, 1984.

[81] J. Salem and L. Powers. Guidelines for the testing of plates. In *27th Annual Cocoa Beach Conference on Advanced Ceramics and Composites B: Ceramic Engineering and Science Proceedings*, volume 24, pages 357–364, 2003.

[82] J. Schneider. *Festigkeit und Bemessung punktgelagerter Gläser und stoßbeanspruchter Gläser.* PhD thesis, TU Darmstadt, 2001. [In German].

[83] J. Schneider. Glass strength in the borehole area of annealed float glass and tempered float glass. *Int J Form Processes*, 7(4):523–541, 2004.

[84] S. Schula. *Characterization of the scratch sensitivity of glasses in civil engineering.* PhD thesis, TU Darmstadt, 2015. [In German].

[85] V. Sglavo, R. D. Maschio, and G. Sorarù. Effect of etch depth on strength of soda-lime glass rods by a statistical approach. *J Eur Ceram Soc*, 11:341–346, 1993.

[86] J. Shelby. *Introduction to glass science and technology*, chapter 4.1, page 191. Royal Society of Chemistry, Cambridge (UK), 2005.

[87] D. Stirzaker. *Elementary probability.* Cambridge University Press, Cambridge (UK), 2003.

[88] S. Timoshenko and S. Woinowsky-Krieger. *Theory of Plates and Shells.* McGraw-Hill, New-York (USA-NY), 1959.

[89] F. Veer, P. Oikonomopoulou, T. Riemslag, P. Carvalho, P. Cruz, Y. Rodichev, and H. Soroka. Consistency of pre-stress and bending strength of annealed, heat stressed and tempered glass. In *Glass Per-*

formance Days (GPD): Conference Proceedings, pages 538–544, 2013.

[90] F. Veer and Y. Rodichev. The relation between pre-stress and failure stress in tempered glass. In *Challenging Glass 4 & COST Action TU0905 Final Conference*, pages 731–738, 2014.

[91] F. A. Veer, P. C. Louter, and F. P. Bos. The strength of annealed, heat-strengthened and fully tempered float glass. *Fatigue Fract Eng M*, 32(1):18–25, 2009.

[92] Z. Wang, L. Liu, X. Li, and L. Zhao. An experimental method for analyzing environmental effects of blowing sands on glass abrasion. *Procedia Environ Sci*, 2:207–217, 2010.

[93] S. Way. Bending of circular plates with large deflection. *Trans Am Soc Mech Eng*, 56:627–636, 1934.

[94] W. Weibull. A statistical theory of the strength of materials. *Ingeniörsvetenskapsakademiens Handlingar*, 151:1–45, 1939.

[95] H. Wensink and M. Elwenspoek. A closer look at the ductile-brittle transition in solid particle erosion. *Wear*, 253:1035–1043, 2002.

[96] A. Wereszczak, M. Ferber, and W. Musselwhite. Method for identifying and mapping flaw size distributions on glass surfaces for predicting mechanical response. *Int J Appl Glass Sci*, 5(1):16–21, 2014.

[97] A. Wereszczak, T. Kirkland, M. Ragan, K. Strong, H. Lin, and P. Patel. Size scaling of tensile failure stress in a float soda-lime-silicate glass. *Int J Appl Glass Sci*, 1(2):143–150, 2010.

[98] H. Westergaard. Bearing pressures and cracks. *J Appl Mech*, 61:A49–A53, 1939.

[99] S. Wiederhorn. Fracture surface energy of glass. *J Am Ceram Soc*, 52(2):99–105, 1969.

[100] S. Wiederhorn and L. Bolz. Stress corrosion and static fatigue of glass. *J Am Ceram Soc*, 53(10):543–548, 1970.

[101] S. M. Wiederhorn, S. W. Freiman, E. Fuller Jr, and C. Simmons. Effects of water and other dielectrics on crack growth. *J Mater Sci*, 17(12):3460–3478, 1982.

[102] X. Xiao and X. Yan. A numerical analysis for cracks emanating from a surface semi-spherical cavity in an infinite elastic body by FRANC3D. *Eng Fail Anal*, 15:188–192, 2008.

[103] D. Yankelevsky. Strength prediction of annealed glass plates - a new model. *Eng Struct*, 79:244–255, 2014.

[104] M. Zaccaria and M. Overend. The mechanical performance of bi−treated glass. In *Challenging Glass 4 and COST Action TU0905 Final Conference*, pages 747–753, 2014.

[105] M. Zaccaria and M. Overend. Thermal healing of realistic flaws in glass. *J Mater Civ Eng*, 28(2):04015127, 2016.

[106] K. Zammit and M. Overend. A computer algorithm for determining the tensile strength of float glass. *Eng Struct*, 45:68 – 77, 2012.

[107] T. Zhang and M. Xie. Failure data analysis with extended weibull distribution. *Commun Stat B-Simul*, 36(3):579–592, 2007.

LIST OF FIGURES

Page

LIST OF TABLES

Page

LIST OF SYMBOLS

Γ	Euler Gamma function
ΔA	Representative area
Θ	Third term of the Extended Weibull distribution
Υ	Normalization constant
Σ	Generic state of stress
Φ	$f_{test}^{n+1}/\dot{\sigma}_{test}$ =constant
Ω	Angle containing the normals to all the potential crack planes for which the component of stress orthogonal to the crack plane exceeds σ_{cr}
α	Scaling parameter of the power law distribution
α^*	$\alpha - 1$
α_R	Coefficient dependent upon T_R (wind action - see equation (C.1))
β	Reliability index (level II method) or angle shown in Figure 4.6
γ_f	Partial factor for the actions
γ_m	Partial factor for the material
γ_p	Partial factor for prestress
δ	Depth of a micro-crack
δ_c	Critical crack depth
δ_i	Initial crack depth
δ_{min}	Lower bound of the power law distribution
δ_{max}	Maximum crack depth
ϵ	Etch depth
ϵ'_θ	Circumferential membrane strain
ϵ''_θ	Circumferential bending strain (non-linear regime)
ϵ'_r	Radial membrane strain
ϵ''_r	Radial bending strain (non-linear regime)
ζ	Vertical displacement of the plate
ζ_0	$\delta_{min}/\Delta A^{1/\alpha^*}$
$\zeta_{0,3m}$	See equation (5.16)

η_0	Scale parameter of the Weibull distribution
$\eta_{0,2p}$	Scale parameter of the two-parameter Weibull distribution
$\eta_{0,2p,3m}$	See equation (5.18)
$\eta_{0,lt}$	Scale parameter of the left-truncated Weibull distribution
$\eta_{0,lt,3m}$	See equation (5.21)
$\eta_{0,tt,3m}$	See equation (5.26)
ϑ, κ, ϖ	See Equations (B.26) and (B.29)
λ	Parameter accounting for the influence of size and stress state in the verification formula of level I methods
μ	Mean value
μ_i	Roof shape coefficient (snow action)
ν	Poisson's ration
ν_0	Conventional sub-critical value of the crack propagation
ξ	Radial displacement of the plate
ρ	Ratio between the principal stresses
ρ_{air}	Air density
ρ_g	Glass density
ϱ	Radius of curvature
σ_0	Lower bound of the glass strength
σ_1	Maximum principle stress
σ_2	Minimum principle stress
σ_{60}	Equivalent uniform stress that leads to failure in 60 seconds
$\sigma_\perp$	Tensile stress at right angle with crack axis
σ_ϵ	Critical stress associated to cracks of depth ϵ
σ_θ	Circumferential bending stress (linear regime)
σ'_θ	Circumferential membrane stress
σ''_θ	Circumferential bending stress (non-linear regime)
σ_ϱ	Stress at the crack tip
σ_τ	Stress causing failure after time τ
$\sigma_R(z)$	Residual stress across the thickness
σ_{ann}	Annealed glass strength
σ_{center}	Equibiaxial stress at the center of the plate
σ'_{center}	Equibiaxial membrane stress at the center of the plate
σ''_{center}	Equibiaxial bending stress at the center of the plate
σ_{cr}	Critical Stress
σ_{edge}	Radial stress at the edge of the plate
σ_{eq}	Equivalent stress
σ_{eqb}	Equibiaxial stress
σ_{fail}	Stress that leads to failure for a ramp stress history
σ_{htg}	Heat treated glass strength
σ_k	Critical stress associated to cracks of depth δ_{min}
σ_{max}	Maximum stress acting within the plate when failure occurs
σ_{pc}	Surface residual stress
σ_r	Radial bending stress (linear regime)
σ'_r	Radial membrane stress
σ''_r	Radial bending stress (non-linear regime)
σ_{unx}	Uniaxial stress

$\dot{\sigma}_{test}$	Stress rate of a test
υ	Standard deviation
ϕ	Angle shown in Figure 3.7(a)
φ	$-\frac{d}{dr}\zeta(r)$
ψ	Angle between the maximum principle stress direction and the normal to the crack plane
χ^2_g	Chi-square distribution
ω	Coefficient major than unity
A	Generic surface area
A_0	Reference unitary surface area
A_{eff} or A_{ef}	$K \cdot A$ Effective area
A_l	Surface area delimited by the inner loading points in the 4PB configuration
A_{sl}	Altitude above sea level
B	Risk of failure
B_0, B_2, C_1, C_3	Constants of the expansions in Taylor' series
C	Center of the Mohr' circle or center of the plate
C_E	Exposure coefficient (snow action)
C_T	Thermal coefficient (snow action)
D	Bending stiffness of the plate
E	Young's modulus
E_d	Design action
F	Force applied by the tensometer during a generic test
F^*	Force applied by the tensometer during the test according to the standard EN 1288-2
$F_a(\sigma_{ann})$	Probability cumulative function for the pristine annealed glass strength
$F_p(\sigma_{pc})$	Probability cumulative function for the surface pre-compressions
$F_t(\sigma_{max})$	Probability cumulative function associated with the failure of a heat-treated specimen at σ_{max}
G	Coefficient for the graphical estimation of the LTW parameters
H_0	Null hypothesis (Chi-square goodness of fit test)
K	Constant lower than unity that, multiplied by A, gives the effective area
K_0	Value of the SIF below which no propagation occurs
K_{FI}	Multiplicative coefficient $K_{FI} < 1 (> 1)$ for the action to pass from CC2 to CC1 (CC3)
K_I, K_{II}, K_{III}	SIF in mode I, mode II and mode III
K_{Ic}	Critical SIF in mode I
K_{Im}	SIF normalized with respect to the value $\bar{\mathrm{K}} = \sigma\sqrt{\pi R}$
K_r	Coefficient depending upon the field exposure category (wind pressure)
K_{unx}	Value of K for an uniaxial state of stress
N	Number of elements
N_0	Number of the elements ΔA in the area A_0

N_{par}	Number of parameters
P_0	Probability of failure corresponding to the stress σ_0 in the original 2-parameter Weibull distribution
P_f	Probability of failure
P_n	Annual probability of exceedance for snow loads
P_s	Probability of survival
Q	Design action of characteristic duration
$\Re$	Domain of the resistances
R_1	Radius of the inner ring (CDR test)
R_2	Radius of the outer ring (CDR test)
R_3	Radius of the circular plate
R_d	Design resistance
R_M	Multiplicative coefficient $R_M < 1 (> 1)$ for the resistances to pass from CC2 to CC1 (CC3)
S	Domain of the actions
$S(\gamma_f Q)$	Maximum stress acting within the plate, induced by action Q multiplied by γ_f
S'_θ	σ'_θ / E
S''_θ	σ''_θ / E
$S_p(\sigma)$	Correlation between the maximum stress acting within the plate and the wind pressure p_w
S'_r	σ'_r / E
S''_r	σ''_r / E
T	Generic constant
T_R	Return period of the applied actions
V	Variation coefficient of the series of maximum annual snow loads
W	Correction coefficient for the effective area
X_0	Intercept with the x-axis
X_g^2	Measure of the discrepancy between the observed and the expected frequencies (Chi-square goodness of fit test)
X_x	Intercept with the y-axis
Y	Shape factor for the stress concentration at the crack tip
Z	Standardized normal variable
a	R/r, see Figure 3.7
b	Specimen width in the 4PB configuration
c_d	Dynamic factor (wind action)
$c_e(z)$, $c_{e1}(z)$	Exposure coefficient (wind action)
c_p	Pressure coefficient (wind action)
c_t	Orographic coefficient (wind pressure)
d	Distance between loading and supporting points in the 4PB configuration
$f_a(\sigma_{ann})$	Probability density function for the pristine annealed glass strength
f_g	Strength of glass
$f_p(\sigma_{pc})$	Probability density function for the surface pre-comressions

$f_t(\sigma_{max})$	Probability density function associated with the failure of a heat-treated specimen at σ_{max}
f_{test}	Tensile stress measured at the end of the test
g	Number of degrees of freedom (Chi-square goodness of fit test)
h	Plate thickness
k	Number of classes (Chi-square test)
k_{mod}	Factor accounting for the static fatigue
l	Side length of a square plate
m	Shape parameter of the Weibull distribution
m_θ	Circumferential moment
m_r	Radial moment
n	Crack velocity parameter
$n(\sigma)$	Material function accounting for the strength properties
p^*	Overpressure according to the standard EN 1288-2
$p_{w,3sec}$	Wind peak pressure corresponding to the average over time 3 s
$p_{w,10min}$	Wind peak pressure corresponding to the average over time 10 min
q_{sk}	Characteristic snow load value on the ground for a 50 years return period
q_{sn}	Snow load
t or τ	Time
t_f	Time to failure
t_r	Shear stress in the radial direction
u	Non-dimensional radial distance ($u = r/h$)
$v_b(T_R)$	Wind velocity corresponding to T_R
$v_{b,50}$	Characteristic wind velocity at 10 m above ground averaged over 10 minutes
z_0, z_{min}	Reference heights (wind pressure)

LIST OF ACRONYMS

2PW	Two-Parameter Weibull distribution
3PB	Three Points Bending
3PW	Three-Parameter Weibull distribution
4PB	Four Points Bending
ASTM	American Society for Testing and Materials
BLW	Bi-Linear Weibull distribution
BMW	Bi-Modal Weibull distribution
BSG	BoroSilicate Glass
CEN	European Committee for Standardization
CC	Class of Consequence
CDR	Coaxial Double Ring
CNR	National Research Council (IT)
CV	Coefficient of Variation
CVT	Change of Variable Theorem
DIN	German Institute for Standardization (DE)
DT	Technical Document (IT)
EN	European Norm
EXW	EXtended Weibull distribution
FEM	Finite Element Method
LEFM	Linear Elastic Fracture Mechanics
LTW	Left-Truncated Weibull distribution
MLE	Maximum Likelihood Estimation
MOD	Model
RAE	Representative Area Element
SCALP	SCAttered Light Polariscope
SF	Section Force for unit width
SIF	Stress Intensity Factor
SLG	Soda Lime silica Glass
SM	Section Moment for unit width
TC	Technical Committee
WG	Working Group